NASA CR-159821
RI/RD79-322

NASA

FINAL REPORT

SMALL, HIGH-PRESSURE LIQUID HYDROGEN TURBOPUMP

by

A. Csomor and D. J. Warren

Rockwell International

Rocketdyne Division

prepared for

NATIONAL AERONAUTICS AND SPACE ADMINISTRATION

NASA-Lewis Research Center

Contract NAS3-21008

R. E. Connelly, Project Manager

Mark 48 H_2 Turbopump

FOREWORD

The work herein was conducted from 7 June 1977 to 26 October 1979 by personnel from the Advanced and Propulsion Engineering and Engineering Test units at Rocketdyne, a division of Rockwell International, under Contract NAS3-21008. Mr. Robert Connelly, Lewis Research Center, was NASA Project Manager. At Rocketdyne, Mr. Harold Diem, Program Manager, and Mr. A. Csomor, Project Engineer, were responsible for the direction of the program.

Important contributions to the conduct of the program and to the preparation of the report material were made by the following Rocketdyne personnel.

Turbomachinery	Mr. C. E. Nielson
Turbomachinery	Mr. J. L. Boynton
Turbomachinery	Mr. A. King
Turbomachinery	Dr. E. D. Jackson
Consultant	Dr. K. Rothe
Structural Dynamics	Mr. B. F. Rowan
Structural Dynamics	Mr. A. Campany
Structural Dynamics	Mr. R. F. Beatty
Chemical and Advanced Component Test	Mr. J. C. Pulte

CONTENTS

ILLUSTRATIONS

TABLES

SUMMARY

The overall objective of the Small High-Pressure Hydrogen Turbopump Program is to establish the technology base for pumping small quantities, 2.72 kg/s (6 lb/sec), of hydrogen to high-pressure levels, 3174 N/cm^2 (4600 psi). Planned future applications in rocket engines for orbital transfer vehicles require, in general, high overall turbopump performance and, specifically, high pump suction capability. Turbopumps in this category are needed for applications in small, high-performance reusable, versatile, staged-combustion and expander-cycle rocket engines.

Prior effort on the small high-pressure hydrogen turbopump has been accomplished by Rocketdyne, under the direction of NASA-Lewis Research Center (LeRC) (Contract No. NAS3-17794). This effort included fluid-dynamic and mechanical analyses and design to establish a configuration that would best meet the design requirements located in Table 1. To accomplish the above design objective, analysis and design effort was expended to produce specifications and shop drawings in sufficient detail to permit fabrication of test hardware. The design shown in Fig. 1 includes a three-stage centrifugal pump with radial diffusers and internal crossovers. Power to the pump is developed by an axial-flow, two-stage, reaction-type turbine, using the combustion products of liquid hydrogen (LH_2) and liquid oxygen (LO_2). Rotor axial thrust control is provided by incorporating a self-compensating, double-acting balance piston as an integral part of the third-stage impeller rear shroud. The rotor is supported on a pair of angular contact ball bearings on each end. All bearings are cooled by recirculating LH_2 internally through them. A floating-ring, shaft-riding seal is used to prevent turbine hot gases from entering the pump region. The design speed of the rotor was established at 9947 rad/s (95,000 rpm). The nominal design parameters for the pump and turbine are listed in Tables 2 and 3, respectively.

Hardware for two turbopump assemblies was fabricated. Two types of impellers were included: (1) an integral impeller whose flow passages were formed by electrical-discharge machining (EDM), and (2) a split impeller, which was fabricated by machining in two pieces then welding to form the assembly.

The LH_2 turbopump assembly was tested at LIMA stand of Rocketdyne's Advanced Programs Test Facility. The assembly was per RS009601E, Appendix A.

Three test series have been performed. A complete summary of the tests conducted to date is included in Table 4. Ten tests were conducted on the first test series on one turbopump assembly, accumulating a total time of 884 seconds. Liquid hydrogen was used as the pump fluid, and the turbine was propelled by ambient-temperature gaseous hydrogen (GH_2). The test speed ranged up to 9739 rad/s (93,000 rpm). Pump discharge pressures ranging up to 2883 N/cm^2 (4182 psia), and flowrates up to 0.032 m^3/s (509 gpm) were generated. The maximum attained speed and output were limited by the available facility pressure of the turbine drive gas.

TABLE 1. MARK 48-F TURBOPUMP NOMINAL DESIGN CONDITIONS

	SI Units	English Units
Pump		
Type	Centrifugal	
Propellant	LH_2	
Inlet pressure	49 N/cm^2	71 psia
Inlet temperature	21-23 K	38-41 R
Discharge pressure	3140 N/cm	4560 psia
Mass flow	2.74 kg/s	6.04 lb/sec
Number of stages	3	
Turbine		
Working fluid	O_2/H_2 combustion products	(H_2 x H_2O)
Inlet temperature	1033 K	1860 R
Inlet pressure	2360 N/cm^2	3420 psia
Pressure ratio	Minimum necessary to develop pump horsepower requirements	
Flowrate	3.02 kg/s	6.66 lb/sec
Number of stages	2	
Type	Full admission	
Turbopump		
Capable of operation at pumped-idle conditions, i.e., approximately 5 to 10% full thrust		
Off-design operation:	+20% Q/N at full thrust down to 30% Q/N at 20% N	
Service life between overhauls:	*300 thermal cycles or 10 hours accumulated run time	
Service-free life:	*60 thermal cycles or 2 hours accumulated run time	
Maximum single run duration:	2000 seconds	
Maximum time between firings during mission:	14 days	
Minimum time between firings during mission:	1 minute	
Maximum storage time in orbit (dry):	52 weeks	

*Thermal cycle defined as engine start (to any thrust level) and shutdown.

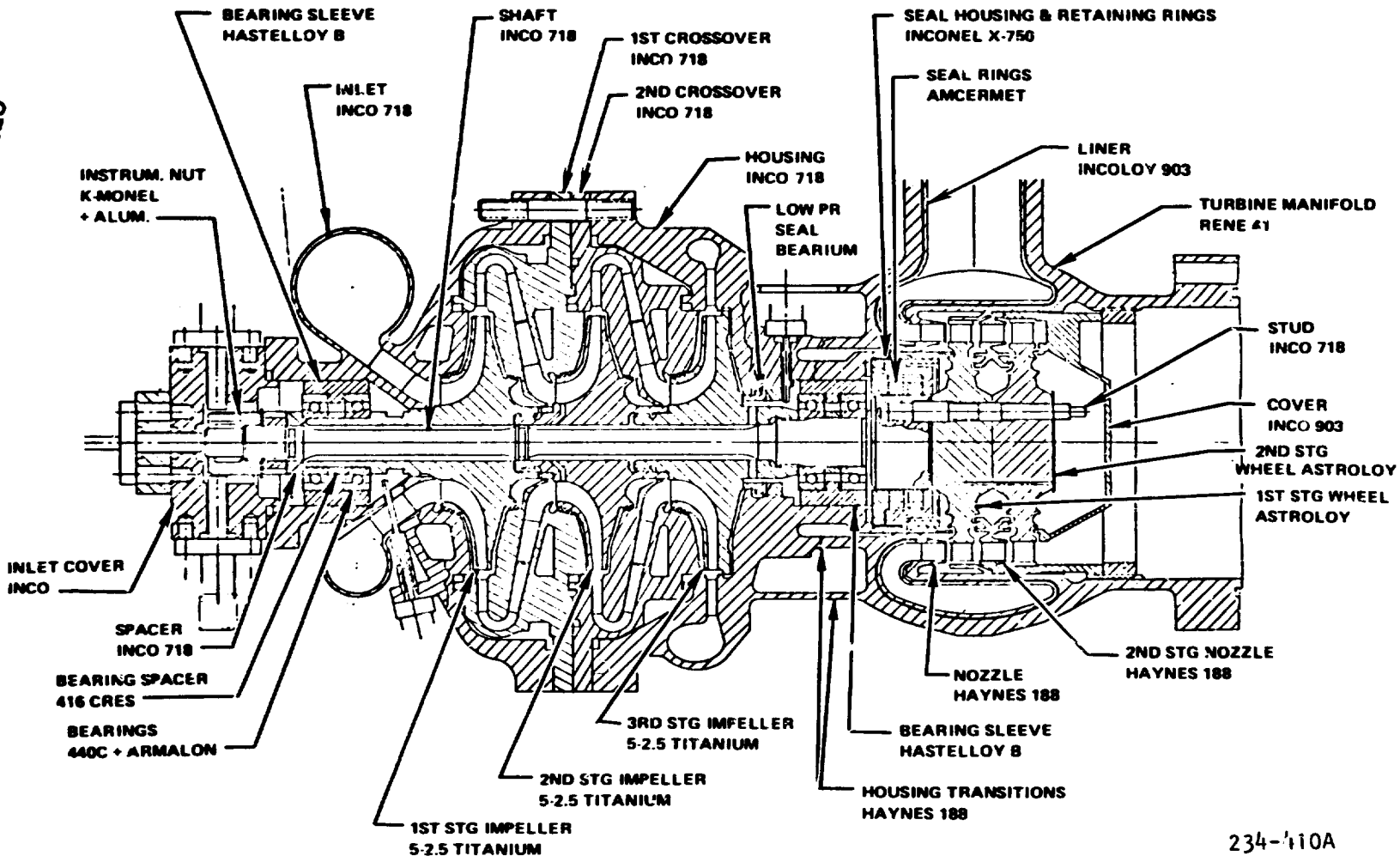

Figure 1. Mark 48 Hydrogen Turbopump Original Design

TABLE 2. MK 48-F PUMP NOMINAL DESIGN PARAMETERS

	SI Units	English Units
Number of Stages	3	3
Impeller Inlet Tip Diameter	4.826 cm	1.90 inches
Impeller Inlet Hub Diameter	3.099 cm	1.22 inches
Impeller Inlet Angle at Tip	0.28 radian	16 degrees
Impeller Inlet Angle at Hub	0.45 radian	26 degrees
Number of Impeller Vanes at Inlet	6	6
Number of Impeller Vanes at Discharge	12	12
Impeller Discharge Diameter	10.31 cm	4.058 inches
Impeller Discharge Angle	0.655 radian	37.5 degrees
Impeller Discharge Width	3.81 mm	0.150 inch
Impeller Tip Speed	512.97 m/s	1683 ft/sec
Vaned Diffuser Inlet Diameter	11.07 cm	4.36 inches
Vaned Diffuser Discharge Diameter	13.91 cm	5.48 inches
Number of Diffuser Vanes	11	11
Diffuser Passage Width	3.81 mm	0.150 inch
Crossover Inlet Diameter	13.72 cm	5.4 inches
Crossover First-Row Discharge Diameter	9.779 cm	3.9 inches
Crossover Second-Row Discharge Diameter	6.35 cm	2.5 inches
Crossover Inlet Angle	0.206 radian	11.8 degrees
Crossover First-Row Discharge Angle	0.471 radian	27 degrees
Crossover Second-Row Inlet Angle	0.394 radian	26.6 degrees
Crossover Second-Row Discharge Angle	1.047 radians	60 degrees
Isentropic Head/Stage	15,647 m	51,334 feet
Overall Isentropic Head	41,415 m	135,876 feet
Stage Head Coefficient	0.576	0.576
Impeller Inlet Flow Coefficient (First Stage)*	0.159	0.159
Impeller Inlet Flow Coefficient (Second and Third Stage)*	0.194/0.1875	0.194/0.1875
Impeller Discharge Flow Coefficient (First Stage)*	0.071	0.071
Impeller Discharge Flow Coefficient (Second and Third Stage)	0.086	0.086
Stage Isentropic Efficiency	70.0%	70.0%
Overall Isentropic Efficiency	58%	58%
Shaft Speed	9946 rad/s	95,000 rpm
Pump Power	1896 kW	2543 hp
Required NPSP	406 m	1332 feet

*Value based on zero blockage

TABLE 3. MK48-F TURBINE DESIGN PARAMETERS

SI Units				
	1		2	
Stage	N-1	1-R	N-2	2-R
Pitch Diameter (DM), cm	8.89	8.89	8.89	8.89
Number of Elements (Z)	41	52	41	52
Height, cm	0.711	0.737	0.762	0.838
Throat Area, cm^2	4.55	6.50	5.34	8.14
Inlet Angle, rad	1.57	0.65	1.24	0.70
Exit Angle, rad	0.30	0.40	0.31	0.42
Pitch Line Velocity (U), m/s	-	442	-	442
Leading Edge, mm	2.39	1.12	0.69	1.12
Trailing Edge (R), mm	0.18	0.18	0.18	0.18

Speed, rad/s	= 9947
Overall Pressure Ratio	= 1.443
First-Stage Reaction, %	= 29.7
Second-Stage Reaction, %	= 26.0
Second-Stage U/C_o	= 0.483
Second-Stage Power, kW	= 1829
Mass Flowrate kg/s	= 3.02

English Units				
	1		2	
Stage	N-1	1-R	N-2	2-R
Pitch Diameter (DM), inches	3.500	3.500	3.500	3.500
Number of Elements (Z)	41	52	41	52
Height, inch	0.280	0.290	0.300	0.330
Throat Area, in^2	0.705	1.008	0.827	1.261
Inlet Angle, degrees	90	37.5	70.8	40
Exit Angle, degrees	17	23	18	24
Pitch Line Velocity (U), ft/sec	-	1451	-	1451
Leading Edge, inch	0.094 (Ellipse)	0.044 (Ellipse)	R = 0.027	0.044 (Ellipse)
Trailing Edge (R), inch	0.007	0.007	0.007	0.007

Speed, rpm	= 95,000
Overall Pressure Ratio	= 1.443
First-Stage Reaction, %	= 29.7
Second-Stage Reaction, %	= 26.0
Second-Stage U/C_o	= 0.483
Second-Stage Power, hp	= 2.543
Mass Flowrate, lb/sec	= 6.66

TABLE 4. MARK 48-F TURBOPUMP TEST HISTORY

First Test Series, 1976 (Turbopump S/N 01-0)						
Test No.	Date	Duration, Seconds	Objective	Speed		Remarks
				rad/s	rpm	
016-001	3-31-76	155	Chilldown H-Q at 200 rad/s (19K rpm)	1047	10,000	Shaft speed display error
016-002	3-31-76	33	H-Q at 200 rad/s (19K rpm)	1619	15,464	Shaft speed display error
016-003	4-7-76	90	H-Q at 4712 rad/s (45K rpm)	1187	11,333	Cut due to facility LH_2 leak
016-004	4-7-76	133	H-Q at 200 rad/s (19K rpm)	3926	37,500	Test cutoff by erroneous overspeed indication
016-005	4-7-76	73	H-Q at 4712 rad/s (45K rpm)	4712	45,000	Test cutoff by turbine radial accelerometer
016-006	4-7-76	168	H-Q at 4712 rad/s H-Q at 6282 rad/s (45K and 66K rpm)	4712 6282	45,000 60,000	H-Q excursions at both speeds. Turbine bearing coolant temperature cut. Chart scaled incorrectly.
016-007	4-9-76	31	H-Q at 9423 rad/s (90K rpm)	6836	65,300	Cutoff by turbine radial accelerometer
016-008	4-9-76	31	H-Q at 9423 rad/s (90K rpm)	7853	75,000	Speed limited by available GH_2 pressure
016-009	4-15-76	36	H-Q at 9947 rad/s (95K rpm)	9737	93,000	Shaft speed display count lost. Pump bearing coolant temperature high (-355 F).
016-010	4-15-76	148	H-Q at 4712 rad/s (45K rpm)	4712	45,000	Successful H-Q test
Total time: 10 starts and 884 seconds						

TABLE 4. (Continued)

Second Test Series, 1978 (Turbopump S/N 01-1)						
Test No.	Date	Duration, Seconds	Objective	Speed rad/s	Speed rpm	Remarks
016-001	1-12-78	136	H-Q at 4712 rad/s H-Q at 6282 rad/s (45K and 65K rpm)	2094 4711 6806	20,000 45,000 65,000	Successful H-Q test, low suction performance
Total time: 1 start, 136 seconds						

Third Test Series, 1979 (Turbopump S/N 01-2)						
Test No.	Date	Duration, Seconds	Objective	Speed rad/s	Speed rpm	Results
001	6-29-79	228	H-Q at 45K	2618 4712	25K 45K	Successful H-Q test programmed cut
002	7-2-79	36	H-Q at 65K	2618 3350	25K 32K	Cut during transition by negative seal-turbine ΔP
003	7-2-79	28	H-Q at 65K	2618 4712	25K 45K	Cut during transition by low pump inlet pressure
004	7-6-79	34	H-Q at 65K	2618 6491	25K 62K	Cut due to facility leak
005	7-6-79	130	H-Q at 65K	2618 6806	25K 65K	Successful H-Q test programmed cut
006	7-10-79	38	H-Q at 95K	2618 9004	25K 86K	Successful H-Q point speed limited by turbine gas

TABLE 4. (Concluded)

Test No.	Date	Duration, Seconds	Objective	Speed		Results
				rad/s	rpm	
007	7-11-79	45	NPSH at nominal Q/N	2618 8271	25K 79K	Successful NPSH test cut by drop in P_D at P_S = 7 psig
008	7-12-79	52	NPSH at high Q/N	2618 8167	25K 78K	Cut by turbine gas supply P_S = 28 psig
009	7-13-79	28	NPSH at low Q/N	8585	82K	Successful NPSH test
010	8-10-79	0	H-Q at 23K and NPSH at nominal Q/N	523	5K	Cut during transition by negative seal-turbine ΔP
011	8-11-79	278	H-Q at 23K and NPSH at nominal Q/N	2400	23K	Successful test. Cut by drop in P_D at P_S = 6 psig
012	8-14-79	141	NPSH at 23K and low Q/N	2408	23K	Successful test. Cut by drop in P_D at P_S = 9 psig
013	8-14-79	148	NPSH at 23K and high Q/N	2408	23K	Successful test. Cut by drop in P_D at P_S = 3.8 psig
014	8-15-79	71	NPSH at 80K and low Q/N	8167	78K	Successful test. Cut by drop in P_D at P_S = 4 psig
015	8-16-79	41	NPSH at 80K and high Q/N	8167	78K	Successful test. Cut by turbine drive gas limitation
016	8-17-79	5	95K at nominal Q/N	9423	90K	VSC cutoff. Radial acceleration exceeded redline of 15 g rms
017	9-11-79	30	NPSH at 80K and high Q/N	8376	80K	Successful test. Cut by turbine gas limitation
018	9-13-79	0	H-Q at 91K	9496	90.7K	VSC cutoff. Radial acceleration exceeded redline of 15 g rms. Shot bags added to detune housing
019	9-26-79	20	54% Q/N at 81K	8585	82K	Turbine overspeed cutoff at 66% Q/N due to pump stall. Shot bags removed.

The initial test series successfully demonstrated, in a single build of a new design, its operating capability to near design speed. Required performance goals were also approached; however, several areas were identified where design deficiencies existed. Analysis of the fluid dynamic data revealed that, at speeds below 8376 rad/s (80,000 rpm), the generated pump head was as predicted and the pump isentropic efficiency was slightly higher than predicted (Fig. 2 and 3. At speeds approaching the design level, and at high flows at lower speeds, the performance of the pump first stage deteriorated, causing the overall head to fall below the predicted value, indicating a cavitation problem in the first stage. The data also disclosed higher-than-predicted temperatures for the coolant of both bearing sets. The suction performance characteristics were not specifically defined on the initial test series.

The purpose of the technical effort covered by this final report was to identify the exact cause of the discrepancies noted above, incorporate corrective modifications, and demonstrate the effectiveness of the modifications by testing. In-depth analysis of the coolant loop of the rear bearing revealed the need for modifications to obtain a higher coolant flow to the turbine-side seal and the turbine bearings. This was done by enlarging the orifices in the supply lines in the turbine housing and by increasing the number of flow passages in the seal housing. The front bearing coolant flow initially originated from the first-stage impeller rear shroud, and was routed along the shaft to the front bearings for cooling. The flow then entered the first-stage impeller eye. These test data indicated that high bearing temperatures were exhibited in the initial test series. This was due to the warm hydrogen being taken from the first-stage impeller rear shroud. A new coolant loop was developed by routing the fluid from the first-stage impeller inlet housing guide wall and passing it through the bearings and discharging it overboard. It was expected that these modifications of rerouting the hot bearing flow from entering the impeller eye would improve the suction performance as well as provide coolant to the bearing at a reduced temperature. The modifications were completed, and in January 1978, a single test of 136 seconds duration was conducted with these modifications, with negative results in terms of suction performance. The head-flow characteristics are compared with the previous scroll inlet data in Fig. 4.

Subsequently, a comprehensive analysis was conducted, supported by component testing to define the hydrodynamic conditions in and around the first-stage impeller. The results of this effort disclosed that the primary cause of the poor suction performance was that part of the front wear ring flow was vaporizing and, as a result, a large-volume flow was ingested into the first-stage impeller, which caused blockage at the impeller inlet for the through flow, which then led to cavitation in a section of the impeller. The tangential inlet housing was identified as a less significant contributor to the problem in that it did not introduce the fluid to the impeller at the optimum incidence angle.

A total of 16 modifications were analyzed. Based on the trade study results, the impeller inlet area was enlarged and an inducer was incorporated immediately upstream of the impeller. The inlet housing was modified to an axial-flow type to provide room for the inducer and to obtain an exact fluid vector angle. The axial inlet turbopump configuration is illustrated in Fig. 5 and per 9R0011560, Appendix B.

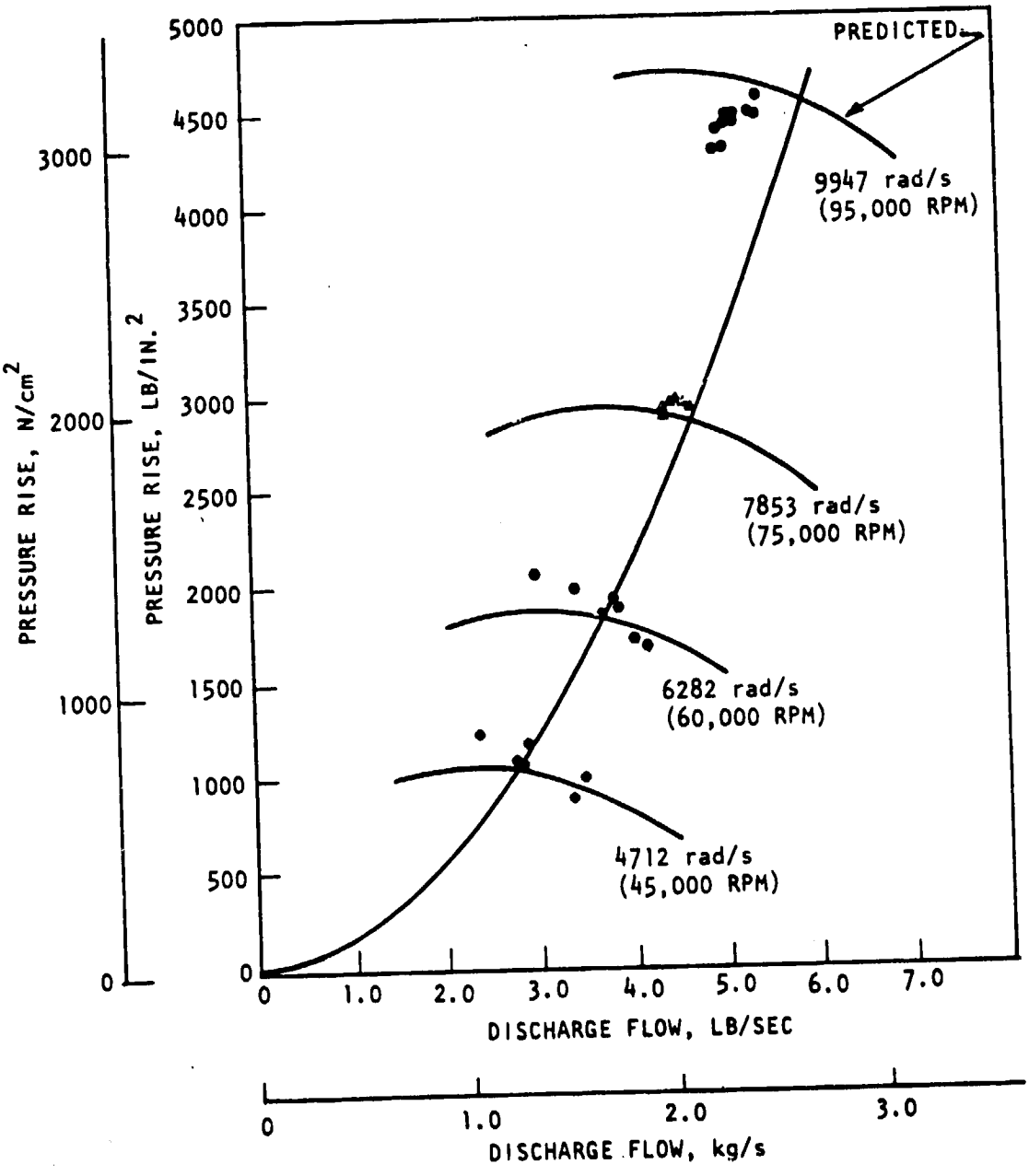

Figure 2. Mark 48-F Pump Performance With Scroll Inlet (1976)

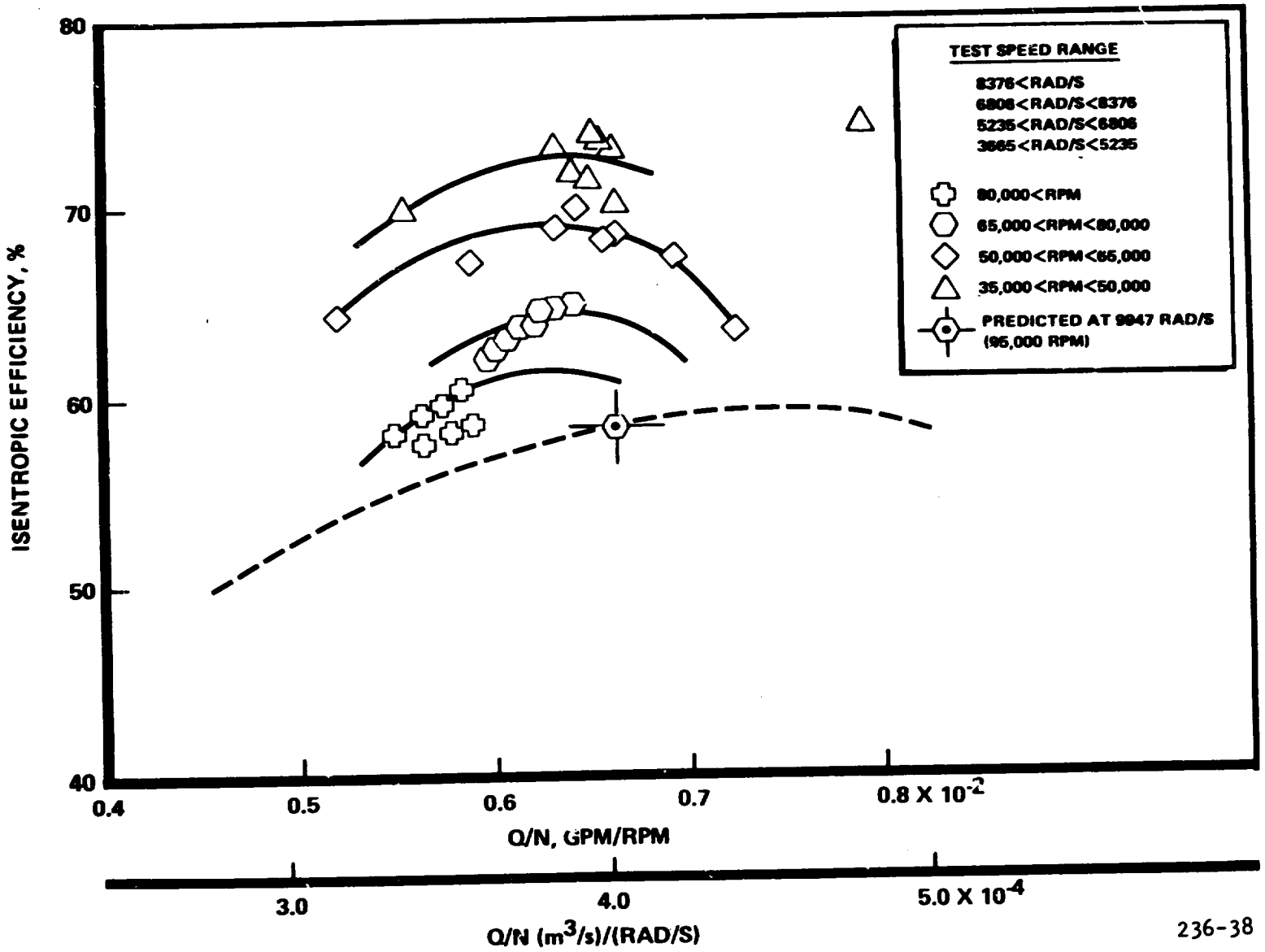

Figure 3. Mark 48-F Pump Efficiency (Scroll Inlet Configuration)

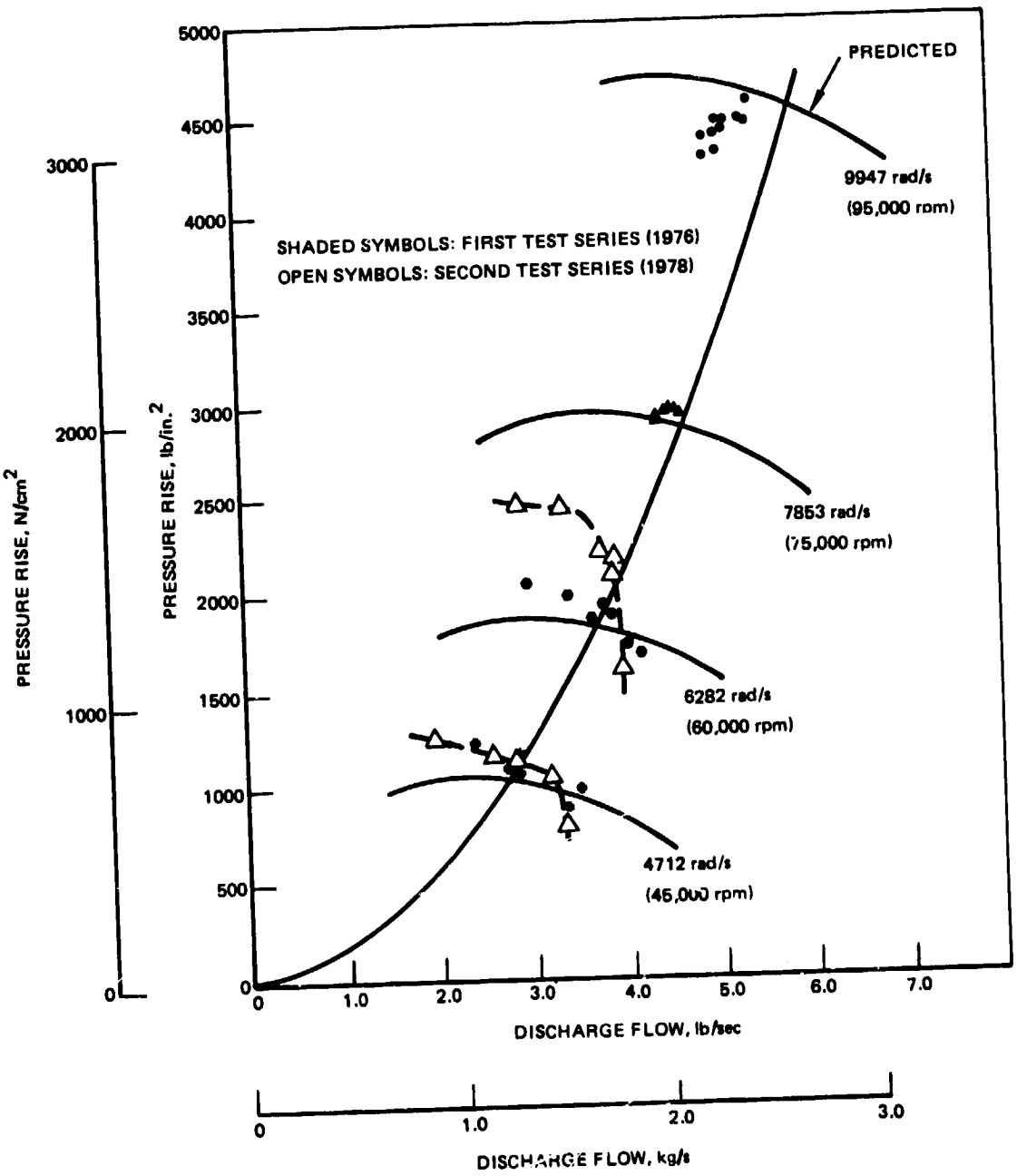

Figure 4. Mark 48-F Pump Performance With Scroll Inlet

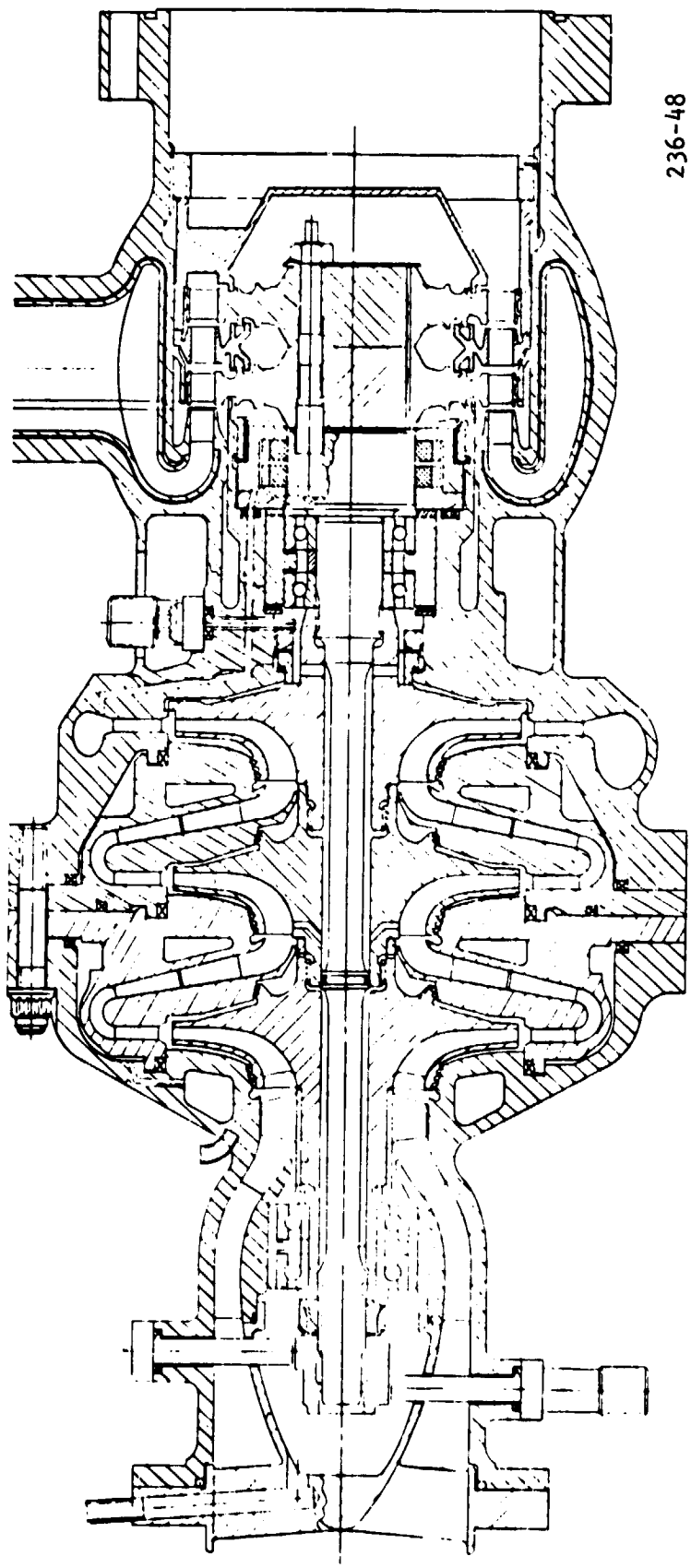

236-48

Figure 5. Mark 48-F Turbopump With Axial Inlet

A total of 19 tests with 1353 seconds total time were performed on this configuration during the interval of June-September 1979 (Table 4).

The results of the testing indicated that the modifications implemented have resulted in a pump with excellent suction specific speeds. Values in excess of 36.7 (rad/s) $(m^3/s)^{1/2}/(J/kg)^{3/4}$ = (100,000 rpm · $gpm^{1/2}/ft^{3/4}$) were obtained (Fig. 6). The pump was tested at engine idle mode conditions (2400 rad/sec, 23,000 rpm), where a capability of operating at zero NPSH without head loss was demonstrated (Fig. 7).

With the cavitation effects removed, the head generated by the pump exceeded design requirements, and the pump isentropic efficiency was higher than predicted (Fig. 8 and 9). A pump stall condition at low flow was detected on the last test (019), and these data are summarized also in Fig. 8 and 9.

During the testing, a resonance condition was identified around 92,000 rpm with an increase in vibration levels. Although indications were that it was a housing or test stand response, additional effort will be needed to isolate and eliminate this phenomenon.

The high-temperature level of the front bearing coolant noted in prior testing evidently was caused by heat soakback from the massive instrumentation cap. With the axial inlet, the temperature rise was minimal. Minor changes introduced in the turbine end bearing coolant system also corrected high temperature levels of the coolant emanating from the bearing.

From the standpoint of mechanical integrity, the turbopump operated well. Disassembly of the unit disclosed a crack in a nonstructural weld in the second-stage impeller which was traced to a weld quality deficiency. All other components were found in excellent condition.

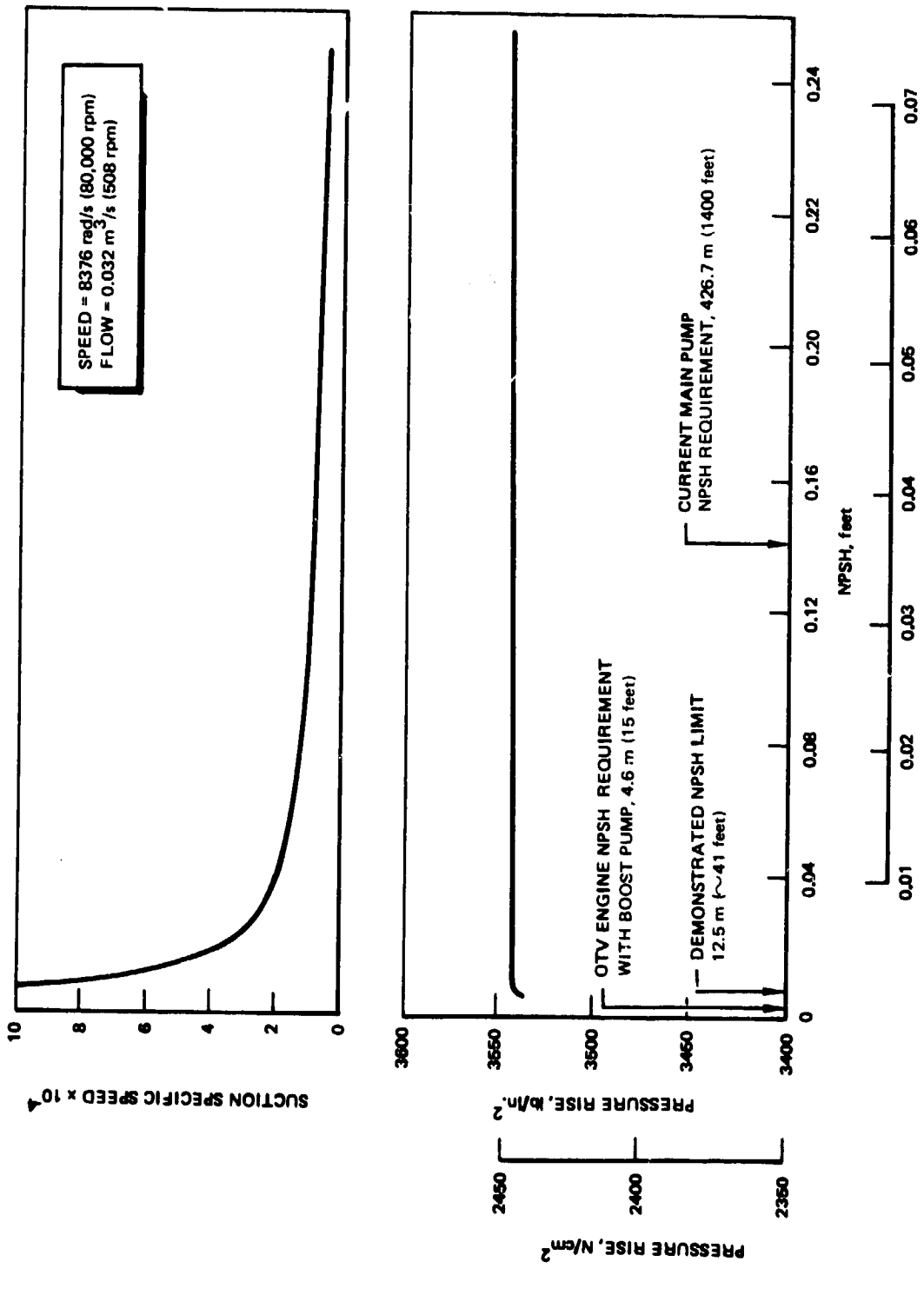

Figure 6. Mark 48-F Turbopump NPSH Performance

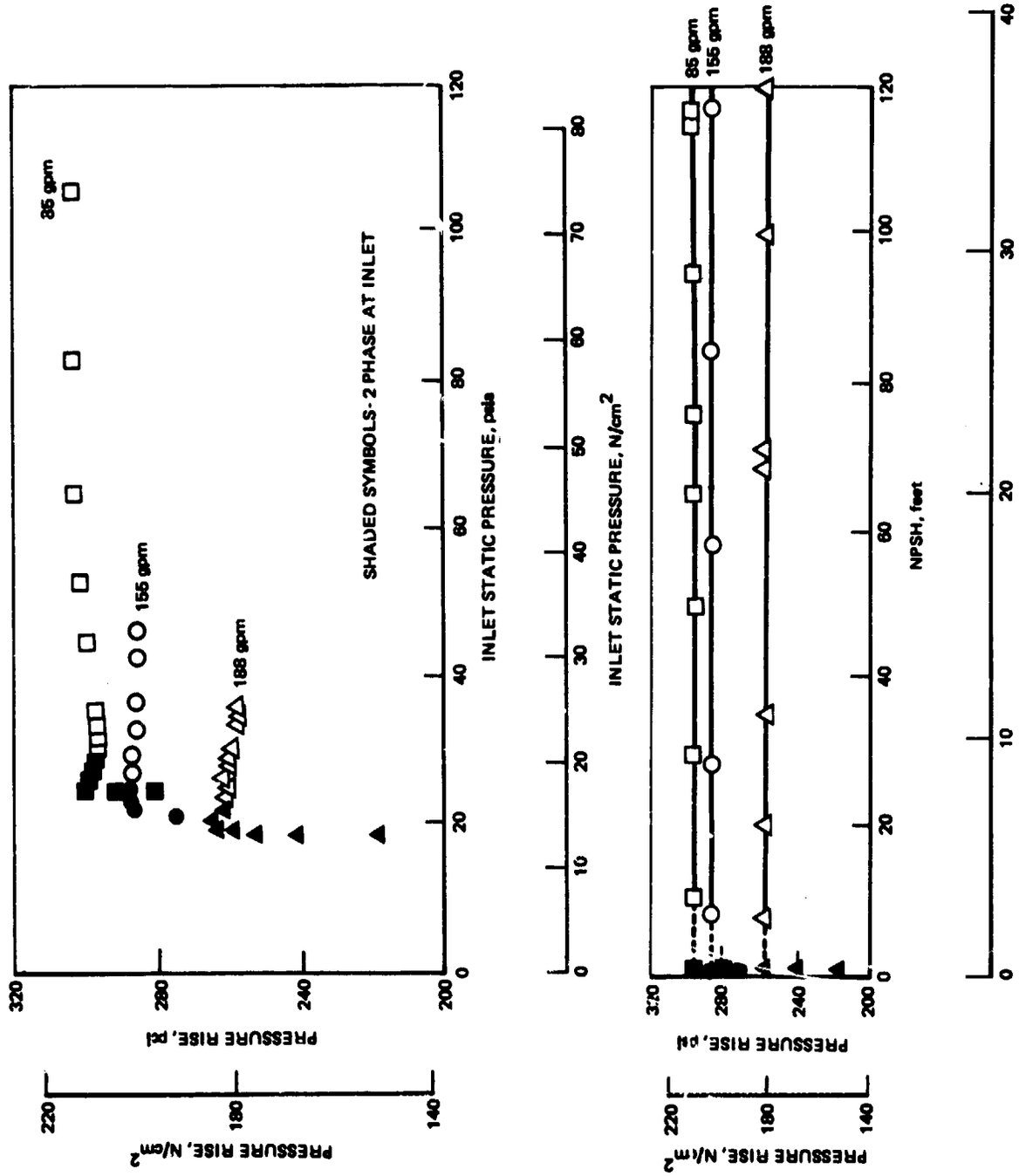

Figure 7. Idle-Mode Suction Performance at 2408 rad/s (23,000 rpm)

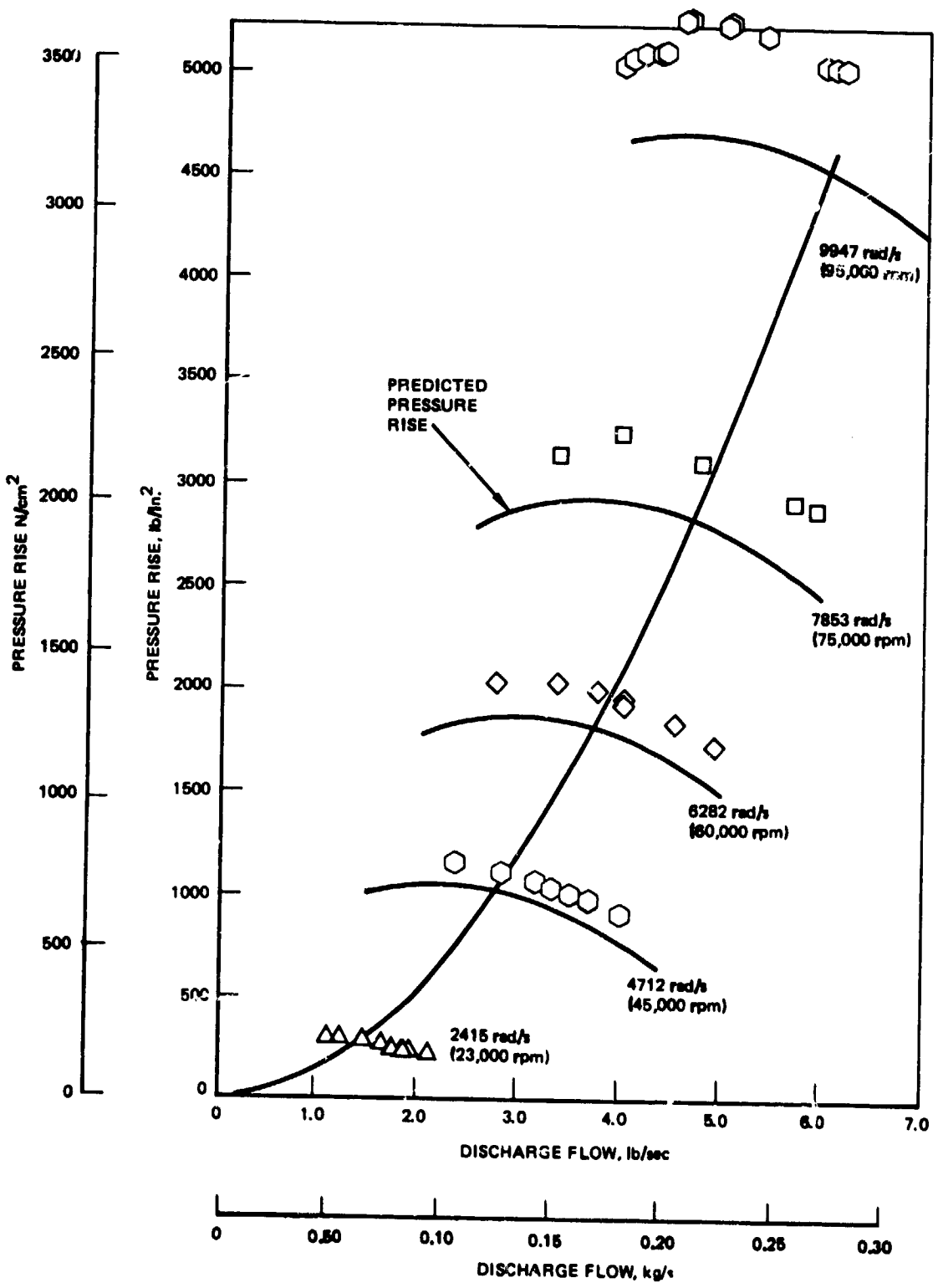

Figure 8. Pump Scaled Performance (Test 001 to 019, 1979)

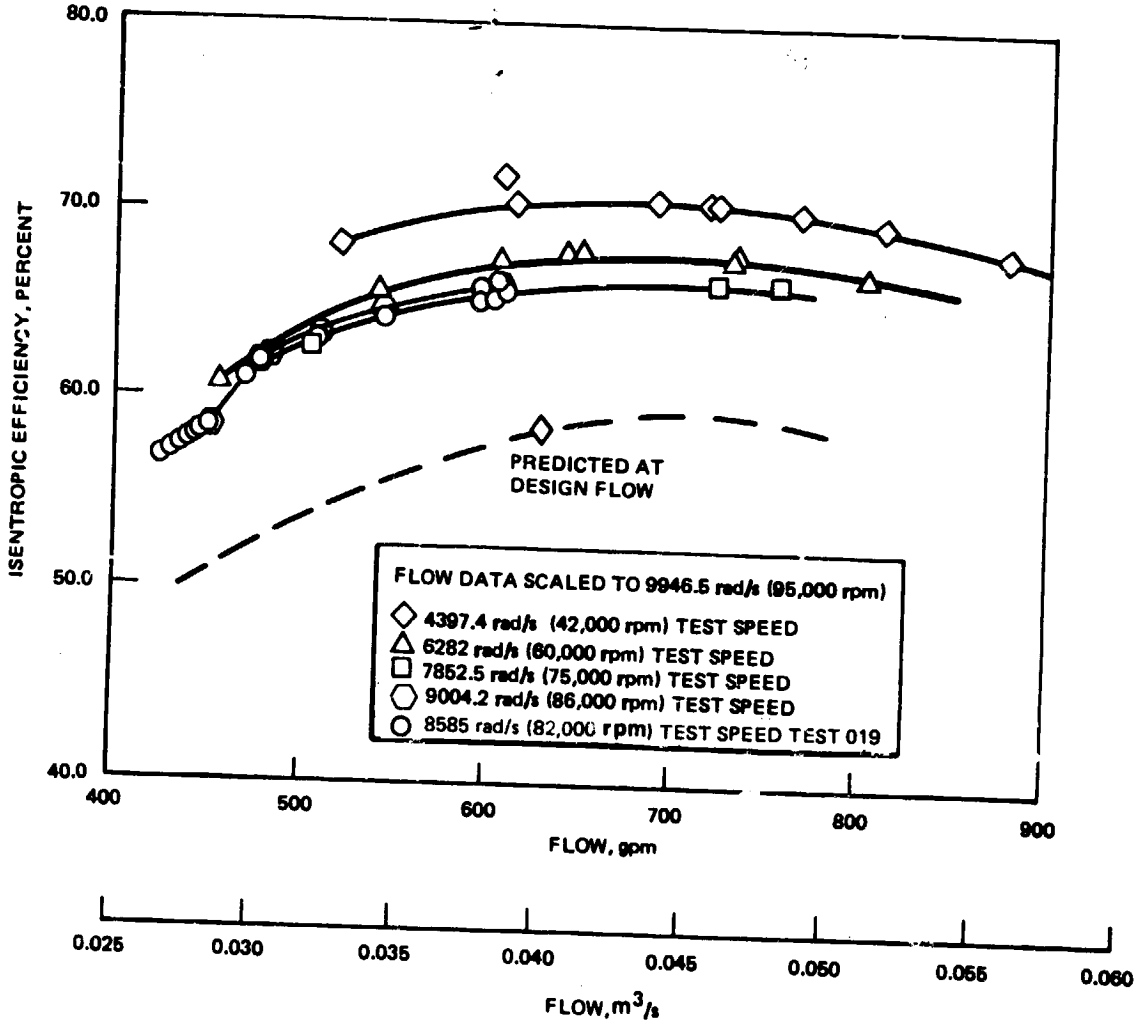

Figure 9. Mark 48-F Turbopump Efficiency
(Tests 001 to 019, 1979)

INTRODUCTION

System studies have been conducted to determine the feasibility of developing a reusable vehicle for performing future Air Force and NASA space maneuvering missions. These studies have shown that, over the thrust range of interest, high-pressure, staged-combustion-cycle engines offer the highest specific impulse and payload capability. A review of the vehicle and engine system study results indicates that a single-bell-nozzle, staged-combustion-cycle engine at 88,964 N (20,000 pounds) thrust level is near optimum for the DOD and NASA mission requirements.

This program was initiated to provide the required hydrogen turbopump technology base for subsequent development of a high-performance, staged-combustion rocket engine. Studies have indicated that, with minor modifications, this turbopump configuration can also be applied to expander cycle engines in the same thrust range.

Technology items of particular interest during the course of the current development program include fabrication of impeller passages by EDM; split impeller design and fabrication techniques; balancing of small, high-speed, multipart shafts; hydrogen-embrittlement protection; balance piston design and operation; high DN bearings; and assembly and measurement procedures for small turbopump assemblies.

The objectives of this program were to design, fabricate, and test a high-pressure LH_2 turbopump capable of meeting the performance requirements of the 88,964 N (20,000 pounds) thrust, staged-combustion-cycle engine; demonstrate its basic capability; and identify areas where additional effort due to technology limitations is required to place a future engine program on a solid basis. The initial phase of this effort, encompassing design, fabrication, and the first test series, was performed under prior NASA Contract NAS3-17794, the results of which are documented in NASA CR-135186 (Rocketdyne Report No. R76-115); "Final Report, Small, High-Pressure Liquid Hydrogen Turbopump."

Rocketdyne has assigned the designation "Mark 48-F Turbopump" to this small, high-pressure, LH_2 turbopump design generated under this contract. The two terms will be used interchangeably through this report.

DISCUSSION

ORIGINAL ANALYSIS AND DESIGN

ASE Engine Configuration

The objective of this program was to establish the technology base for small, high-pressure LH_2 pumping capability for application on the Advanced Space Engine (ASE). The basic performance parameters for the ASE have been established in a preliminary design task, the results of which are reported in NASA CR-135186 (Rocketdyne Report No. R76-115), Final Report, Small, High Pressure Liquid Hydrogen Turbopump.

A schematic of the ASE is presented in Fig. 10. It is a staged combustion cycle engine using LH_2 and LO_2 as propellants. The major components comprising the engine are two low-pressure, gas-driven boost pumps; two high-pressure pumps; a preburner; a regeneratively cooled combustion chamber and nozzle; a dump cooled nozzle extension; and valves.

The small, high-pressure LH_2 turbopump effort performed under this contract was directed toward establishing the technology for the main high-pressure hydrogen turbopump.

Turbopump Requirements

The performance requirements for the Mark 48-F turbopump are listed in Table 5. The pump is required to deliver 2.74 kg/s (6.04 lb/sec) of LH_2 starting with an inlet pressure of 49 N/cm^2 (71 psia) provided by the low-pressure pump, to a discharge pressure of 3140 N/cm^2 (4560 psia). The propellant gas for the turbine is a mixture of free hydrogen and steam resulting from the combustion of LH_2 and LO_2. The gas is provided at a temperature of 1033 K (1860 R) and an inlet pressure of 2360 N/cm^2 (3420 psia). The total gas flowrate available is 3.02 kg/s (6.66 lb/sec). The horsepower requirements of the pump are matched by adjusting the pressure ratio across the turbine. Since turbine pressure ratio has a strong influence on the attainable engine combustion pressure in a staged combustion cycle, it is to be maintained at the lowest possible level. As noted in Table 5, the mechanical operating requirements included multiple starts with long operating durations and potentially long coast times between operations.

Certain elements of the requirements noted above had a particularly significant impact on the technology requirements of the turbopump and the ensuing design configuration. In the pump, the combination of low flowrate and high discharge pressure imposed a difficult impeller fabrication task because of the relatively narrow passages required compared with the outer diameter. The desire for high efficiency, compact packaging, and light weight placed the rotor speed into the 9423 to 10,470 rad/s (90,000 to 100,000 rpm) range, pushing bearing DN values to the 2.0×10^6 mm·rpm limit noted in the design ground rules. The bearing operation at high speeds needed to be demonstrated.

Because of the high operating speed involved, the bearings would not be able to take an appreciable axial thrust load. This condition dictated that an axial thrust balance device be employed. The operating characteristics of such a

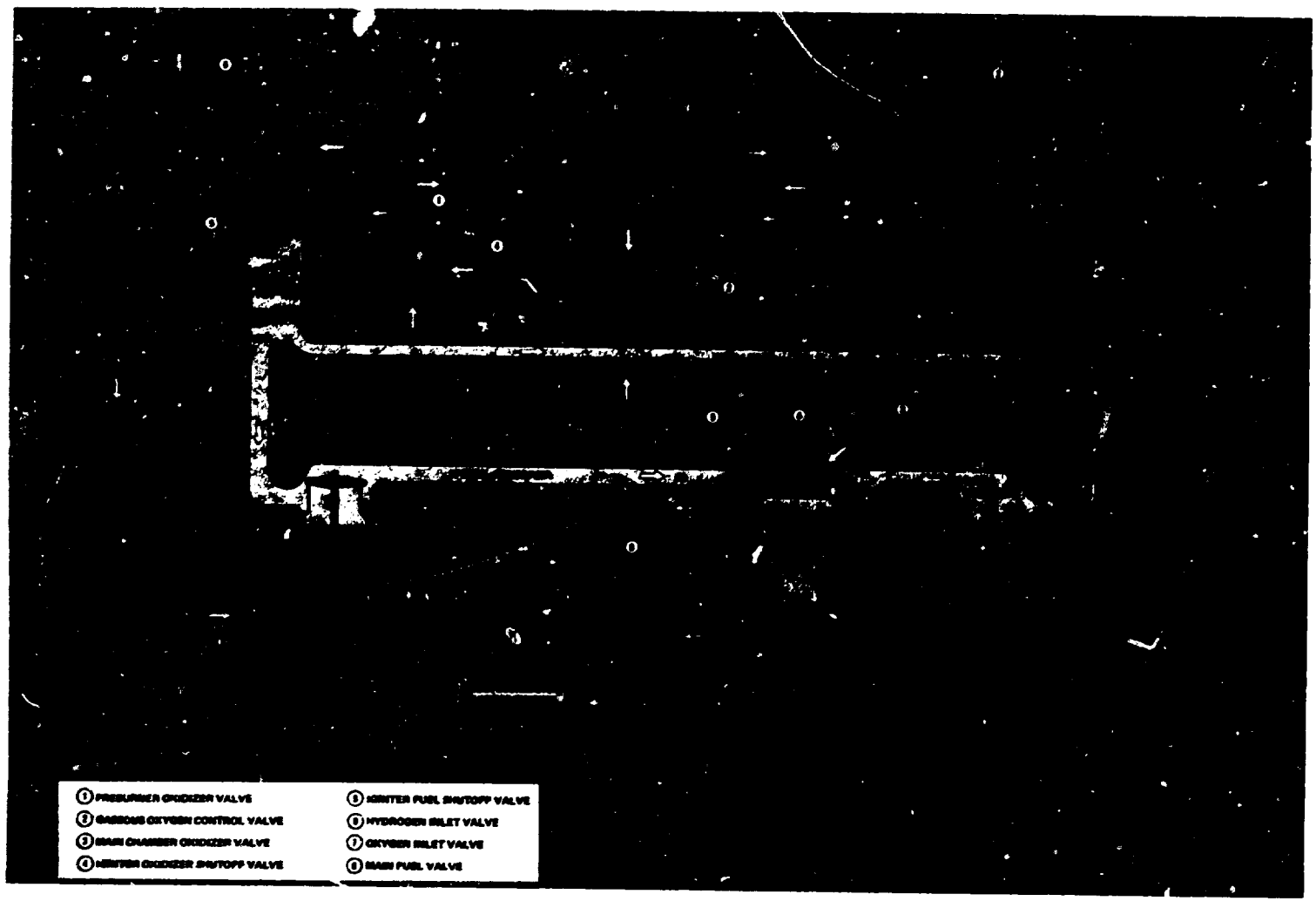

Figure 10. ASE System Schematic

TABLE 5. MARK 48-F TURBOPUMP NOMINAL DESIGN CONDITIONS

	SI Units	English Units
Pump		
Type	Centrifugal	
Propellant	LH_2	
Inlet pressure	49 N/cm^2	71 psia
Inlet temperature	21-23 K	38-41 R
Discharge pressure	3140 N/cm	4560 psia
Mass flow	2.74 kg/s	6.04 lb/sec
Number of stages	3	
Turbine		
Working fluid	O_2/H_2 combustion products	(H_2 + H_2O)
Inlet temperature	1033 K	1860 R
Inlet pressure	2360 N/cm^2	3420 psia
Pressure ratio	Minimum necessary to develop pump horsepower requirements	
Flowrate	3.02 kg/s	6.66 lb/sec
Number of stages	2	
Type	Full admission	

Turbopump

Capable of operation at pumped-idle conditions, i.e., approximately 5 to 10% full thrust

Off-design operation:	+20% Q/N at full thrust down to 30% Q/N at 20% N
Service life between overhauls:	*300 thermal cycles or 10 hours accumulated run time
Service-free life:	*60 thermal cycles or 2 hours accumulated run time
Maximum single run duration:	2000 seconds
Maximum time between firings during mission:	14 days
Minimum time between firings during mission:	1 minute
Maximum storage time in orbit (dry):	52 weeks

*Thermal cycle defined as engine start (to any thrust level) and shutdown.

device also required evaluation. In the turbine, the performance of a small turbine with a high-power density and low-pressure ratio, (approximately 1.4) needed to be demonstrated.

From a structural consideration, the requirement for 300 thermal cycles was significant in that it established low-cycle fatigue criteria and eventually necessitated incorporating a liner in the turbine manifold to limit the maximum thermal gradients in structural walls.

Original Turbopump Configuration Description

The initial configuration of the Mark 48-F turbopump is shown in Fig. 11. The pumping elements consist of three centrifugal impellers containing six full and six partial vanes, a radial diffuser after each impeller, and an internal crossover passage following the first- and second-stage diffusers. Liquid hydrogen is introduced to the pump through a tangential inlet and delivered from the pump through a scroll-shaped discharge. The pump end of the rotor assembly is formed by the impeller hubs, which are piloted relative to each other and maintained axially tight by a central tie bolt. The two pump crossovers are mounted on the pump through the externally accessible flanges. Although this feature results in additional external seal joints and weight, it facilitates measuring all significant interstage pressure levels. The cavities between the crossovers and the external housings are sealed from the main flow passages by axial flange seals, and they are vented to the pump inlet. Thus, the external flange seals are subjected to pump inlet pressure only, and should not pose a leakage problem. Internal recirculation around the impellers is minimized by step labyrinth seals in the front and rear shrouds. The seal lands are plated with silver to prevent hard metal-to-metal rubbing, and still maintain close radial clearances.

The turbine is a two-stage reaction type with an overall pressure ratio of 1.443. Approximately 52% of power is developed in the first stage and 48% in the second stage. The wheels are attached to the shaft by three body-bound studs which also transmit the torque. Axial holes are incorporated in the disks to provide a path for the shaft seal leakage which is used as a coolant. The downstream side of the second-stage wheel is covered with a shield to reduce heating effect of the exhaust gas on the disk. Low-cycle fatigue necessitates incorporating a sheet metal liner into the inlet manifold to reduce thermal gradients during start and cutoff. The liner is approximately 1.57 mm (0.062 inch) thick, and includes bleed holes to equalize the pressure on either side.

Axial thrust control is maintained by using a self-compensating balance piston incorporated in the back shroud of the third-stage impeller. To operate the balance piston, fluid from the discharge of the third-stage impeller is passed through a high-pressure orifice at the tip of the impeller, then through a low-pressure orifice located near the hub into the rear bearing cavity. From the bearing cavity, the fluid is returned to the inlet of the second-stage impeller through an annular passage between the shaft and the impeller hubs.

The rotor is supported radially by two pairs of duplex, angular-contact, 20 mm ball bearings, axially preloaded to prevent the balls from skidding. The rear bearings are retained axially through a spring-loaded cartridge so that they

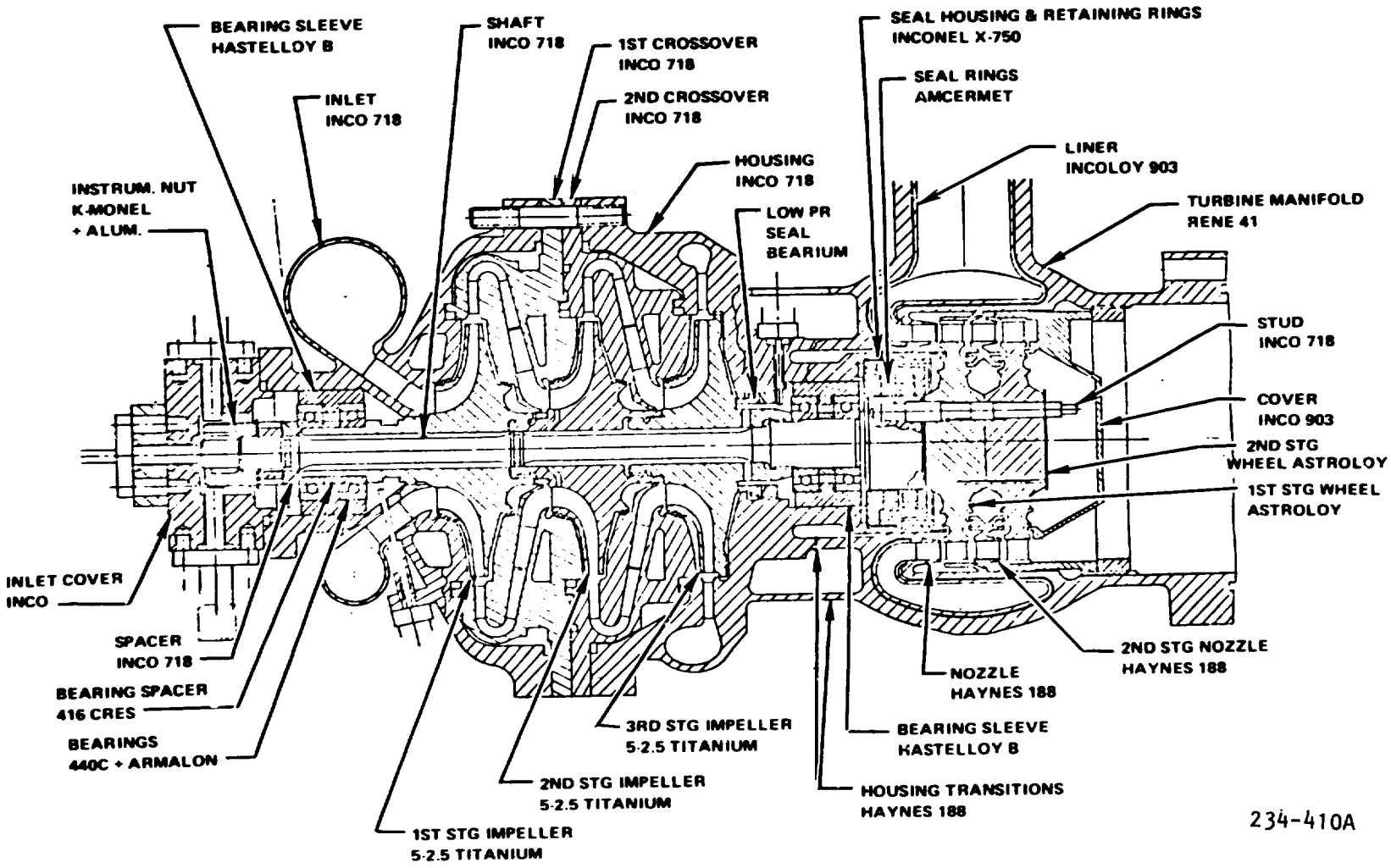

Figure 11. Mark 48 Hydrogen Turbopump Original Design

will absorb transient axial rotor loads. Cooling of the pump end bearings is accomplished by bleeding LH_2 from the hub area between the first- and second-stage impellers, passing the fluid through an annular passage between the tie bolt and the ID bore of the first-stage impeller to the pump inlet end, then in a reverse direction through the bearings and back to the eye of the first-stage impeller. Cooling of the turbine and bearings is effected by bleeding coolant fluid from the pump discharge, introducing it to an area on the turbine side of the bearings, and allowing it to flow through the bearings where it joins the balance piston fluid and returns to the eye of the second-stage impeller. Additional coolant is provided for the rear bearings by the fluid which leaks through the pump side of the shaft seal.

To separate the pump and turbine regions, a controlled-gap, shaft-riding seal is employed. Since the pressure on the pump side of the seal is lower than on the turbine side, the middle of the seal is pressurized with LH_2 supplied from the pump discharge. In this manner, a positive flow of liquid hydrogen toward the turbine is ensured, and entry of hot gas into the pump is prevented. As noted above, the LH_2 which leaks through the shaft seal toward the pump is used to lubricate the bearings. The fluid which leaks to the turbine is used to cool the turbine disks.

PRIOR TEST HISTORY (Test Series No. 1)

The initial testing of the Mark 48-F turbopump was performed on a prior contract during the period 31 March through 15 April 1976. A total of 10 tests were conducted for a total accumulated time of 884 seconds, using turbopump S/N 01-0. Table 6 presents a test-by-test summary of the initial series. Testing was performed at Lima Stand of Rocketdyne's Advanced Programs Test Facility shown in Fig. 12. A summary of significant information about the results of the series is presented in Table 7.

The most significant conclusions from the initial test series were that the turbopump was operating satisfactorily mechanically, but at high speeds and high flowrates the pump first stage was cavitating and resulting in lower than predicted head. This condition is illustrated in Fig. 13, where the measured head flow values are plotted on the predicted pump characteristics curves. The isentropic efficiency of the pump, computed on the basis of fluid temperature rise, shown in Fig. 14, was better than predicted.

INTERIM MODIFICATION EFFORT

Effort on Contract No. NAS3-21008 was initiated in June 1977. The objectives of the program were to conduct additional analysis of the data obtained in the initial test series conducted in 1976; take remedial action to resolve high temperature levels of the front and rear bearings; implement design modifications to improve the pump suction performance; and to demonstrate by testing the effectiveness of the changes incorporated. The test effort was planned to include hot firing the turbine. This goal was later deleted from the program and the funding was applied to a second iteration to resolve pump performance deficiencies.

TABLE 6. MARK 48-F S/N 01-0 TURBOPUMP TEST SUMMARY

Test No.	Date	Duration, Seconds	Accumulated Time, Seconds	rad/s (Maximum rpm)	Remarks
1	3-31-76	155	155	1,047 (10,000)	Cut for low indicated discharge pressure
2	3-31-76	33	188	1,619 (15,464)	Cut for erroneous discharge pressure measurment (range error)
3	4-7-76	90	264	1,178 (11,250)	Cut due to facility H_2 leak
4	4-7-76	133	397	3,926 (37,500)	Erroneous speed indication cut
5	4-7-76	73	470	4,712 (45,000)	Turbine radial accelerometer cut
6	4-7-76	168	638	6,439 (61,500)	Turbine bearing temperature cut (chart scaled incorrectly)
7	4-9-76	31	669	6,387 (61,000)	Turbine radial accelerometer cut
8	4-9-76	31	700	7,884 (75,300)	Cut for low GH_2 supply pressure
9	4-15-76	36	736	9,737 (93,000)	Cut for erratic speed indication
10	4-15-76	148	884	4,712 (45,000)	Constant rpm, facility duration test

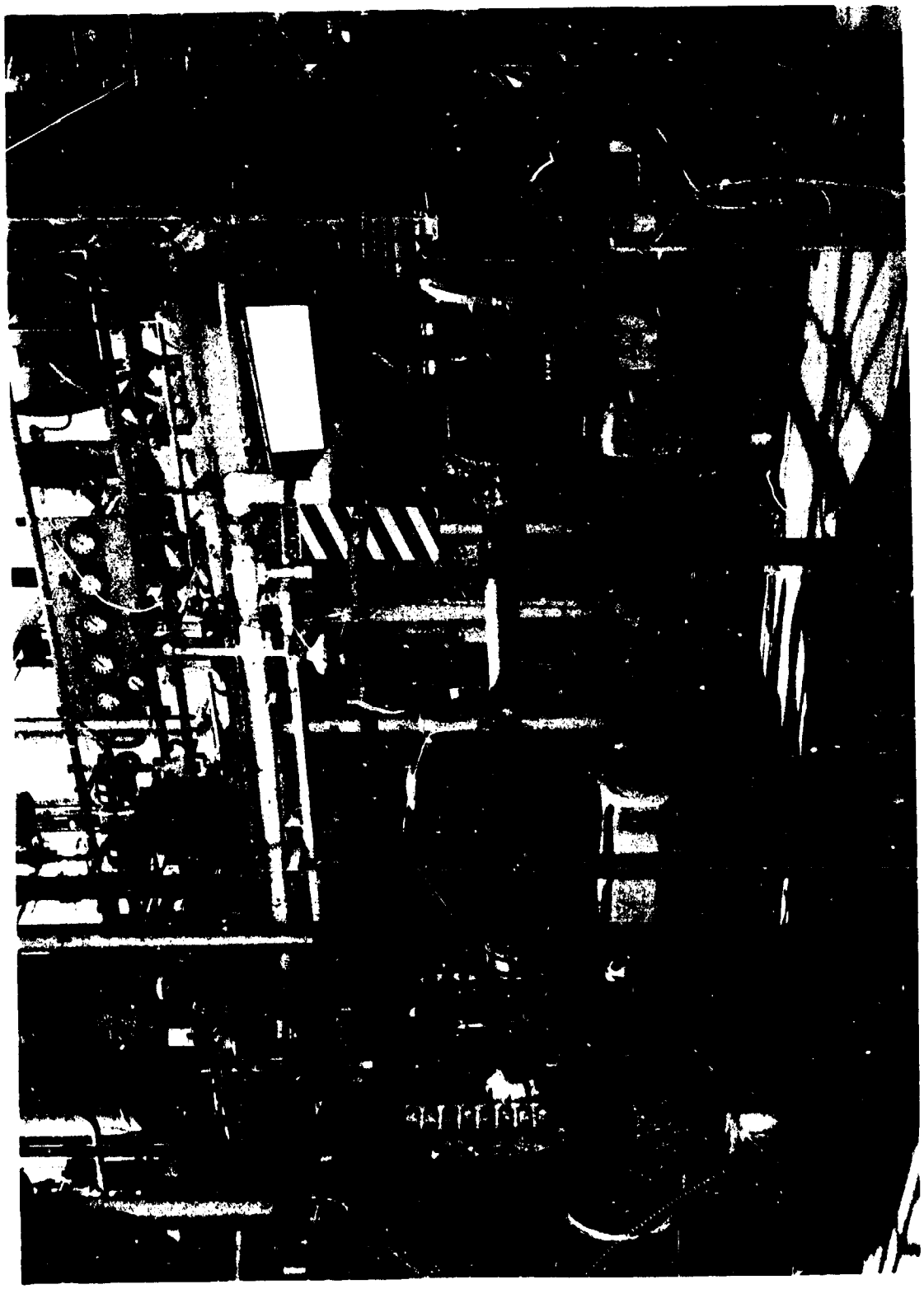

Figure 12. Advanced Programs Test Facility

TABLE 7. MARK 48-F TEST HISTORY

- Initial Test Series 31 March through 15 April 1976
  - 10 Tests, 384 seconds
  - LH_2 Pump Fluid, GH_2 Turbine Propellant
  - H-Q Data
    - 4712 rad/s (45,000 rpm)
    - 6282 rad/s (60,000 rpm)
    - 7853 rad/s (75,000 rpm)
    - 9423 rad/s (90,000 rpm +)
  - Maximum N = 9738 rad/s (93,000 rpm)
  - Maximum Q = 0.032 m^3/s (508 gpm)
  - Maximum P_D = 2884 N/cm^2 (4183 psia)
  - Performance
    - Cavitation at 9423 rad/s (90,000 rpm)
    - Cavitation at 6282 rad/s-7329 rad/s (60,000-70,000 rpm) at high Q/N
  - Mechanical Conditions
    - Front and Rear Bearing Temperatures Higher Than Predicted
    - Axial Thrust Control Satisfactory
    - Rotordynamic Behavior Satisfactory
    - Structurally Adequate

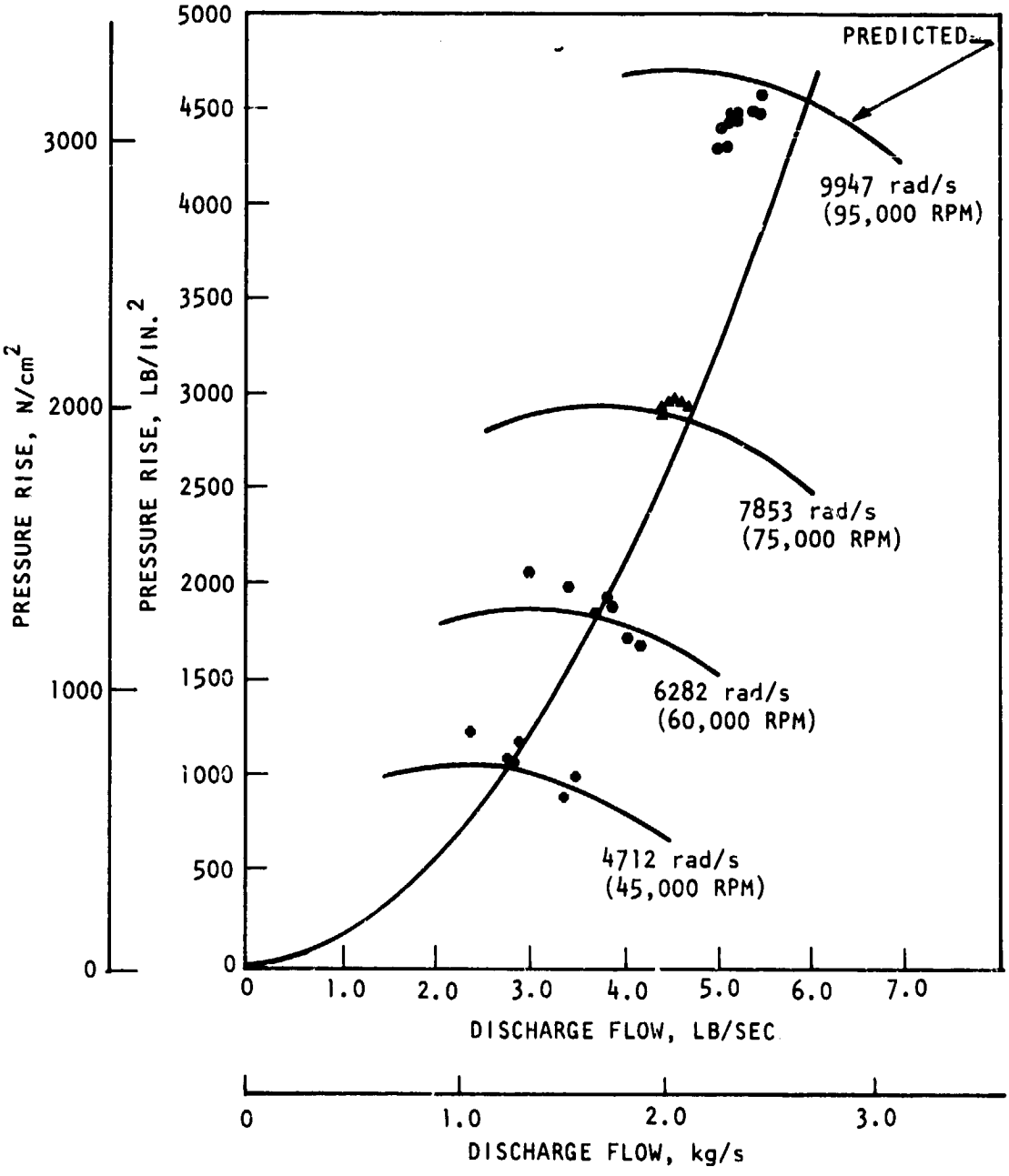

Figure 13. Mark 48-F Pump Performance With Scroll Inlet (1976)

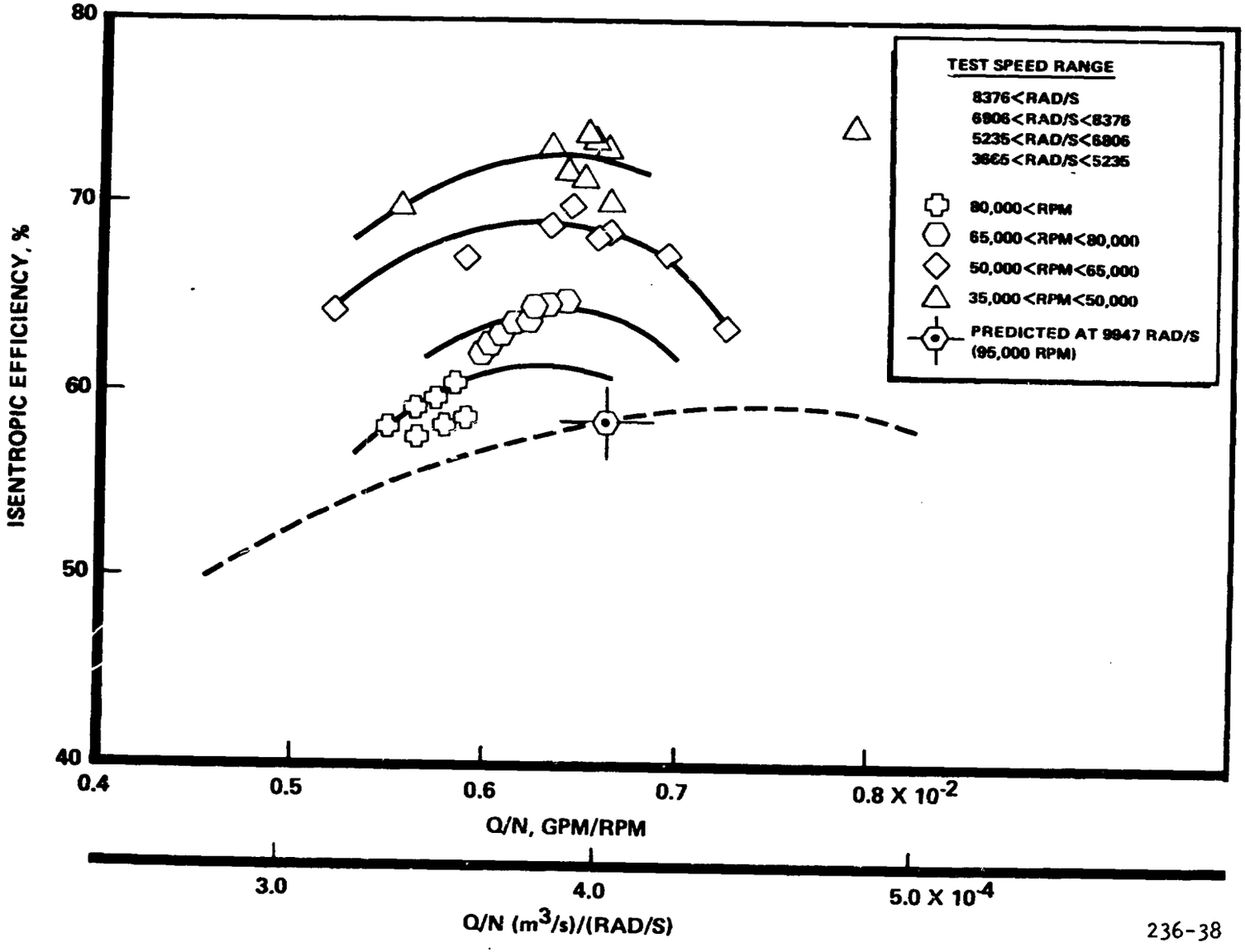

Figure 14. Mark 48-F Pump Efficiency

Rear Bearing Cooling Improvement

An in-depth analysis of the rear (turbine end) bearing coolant flow loop was conducted to determine the cause for the higher than predicted fluid temperature measured at the exit from the bearing.

A schematic of the bearing coolant flow loop is shown in Fig. 15. The temperature rise of the flow between the pump discharge, point D, and the balance piston sump, point S, is plotted as a function of pump rotational speed in Fig. 16 for representative slices of the tests conducted in 1976. A plot of temperature rises as a function of time is shown for tests 8, 9, and 10 in Fig. 17. From Fig. 18 it would appear that above speeds of approximately 8901 rad/s (85,000 rpm) there is a large increase in the temperature rise of the coolant flow.

An analysis was performed to predict the flowrate and temperature rise in this system. The analytic model solves for the flow through the seals using the measured turbine seal pressure, the balance piston sump pressure, and the nozzle static pressure. The heat input due to the bearing as well as the heating through the seal are calculated and contribute to the predicted temperature rise. At some operating conditions, throttling to lower pressure also causes a temperature rise and is accounted for. The total flowrate through the seal can also be calculated from the drop in pressure measured between the pump discharge pressure and the turbine seal pressure. Note that these two predicted flowrates agree within 3%. The flowrate calculated in this manner (pump discharge pressure - turbine seal pressure) is higher than the seal flow predicted at a pump rotational speed of 9948 rad/s (95,000 rpm). This is shown in Fig. 18.

The flow exiting the bearing mixes with some portion of the balance piston flow before it enters the second-stage impeller hub. A calculation of the disk friction heating of the balance piston was made. It was found that even at 9948 rad/s (95,000 rpm) the disk friction heating is low, and with nominal balance piston flow, 0.423 kg/s (0.933 lbm/sec) the temperature rise is approximately 2.7 K (4 R).

The flow through the balance piston was calculated for the first five slices of test 9. For all of these slices, the predicted balance piston flow is above 0.4 kg/s (0.9 lbm/sec). Therefore, any portion of the balance piston flow mixing with the bearing coolant flow upstream of the temperature probe would tend to lower the temperature measurement. For this reason, the analysis assumed that no mixing with the balance piston flow occurs until some point downstream of the temperature measurement.

The results of the analysis thus far have been exclusively of slices in test 9. They indicate that with nominal heating and seal gaps the expected temperature rise is approximately 5 to 7 K (10 to 12 R) as shown in Fig. 19.

An analysis was performed of the heat transfer from the turbine drive gas to the bearing coolant flow through the casing. This heat transfer was found to cause less than 0.1 degree increase in the coolant flow temperature.

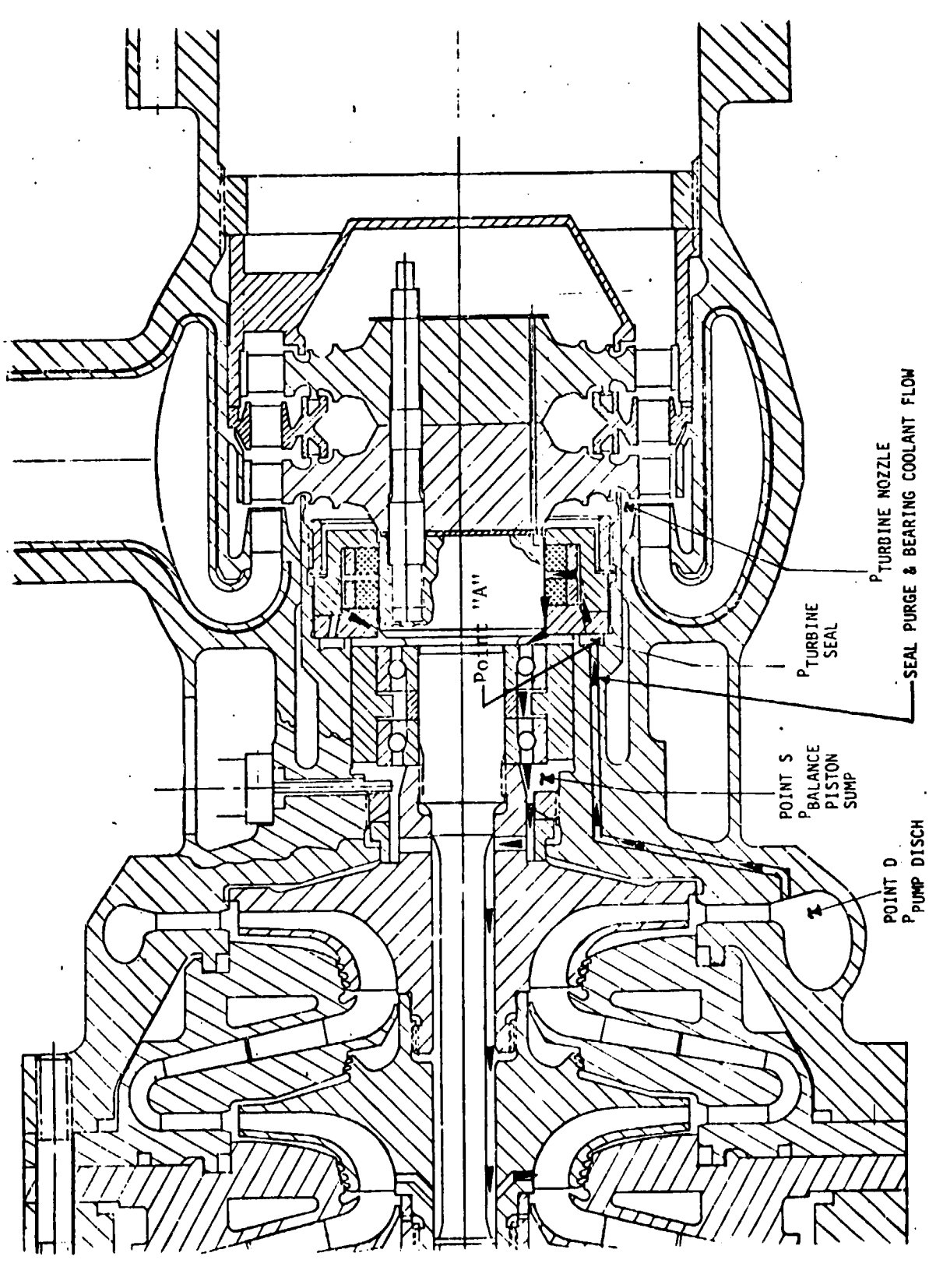

Figure 15. Mark 48-F Rear Bearing Coolant Loop

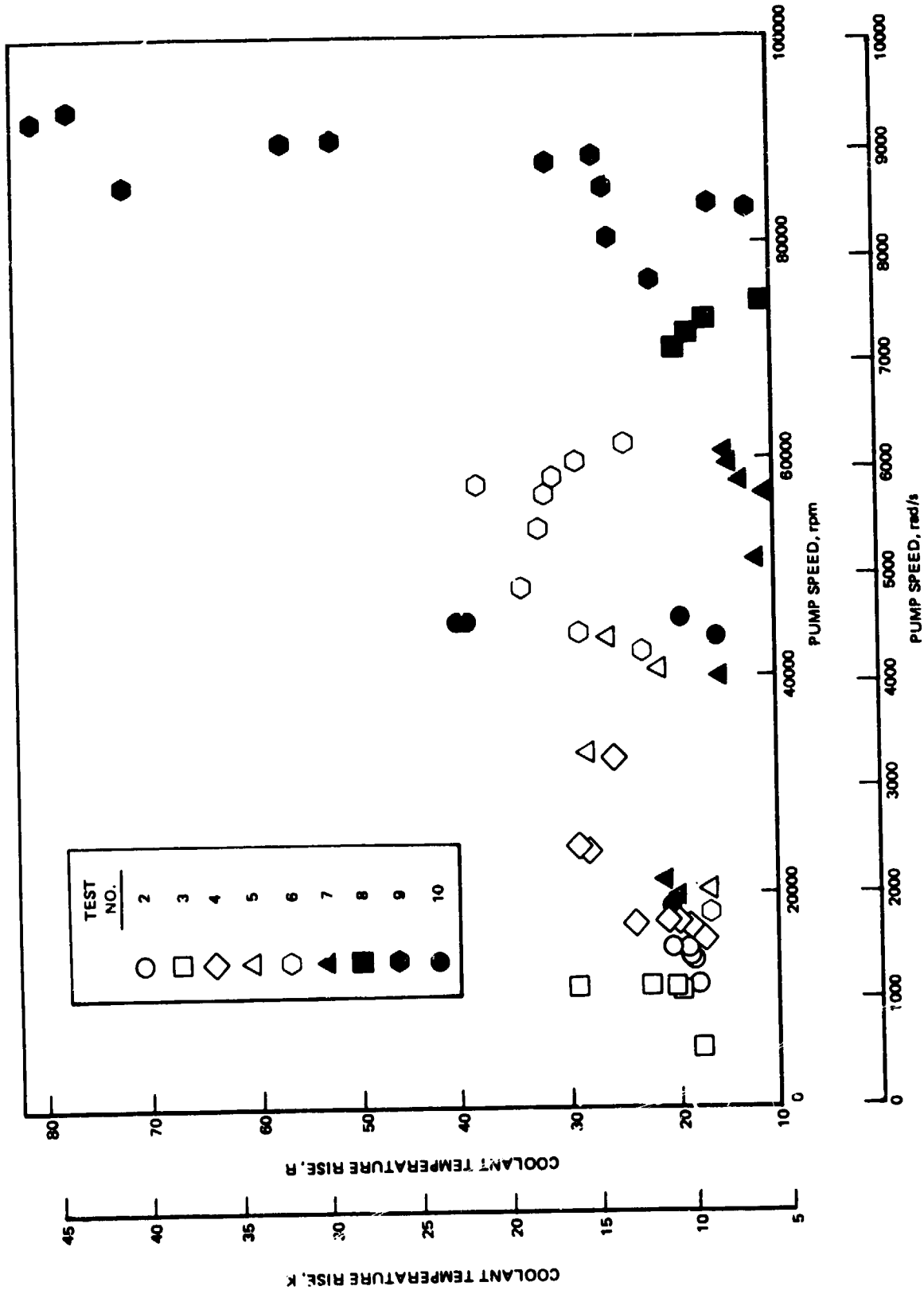

Figure 16. Rear Bearing Coolant Temperature Rise With Speed

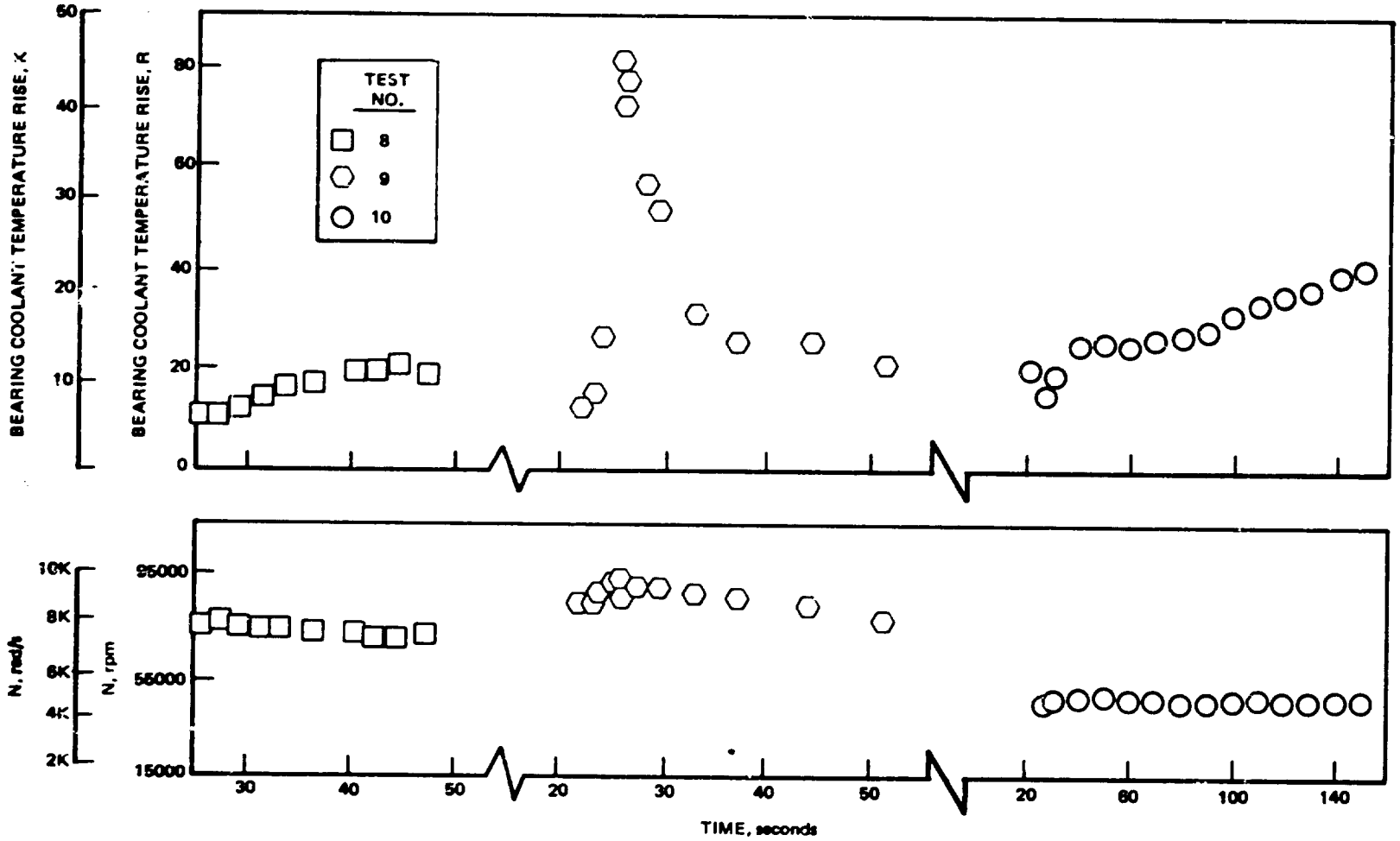

Figure 17. Rear Bearing Coolant Temperature Rise With Time

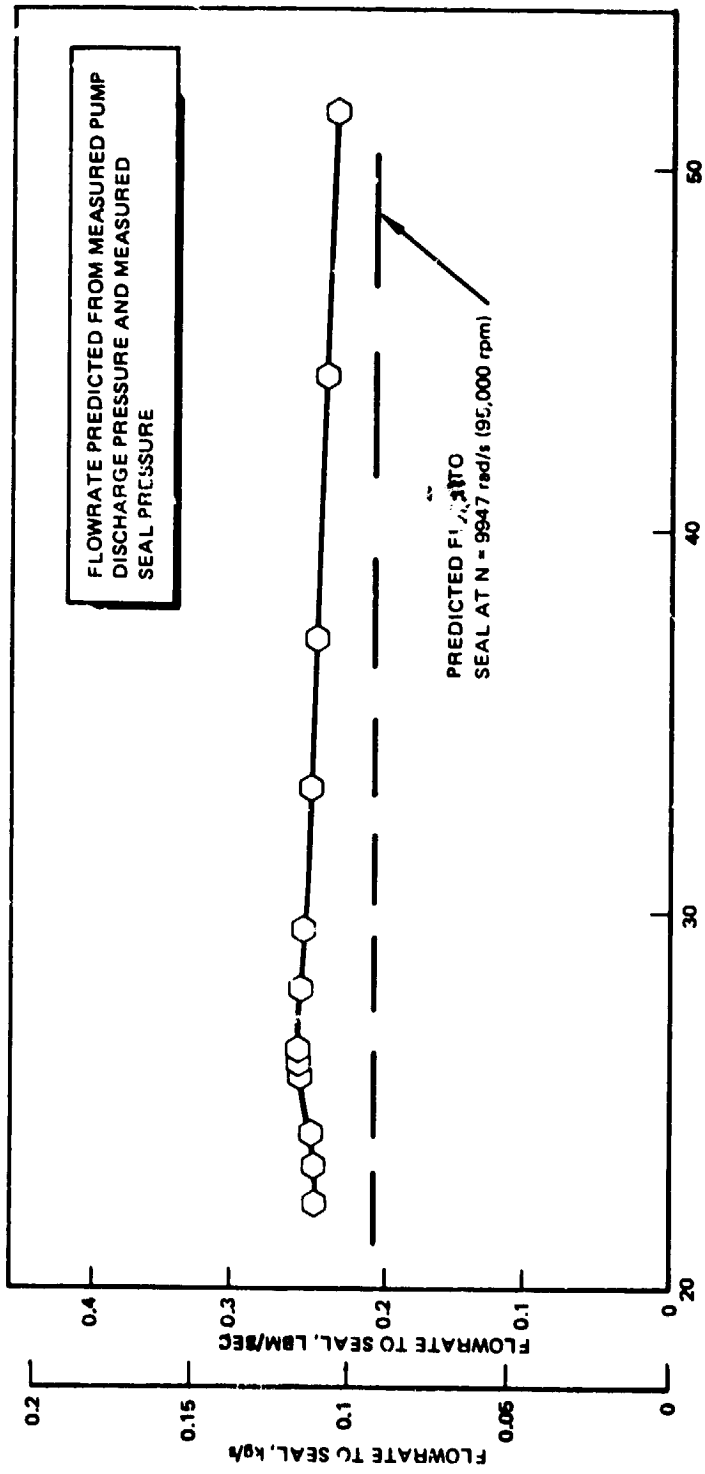

Figure 18. Mark 48-F Coolant Flow to Turbine Seal (Test 009)

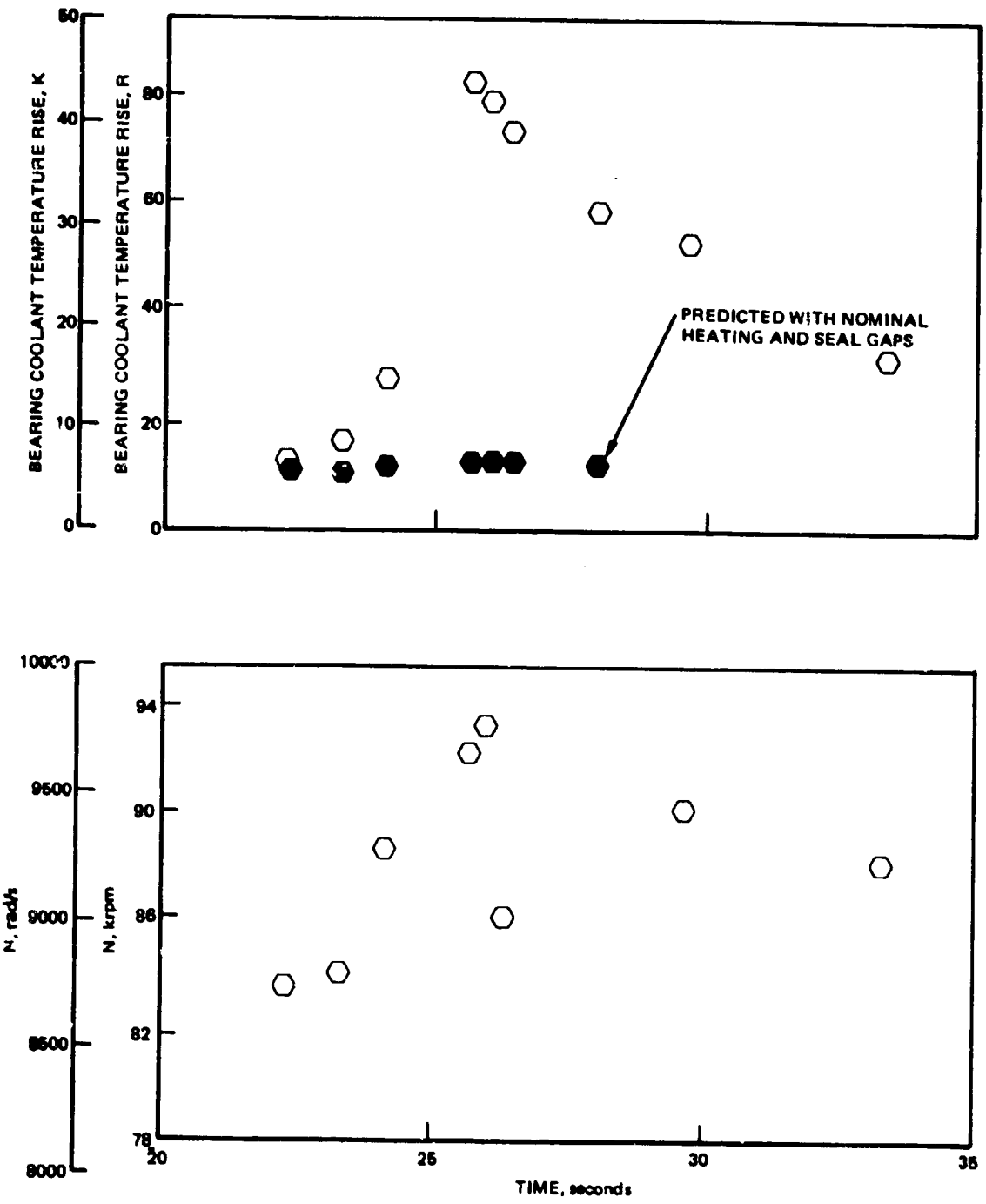

Figure 19. Bearing Coolant Temperature Rise With Time and Speed

The possibility that the peak in temperature rise during test 9 could be caused by turbine fluid leaking through the seal to the bearing was considered. The three pressures controlling the flow direction through the seal are plotted in Fig. 20 and 21 for tests 9 and 10, respectively. Since the measured seal pressures is always considerably higher than the turbine nozzle pressure, it was not considered likely that turbine fluid is entering the bearing cavity and causing the high temperatures.

Since the total flowrate to the seal predicted for the pump discharge and turbine seal pressure matched very closely the predicted flowrate of the analytic model of the seal flow, it was postulated the high fluid temperature downstream of the bearings could be resulting from one of two sources, or possibly a combination of both:

1. An increase in the gap of the turbine-side seal ring, accompanied by a reduction in the gap of the bearing-side ring would keep the total flow constant, while lowering the flow to the bearing.

2. The heat input from the bearings could be substantially higher than predicted by analysis.

Irrespective of which hypothesis was valid, a higher flow to the seal and to the bearing was seen as the solution to the problem. To effect a higher flowrate to the bearings, three modifications were made. The orifices located at the end of four transfer passages in the housing (at Point A, Fig. 15) were deleted and the number of passages in the seal housing which are used to feed liquid hydrogen to the seal were increased from 4 to 24. Both of these changes were designed to increase the available pressure in the seal, which results in higher coolant flow to the bearings. The analysis disclosed that the increased seal pressure was needed not only to ensure increased flow to the bearing but to ensure that an effective barrier is maintained to prevent turbine gases from entering the pump region. The latter is of particular importance when operating at high pump Q/N values where pump pressure is lower, but the turbine gas pressure is still high, commensurate with the high power demand of the pump.

The third change involves increasing the number of bypass holes from one to three in the seal housing leading to the bearings. In Table 8 the predicted parameters with the above modifications are noted for speed levels and Q/N ranges of interest. The obtained coolant flowrates and pressure levels were satisfactory; therefore, the hardware was modified to implement these changes.

Front Bearing Cooling Improvement

Analysis of two candidate coolant system modifications was performed for the pump-end bearings. In the first approach studied the flow path initiates at the rear hub of the first-stage impeller, (Fig. 22) and from there the flow is directed toward the bearings in the annular space formed by the shaft and first-stage impeller hub. From there the fluid is introduced to the bearing cavity on the impeller side of the bearings through four radial holes in the impeller hub. Subsequently, the coolant passes through the bearings and it is either dumped overboard through the front cap in an interim test mode or it is recirculated externally to the pump inlet line where it has an opportunity to mix with fresh fluid before entering the first-stage impeller.

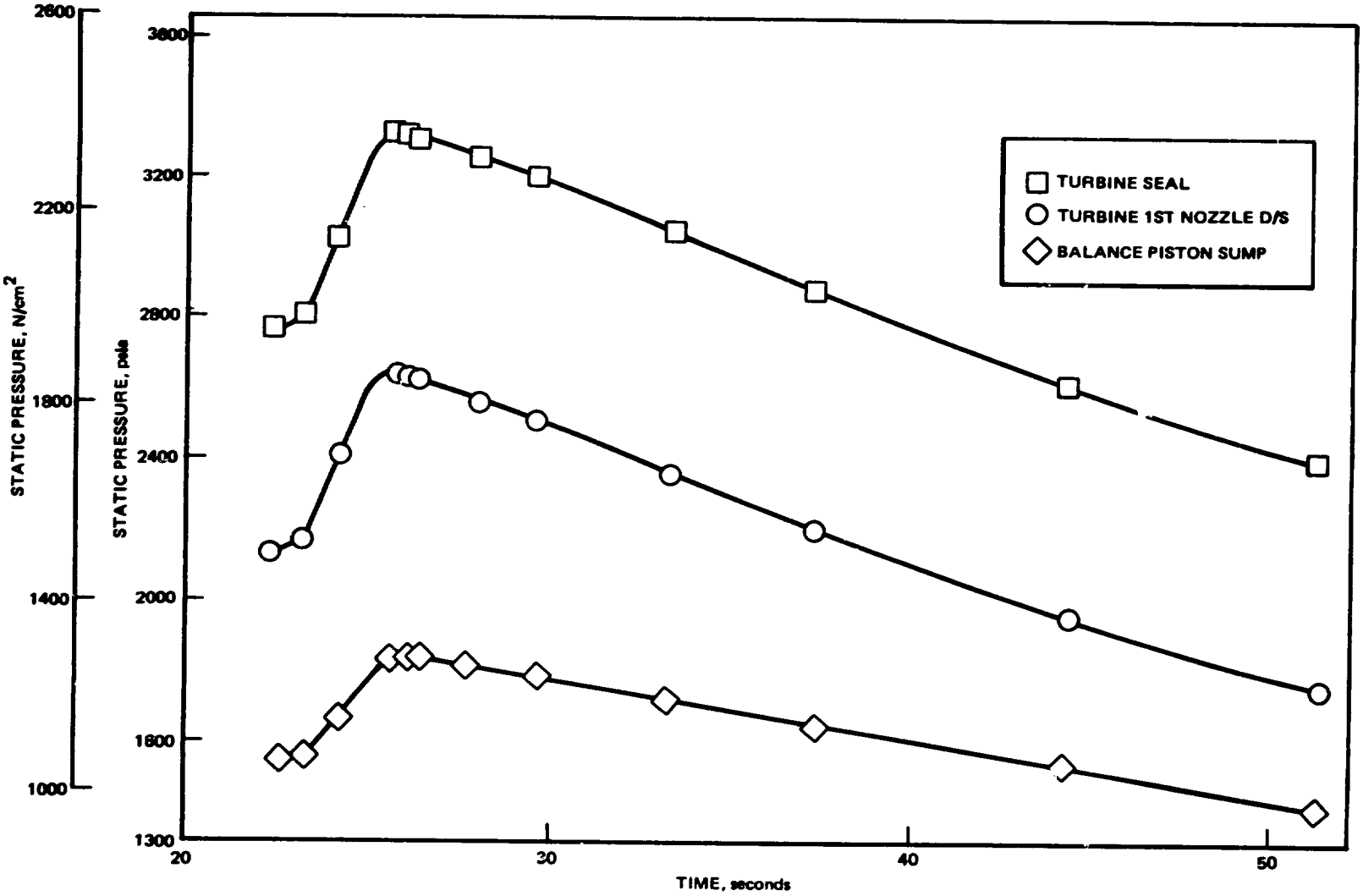

Figure 20. Turbine First Nozzle Downstream, Turbine Seal and Balance Piston Sump Pressure as Function of Time (Test 009)

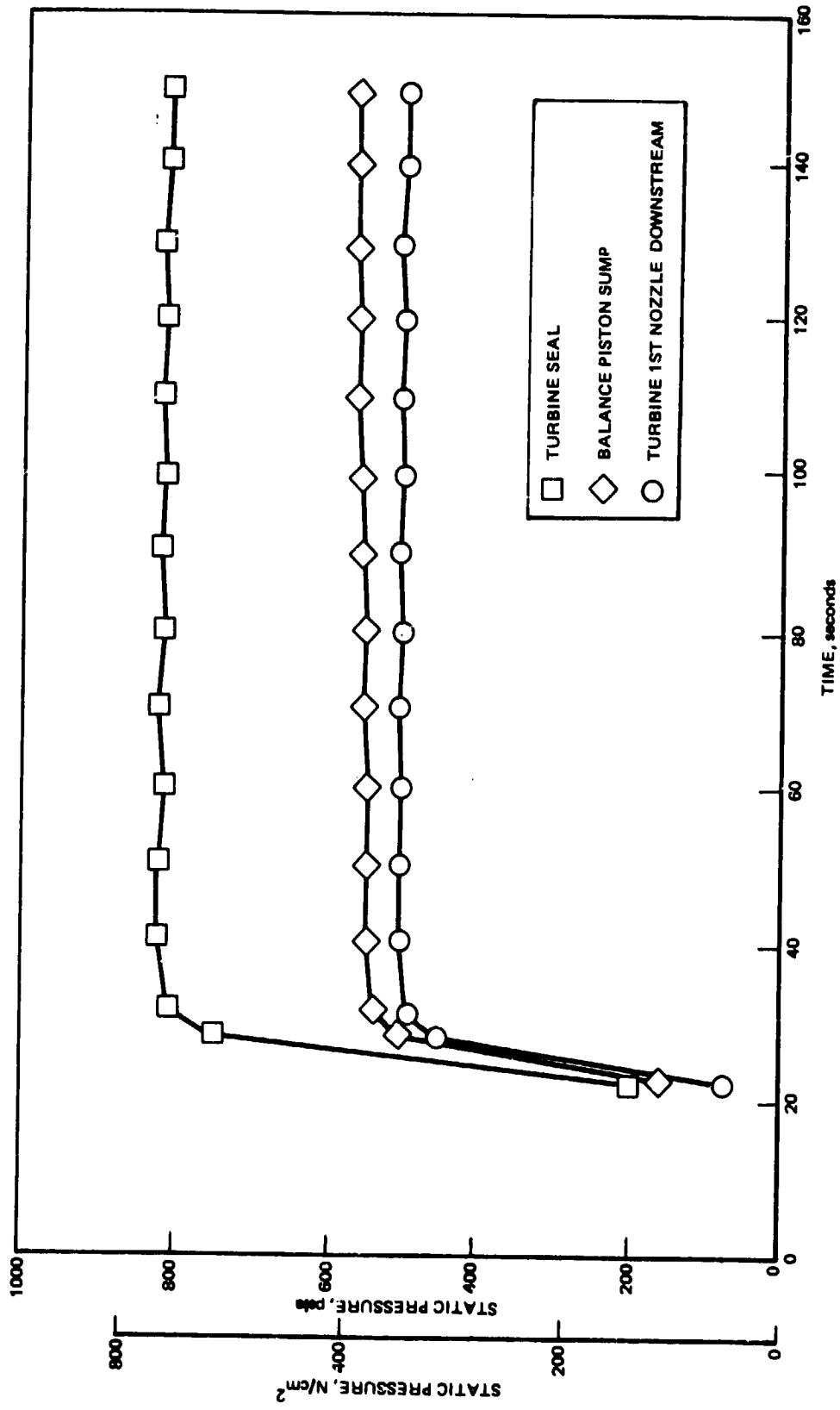

Figure 21. Turbine First Nozzle Downstream, Turbine Seal and Balance Piston Sump Pressure as Function of Time (Test 010)

TABLE 8. MARK 48-F TURBINE END BEARING COOLANT FLOW

Case	Pump Speed, rad/s (rpm)	Pump Discharge Pressure, N/cm^2 (psia)	Balance Piston Sump Pressure N/cm^2 (psia)	Turbine Nozzle Pressure N/cm^2 (psia)	Pressure In Seal N/cm^2 (psia)	Flow To Bearing kg/s (lbm/sec)	Flow To Turbine kg/s (lbm/sec)
Nominal Operation	9,947 (95,000)	3149 (4567)	1464 (2123)	2310 (3350)	2434 (3531)	0.140 (0.31)	0.054 (0.12)
Q/N = 110% (Q/N) Nominal	8,901 (85,000)	2419 (3509)	1060 (1537)	1841 (2671)	1976 (2866)	0.135 (0.30)	0.018 (0.04)
Q/N = 120% (Q/N) Nominal	8,901 (85,000)	2279 (3305)	998 (1447)	1917 (2780)	1929 (2798)	0.135 (0.30)	0 (0)

Turbine Nozzle Pressure Based on Cold Gas Drive

Seal Radial Gaps:

Bearing Side = 0.03683 mm (0.00145 inch)

Turbine Side = 0.03429 mm (0.00135 inch)

Seal Bypass Configuration:

3 Holes 0.9906 mm (0.039 inch) Diameter

Maximum Pressure Drop Through Bearing = 13.8 N/cm^2 (20 psi)

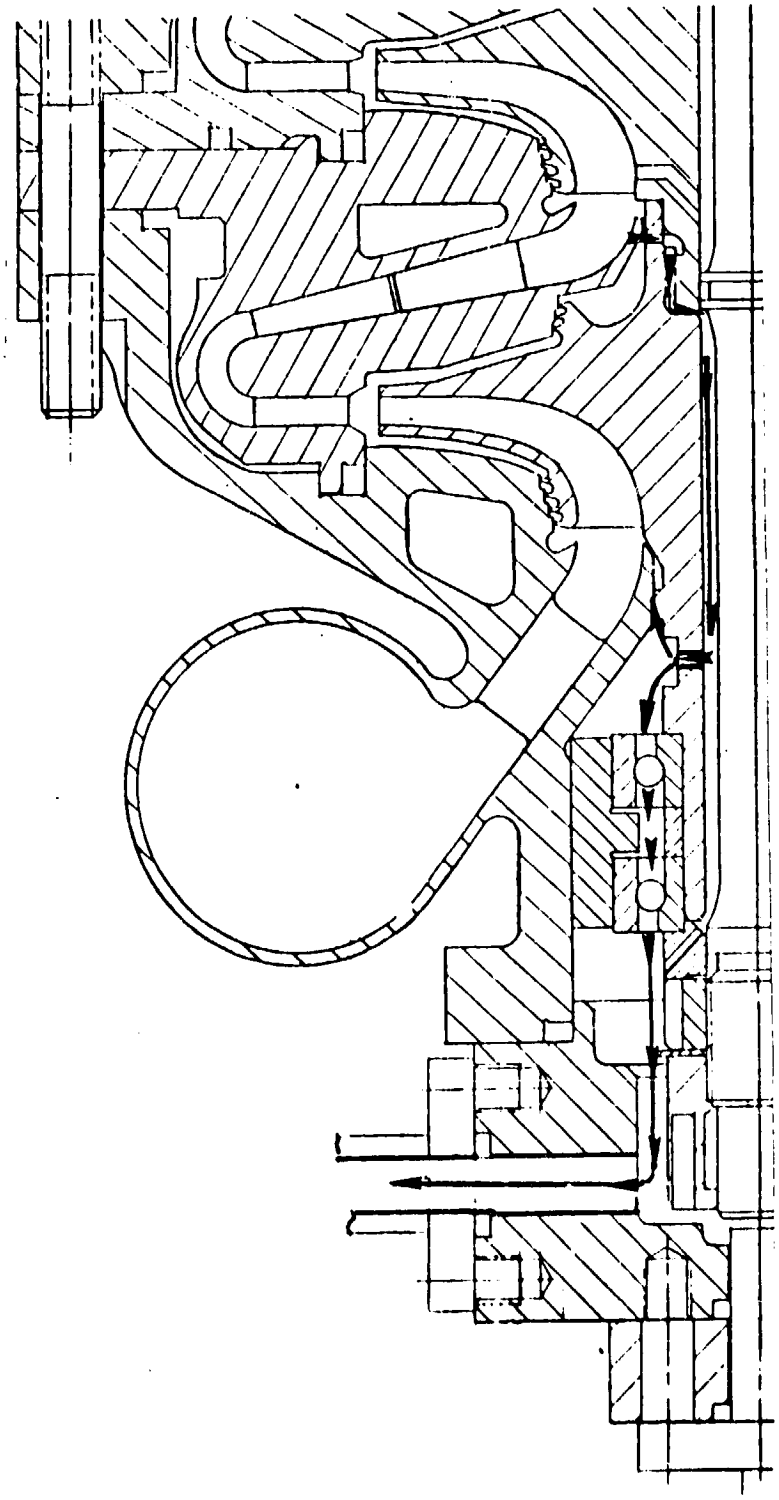

Figure 22. Candidate Pump End Bearing Coolant Flow Route

This approach offers the advantage of being able to increase the coolant flowrate through the bearings without increasing the amount of fluid injected immediately into the eye of the impeller. Because of the relatively high source pressure, the coolant can be reintroduced into the inlet line and, therefore, it represents a potential engine operating mode.

The predicted pressure and flow schedule under various speeds and inlet pressure conditions is presented in Table 9. Generally satisfactory bearing flow levels are achieved at each condition, but the system presents one major undesirable feature: To ensure that the fluid passing through the bearing is in a liquid state, which is desirable from the standpoint of effective cooling, the pressure level in the bearing cavity must be maintained above the critical pressure of 129.3 N/cm^2 (187.5 psia). This causes a significant amount of fluid to flow from the cavity directly into the eye of the impeller. This condition presents a problem in establishing the basic suction performance of the first-stage impeller without the influence of the coolant flow. After reviewing the characteristics and relative merits of the system, it was concluded that another alternative should be evaluated.

The alternate approach analyzed is illustrated in Fig. 23. The coolant originates from the first-stage impeller inlet, passes into the bearing cavity through four holes in the inlet housing guide wall and, after passing through the bearing, it is discharged overboard.

This routing for the pump-end bearing coolant offers one distinct advantage over the previous approaches considered; it facilitates evaluation of the suction performance of the first-stage impeller without the adverse effects of relatively high temperature LH_2 being ingested into the impeller. Since a major objective of the next test series was to establish the suction capability of the first-stage impeller, this coolant flow routing was accepted.

The effect of pressure differentials across the bearings on the axial loading of each member of the duplex set, and the resulting secondary effect on the radial load sharing were reviewed. The conclusion was that the predicted pressure differentials should not present a hazard to the bearings, but if the actual pressure drop is substantially higher, bearing life could be reduced. To establish the flow-speed-pressure drop characteristics of the bearings, a special pressure tap was fabricated which could be installed in place of the front bearing coolant temperature transducer. Thus, pressure measurements were planned to be taken upstream and downstream of the front bearings on several tests to verify that the pressure differentials were within acceptable limits.

Suction Performance Improvement

As discussed earlier, during the initial test series conducted in 1976, the pump experienced a cavitation related head loss at high speeds and high flowrates. The fact that the temperature of the front bearing coolant fluid which is injected into the first-stage impeller inlet, was substantially higher than anticipated, indicated that there may be an interrelationship between the two occurrences. It was postulated that the relatively hot fluid injected into the first-stage impeller was causing blockage at the inlet of the impeller and led to cavitation and attendant head loss. It was anticipated that rerouting of the

TABLE 9. MARK 48-F PUMP-END BEARING COOLANT FLOW

Case	Pump Speed rad/s (rpm)	Pump Inlet Pressure N/cm^2 (psia)	Impeller Inlet Pressure N/cm^2 (psia)	First Stage Impeller Discharge Pressure N/cm^2 (psia)	First Stage Crossover Discharge Pressure N/cm^2 (psia)	Shaft Hole Size; Four Holes, Two Places, mm (Inch)	Flow Through Bearing kg/s (lbm/sec)	Flow To Impeller Eye kg/s (lbm/sec)	Bearing Cavity Pressure N/cm^2 (psia)	Bearing Pressure N/cm^2 (psi)
Nominal Two Stage Labyrinth at R_4 Diametral Clearance = 0.005	9,947 (95,000)	69 (100)	62 (90)	800 (1160)	1055 (1531)	1.612 (0.0635)	0.090 (0.20)	0.040 (0.09)	194 (281)	9 (13.0)
Low Inlet Pressure Noncavitating	9,947 (95,000)	21 (30)	14 (20)	751 (1090)	1076 (1561)	1.612 (0.0635)	0.090 (0.20)	0.040 (0.09)	159 (231)	9 (13.0)
Cavitation 10% Head Drop Low Inlet Pressure	8,901 (85,000)	21 (30)	14 (20)	544 (789)	778 (1128)	1.612 (0.0635)	0.076 (0.17)	0.031 (0.07)	119 (173)	7 (9.6)

Critical Pressure = 129.3 N/cm^2 (187.5 psia)

Projected density of fluid discharging to the eye of the impeller is about 0.0064 g/cm^3 (0.4 lbm/ft^3)

Labyrinth seal upstream of impeller eye having 0.127 mm (0.005 inch) diametral clearance

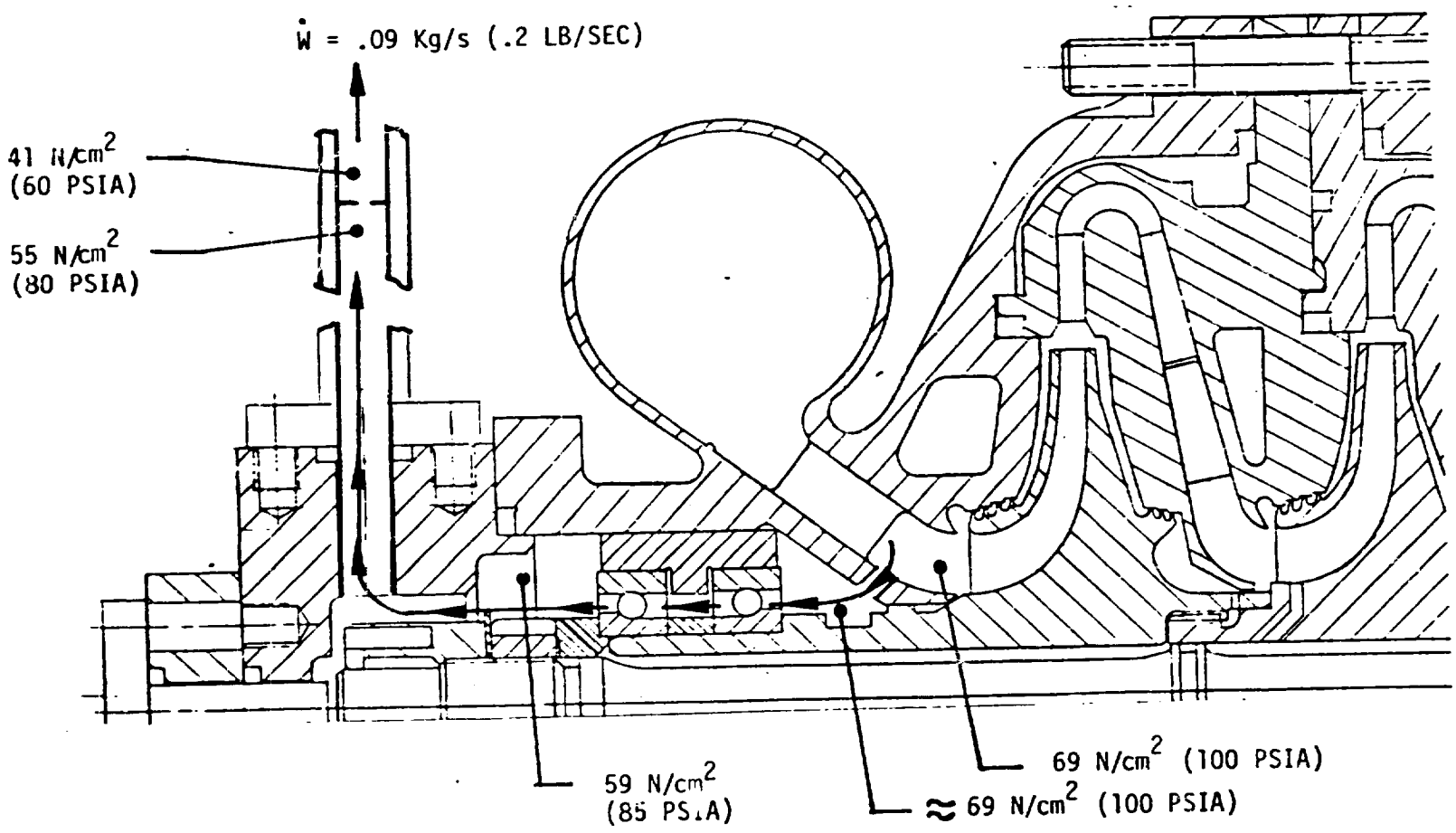

Figure 23. Mark 48-F Front Bearing Coolant System

flow as described above would produce an improvement in the cavitation performance.

Another potential cause for low suction performance was attributed to the poor quality of the impeller hydrodynamic surfaces which were electrical discharge machined from an integral piece of forging. A spare set of impellers had been fabricated by an alternate method, in which the impeller was machined in two sections and subsequently welded into a single unit. The quality, i.e., surface finish of this "split impeller" was better than that of the integral impeller tested in the initial (1976) test series, and therefore, it was incorporated for the next test series in anticipation of a performance improvement.

Assembly of Turbopump S/N 01-1

The changes incorporated into turbopump S/N 01-1 to form the Mod 1 configuration are summarized below.

- Split Impellers
  - Original impellers too difficult to fabricate
  - Eliminate dimensional discrepancies
  - Improve finish, etc.
- Front Bearing Coolant Routing Modified
  - Redirect warm fluid
  - Improve suction performance
- Rear Bearing Coolant passages modified
  - Ensure blocking turbine gas from pump at high Q/N
  - More coolant flow to bearing

Balancing of the turbopump rotor was accomplished in accordance with the procedure established during the initial assembly of the Mark 48-F turbopump. To minimize the locked-in moments in the rotor, a multiplane balance correction was made. Initially temporary correction was made in an assembly which included only the first- and third-stage impellers, the shaft, the balance bearings, the retaining fasceners, and a dummy spacer in place of the second-stage impeller (Fig. 24). The temporary correction was applied in the planes of the first- and third-stage impeller rear shrouds. Subsequently, the second-stage impeller was added (Fig. 25) and its unbalance was corrected in its shroud. Next, the turbine wheels were added and correction was made in their plane (Fig. 26). At each step, radial and axial runouts were measured and recorded as indicated in Fig. 24 through 26. Several repeatability checks were performed in which the rotor was completely disassembled, reassembled, and the residual unbalance was determined. The final balance was effected to 0.105 g-cm (0.25 gr-in.), the machine limit.

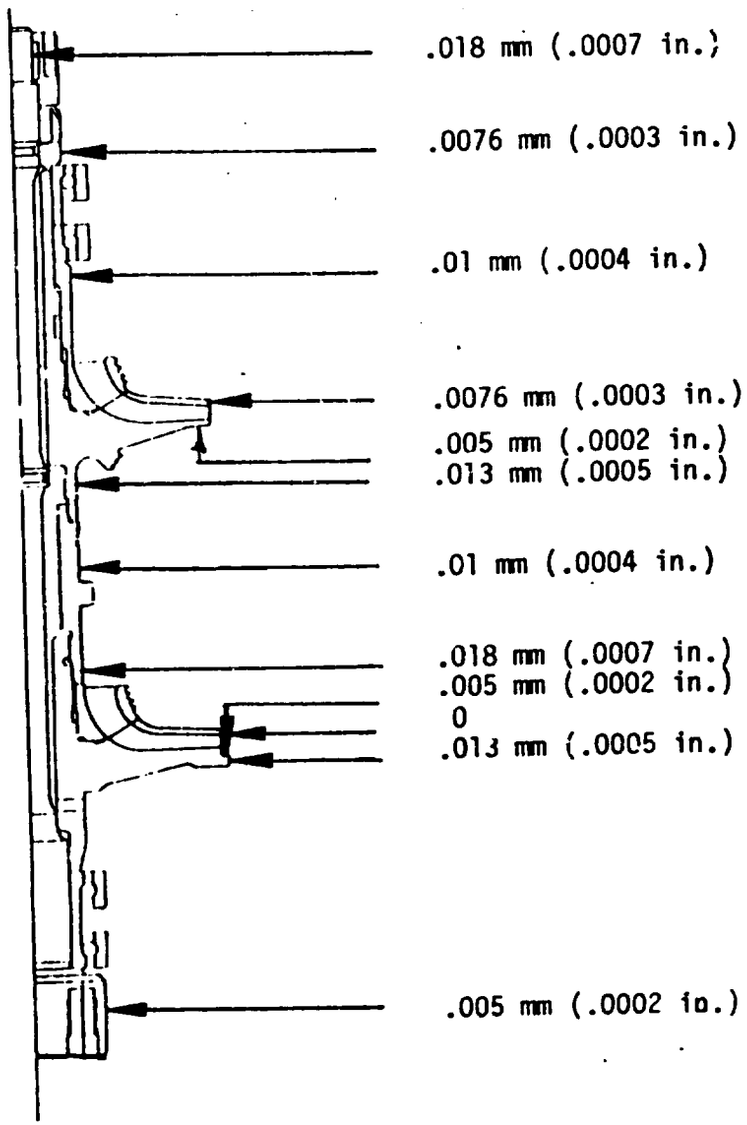

Figure 24. Mark 48-F Partial Balance Assembly Runouts

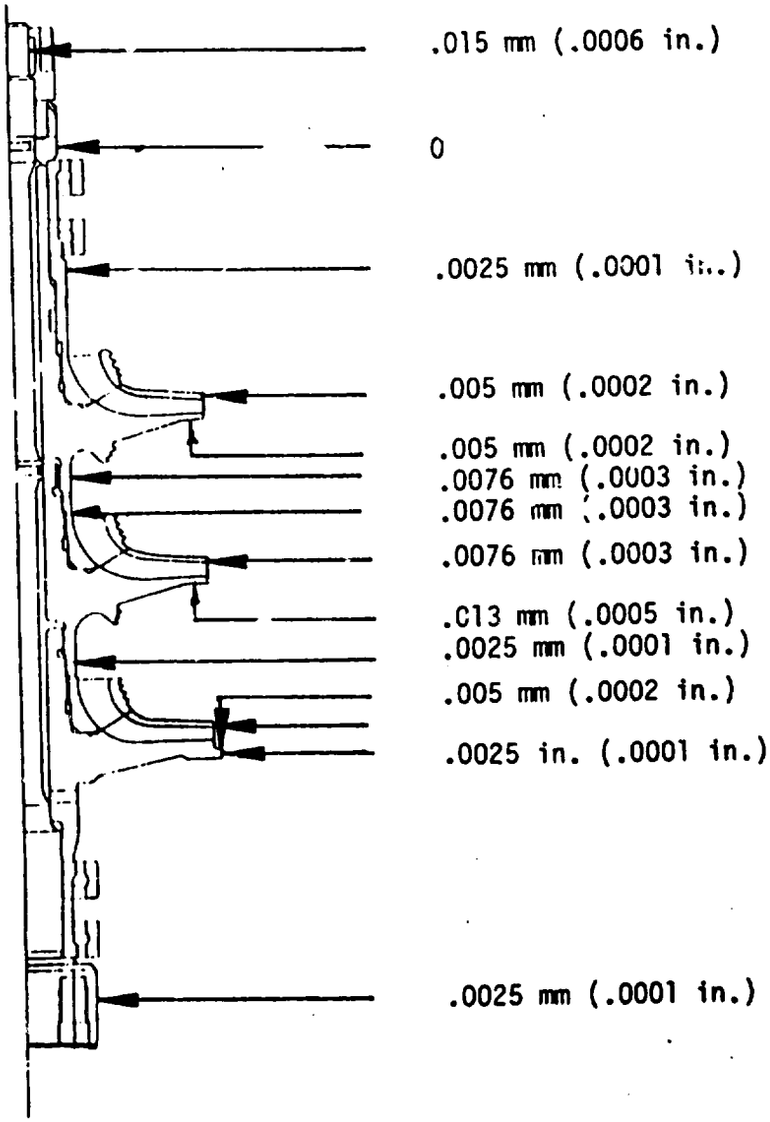

Figure 25. Mark 48-F Partial Balance Assembly Runouts

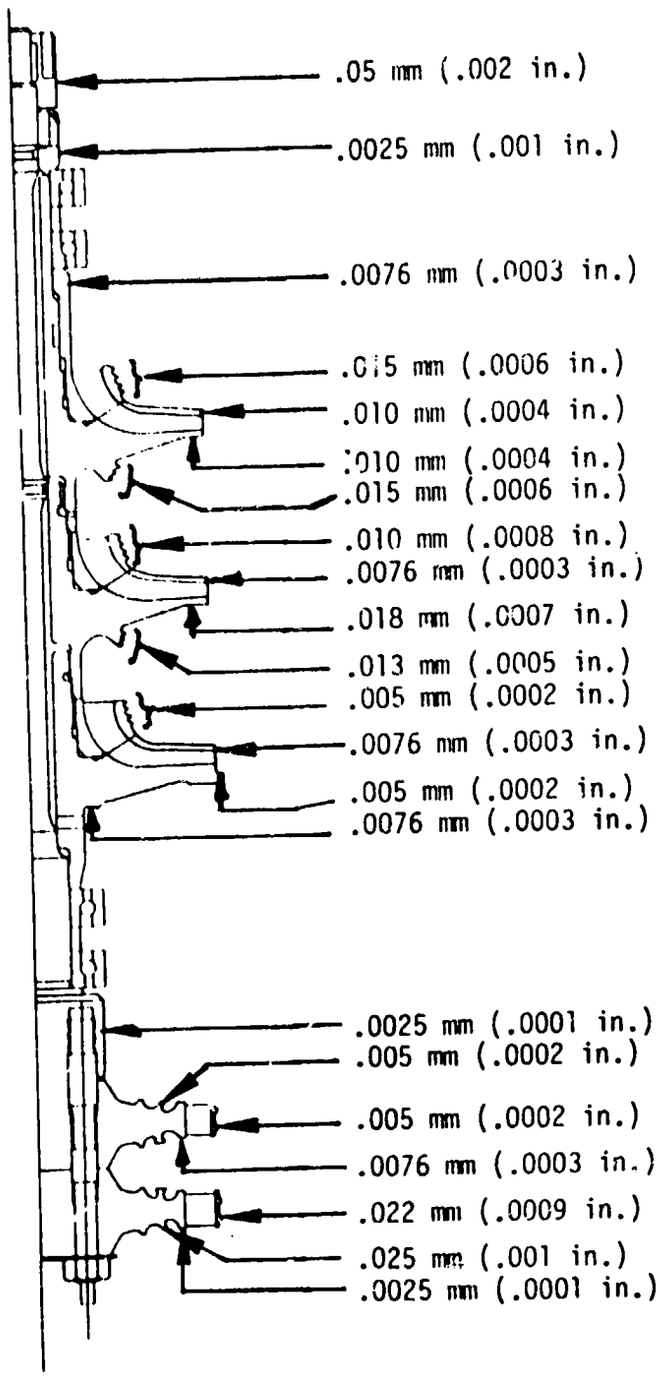

Figure 26. Mark 48-F Final Balance Assembly Runouts

The load-deflection characteristics of the front and rear bearing cartridge subassemblies are illustrated in Fig. 27 and 28, respectively. The springs at the bearing outer races were installed with a slightly higher axial clearance 0.00254 cm (0.001 inch) total than in the previous build. This was done because there is potential that the higher than anticipated bearing fluid temperature rise was caused by too high an axial load on the bearings.

The load-travel characteristics of the rotor at ambient temperature are shown in Fig. 29. A rotor load-travel test was performed at LN_2 temperature also; the data obtained with the final cartridge shims is illustrated in Fig. 30.

The critical clearances and fits measured during assembly are shown in Fig. 31 through 34.

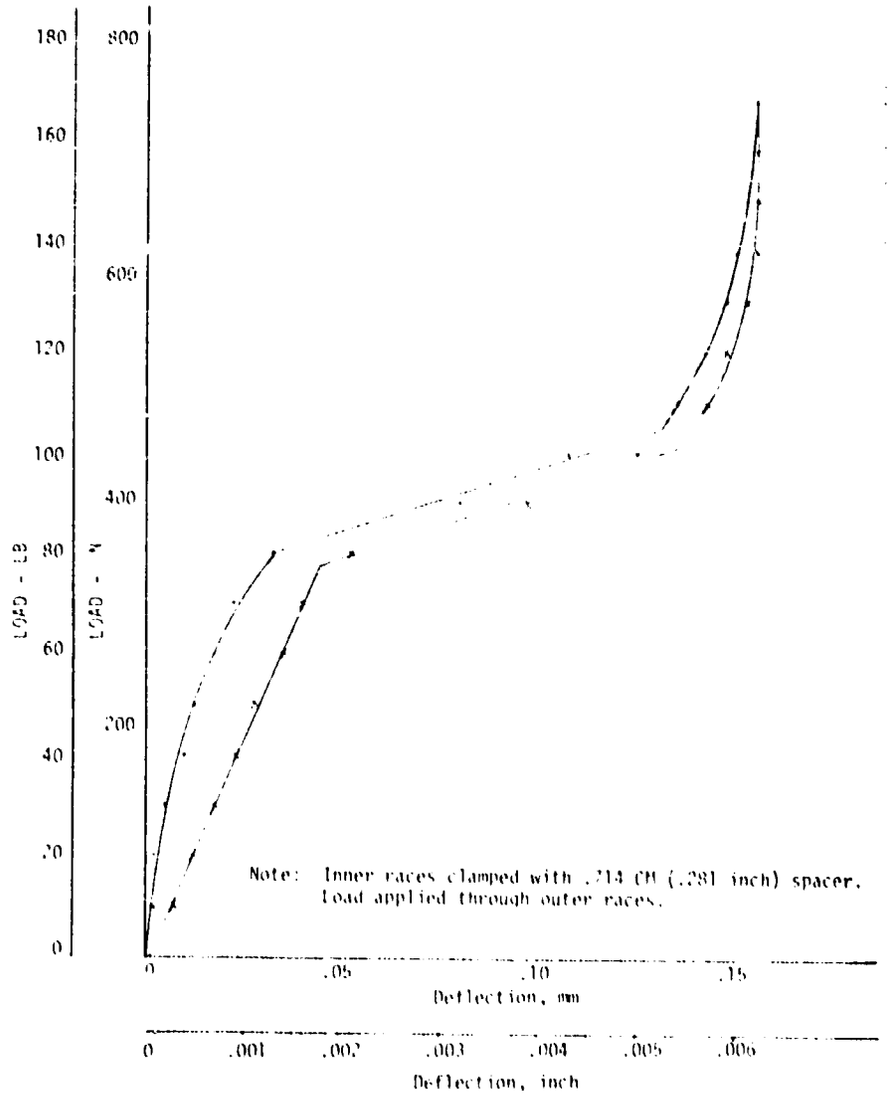

Figure 27. Forward Cartridge Preload Curve

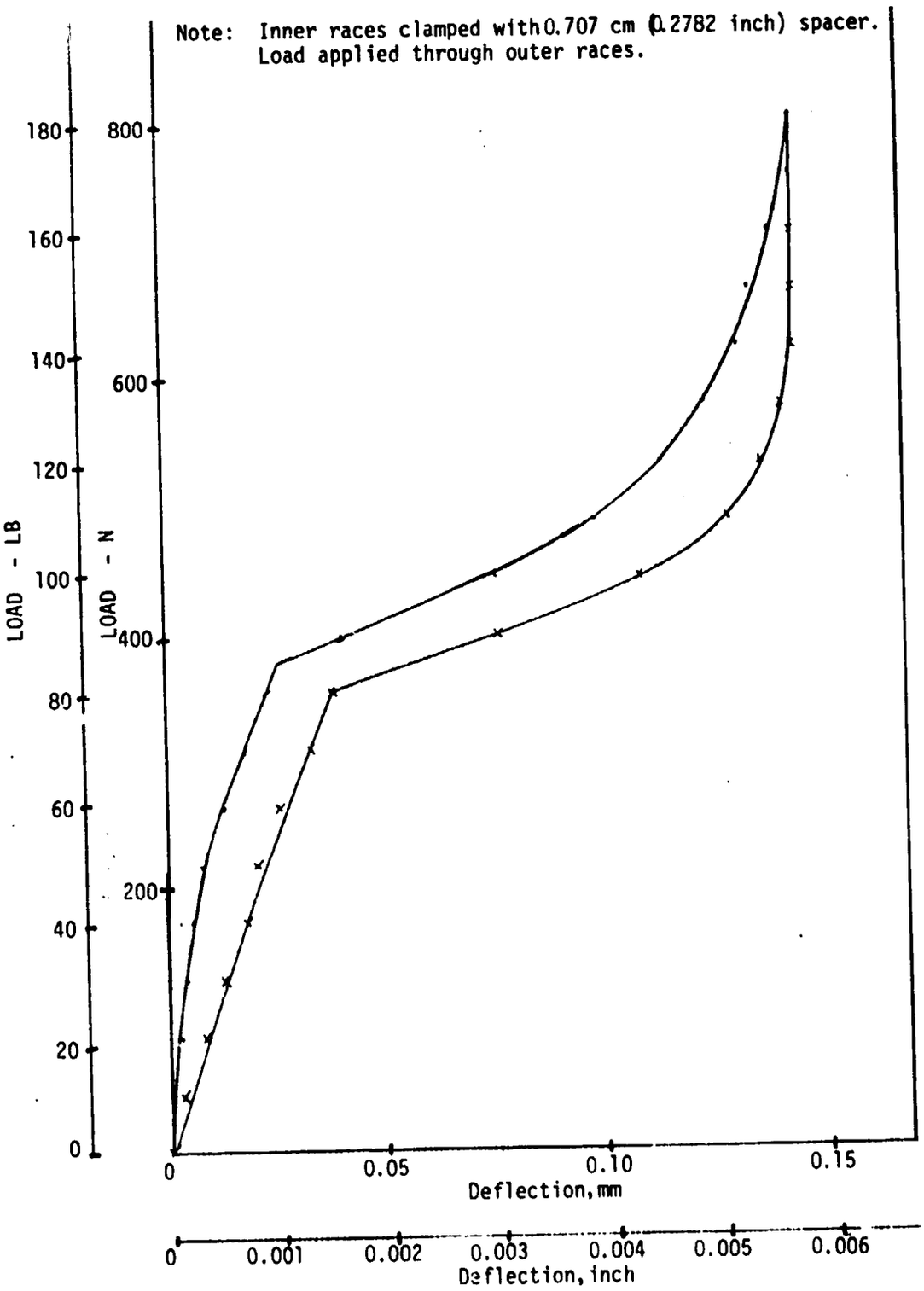

Figure 28. Mark 48-F Aft Cartridge Preload Curve

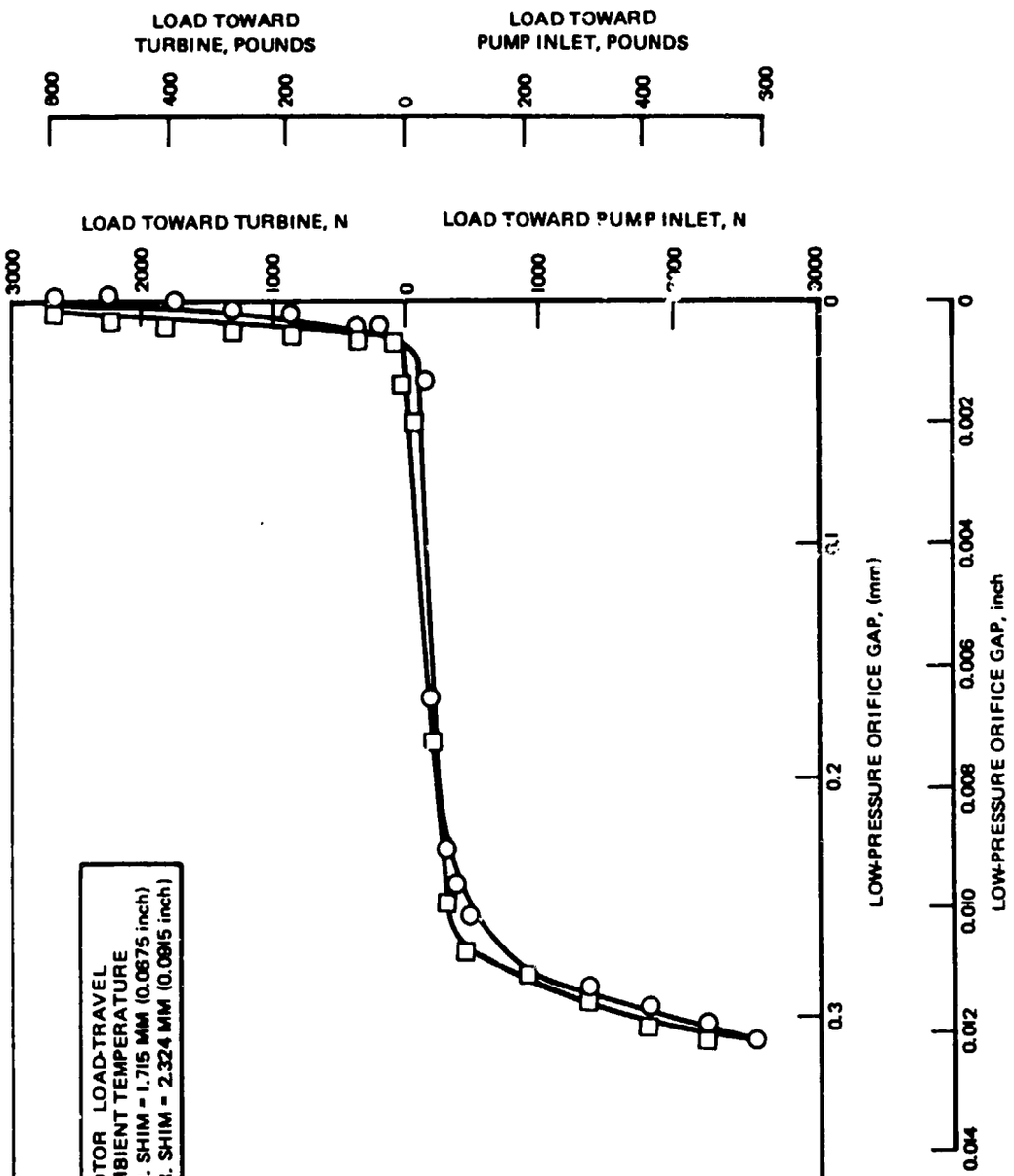

Figure 29. Rotor Load-Travel Characteristics - Ambient Temperature

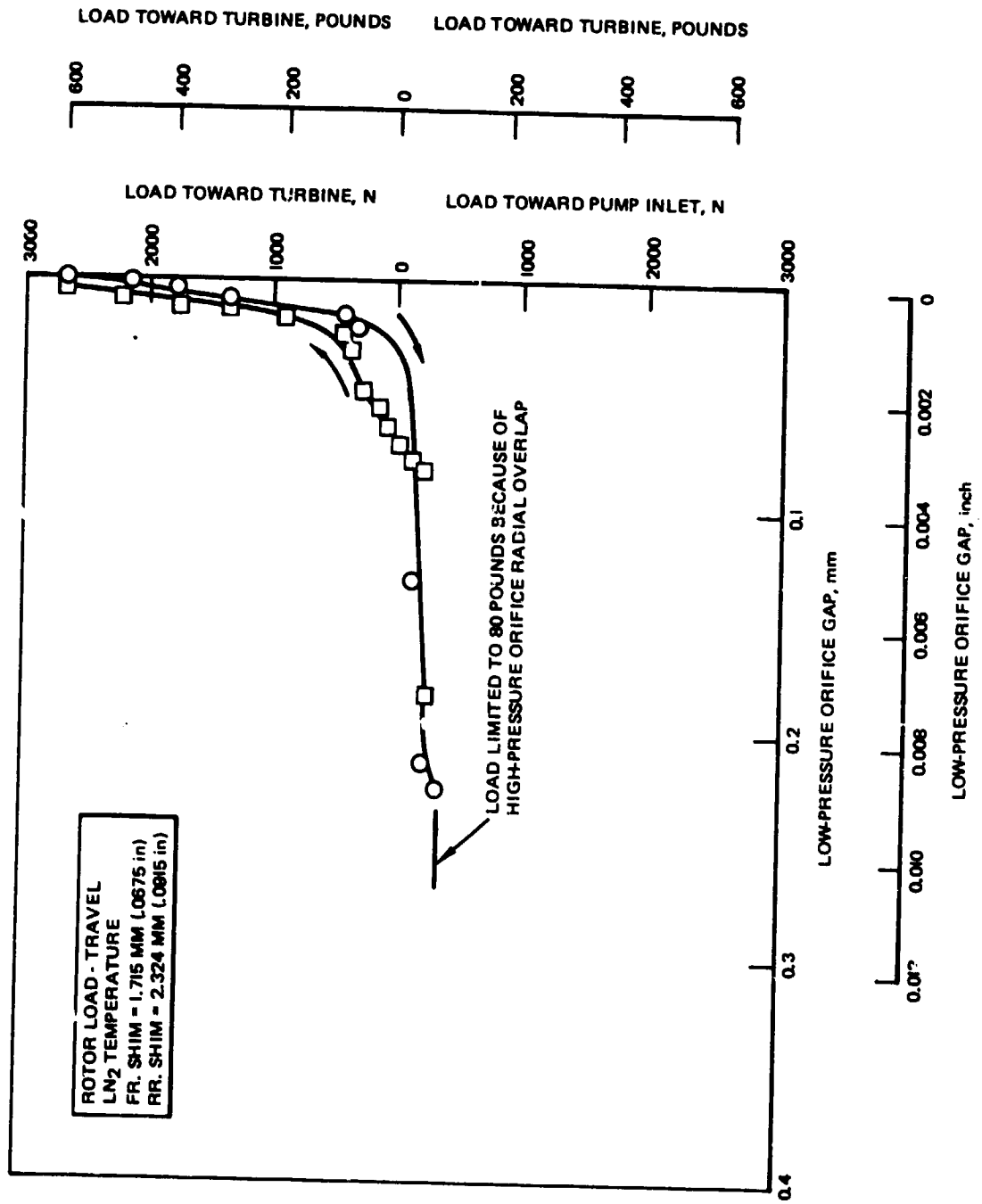

Figure 30. Rotor Load-Travel Characteristics - LN_2 Temperature

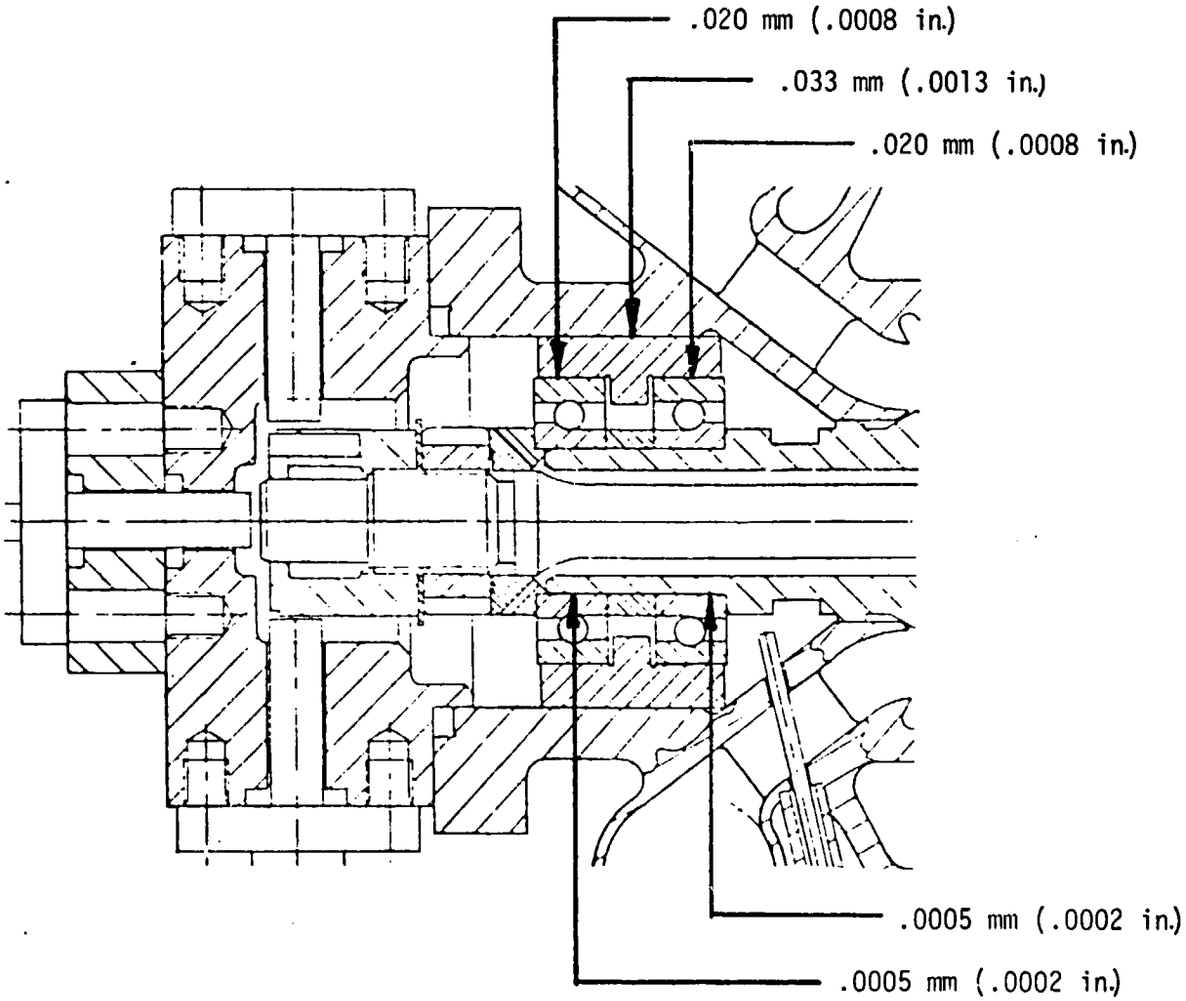

Figure 31. Mark 48-F Turbopump (S/N 01-1)
Front Bearing Fits

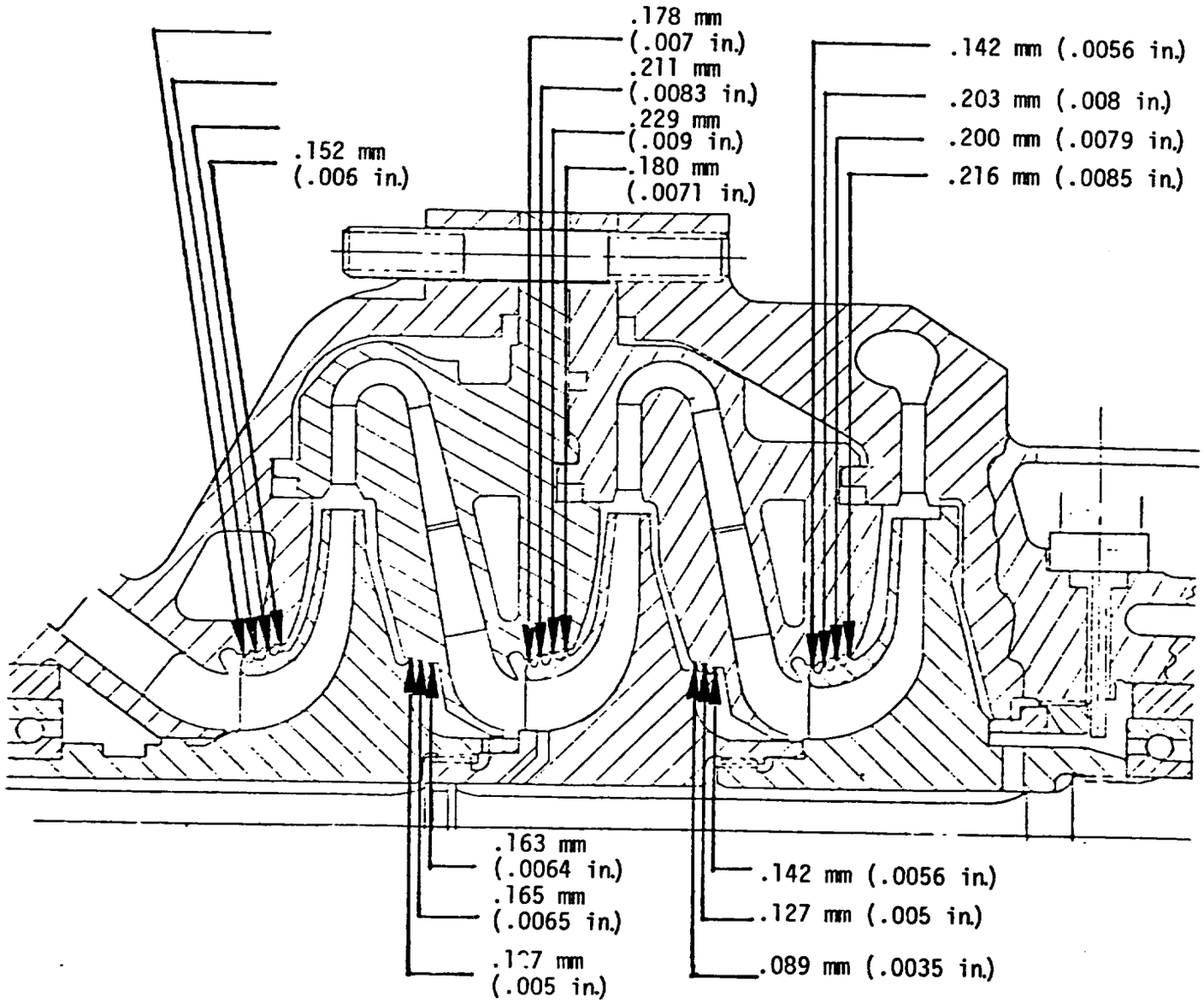

Figure 32. Mark 48-F S/N 01-1 Impeller Labyrinth Clearances

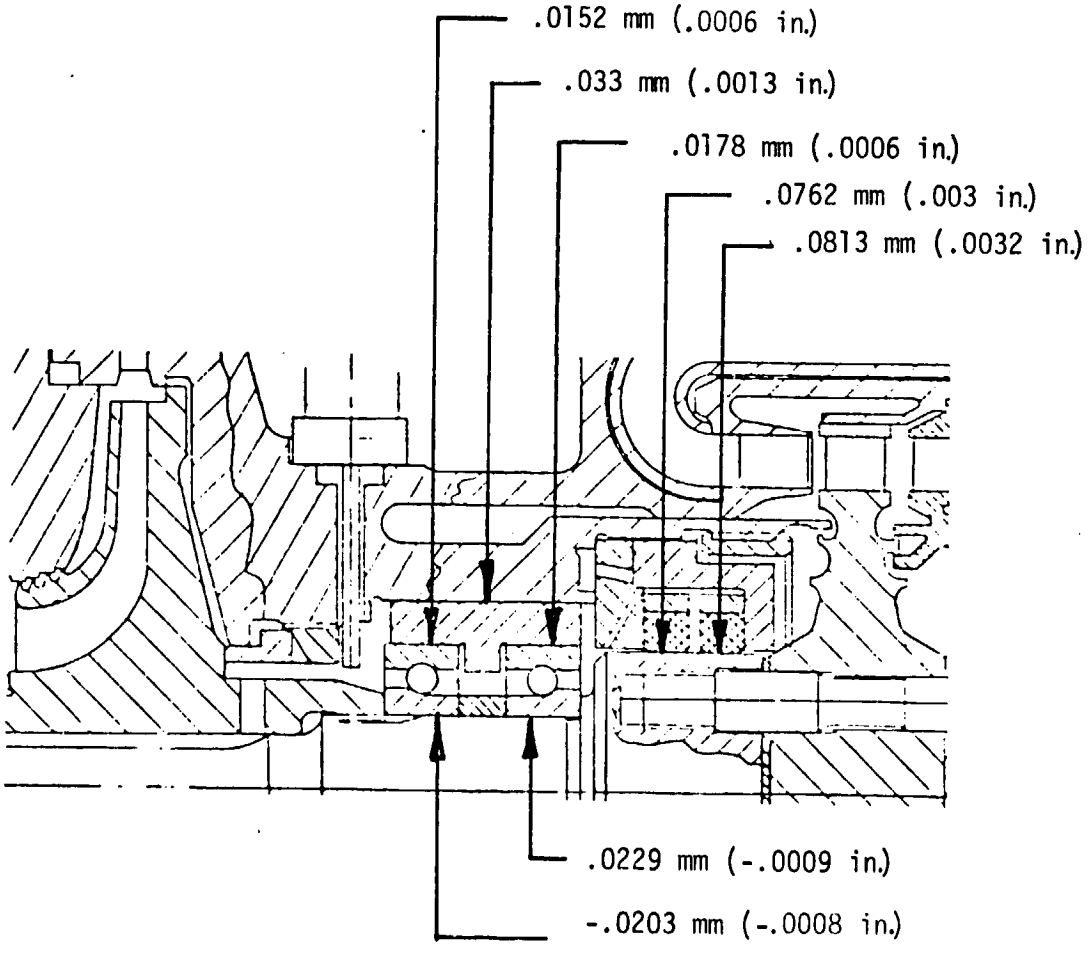

Figure 33. Mark 48-F Turbopump (S/N 01-1)
Bearing and Seal Clearances

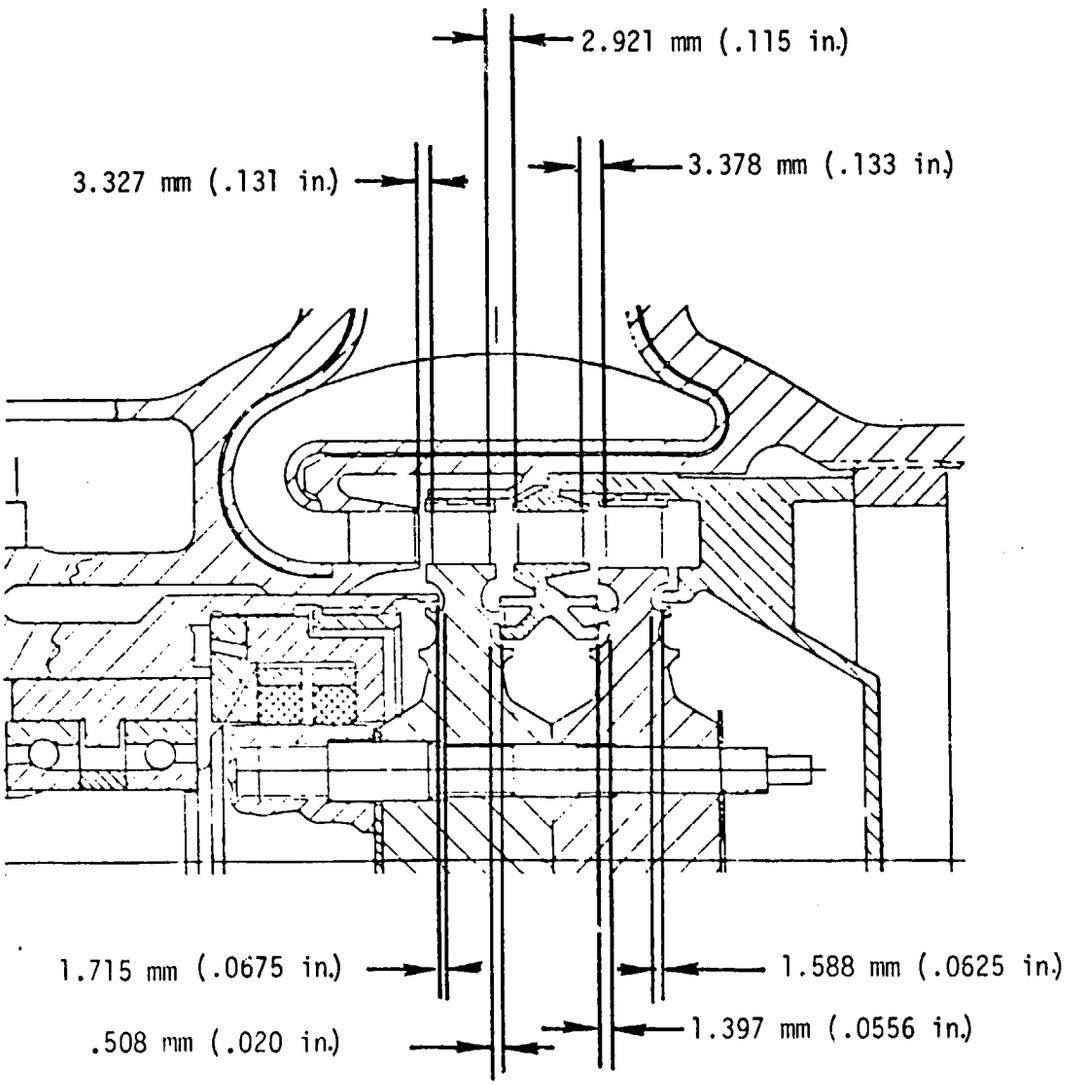

Figure 34. Mark 48-F Turbine (S/N 01-1)

Test Series No. 2

The test series was performed with ambient temperature gaseous hydrogen as the turbine propellant, and the objective was to obtain head-flow characteristics and suction performance data for the pump. The turbopump installation for this purpose is shown in Fig. 35 through 37. A simplified schematic of the primary fluid flow system is presented in Fig. 38.

The pump performance was characterized in a single 136-second duration test conducted on 12 January 1978. Liquid hydrogen was used as the pump fluid, and the turbine was propelled by ambient temperature gaseous hydrogen.

The operating sequence observed during the test was as follows: After facility preparations were completed and the turbopump was adequately primed and chilled, the rotor speed was slowly increased to 2408 rad/s (23,000 rpm) the turbopump was allowed to stabilize after the pump discharge throttle valve position was adjusted to bring the flow to a nominal value. The speed was then increased to 4712 rad/s (45,000 rpm) using an automatic feeback control device to regulate the supply pressure to the turbine to the level needed to maintain approximately 4712 rad/s (45,000 rpm). The prime purpose of using an automatic control device was to facilitate a quick transition through the first rotor critical speed located at 3455 rad/s (33,000 rpm).

Once stabilized at 4712 rad/s (45,000 rpm), the pump discharge throttle valve position was varied to obtain data at 85% and 69% of nominal flow. The throttle valve was then opened to obtain a repeat data point at 86% of nominal flow, and subsequently to operate at 100%, 110% and 118% of nominal flowrate.

With the data objectives achieved at 4712 rad/s (45,000 rpm), the speed was stepped up to 6807 rad/s (65,000 rpm), again using the turbine pressure control system. At the 6807 rad/s (65,000 rpm) level, data points were obtained at 89%, 80%, 67%, 90% and 100% of nominal flowrates. The test was terminated by the vibration sensor cutoff device. Posttest examination disclosed that the accelerometer being monitored was loose and evidently gave an erroneous signal. No hardware problem was evident.

Data Analysis. Reduction of the data revealed the discharge pressure-flow characteristics shown in Fig. 39. Although sufficient pressure is being produced at low flowrates, above a certain flow level a sudden drop in discharge pressure is evident. In Fig. 40 through 42, the performance of the pump on an individual stage basis is examined. It is evident that the pressure rise through the second and third stages remains normal with increasing flowrates. In contrast, Fig. 39 indicates a sharp drop in the pressure rise of the first stage above a certain flowrate, both at 4608 rad/s (44,000 rpm) and at 6807 rad/s (65,000 rpm). The data in Fig. 39 further pinpoints the problem to the impeller, in as much as the diffuser pressure rise remains continuous.

The performance of the axial thrust control balance piston was satisfactory throughout the operating range, as shown in Fig. 43. The balance piston parameter, a measure of the pressure drop through the low pressure orifice versus the overall pressure drop, is expected to have value of approximately 0.5.

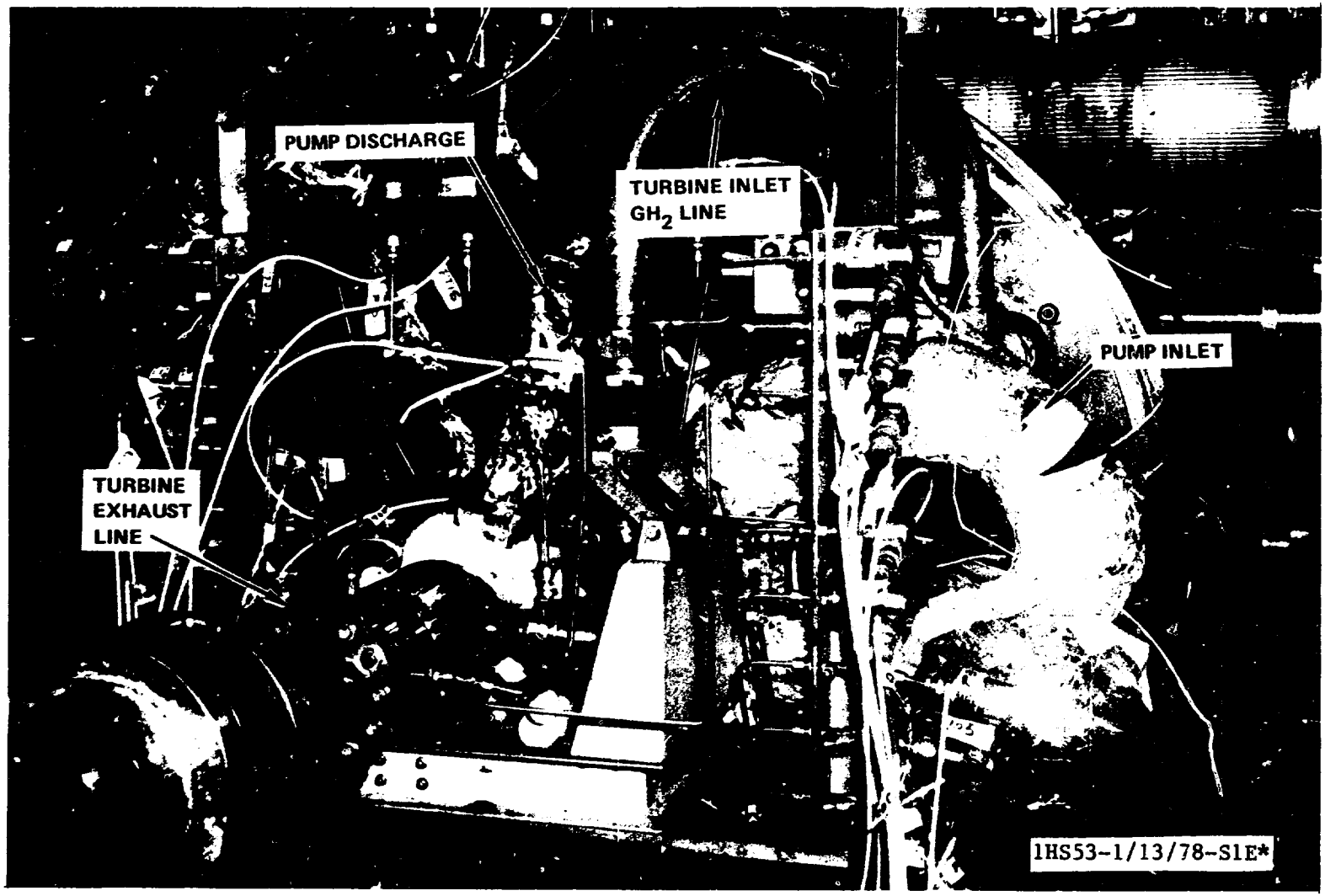

Figure 35. Mark 48-F Turbopump Test Installation (1978)

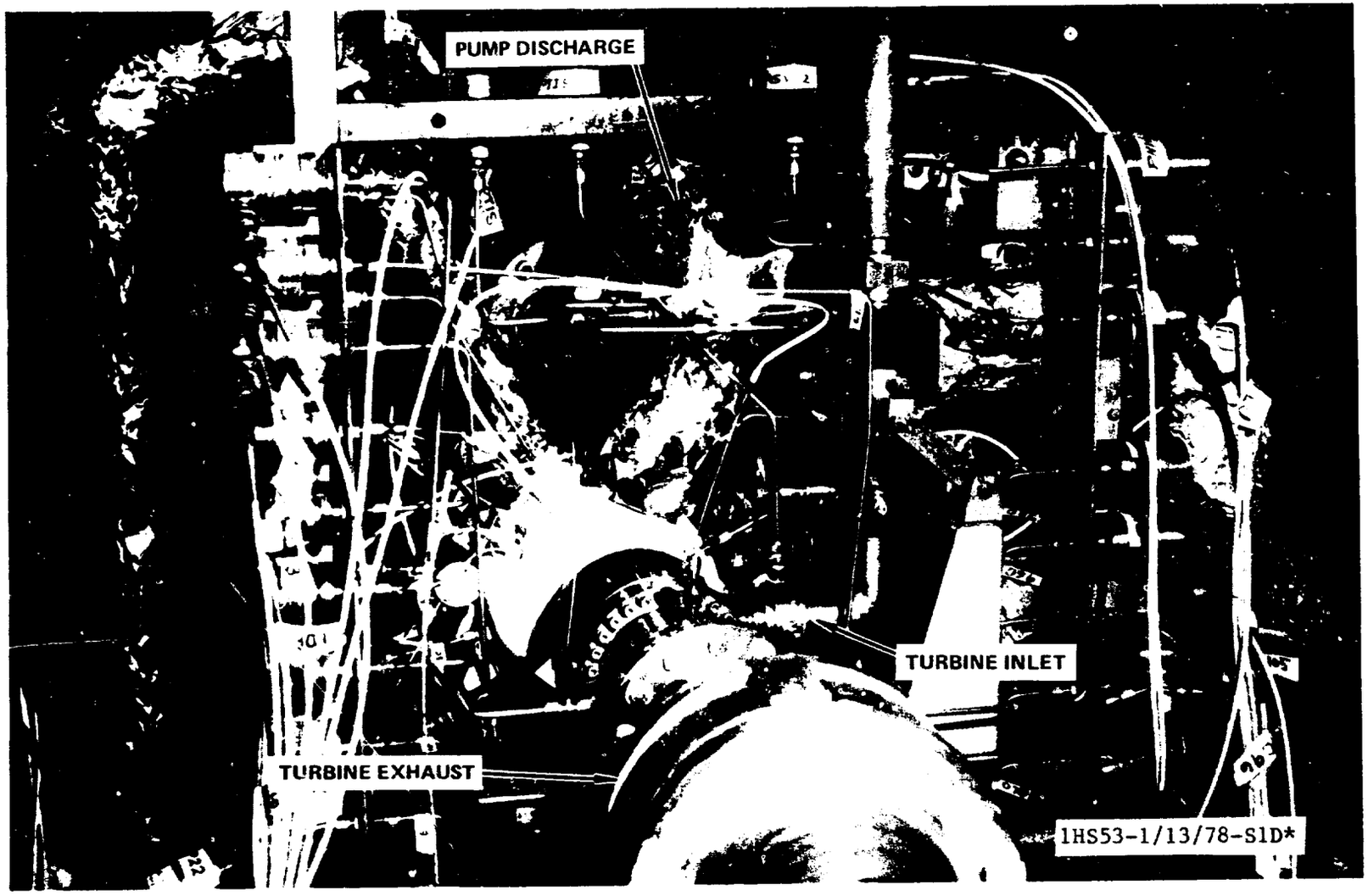

Figure 36. Mark 48-F Turbopump Test Installation (GH_2, 1978)

Figure 37. Mark 48-F Turbopump Test Installation (1978)

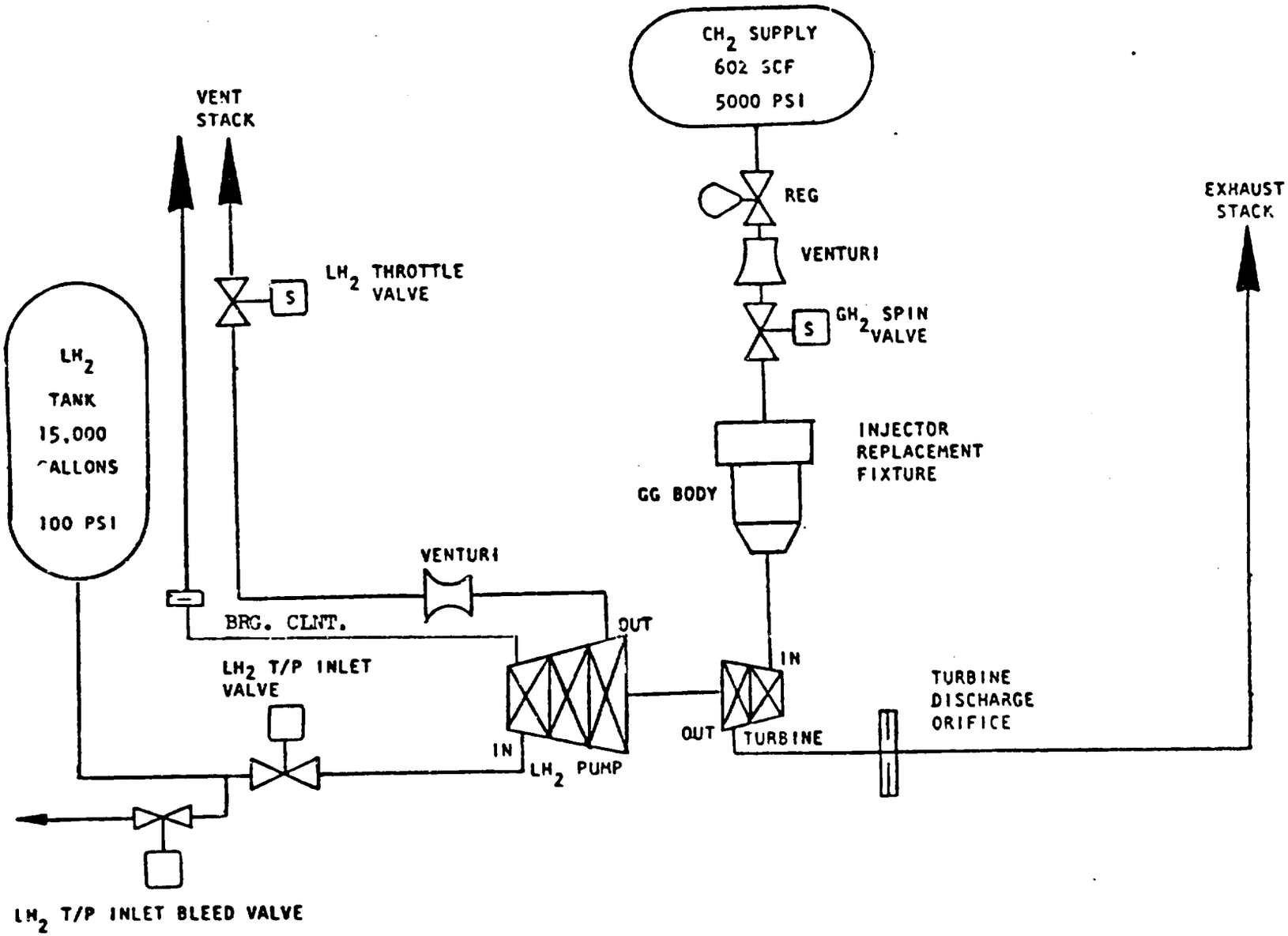

Figure 38. Gaseous Hydrogen Turbine Drive System

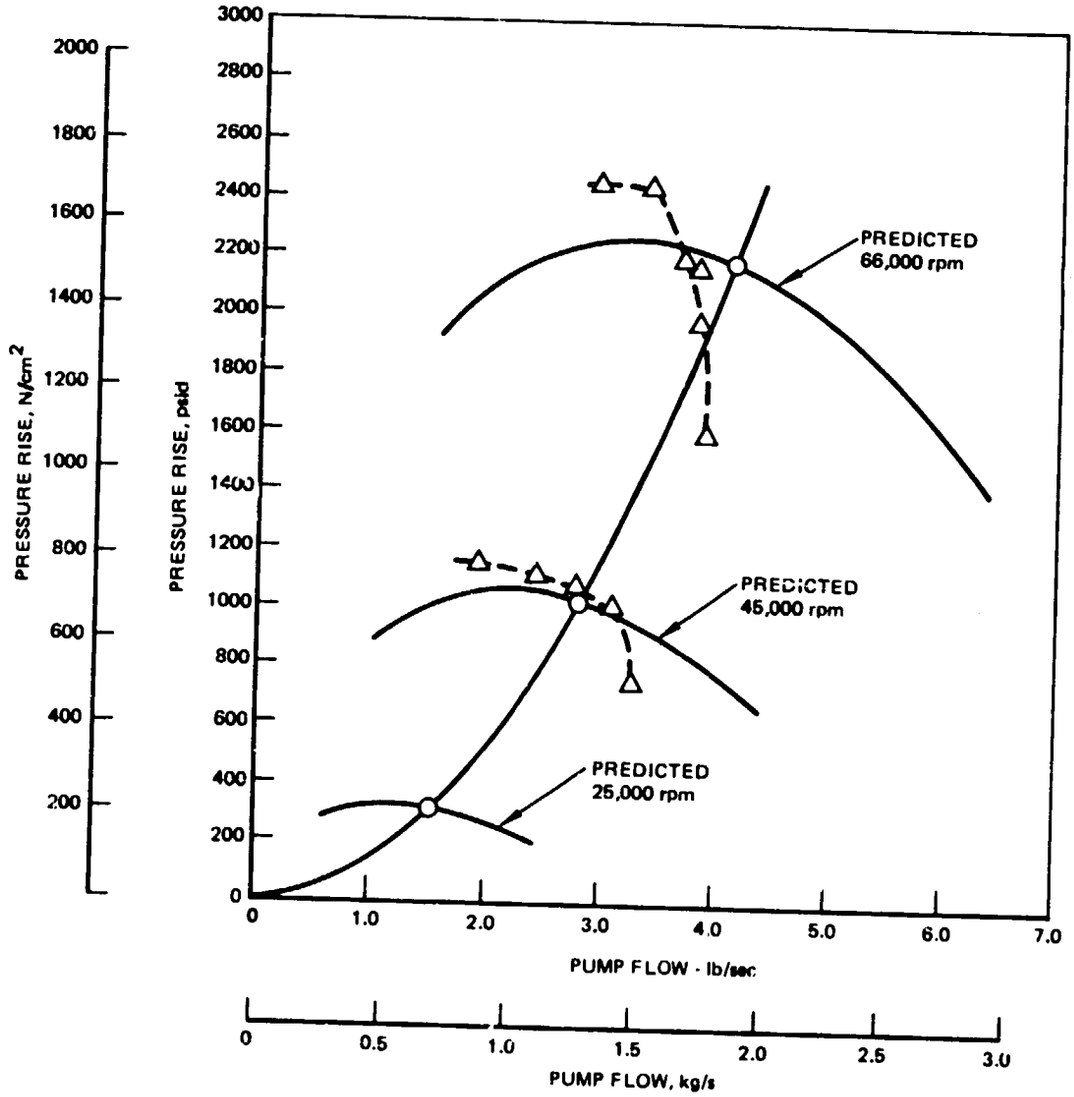

Figure 39. Mark 48-F Pump Performance Test 001 (1978) Data

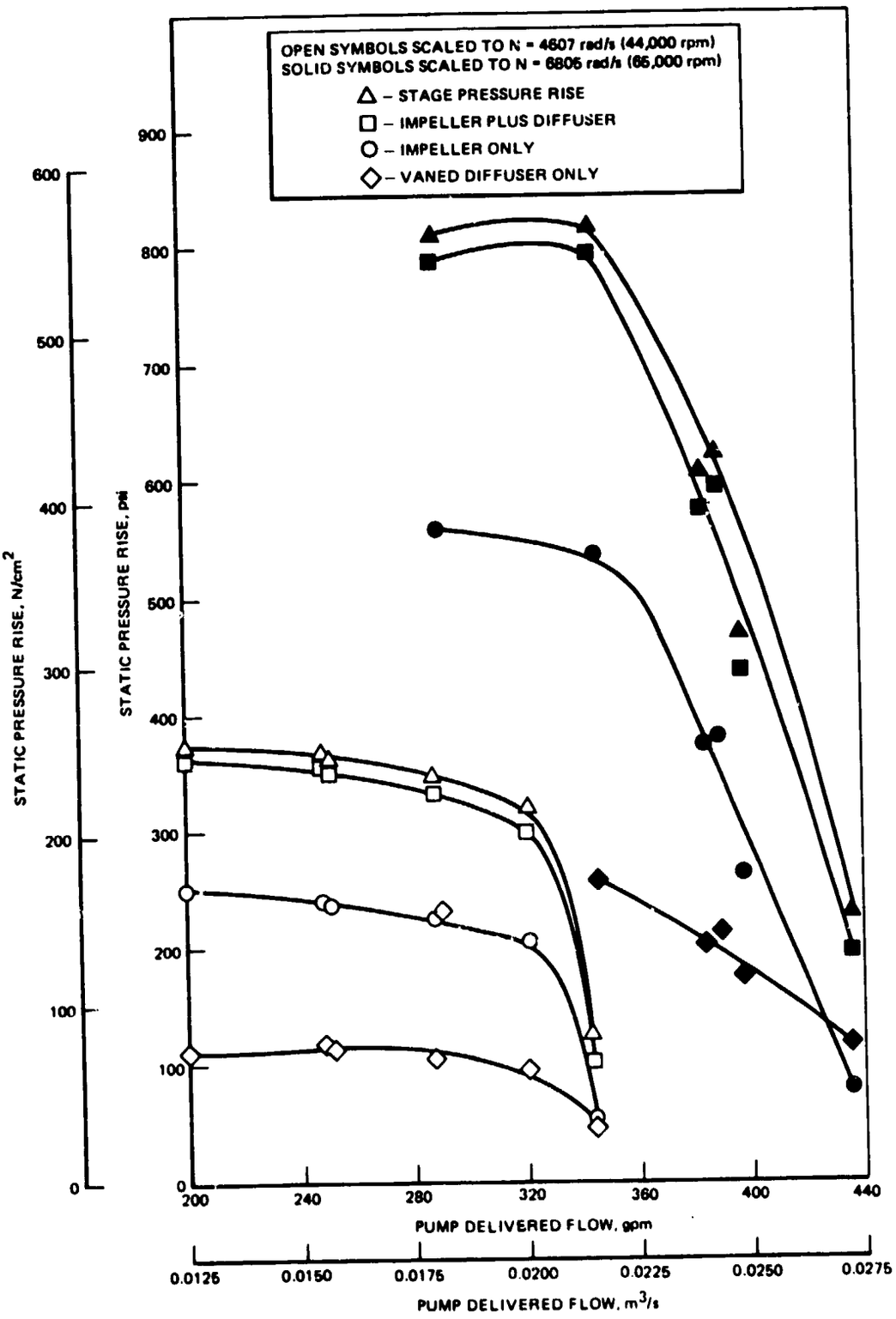

Figure 40. Mark 48-F Pump First-Stage Data (Test 001)

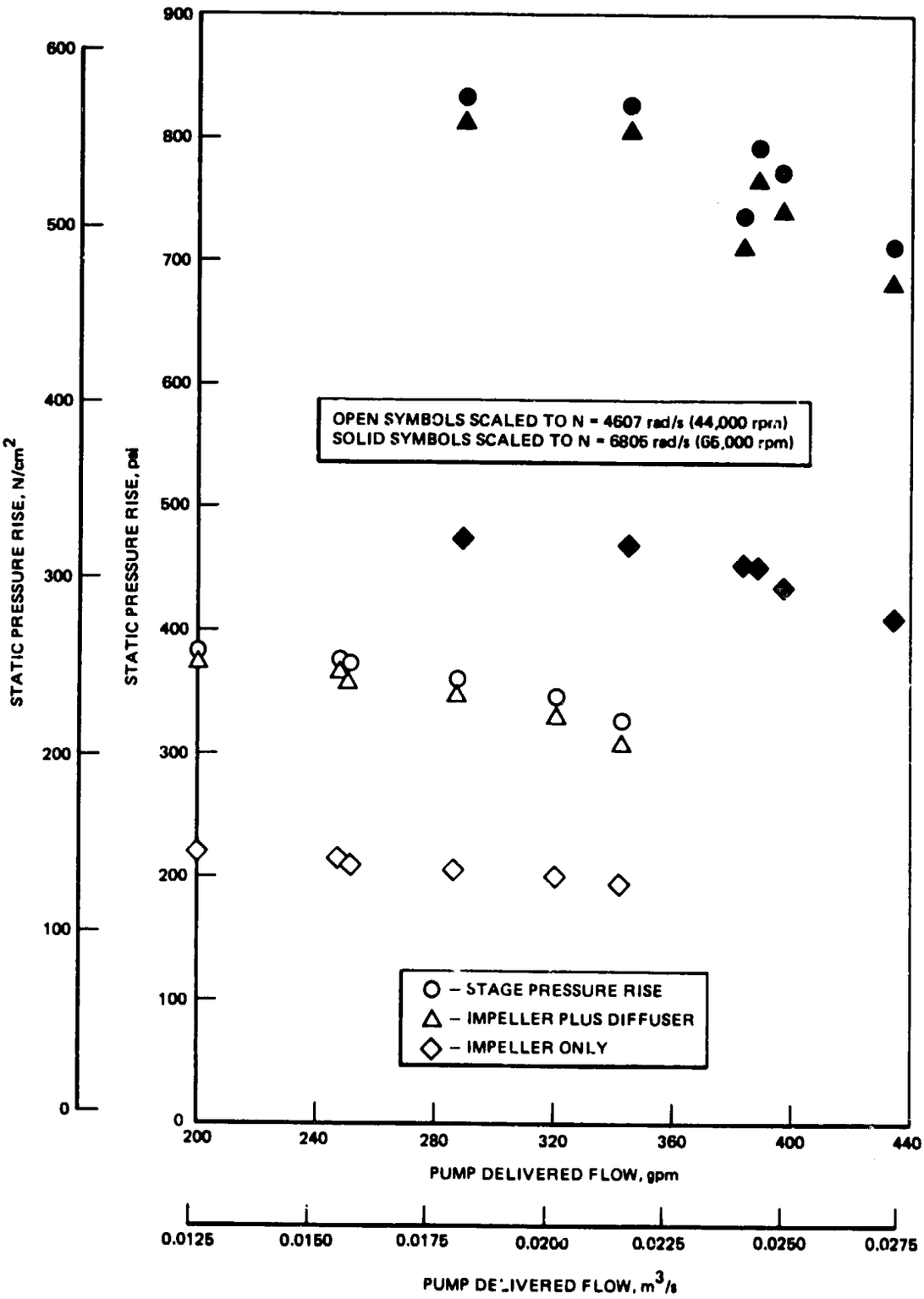

Figure 41. Mark 48-F Pump Second-Stage Data (Test 001)

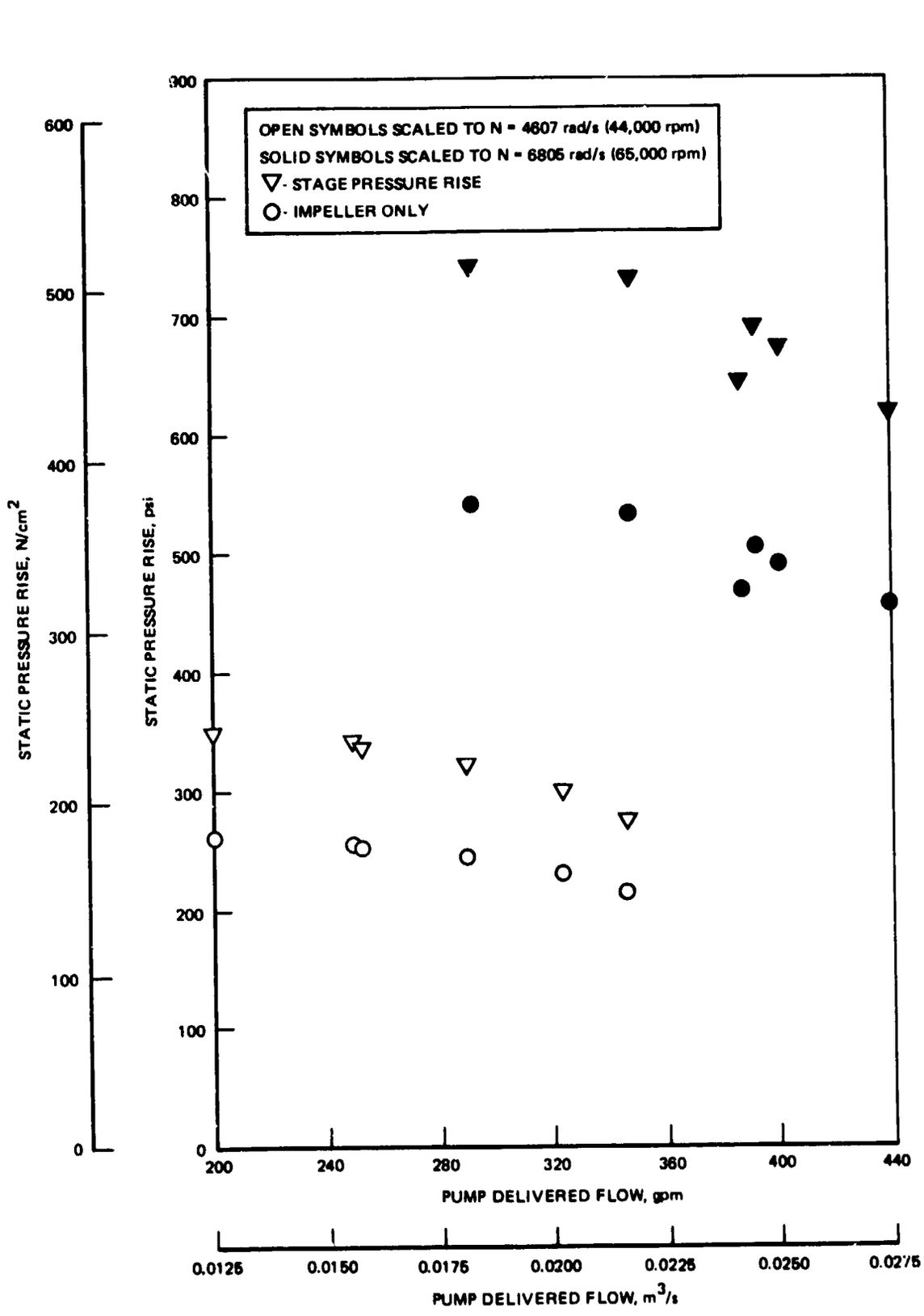

Figure 42. Mark 48-F Pump Third-Stage Data (Test 001)

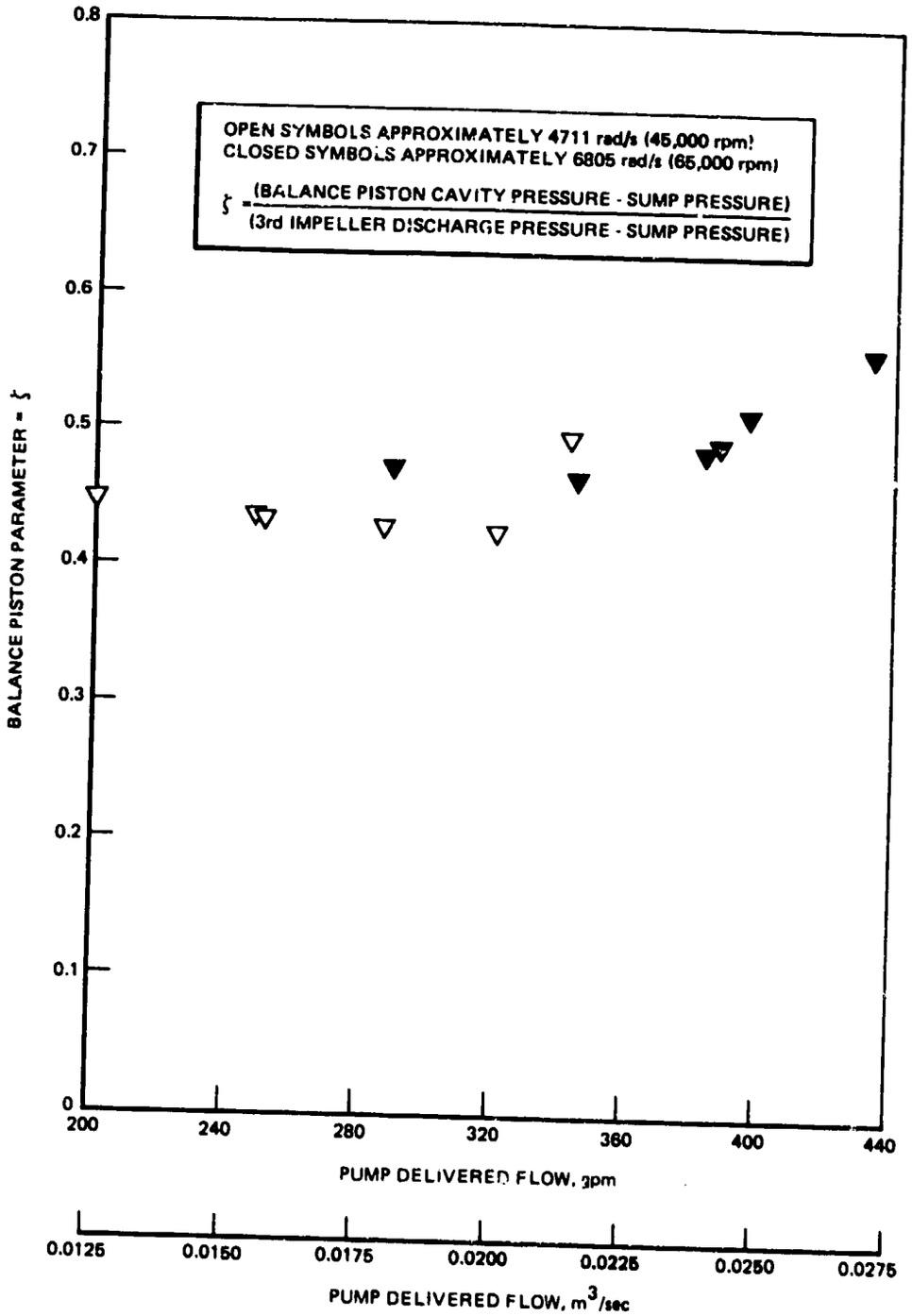

Figure 43. Mark 48-F Balance Piston Characteristics (Test 001)

Mechanically, the turbopump operated satisfactorily. Figures 44 and 45 show the accelerometer output and rotor deflection measured as a function of speed. The first and second critical speeds are clearly evident at 3456 rad/s (33,000 rpm) and 6388 rad/s (61,000 rpm), respectively. Both the accelerometer levels and shaft deflections magnitudes indicate a smooth operation with a good rotor balance.

Because of the first-stage performance problem at intermediate speeds, the suction performance tests at higher speed levels 8378 rad/s (80,000 rpm) were not carried out. The turbopump was removed from the facility for further analysis and corrective action.

Turbopump Disassembly. The turbopump was completely disassembled after the test. Primary purpose was to inspect the first-stage impeller front wear ring for damage or deterioration. No mechanical discrepancies were found.

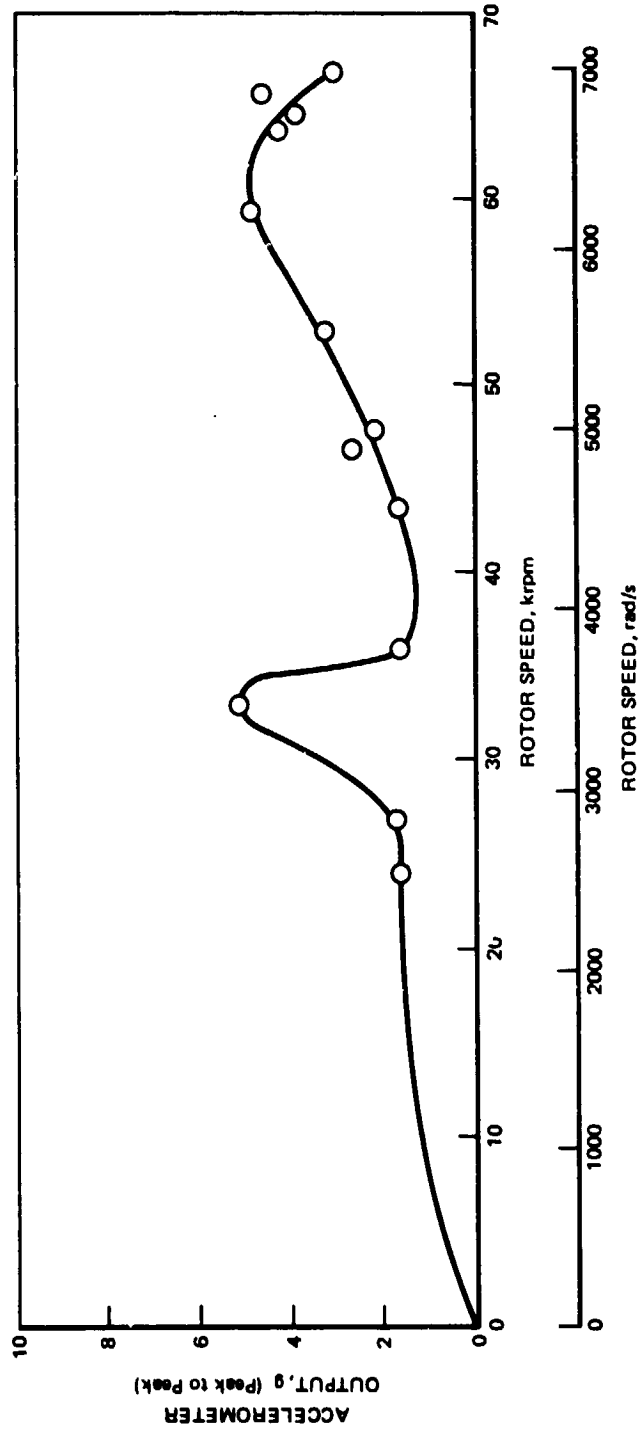

Figure 44. Vibration Characteristics (Test 001)

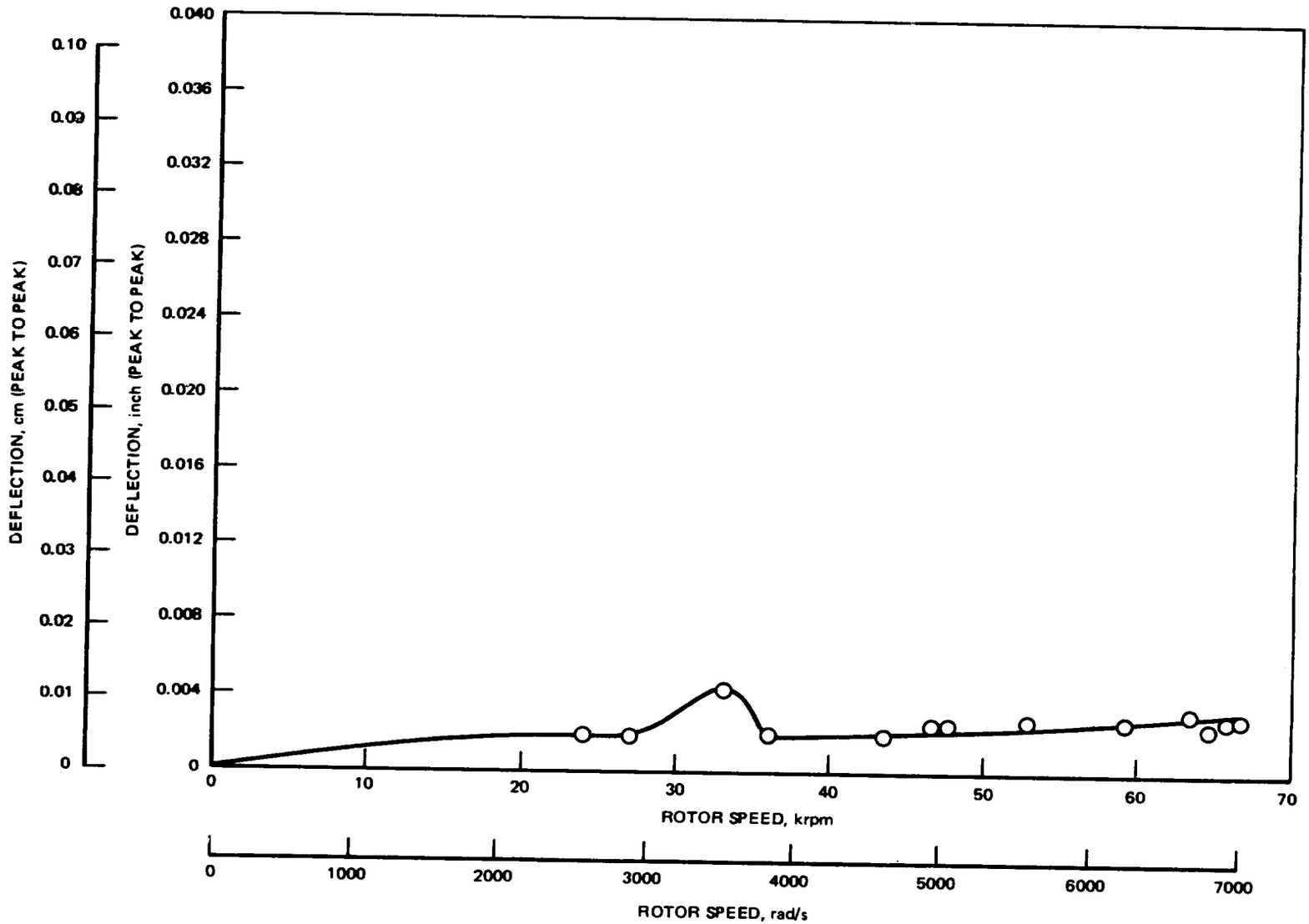

Figure 45. Rotor Deflection Characteristics (Test 001)

AXIAL PUMP INLET CONFIGURATION

Component Testing and Analysis

The results of the second test series revealed that the poor suction performance was not caused by the effect of the bearing coolant fluid entering the first-stage impeller. Thus it was concluded at this point that a more extensive effort, involving component testing and analysis followed by a significant hardware modification, would be required to realize the desired improvement in suction performance.

The effort was concentrated in two principal areas: (1) Establish whether the inlet housing guide vanes are introducing the fluid to the impeller at the proper incidence angle, and (2) perform a thermodynamic and hydrodynamic analysis of the flow loops affecting the first-stage impeller inlet to locate deficient areas and potential methods of correcting them.

Inlet Housing Air Flow Tests. To determine the role of the inlet housing in the cavitation, an air flow test was conducted in which the fluid angle exiting from the guide vanes was measured by means of a yaw probe. The test setup is illustrated in Fig. 46 and 47, and in the schematic in Fig. 48.

Flowrate through the housing was determined by surveying the total pressure profile with a Kiel probe in the upstream duct, and recording wall static pressure and air temperature. Velocity angle and amplitudes were measured with a yaw probe. Both prism-wedge and cobrahead probes were used, and the exit static wall pressure was recorded. The flow vector angle and amplitude were surveyed both in the radial and circumferential direction.

The results of the air tests revealed that the velocity magnitude and angle were uniform in the circumferential direction (Fig. 49). On the other hand, both vector components varied with radius as illustrated in Fig. 50 and 51. The most significant results of the air tests was that the fluid velocity angle (Fig. 50) as measured from the axial direction was substantially higher than what is required to provide the desired incidence angle for the impeller.

A continuity check indicated that the exit angle should be approximately 1.096 radians (63 degrees) axial as compared with the 1.28 radians plus (70 + degrees) measured with the yaw probe. This was confirmed with a paint test in which a drop of paint was applied to the flow guide fixture surface located at the exit of the inlet housing, and the angle at which the paint was smeared by the flowing air was observed. The paint smear test, illustrated in Fig. 52, indicated an exit angle of 1.096 radians (63 degrees) from axial.

The desired exit angle to obtain a good match with the impeller is 0.783 radian (45 degrees). Therefore, the liquid hydrogen is not being turned enough by the guide vanes in the inlet housing. This has two adverse effects. The local static pressure upstream of the impeller is reduced because of the higher velocity, and the incidence angle on the impeller vanes becomes negative. The drop in static pressure as a function of flowrate is shown in Fig. 53. The suction performance of the impeller is reduced significantly by these factors, particularly by the adverse incidence angle.

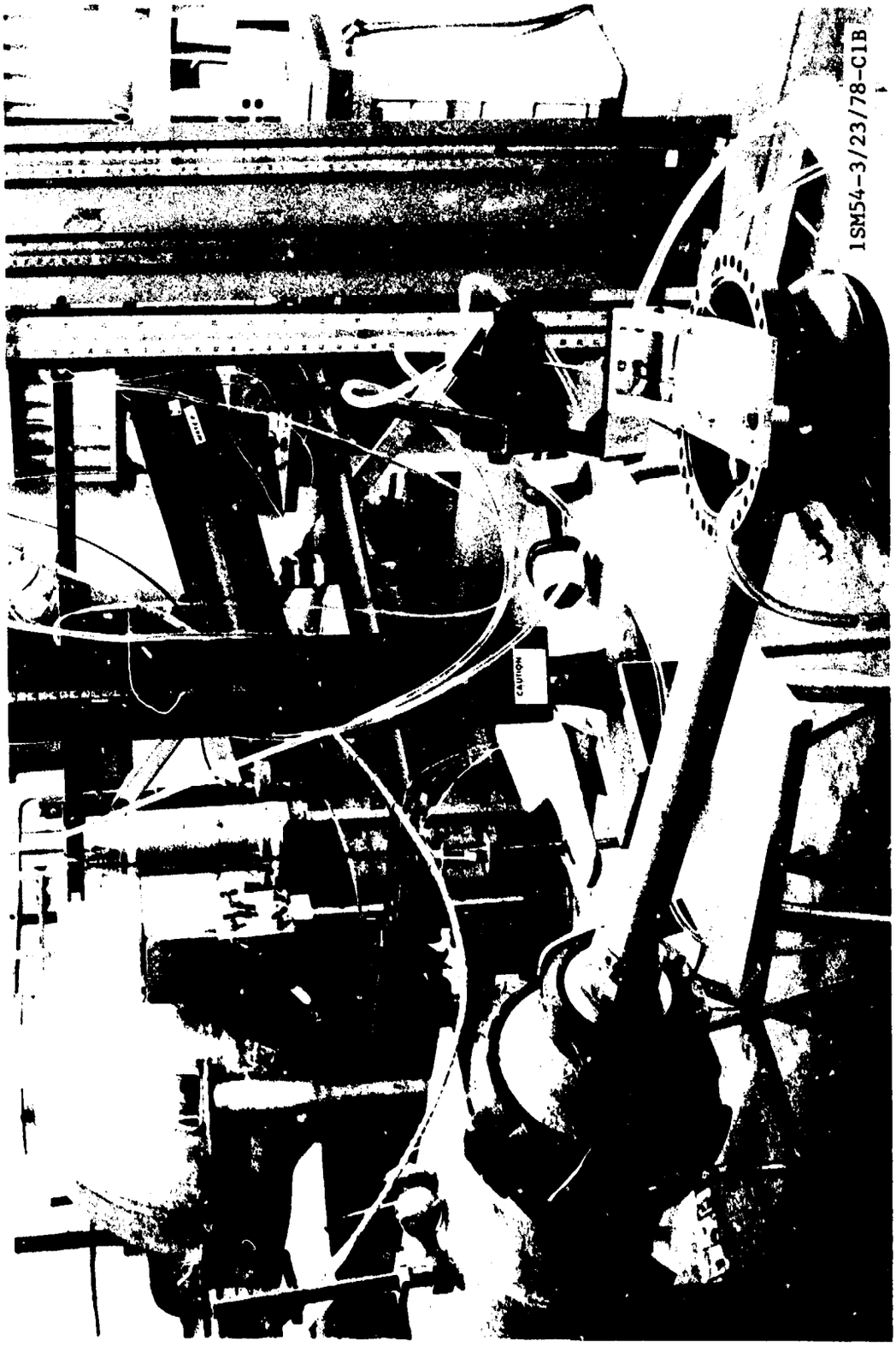

Figure 46. Mark 48-F Inlet Housing Air Flow Test Installation (View 1)

Figure 47. Mark 48-F Inlet Housing Air Flow Test Installation (View 2)

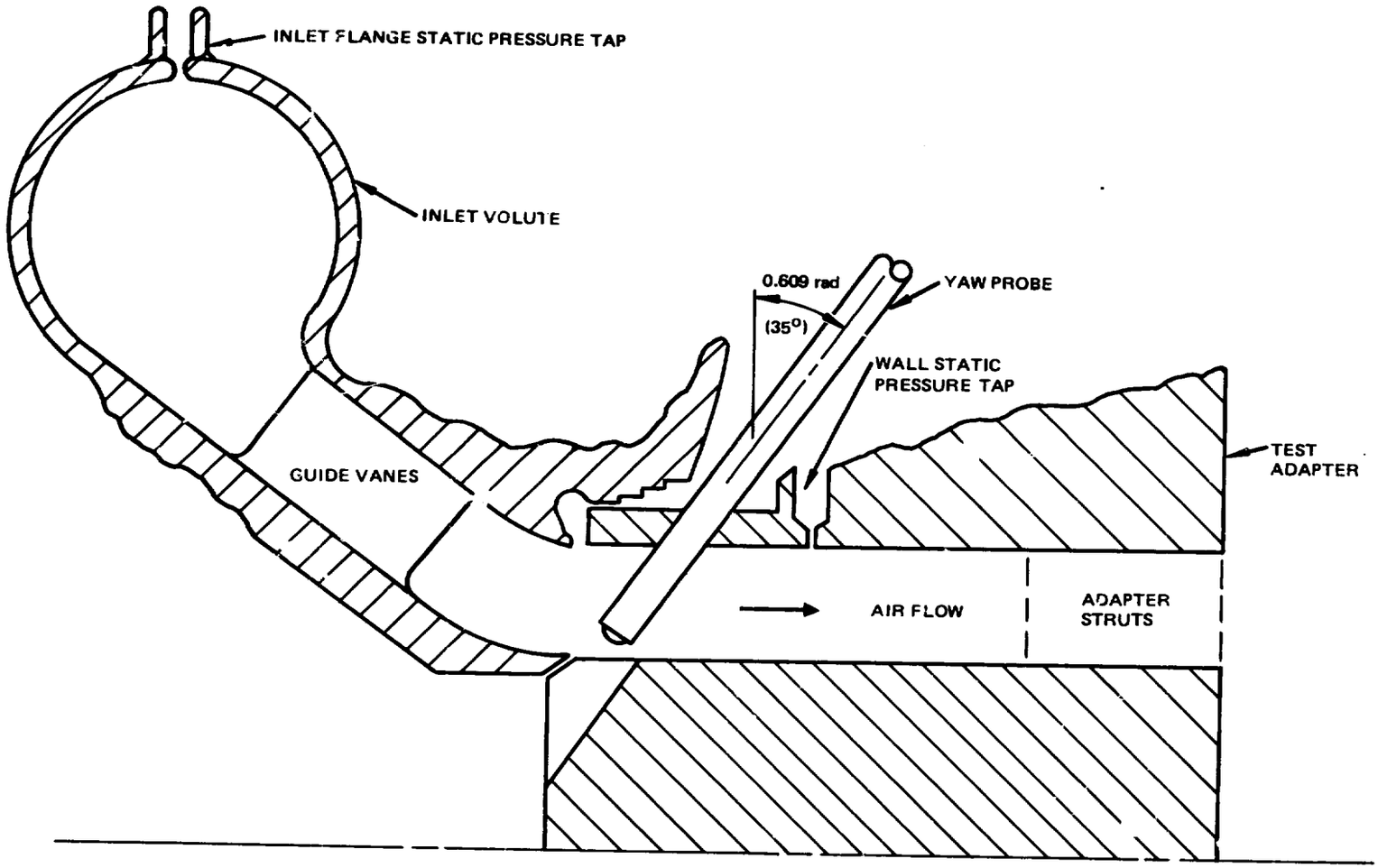

Figure 48. Inlet Air Test Schematic

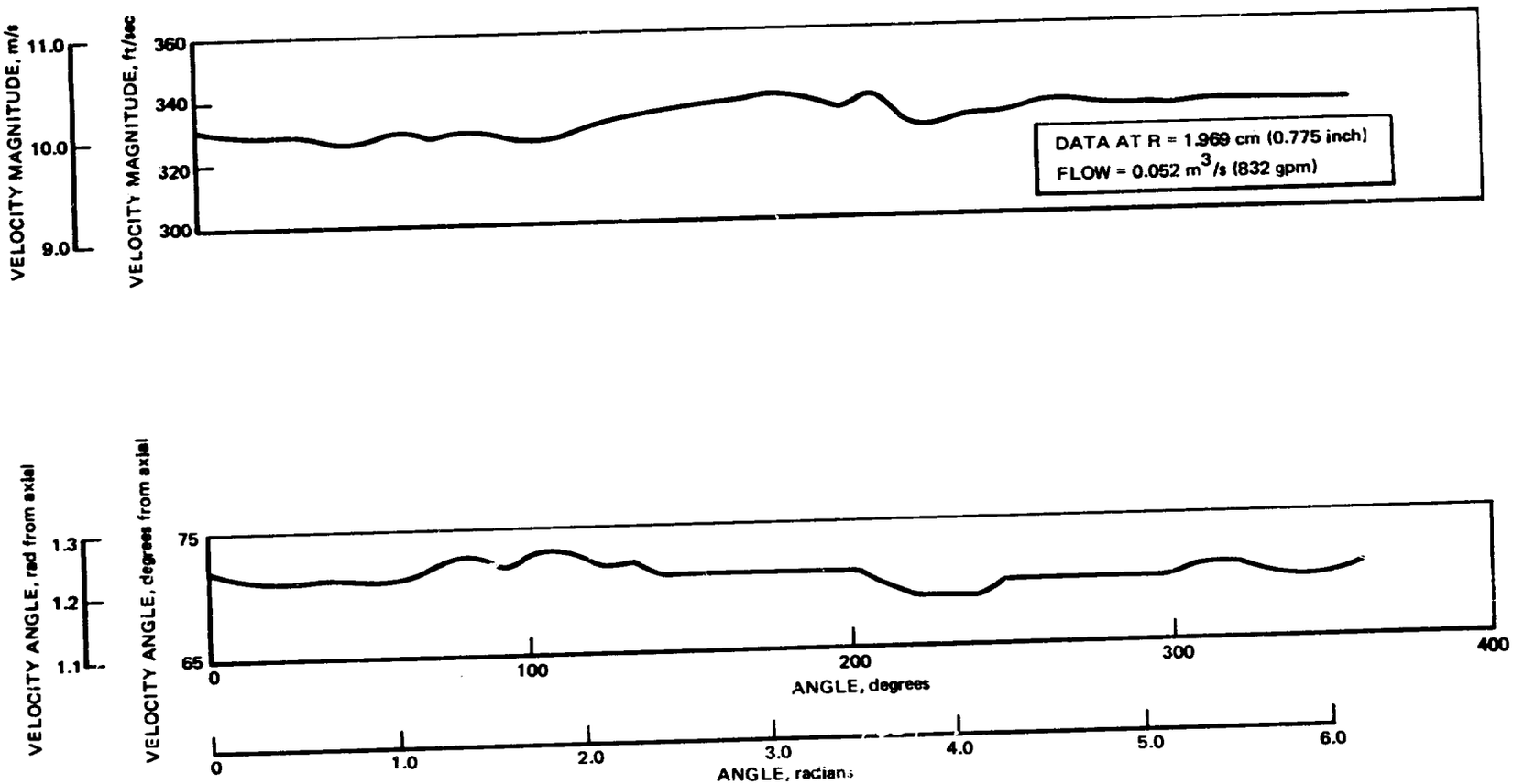

Figure 49. Inlet Air Test Velocity and Angle with Angular Position

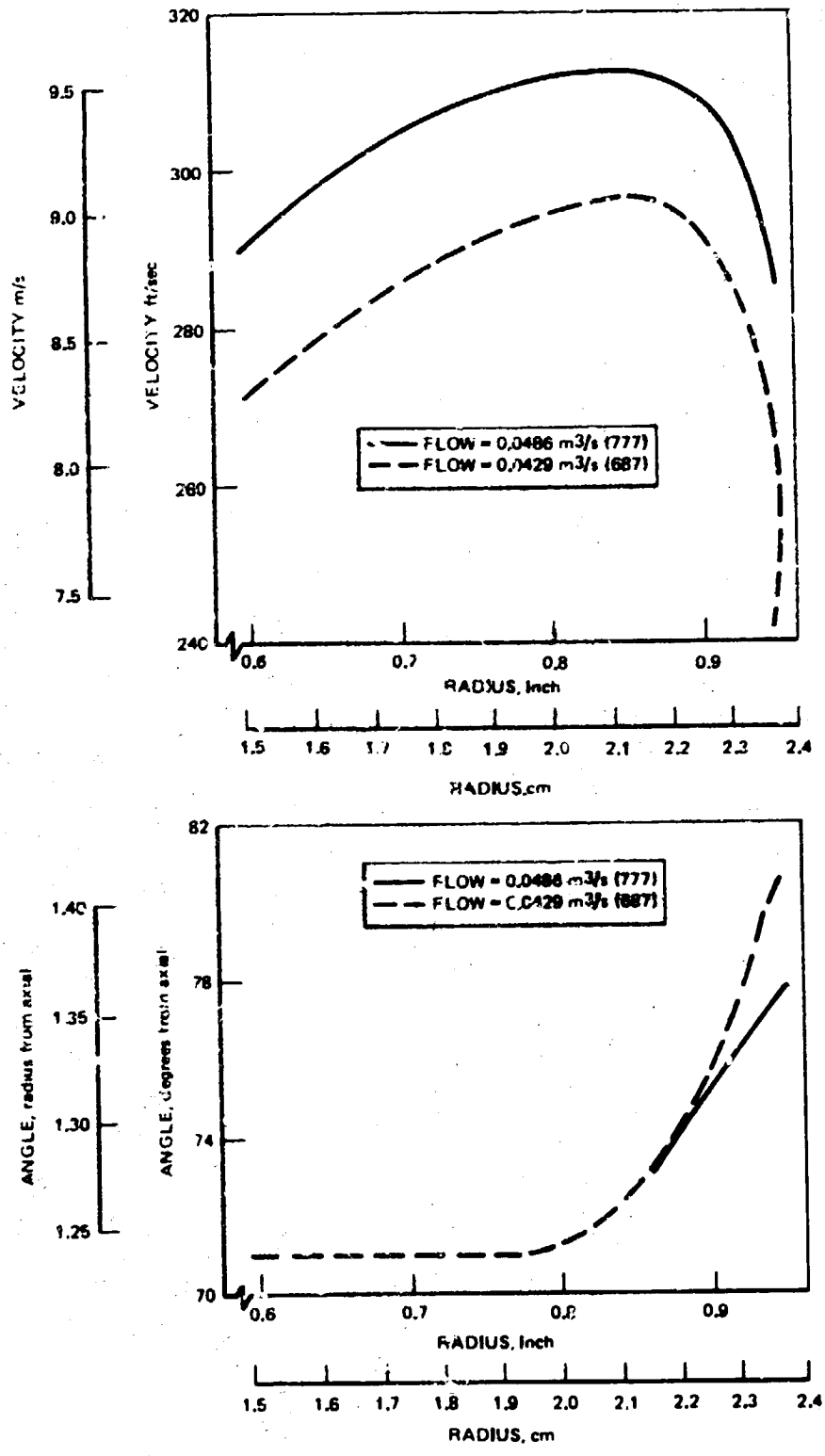

Figure 50. Inlet Air Test Velocity and Angle Distribution With Radius

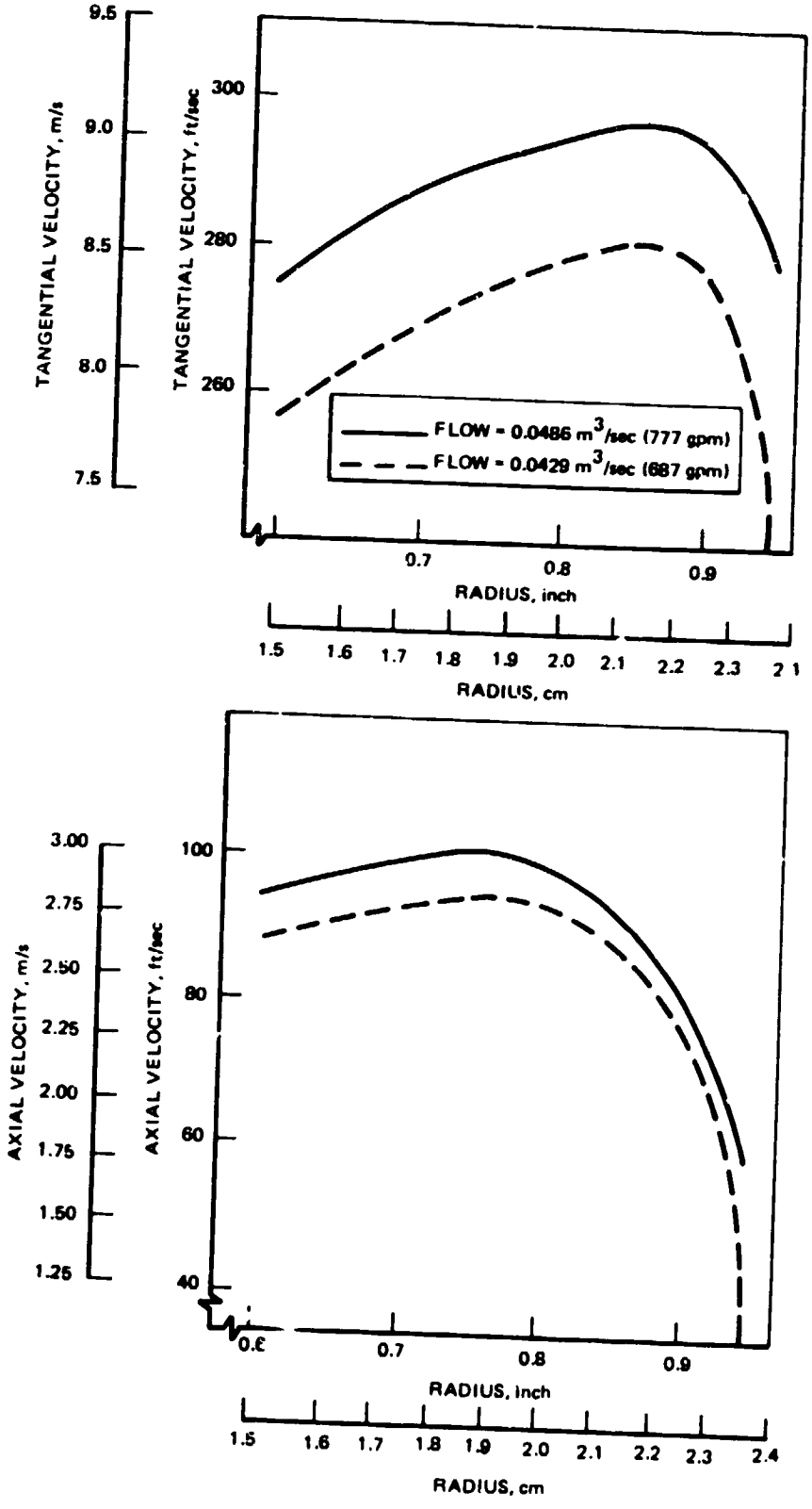

Figure 51. Inlet Air Test Component Velocity Distribution With Radius

Figure 52. Air Flow Paint Smear Pattern

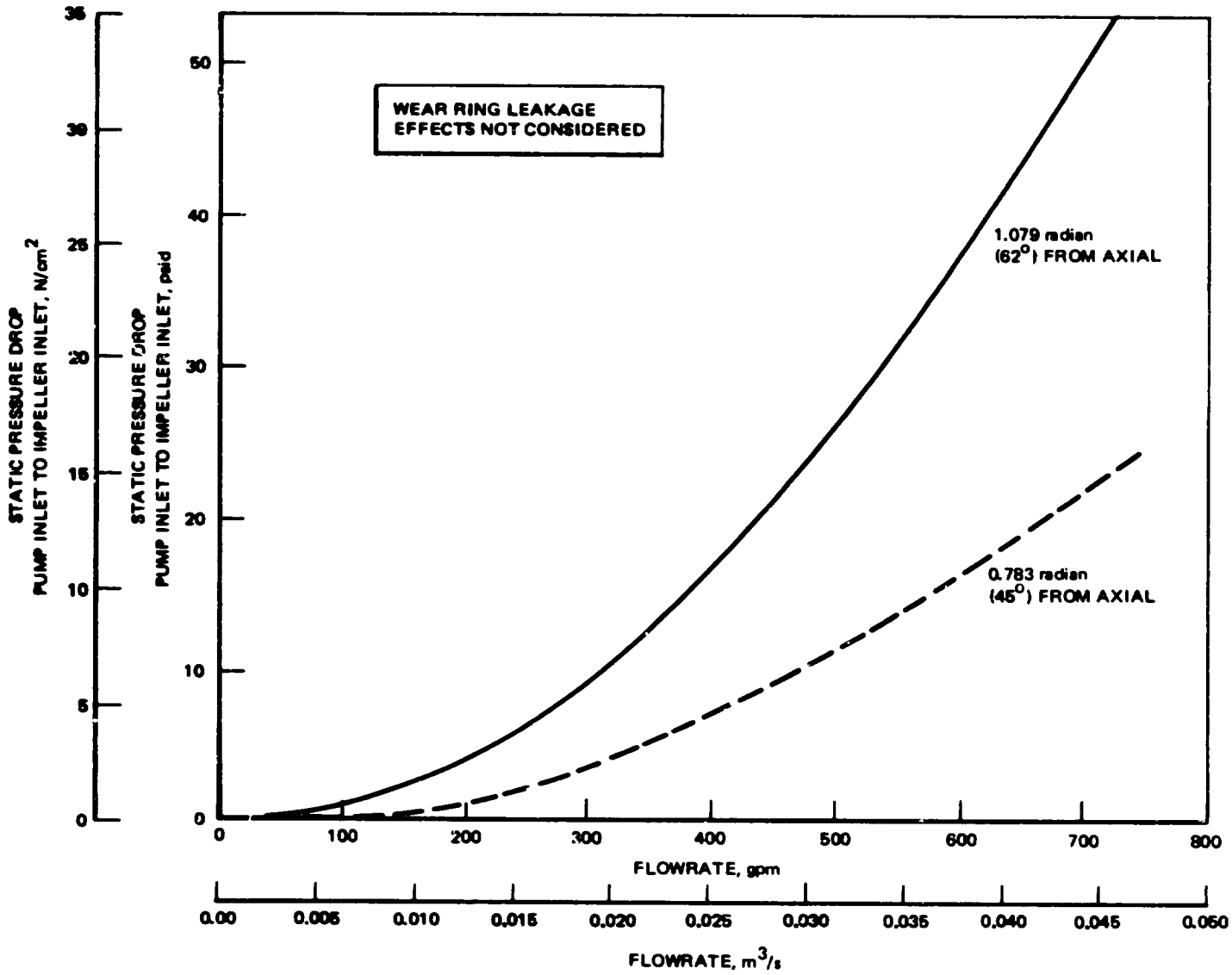

Figure 53. Inlet Effects on Static Pressures

It was concluded that the inlet housing unit must be modified to provide a better match in the fluid and impeller angles.

Hydrodynamic Analysis. An in-depth analysis to determine the fluid behavior in and around the first-stage impeller and to correlate it with actual measured data was also performed. This effort had two principal phases: (1) Generating a thermodynamic model of the impeller fluid and applying it to establish the fluid properties at significant stations, and (2) upgrading the existing hydrodynamic model which, in conjunction with the data obtained from the thermodynamic analysis, was used to determine fluid behavior along the impeller flow path.

In the thermodynamic analysis, the significant stations were identified as shown in Fig. 54 , starting with "0" in the inlet scroll and ending in "5" at the end of the front wear ring flow loop. The principal thrust of the investigation was to determine the condition of the fluid entering fresh from the inlet and how it is affected by the recirculating wear ring flow. The flowrate entering from the inlet was assumed "given", as were the inlet pressure, temperature, and rotor speed. At each of the indicated points on Fig. 54, flow, pressure, temperature, enthalpy, specific head, and fluid quality were calculated.

The state condition at Station 3 was calculated based on the work performed by the impeller. From Station 3 to 3', a rise in static enthalpy is realized because the radial velocity component becomes zero. The static enthalpy rises further in proceeding to Stations 5 and 5' because of disc friction heating and a reduction in the tangential velocity head. From Station 4' to 4 and 5' to 5, constant enthalpy throttling is assumed.

A typical printout obtained from the thermodynamic model is shown in Table 10, where significant fluid parameters are defined at each station. Of paramount interest are two values: The percent of the front wear ring fluid, which is gas before it mixes with the through flow (39.61% in Table 10), and the percent volume of the total flow of fluid entering the impeller from the front wear ring is 10.05%.

Several cases were examined at the design speed of 9947 rad/s (95,000 rpm), and 6743 rad/s (64,400 rpm) where empirical results were available from the previous test series. A summary of these is presented in Table 11. The significant conclusion which is drawn from Table 11 is that a large part of the front wear ring flow enters the impeller as gas. It is surmised that this gas does not mix with the through flow immediately, and as a result it acts as blockage in the impeller inlet. Therefore, the hydrodynamic analysis of the impeller must include this blockage as a factor. The possibility of diverting the wear ring flow and introducing it further upstream must be considered inasmuch as this would permit the gas to be mixed and reliquified before it enters the impeller.

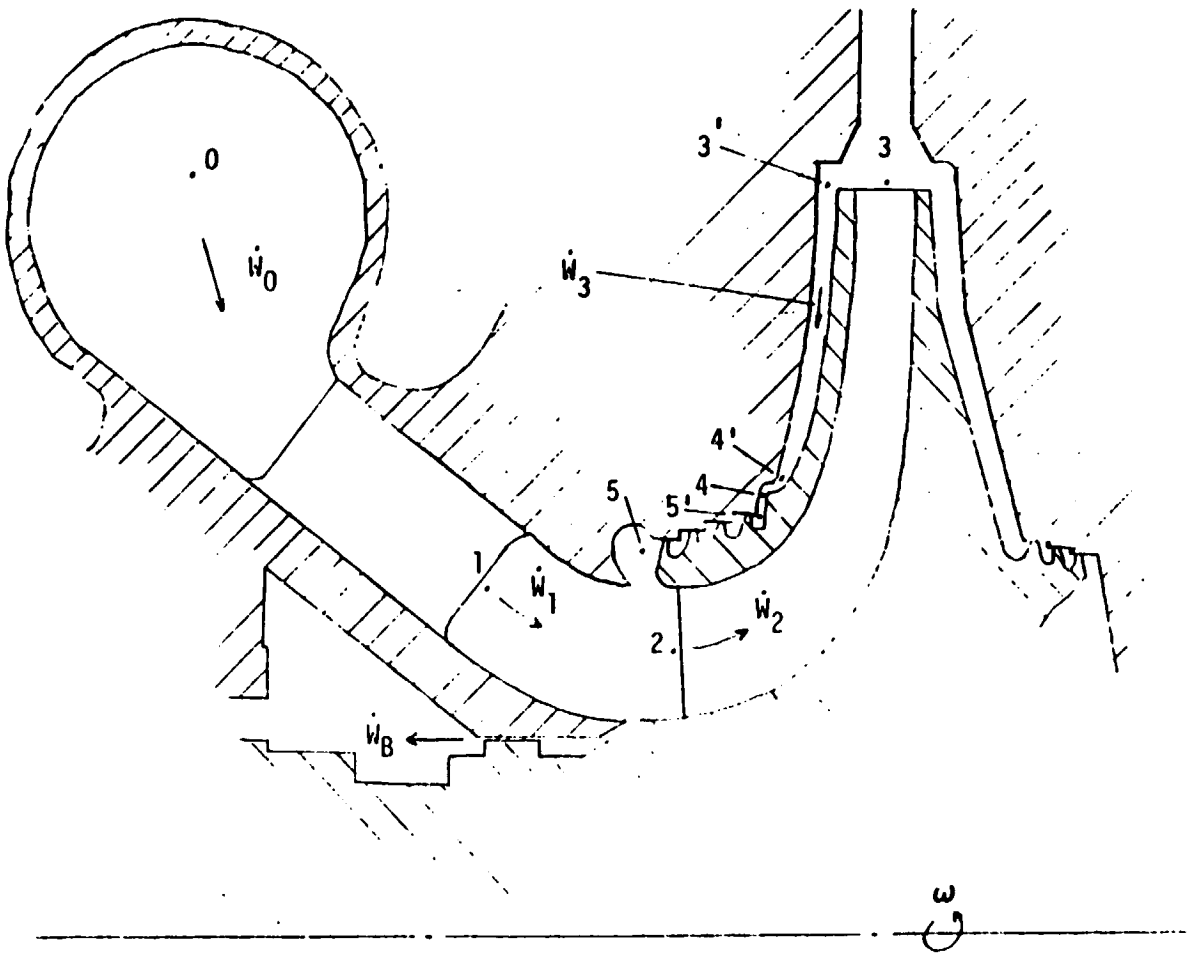

GIVEN: FLOW, PRESS, TEMP @ STATION "0" AND ω

CALCULATE: FLOW, PRESS, TEMP, ENTHALPY, SPECIFIC WEIGHT, QUALITY AT ALL INDICATED POINTS

Figure 54. Thermodynamic Analysis Model Schematic

TABLE 10. THERMODYNAMIC TYPICAL MODEL RESULTS
MARK 48 HPFP
FIRST-STAGE IMPELLER THERMODYNAMIC ANALYSIS
6744.3 rad/s (64,412.0 rpm)

Station	Weight Flow, kg/s (lb/sec)	Pressure, N/cm^3 (psia)	Temperature, K (R)	Enthalpy, kJ/kg (Btu/lb)	Specific Weight, g/cm^3 (lb/ft^3)	Vapor Pressure, N/cm^3 (psia)	Quality at Discharge	GAS, % by volume
0	1.698 (3.773)	73.31 (106.33)	22.26 (40.08)	228.80 (-98.62)	0.069 (4.318)	17.59 (25.52)	0.000	0.00
1	1.698 (3.773)	13.43 (106.51)	22.27 (40.09)	228.70 (-98.58)	0.069 (4.318)	17.63 (25.57)	0.000	0.00
2	1.7496 (3.888)	73.43 (106.51)	22.95 (41.31)	221.12 (-95.31)	0.069 (4.254)	21.26 (30.84)	0.000	0.00
3	0.0967 (0.215)	438.14 (636.35)	25.27 (45.49)	165.21 (-71.21)	0.071 (4.417)	35.46 (51.44)	0.000	0.00
3'	0.0967 (0.215)	438.74 (636.35)	26.72 (48.10)	148.76 (-64.12)	0.069 (4.315)	46.58 (67.56)	0.000	0.00
4'	0.0967 (0.215)	375.84 (545.13)	31.09 (55.97)	98.23 (042.34)	0.062 (3.903)	97.90 (142.08)	0.000	0.00
4	0.0967 (0.215)	375.61 (544.79)	31.09 (55.97)	98.23 (-42.34)	0.062 (3.902)	97.97 (142.10)	0.000	0.00
5'	0.0967 (0.215)	365.98 (530.83)	31.31 (56.36)	95.56 (-41.19)	0.062 (3.869)	101.11 (146.65)	0.000	0.00
5	0.0967 (0.215)	13.43 (106.51)	29.27 (52.70)	95.56 (-41.19)	0.053 (3.313)	73.43 (106.51)	0.100	39.61

PCT. VOL. of Flow at 5 of Total Flow at 2 = 10.05

Station 0 - PUMP INLET
1 - DISCHARGE OF INLET STATOR
2 - IMPELLER EYE
3 - IMPELLER DISCHARGE
3P - TOP OF REAR SHROUD

Station 4P - SHELF CLEARANCE INLET
4 - SHELF CLEARANCE EXIT
5P - FRONT WEARING RING INLET
5 - FRONT WEARING RING EXIT

TABLE 11. MK 48-F WEAR RING FLOW QUALITY

Variable	Speed, rad/s (rpm)	Wear Ring Flow, kg/s (lb/sec)	Quality at Discharge	Gas, % by vol.	$\frac{Q_{Wear\ Ring}}{Q_{Impeller}}$
Baseline	9947 (95,000)	0.137 (0.303)	0.582	89.1	0.22
Front Wear Ring Clearance Doubled	9947 (95,000)	0.270 (0.594)	0.433	81.7	0.34
Inlet Pressure Increased by 30.4 N/cm^2 (44 psi)	9947 (95,000)	0.139 (0.306)	0.579	81.3	0.15
Baseline	6743 (64,400)	0.0976 (0.215)	0.100	39.6	0.10
Disk Friction Doubled	6743 (64,400)	0.0826 (0.182)	0.306	72.3	0.14
Impeller Discharge Static Pressure Reduced 20%	6743 (64,400)	0.080 (0.177)	0.121	44.7	0.09

The hydrodynamic model used to analyze the impeller is a three-dimensional program obtained from Dynatech Corporation and modified to enhance Rocketdyne useage. It permits evaluation of the impeller suction performance by calculating the flowfield at numerous stations through the impeller and, in the process, establishing local pressure levels.

The location of the stations selected for analysis is illustrated in Fig. 55. In Fig. 56, a typical pressure characteristic as a function of computing stations is presented. Of particular interest here is the region near the leading edge, i.e., stations 5, 6, 7, and 8, where the local static pressure is below the total inlet pressure at the impeller inlet. If the decrease in pressure is high enough, cavitation and attendant impeller head loss will ensue.

A principal objective of the hydrodynamic analysis was to correlate the analytical results with empirical data obtained on turbopump tests. To this end, data obtained with the original integrally machined impeller as well as the split (two-piece) impeller was re-examined. Figure 57 illustrates the pressure rise measured with each impeller as a function of normalized flowrate. At 4725 rad/s (45,000 rpm), no indication of cavitation was evident with the integral impeller; whereas, with the two-piece impeller, a 20% head loss was evident at 110% of nominal flow. At 6825 rad/s (65,000 rpm), extensive cavitation was evident at 110% of nominal flow with the integral, and 90% of nominal flow with the two-piece impeller. The two impellers (Fig. 58) differed in that the vanes on the integral type were thinner and the contour somewhat different, which resulted in approximately 17% larger inlet flow area. The higher suction performance of the integral impeller is attributable to this larger area.

To effect a data correlation, the following approach was used. The minimum value of the difference between the local static pressure and total impeller inlet pressure was computed for a range of Q/N values, and these data were plotted for the suction and pressure side of the blade, as illustrated in Fig. 59 and 50, respectively. Curves were generated for 4725 rad/s (45,000 rpm), 6825 rad/s (65,000 rpm), and 9947 rad/s (95,000 rpm). In the next step, the Q/N levels at which cavitation was experienced were noted for each speed level. These are identified by the solid triangles in Fig. 59 and 60. It should be noted that the test data were obtained at an inlet pressure of approximately 69 N/cm^2 (100 psia).

The intention was to use this approach to evaluate the relative merits of design modifications under consideration. To show an improvement, any design change must produce a curve which is to the right of the cavitation region indicated by the plotted data shown in Fig. 59 and 60.

Following completion of the thermodynamic and hydrodynamic analysis of the two impeller types tested, effort was initiated to evaluate potential fixes to improve suction performance. A total of 16 configurations were examined.

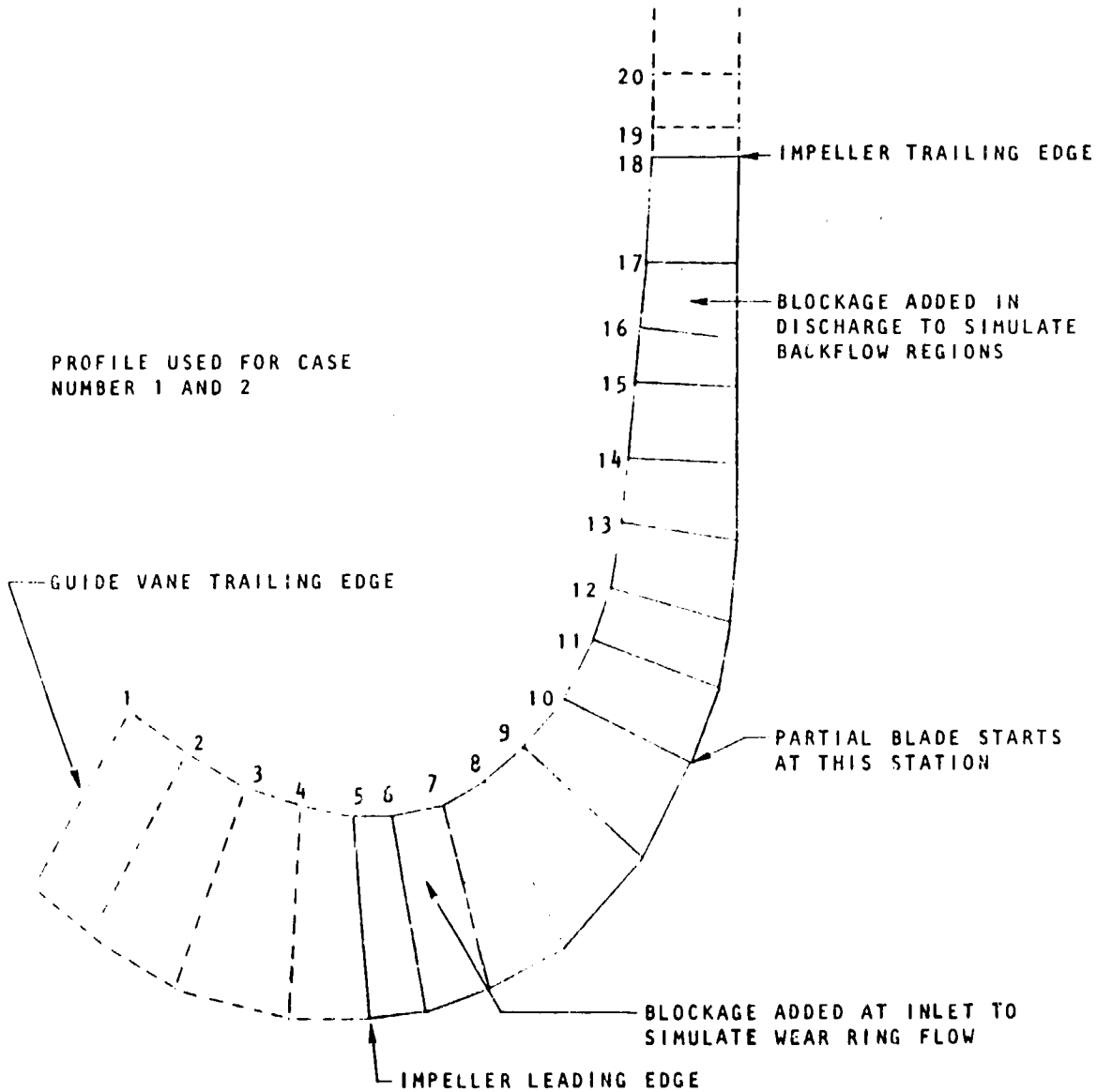

Figure 55. MK 48-F First Stage Impeller Model

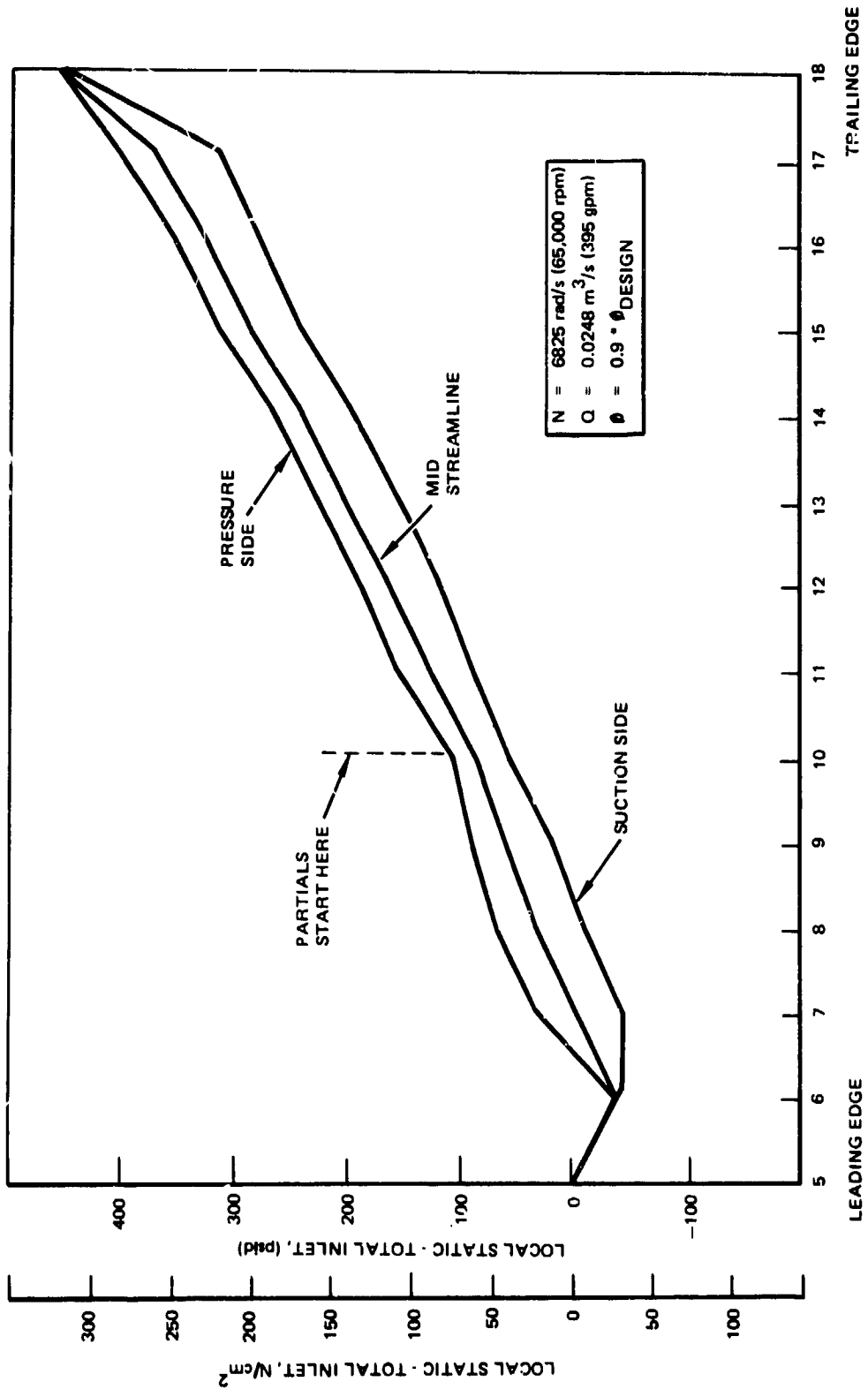

Figure 56. Impeller Tip Streamline Pressure Distribution Model Results

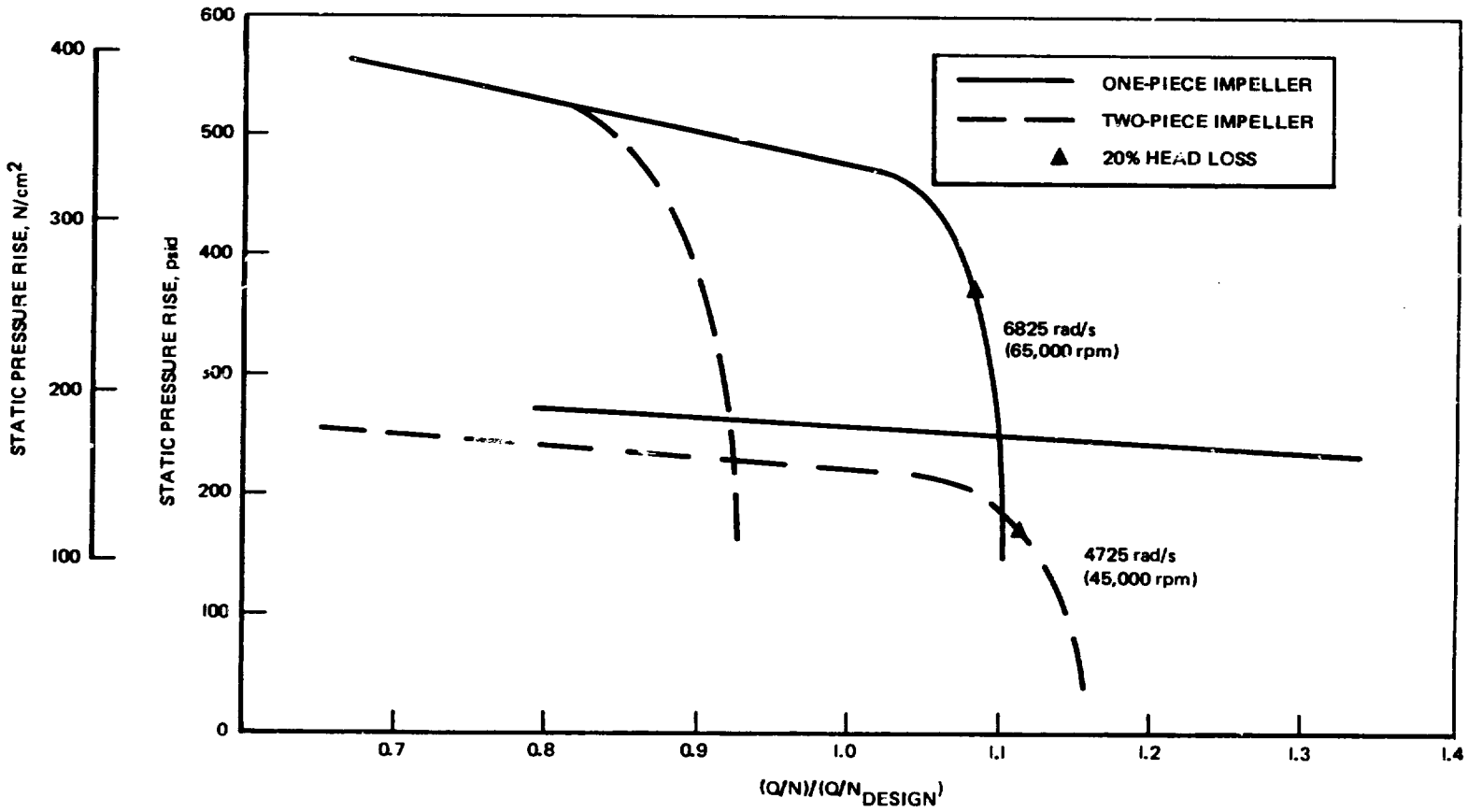

Figure 57. Fuel First-Stage Rotor Static Pressure as a Function of Flowrate

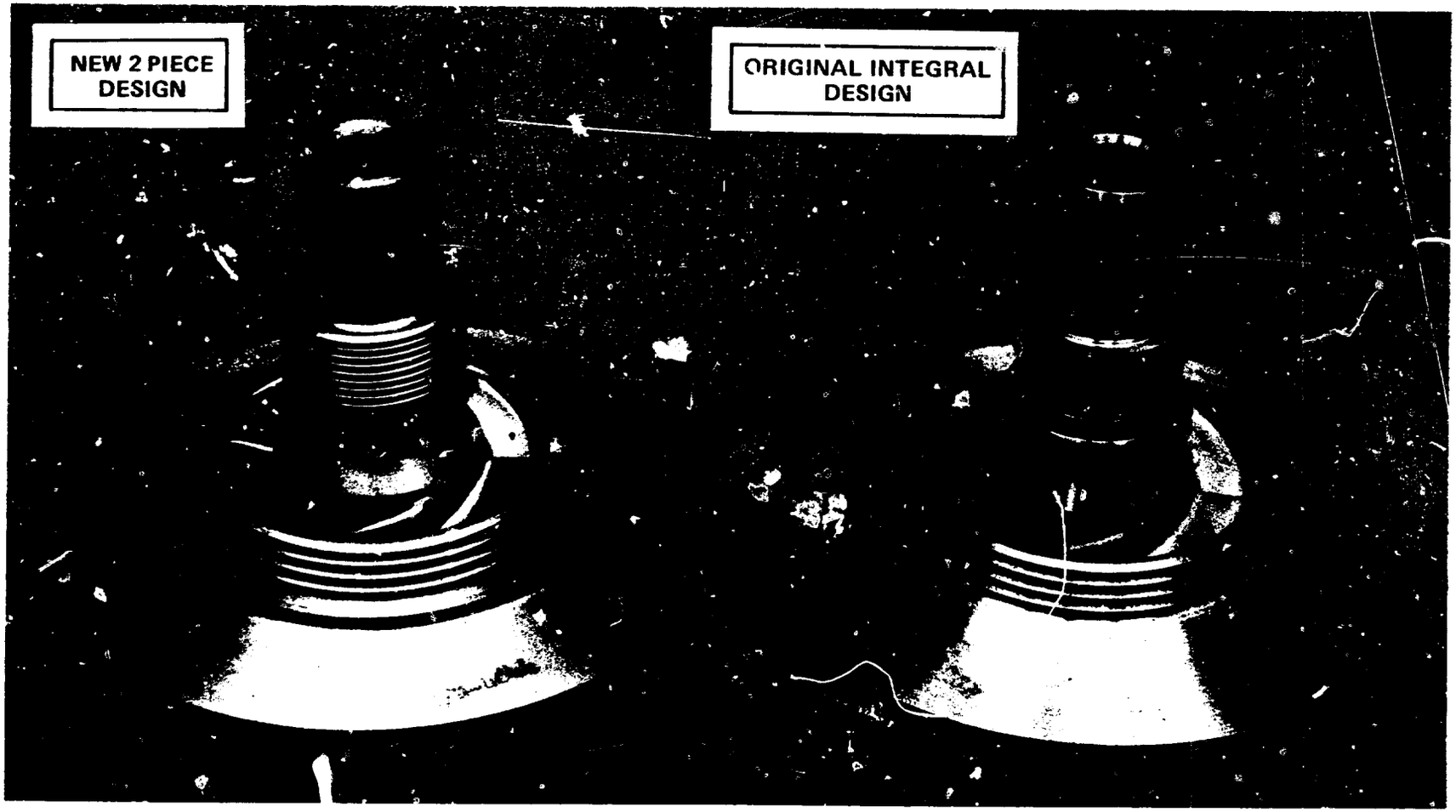

Figure 58. Mark 48-F Impeller

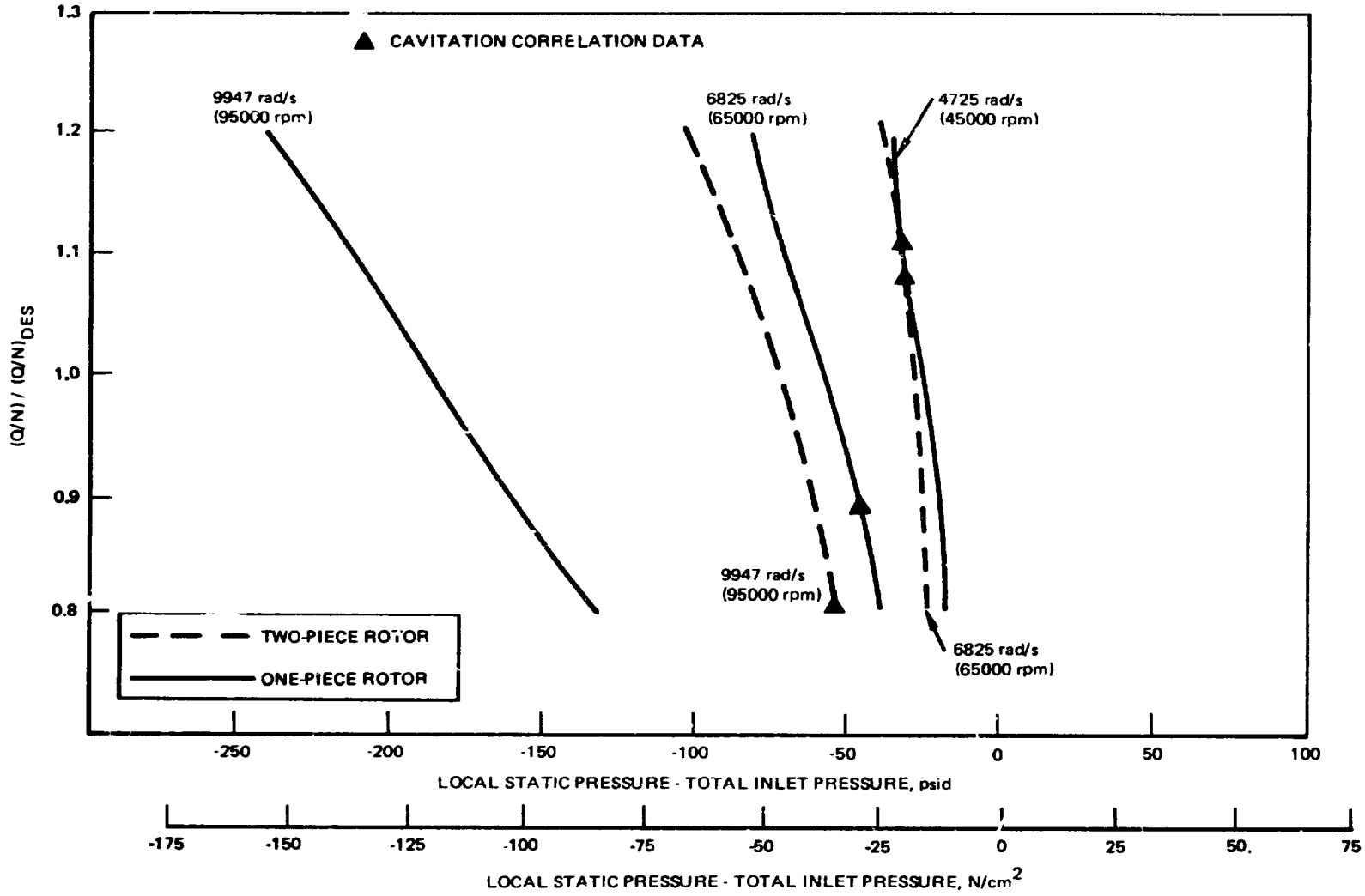

Figure 59. Minimum Calculated Impeller Surface Pressure (Suction Side)

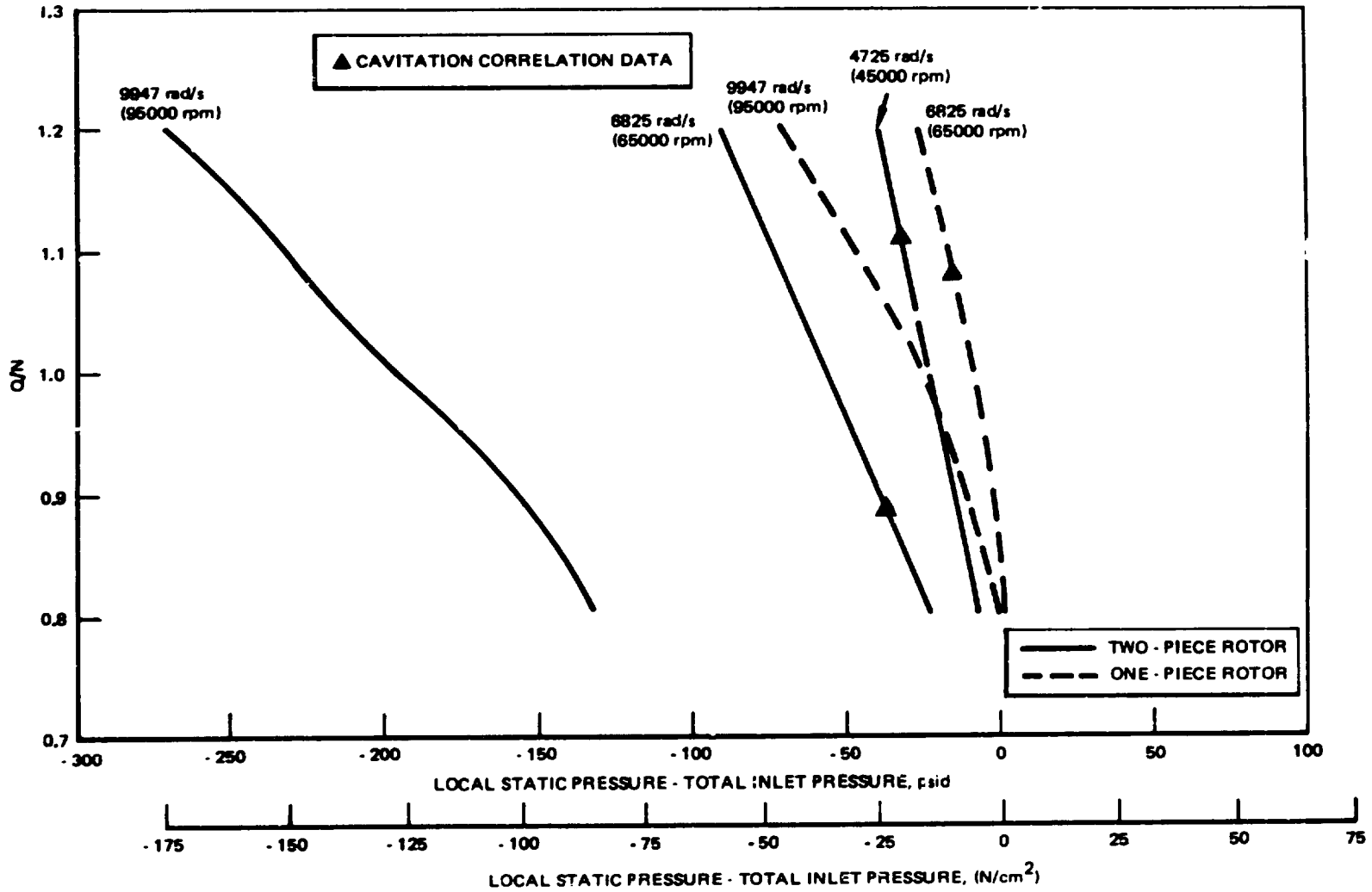

Figure 60. Minimum Calculated Impeller Surface Pressure (Pressure Side)

The characteristics of the key configurations are noted in Table 12, and illustrations of representative configurations are provided in Fig. 61 through 66.

TABLE 12. MK 48-F DESIGN MODIFICATIONS STUDIED

Modification No.	Description
1	As-Built Two-Piece Impeller
2	Same as 1 With 80% Wear Ring Flow Diverted Upstream
3	Inlet Area Increased • Eye Diameter Increased From 4.826 to 4.978 cm (1.90 to 1.96 inch) • Hub Diameter Decreased From 3.099 to 2.845 cm (1.22 to 1.12 inch) • Six Blades Cutback 30 Degrees Wrap
7	Combines 1, 2, 3
8	Open-Face Impeller With Cutback Blades
10	New Impeller Design, Inlet Area Increased 40% From 1
12	Same As 10 With Inducer Added Upstream
13	Same As 12 With 80% Wear Ring Flow Diverted Upstream
14	Same As 3 With Added Inducer
15	Same As 14 With 80% Wear Ring Flow Diverted Upstream
16	Axial Entry With Inducer With Same Impeller Mods As 7

The Q/N-local static pressure curves are presented in Fig. 67 and 68 for the suction and pressure sides for the candidate configurations at 9947 rad/s (95,000 rpm). It is evident from these figures that each of the considered design changes would effect a significant increase in the local static pressure compared with that produced by the basic split impeller, and each should register a corresponding improvement in the suction performance.

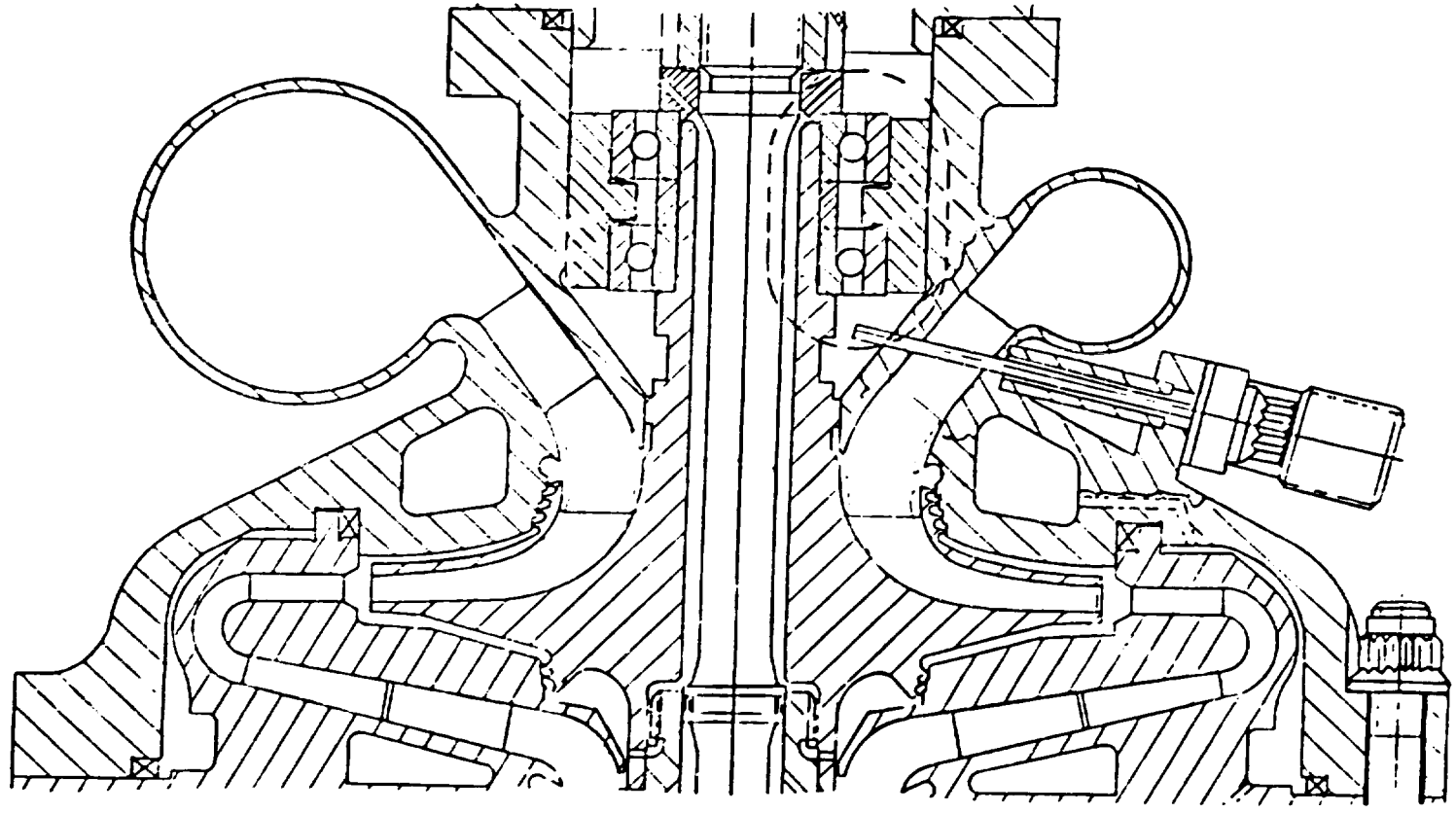

Figure 61. Design Modification No. 7 (Features: Impeller Inlet Area Increased, Blades Cut Back, Wear Ring Flow Diverted Upstream)

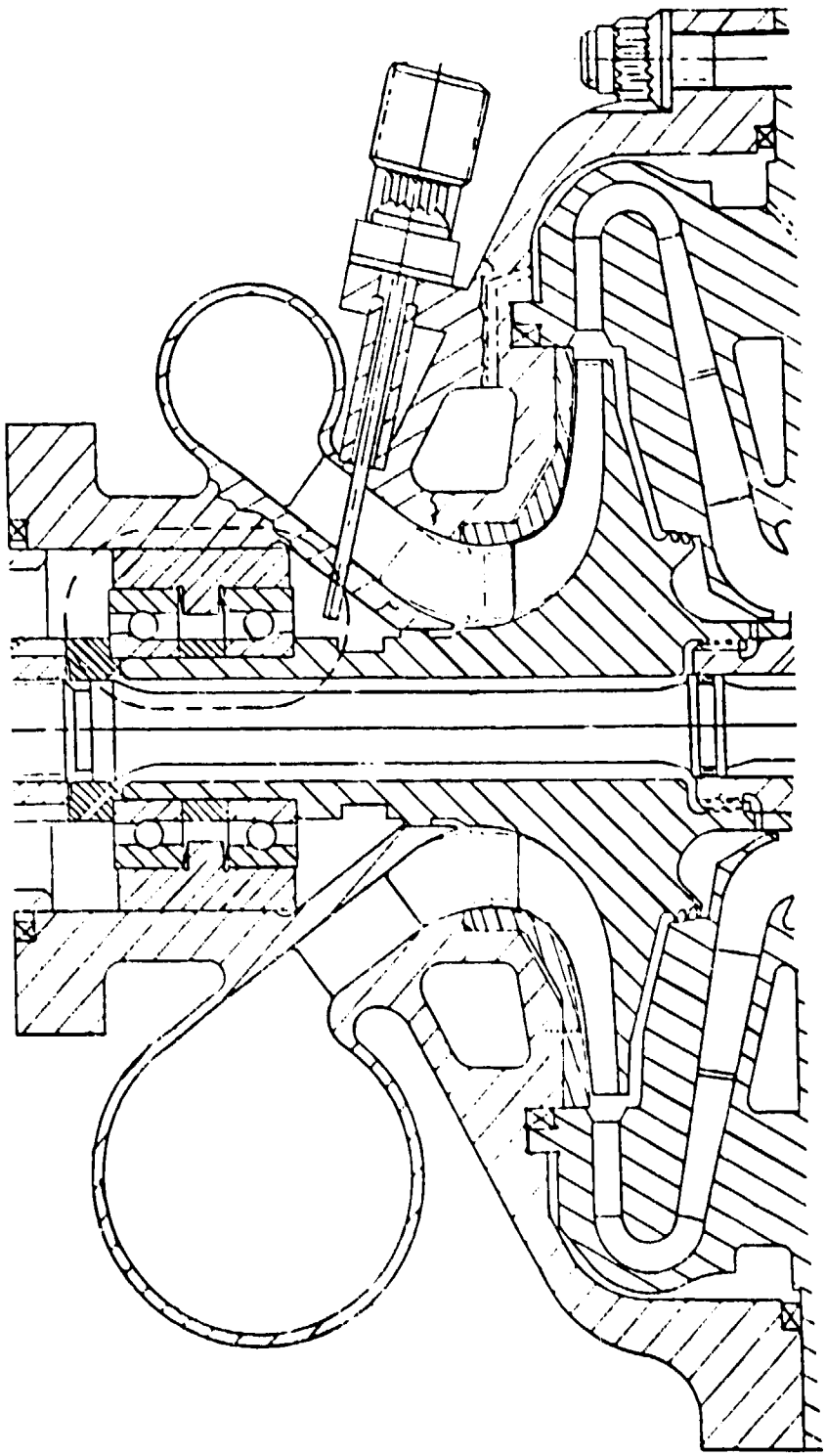

Figure 62. Design Modification No. 8 (Features: Open-face Impeller, Cutback Blades)

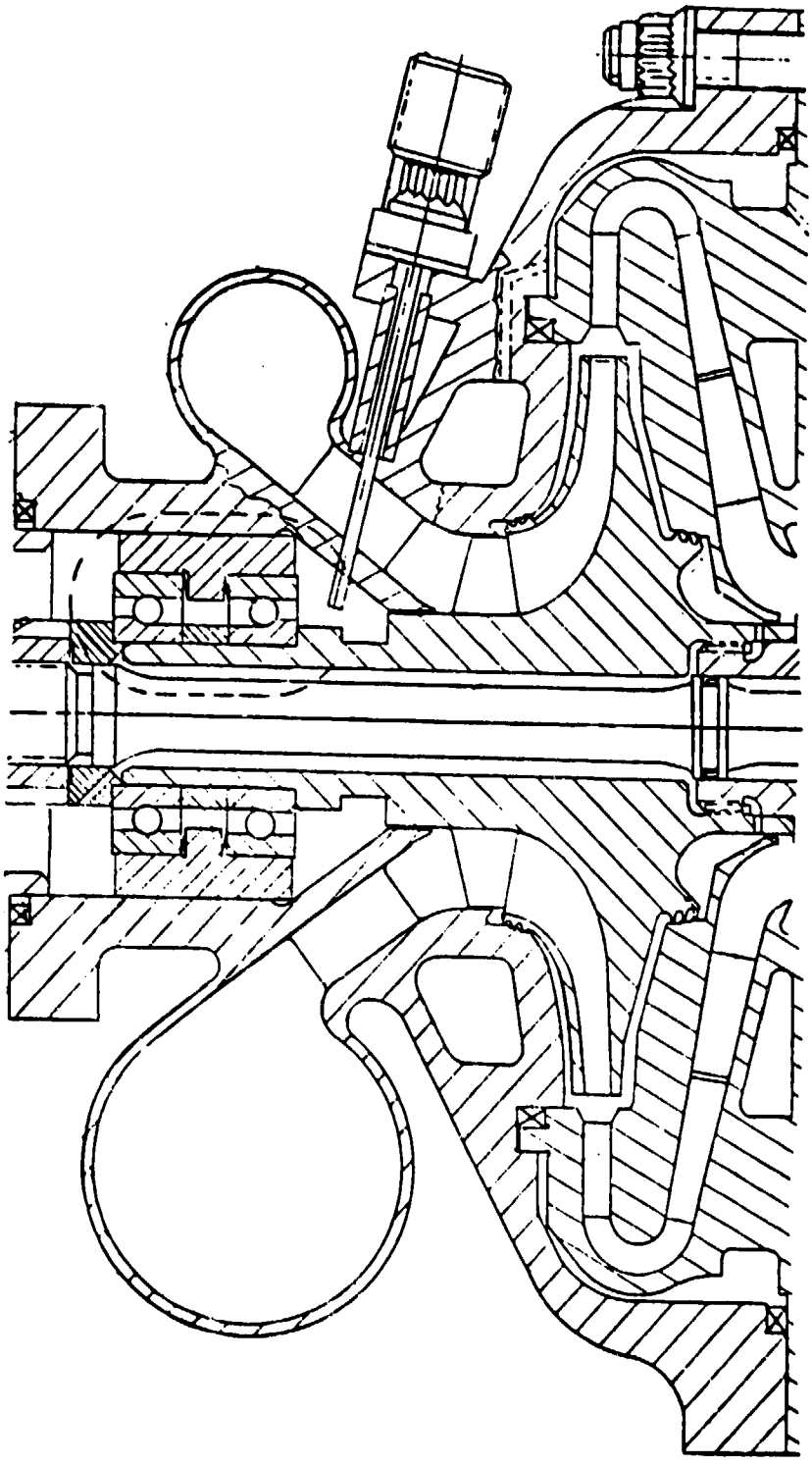

Figure 63. Design Modification No. 12 (Features: New Impeller, Inducer Section Added Upstream)

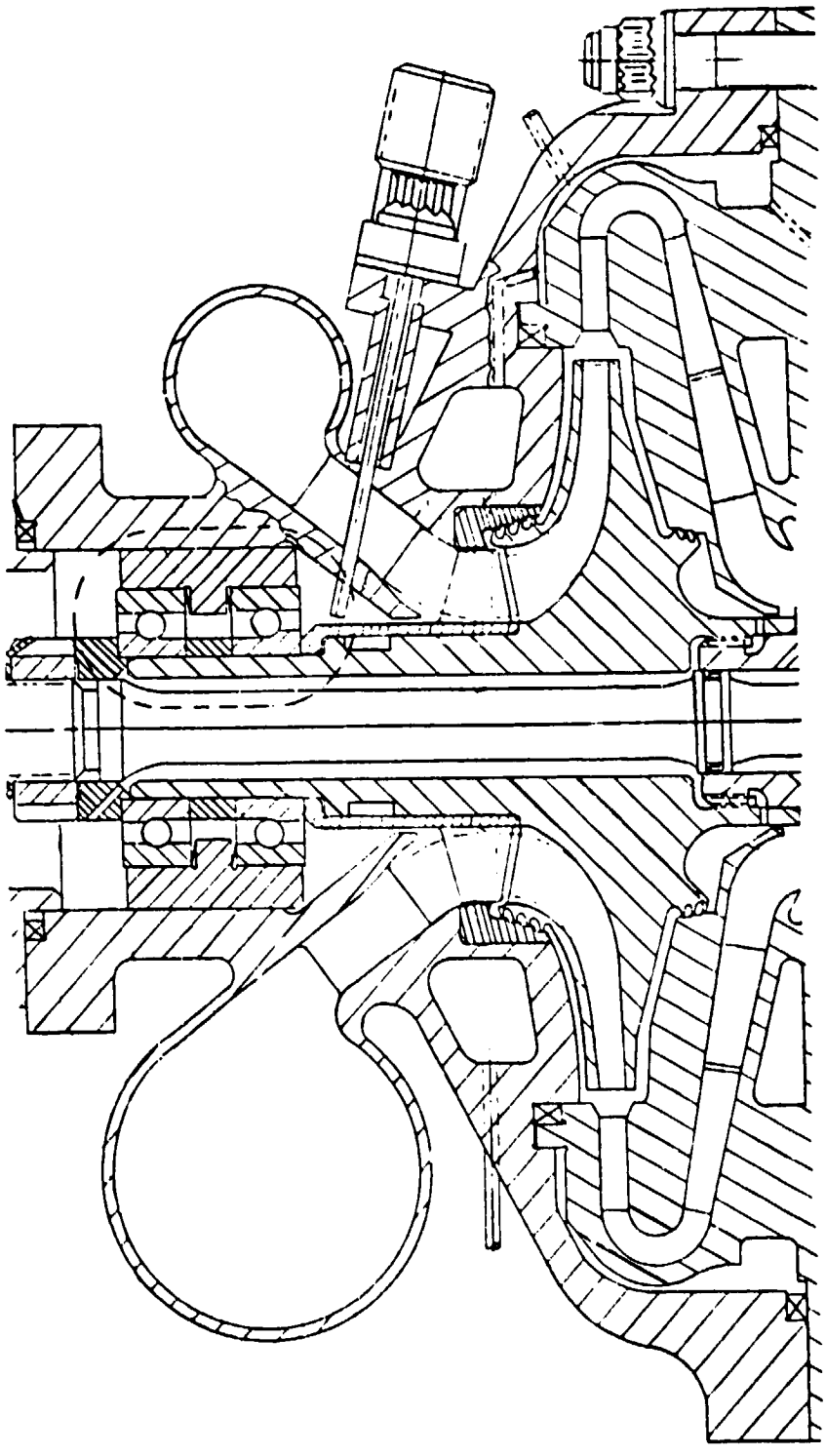

Figure 64. Design Modification No. 14 (Features: Impeller Inlet Area Increased, Added Inducer)

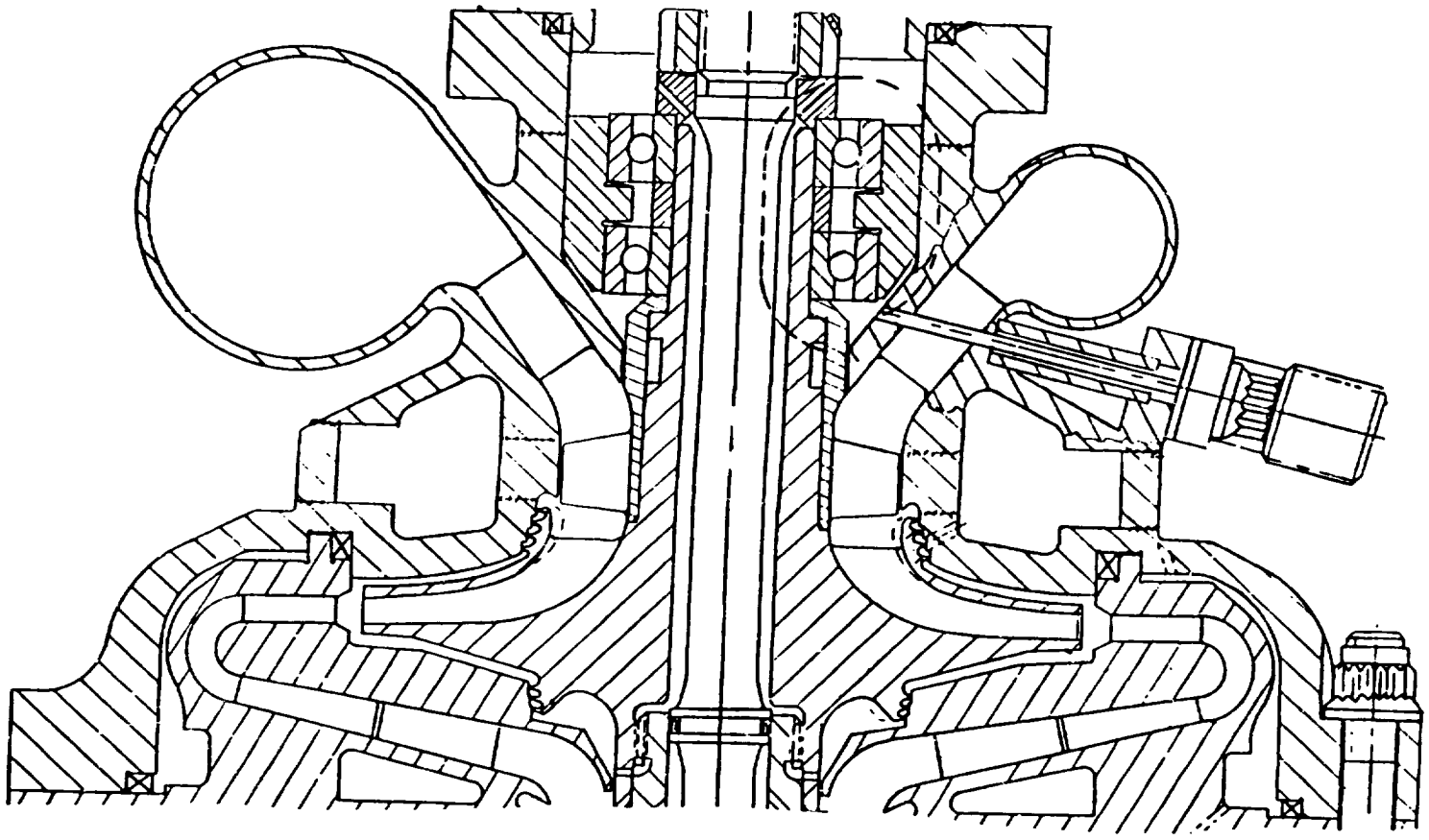

Figure 65. Design Modification No. 14, Stretched
(Features: More Room For Inducer)

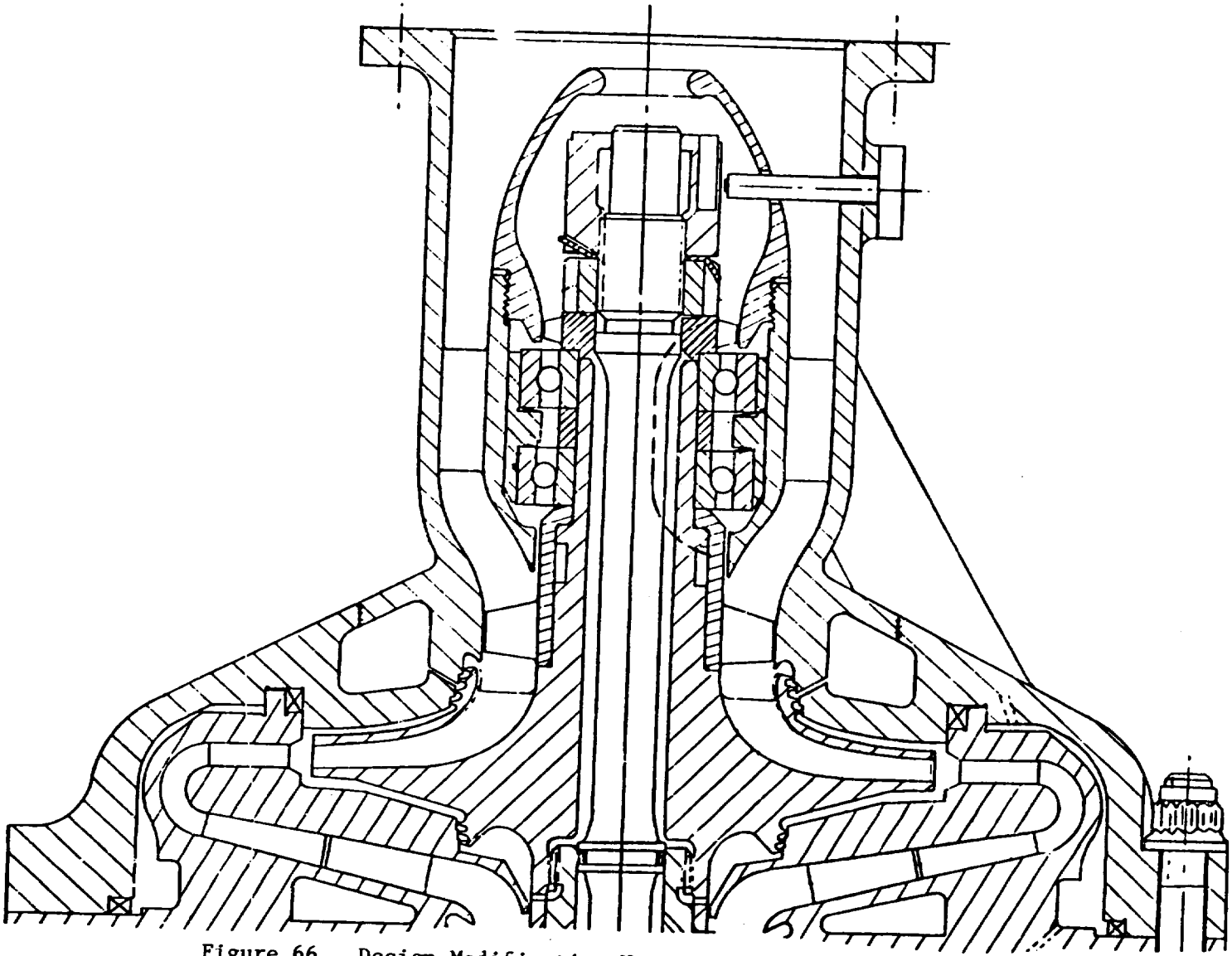

Figure 66. Design Modification No. 16 (Features: Axial Entry Inlet, Inducer, Impeller Modifications)

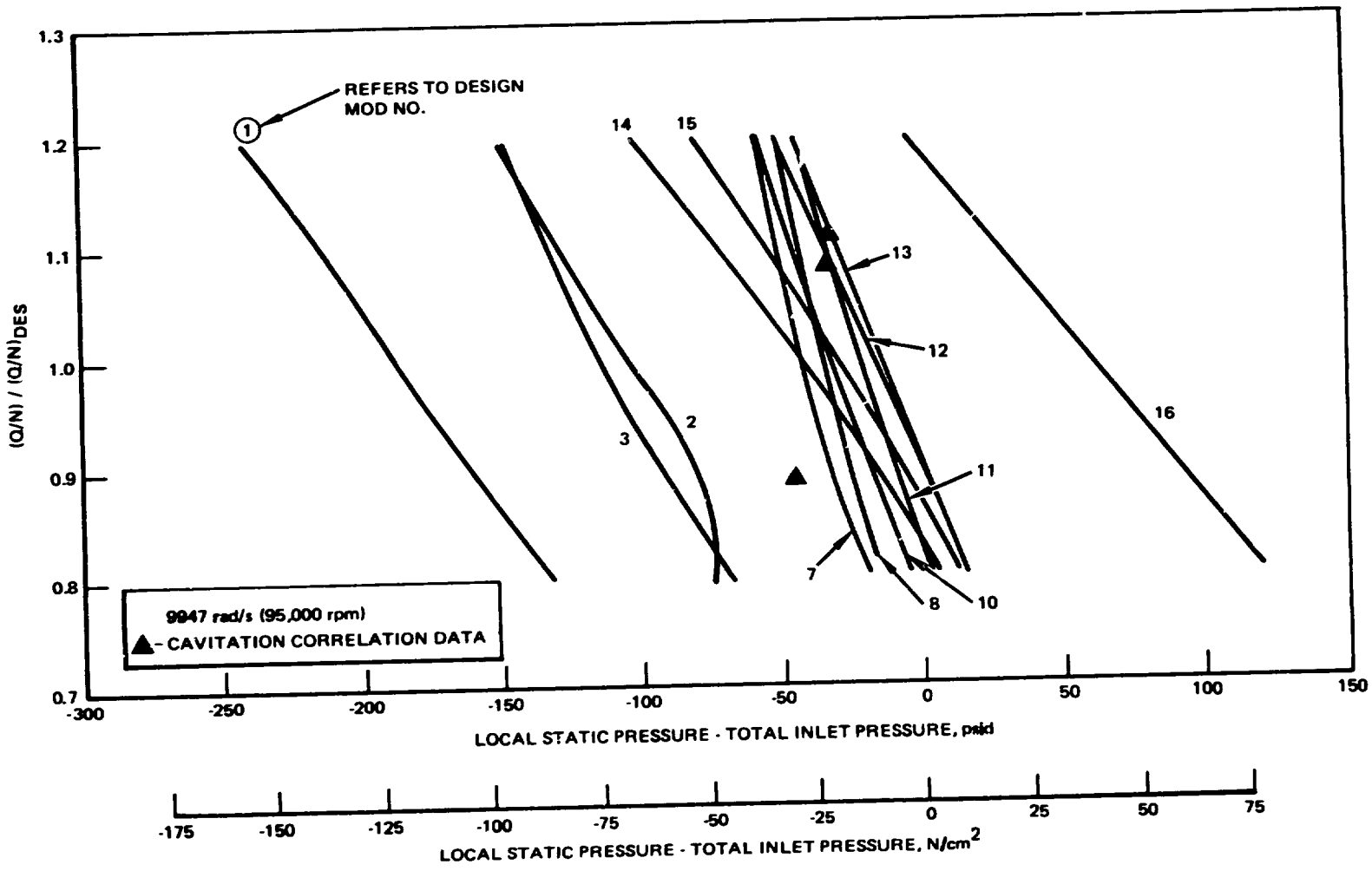

Figure 67. Minimum Impeller Surface Pressures for Inlet Modifications 1-16 (Suction Side)

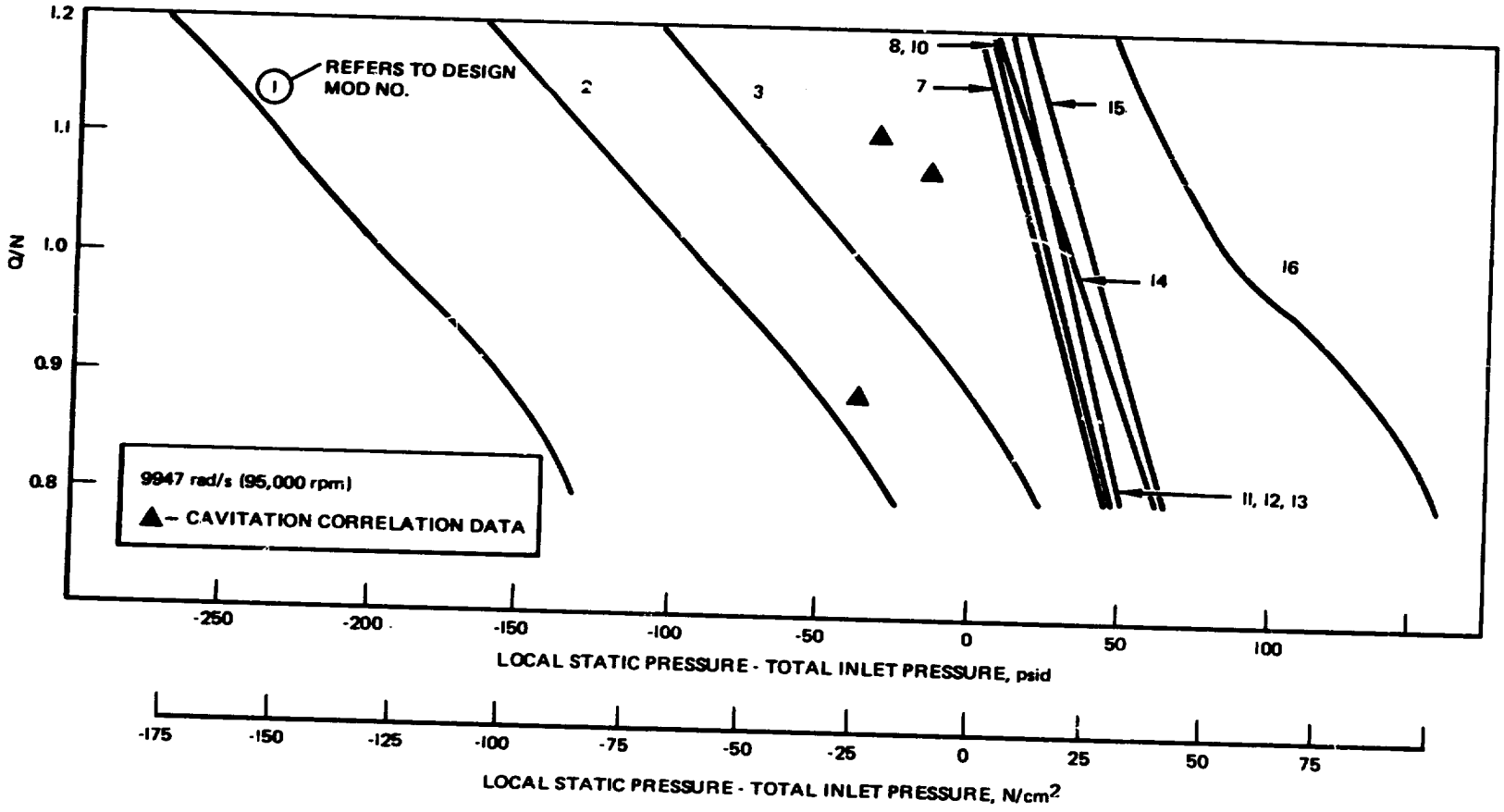

Figure 68. Minimum Impeller Surface Pressures for Inlet Modifications 1-16 (Pressure Side)

Nevertheless, examination of the suction-side pressure levels (Fig. 67) reveals that despite the sizeable improvement, all configurations but one fall into a regime where at high Q/N values cavitation may be experienced. The only design modification which exhibits a clear margin both on the suction and pressure side and even at high Q/N values is No. 16, which includes an axial-flow inlet and an inducer in front of the impeller.

In summary, it is concluded that the suction performance problem encountered was caused by two major effects: (1) The angle at which the fluid discharges from the inlet housing guide vanes into the impeller was improper, and (2) the impeller inlet area was insufficient. The solution required matching the flow angles to the impeller with a new inlet or new inlet guide vanes, increasing the inlet area of the impeller, and providing additional pressure to the impeller with an inducer. Each of the above improvements were incorporated in modification 16, (Fig. 66).

The design involved reworking an existing integral impeller by opening up the shroud inner diameter at the eye; modifying the front bearing cartridge; and designing and procuring a new axial inlet housing, main inducer, bearing coolant inducer, an inlet flow guide, and new speed and Bentley transducers.

The above material was presented to the NASA project manager in an oral briefing held at NASA-Lewis Research Center, Cleveland, Ohio, on 12 April 1978, with a recommendation to restructure the program to include the effort to design, procure, and test the axial inlet configuration. NASA concurred with the conclusion and directed Rocketdyne to initiate the design effort.

Axial Pump Inlet Design

Effort was expended to define the configuration of the axial-flow pump inlet in detail. The approach presented in Fig. 66 had to be modified in two respects to accommodate future test plans for the liquid hydrogen turbopump: (1) additional radial space had to be included outboard of the bearing outer races to provide room for future incorporation of a hydrostatic bearing, and (2) the design change had to be made compatible with future plans to incorporate a rotor brake system.

Considerable effort was expended on the analysis of the inlet passage into the inducer. The inlet passage design presented a problem because of a number of conflicting requirements, and mitigating solutions had to be worked out. To achieve good hydrodynamic performance of the inducer, it is necessary to keep the inlet fluid velocity to the inducer as uniform as possible.

Several design configurations were studied both from a mechanical and hydrodynamic standpoint. Figure 69 is a configuration with a minimum of mechanical changes. The rolling-element bearing locations and configuration was kept the same as the original design. The bearing cartridge OD was increased to provide for future incorporation of the hybrid bearing, and provision was made for the installation of a brake outboard of the bearings to satisfy a requirement for preventing rotation during tank head starts. The resulting inlet configuration, analyzed using the Rocketdyne three-dimensional computer program, was found to be unsatisfactory because of high fluid velocities

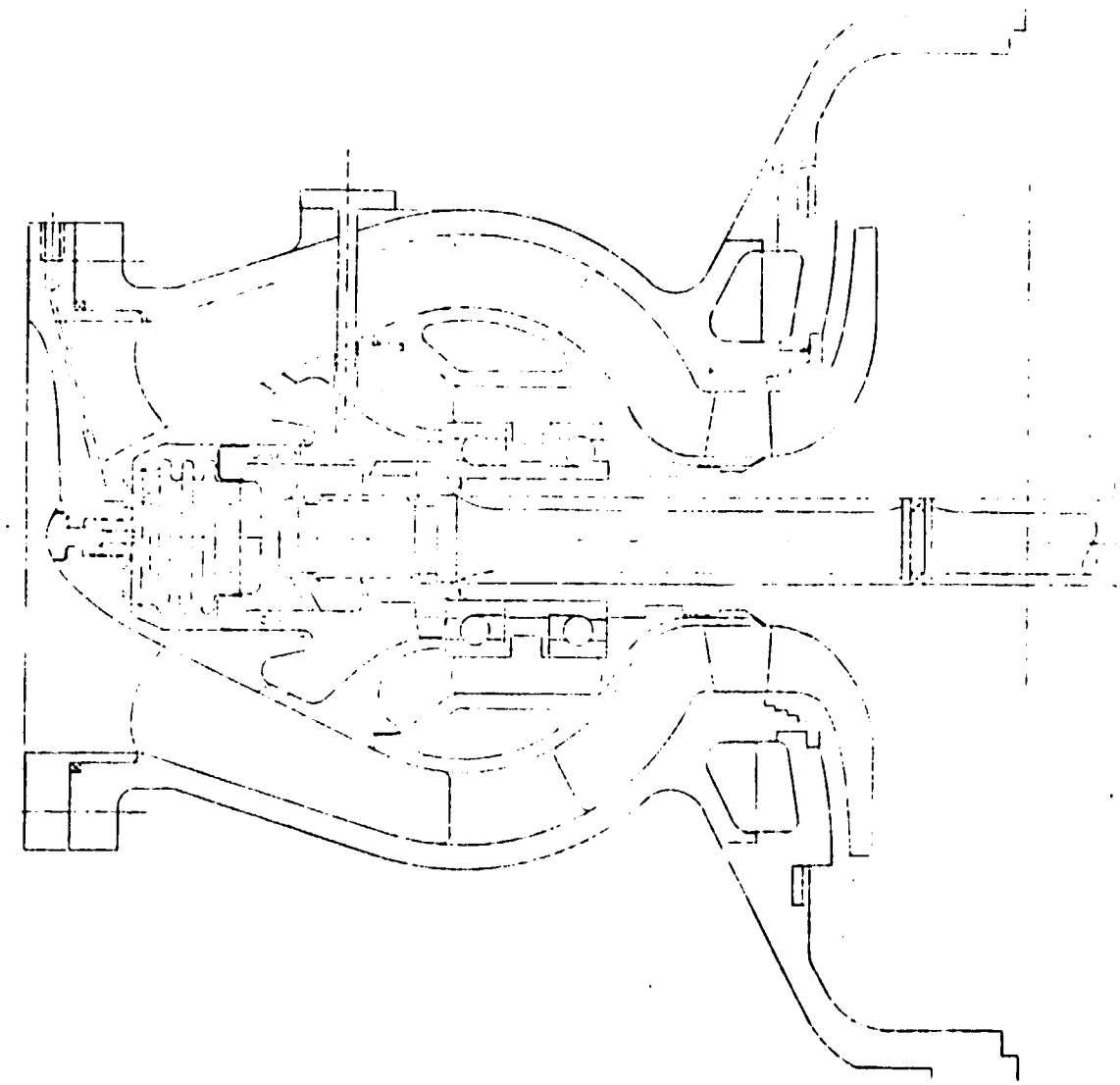

Figure 69. MK 48 Fuel Turbopump - Axial Inlet Configuration (1)

generated by the abrupt entrance of the fluid at the outer wall of the passage at the entrance to the inducer.

The configuration presented as a sketch in Fig. 70 represents a hydrodynamically satisfactory design; however, it requires additional redesign and also increases the overall length of the turbopump assembly. The rolling-element bearing was moved outboard, which allows a smooth transition passage to the inducer. The design incorporates provisions for both the hybrid bearing and the turbopump brake, and requires a new shaft extension for the bearings as well as a new tie-bolt.

A satisfactory compromise configuration is shown in Fig. 71. This design exhibits good hydrodynamic performance along with a minimum of redesign, and incorporates the required provisions for the hybrid bearing and the rotor brake. No new shaft or tie-bolt is required. Minor modifications to the design include moving the bearings closer together in the housing, the use of an offset cartridge, and thus also, an offset hydrostatic bearing.

The bearings are moved closer by 0.254 cm (0.100 inch) and the cartridge offset is only 0.254 cm (0.100 inch). Neither of these modifications appeared to have any adverse effects.

Inducer. Detailed analysis of the inducer was initiated following the finalization of the axial inlet hydrodynamic flow passage. The Mark 48 fuel pump inducer was designed to pump 0.0403 m^3/s (642 gpm) of liquid hydrogen with a density of 70.3 kg/m^3 (4.39 lb/ft^3) and an NPSP of 20.7 N/cm^2 (30 psi) at 9947 rad/s (95,000 rpm). The inducer tip diameter was fixed at 4.978 cm (1.96 inches) and the hub diameter at a constant value of 2.845 cm (1.12 inches) giving a hub/tip ratio of 0.57.

Cavitation Performance. An NPSP of 20.7 N/cm^2 (30 psi) is equivalent to an NPSH of 300 m (984 ft), and the corresponding operating suction specific speed is 5.05 $rad/s(m^3/s)^{1/2}(J/kg)^{-3/4}$ (13,700 $rpm \cdot gpm^{1/2} \cdot ft^{-3/4}$). It was calculated that the head breakdown point in water would occur at an NPSH of 229 m (752 ft); this gives a suction specific speed of 6.12 rad/s $(m^3/s)^{1/2}$ $(J/kg)^{-3/4}$ (16,760 $rpm \cdot gpm^{1/2} \cdot ft^{-3/4}$). This is the inducer's potential.

Design Parameters. An attempt was made to put in sufficient whirl with the inducer to match exactly the impeller inlet angles. However, the nonisentropic simple radial equilibrium computer program showed that the blade loading at the hub was much too high. This was partly because the inducer has no hub taper and partly because the impeller angle variation hub and tip is helical ($R \tan \beta_b = K$).

Successive trials were made with the computer program until a satisfactory solution was obtained. With this design, the diffusion factor at the tip was 0.227, at the rms 0.373, and at the hub 0.678. The last value is high (separation occurs at a D-factor of approximately 0.7) because the axial velocity leaving the inducer at the hub is relatively low. The resultant

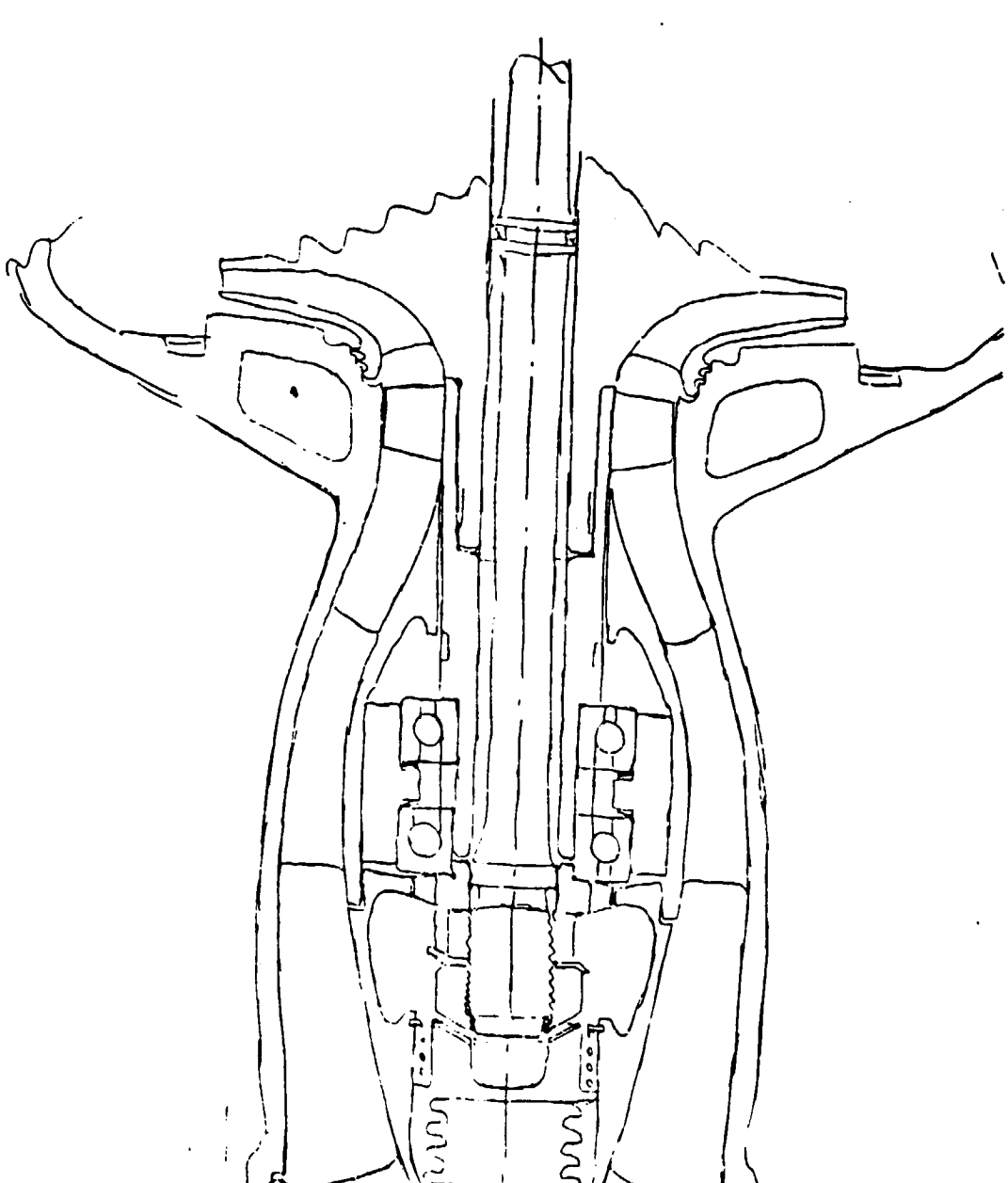

Figure 70. MK 48 Fuel Turbopump - Axial Inlet Configuration (2)

Figure 71. MK 48 Fuel Turbopump - Axial Inlet Configuration (3)

incidence angles on the impeller blades were 0.111 radian (6.4 degrees) at the tip and 0.202 radian (11.6 degrees) at the hub. These values are acceptable.

The average head produced by the inducer was calculated by the Rocketdyne three-dimensional program (R3DP) to be 782 m (2563 feet) with a corresponding head coefficient of 0.125. When this head is added to the inlet NPSH, it gives an impeller suction specific speed of 1.91 rad/s$(m^3/s)^{\frac{1}{2}}(J/kg)^{-3/4}$ (5237 rpm $gpm^{\frac{1}{2}}$ $ft^{-3/4}$). The calculated inducer efficiency is 72%.

The nominal flow coefficient of the inducer based on an average inlet axial velocity is 0.1248. The curvature of the inlet passage, however, induces a higher axial velocity at the tip than at the hub, resulting in the following inlet condition at the inducer tip where the blade angle is 0.225 rad (12.93 degrees).

% Speed	% Flow	Incidence Angle, rad (degrees)	i/β_b
100	70	0.113 (6.47)	0.500
100	100	0.0679 (3.90)	0.302
100	130	0.0240 (1.38)	0.107

At 130% Q and at 9947 rad/s (95,000 rpm), the inducer produces 203 m (664 feet) of head. At this point, the impeller will operate at a suction specific speed of 3.87 rad/s$(m^3/s)^{\frac{1}{2}}(J/kg)^{-3/4}$(10,610 rpm · $gpm^{\frac{1}{2}}$ · $ft^{-3/4}$).

Inducer Design Values. The inducer has six blades (the same number as the impeller). It has an inlet sweep of 0.348 rad (20 degrees) and a cant angle of 0.087 rad (5 degrees). The tip blade thickness is 0.381 mm (0.015 inch), and the hub blade thickness 1.91 mm(0.075 inch). The solidity at the tip is 1.5, a value that has been very successful on recent model waterjet inducers and on an inducer for the SSME LOX pump.

Figure 72 shows the H-Q and efficiency of the inducer as calculated by the Rocketdyne INDANA computer program.

Figure 73 shows the head rise through the inducer at design speed and flow as calculated by R3DP. Figures 74 and 75 show the blade loading at 110% speed and at 100% speed and 80% flow, as calculated by R3DP and the Rocketdyne leading-edge wedge program. Figure 76 shows the design blade angle variation as a function of inducer axial length.

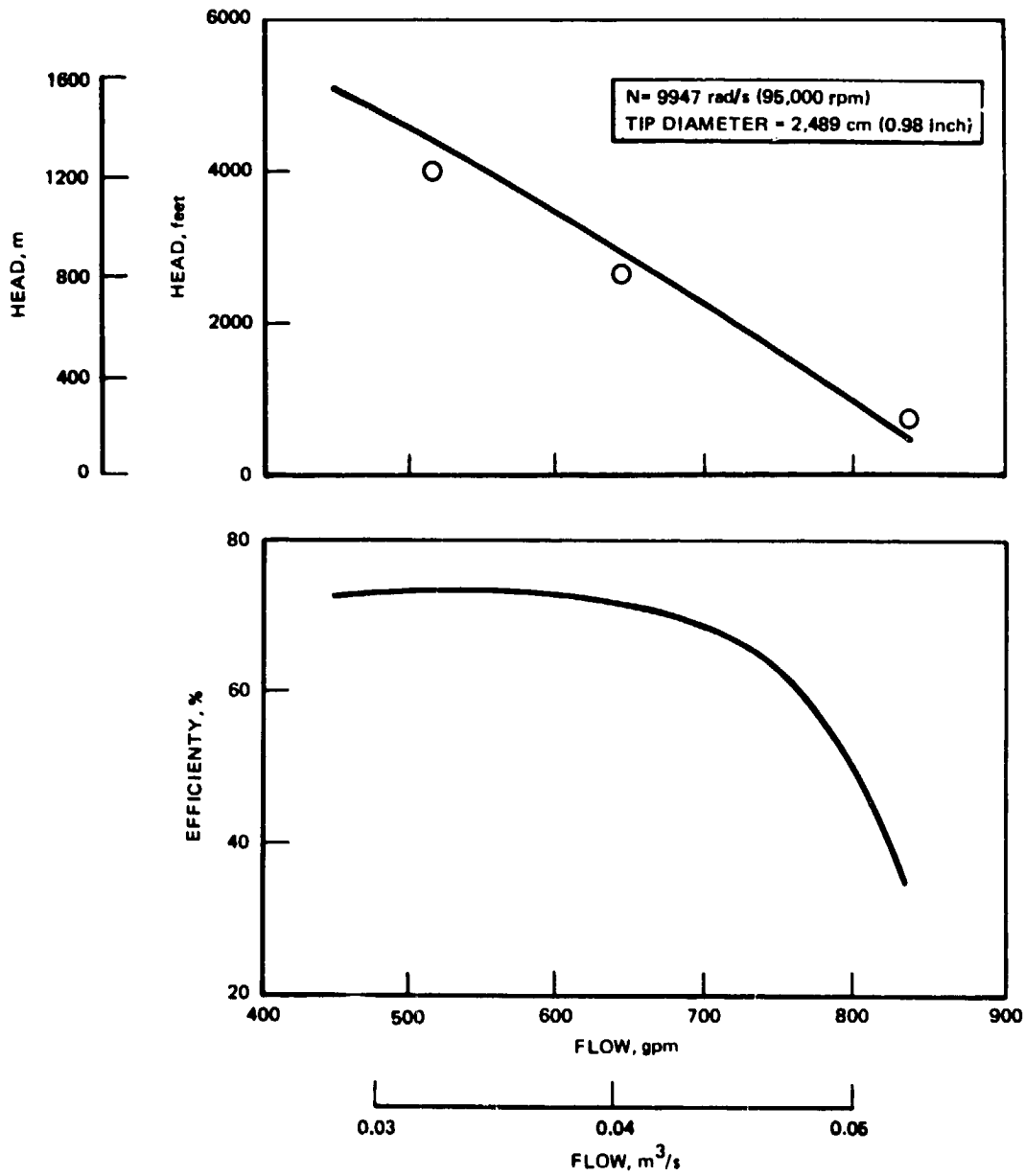

Figure 72. Fuel Pump Inducer Predicted Performance

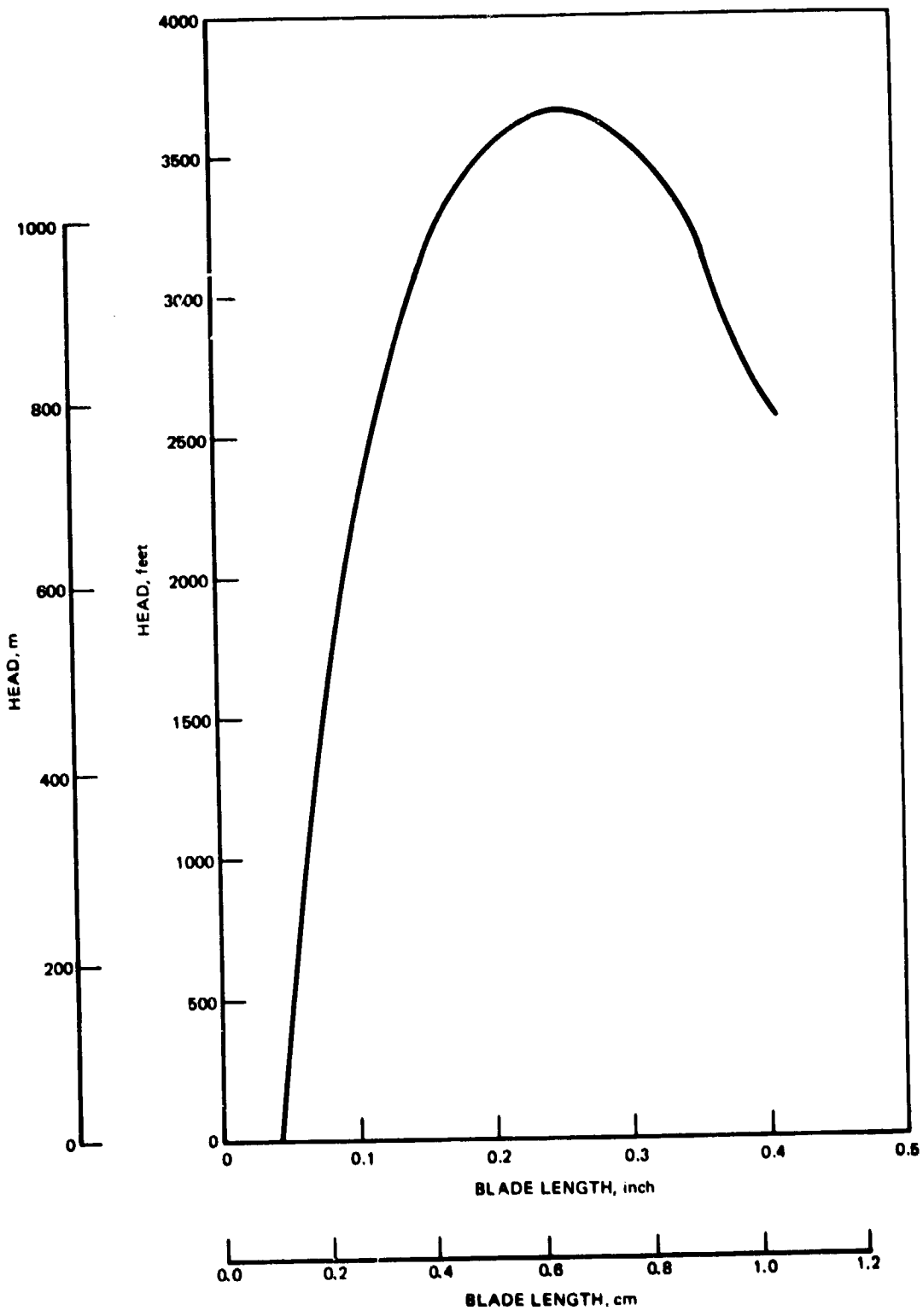

Figure 73. Inducer Head Distribution Along Blade Length

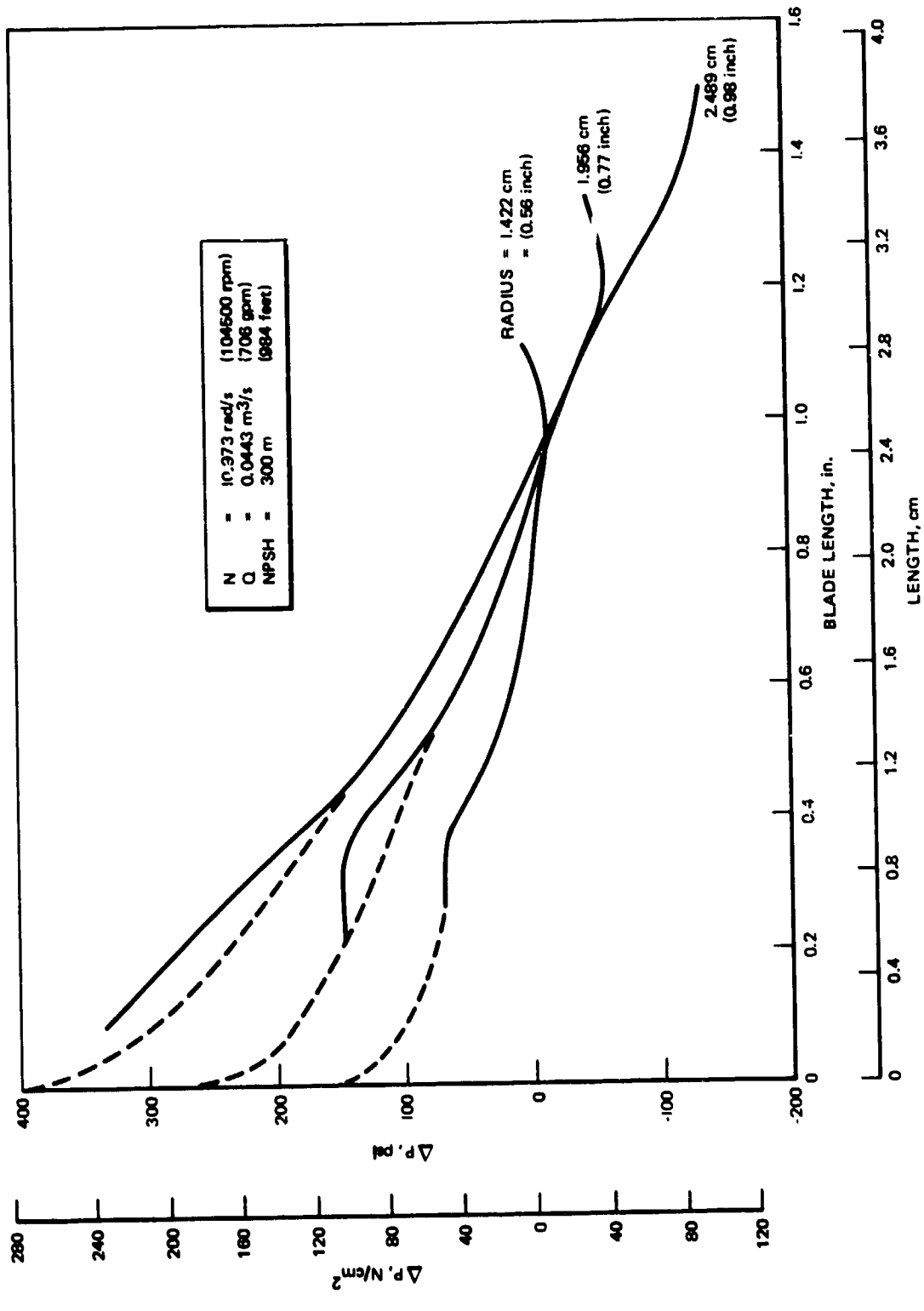

Figure 74. Inducer Blade Loading 10973 rad/s (104500 rpm)

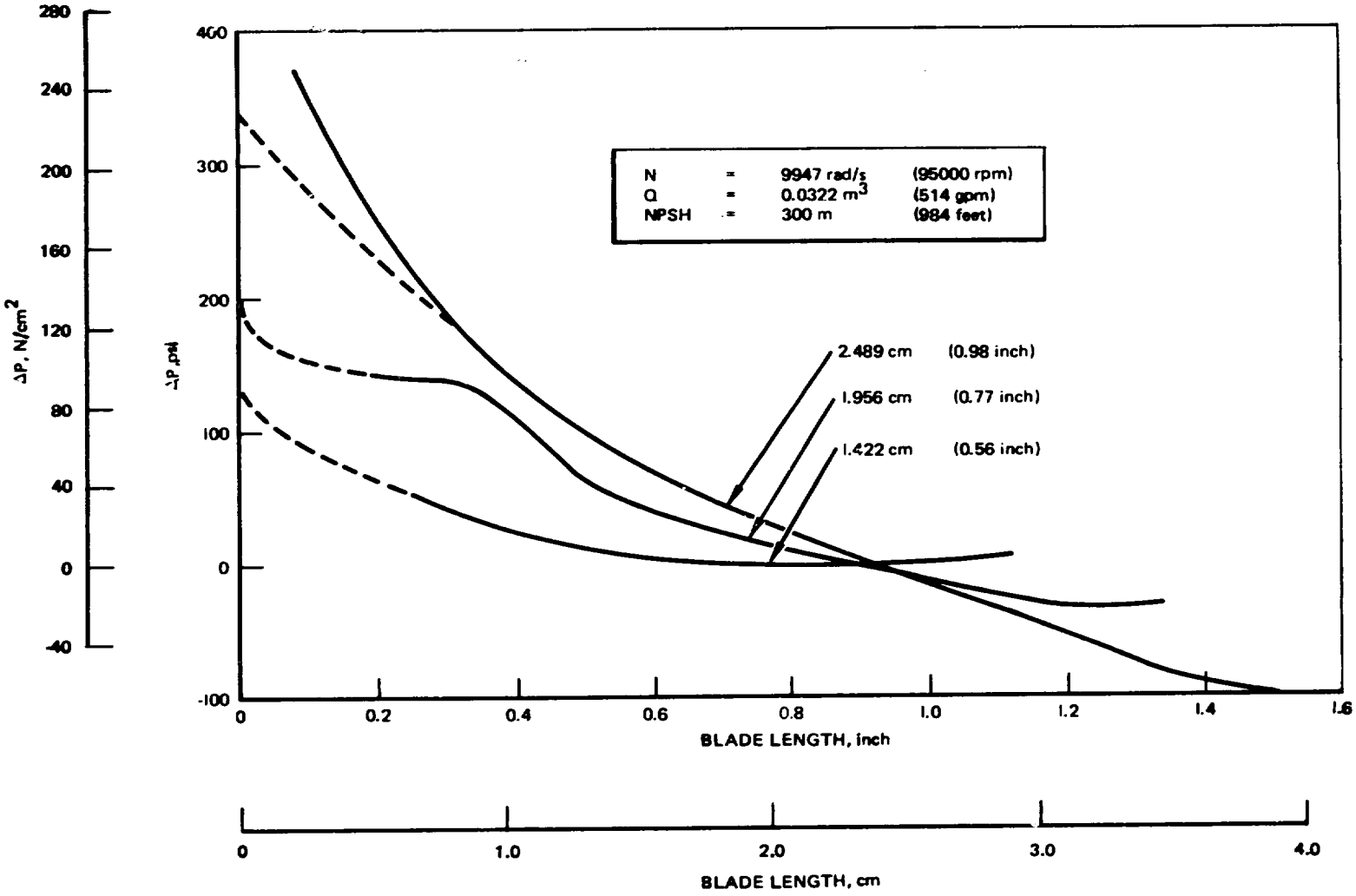

Figure 75. Inducer Blade Loading 9947 rad/s (95000 rpm)

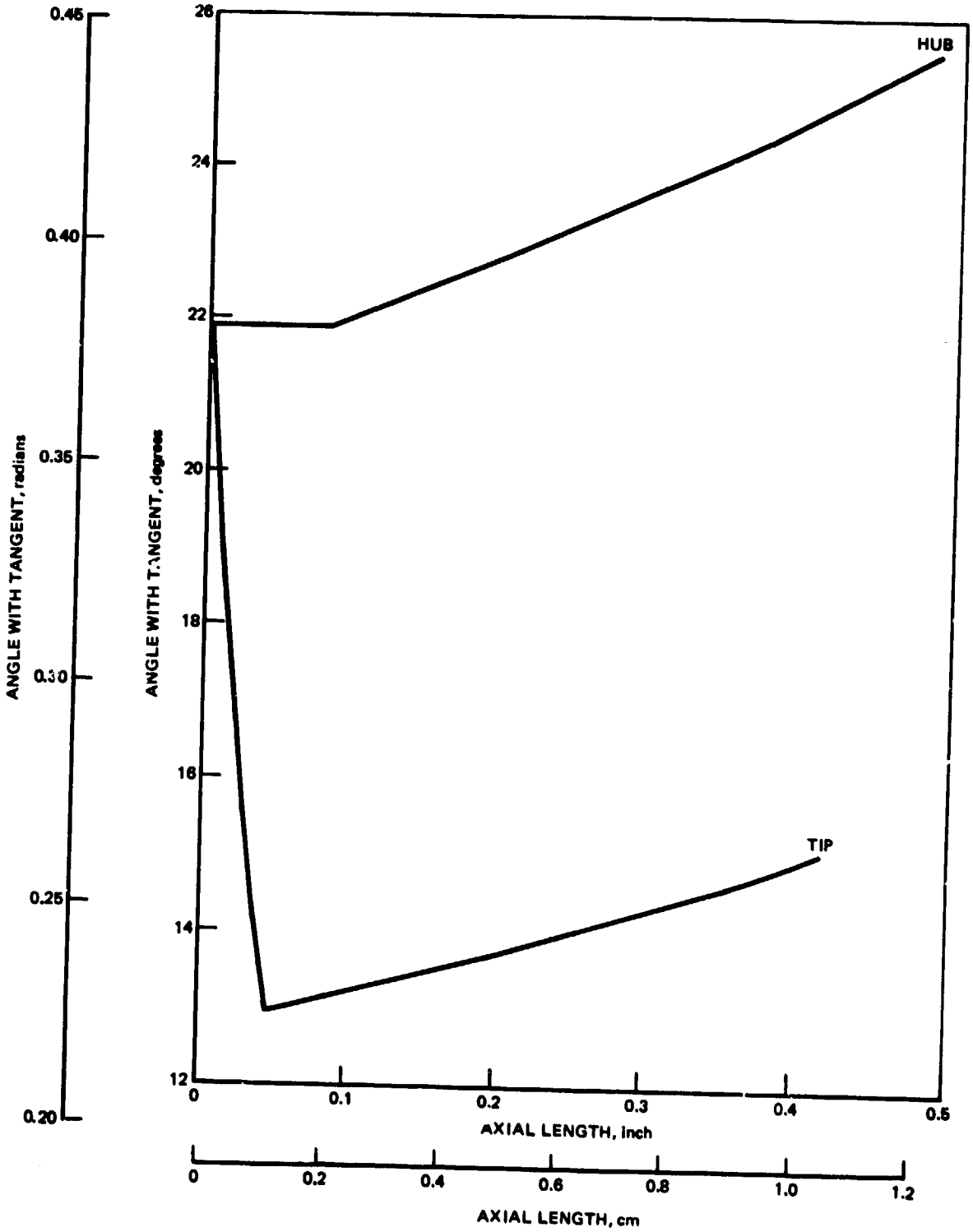

Figure 76. Mark 48-F Blade Angle Distribution

Inlet Passage. The design of the passage into the inducer was a difficult problem because the front bearing size and location were fixed. The flow had to pass out around the bearing, then radially inward before it entered the inducer. The location of the bearing, the maximum diameter of the bearing support, and the location and hub diameter of the inducer fixed the inner wall within narrow limits. The outer wall, however, could be designed to produce a high rate of convergence; this resulted in a small radius of curvature near the inducer entrance. A small rate of convergence resulted in a larger radius of curvature.

R3DP was used to evaluate the different passage designs. Many different contours were tried with various rates of convergence. The most favorable design was selected. The resultant velocities along the walls as a function of the distance along the walls are shown plotted in Fig. 77.

Bearing Cooling. To cool the front bearing it was desired to have 3.14 x 10^{-4} m^3/s (5 gpm) flow through it at the pump speed 3150 rad/s (30,000 rpm). A formula using theoretical and empirical data gathered over a period of time was used to calculate the pressure drop across the bearing at design Q/N at speeds of 3150, 6300, and 9947 rad/s (30,000, 60,000, and 95,000 rpm) and at 80 and 120% flow at the high speed. The losses in the flow passage were also calculated at various flowrates. The static pressures along the inlet passage inner wall were taken from the R3DP printout of the final passage shape, and the ram pressure available from the scoop-entrance to the inducer hub entrance was also plotted as a function of flow through the pump. The losses and ram pressure were then combined into one set of curves called bearing resistance. These are shown plotted in Fig. 78 . A small helical pump was then designed and evaluated in the INDANA loss program.

The performance of this pump at speeds of 3150, 6300, and 9947 rad/s (30,000, 60,000, and 95,000 rpm) is also plotted in Fig. 78. The intersection of these curves with the bearing resistance curves are shown as circles on the map, and the corresponding bearing flow can be read from the abscissa on the curve. Note that the H-Q curves are very steep, so that an error in the calculated pressure will have little effect on the volume flow through the bearing. Note also that, without any helical pump, the flow through the bearing would be at the value where the bearing resistance curves cross the zero coordinate. From the analysis of Fig. 78 it is clear that the small helical pump is not required.

Next in order was the design integration and optimization of the inducer into the axial pump inlet. A prime motivation was to provide design capability for incorporating the turbopump shaft brake and a cleanly configured pump end bearing coolant flow circuit. The bearing coolant flow circuit decided upon takes liquid hydrogen fluid from in front of the inducer and directs this flow through the duplex angular-contact bearing set, then is routed overboard where flowrate can be measured and adjusted by orificing, and where pressure and temperatures are measured.

The results of this design optimization is shown in Fig. 79 and 80 . These figures show the final approved design.

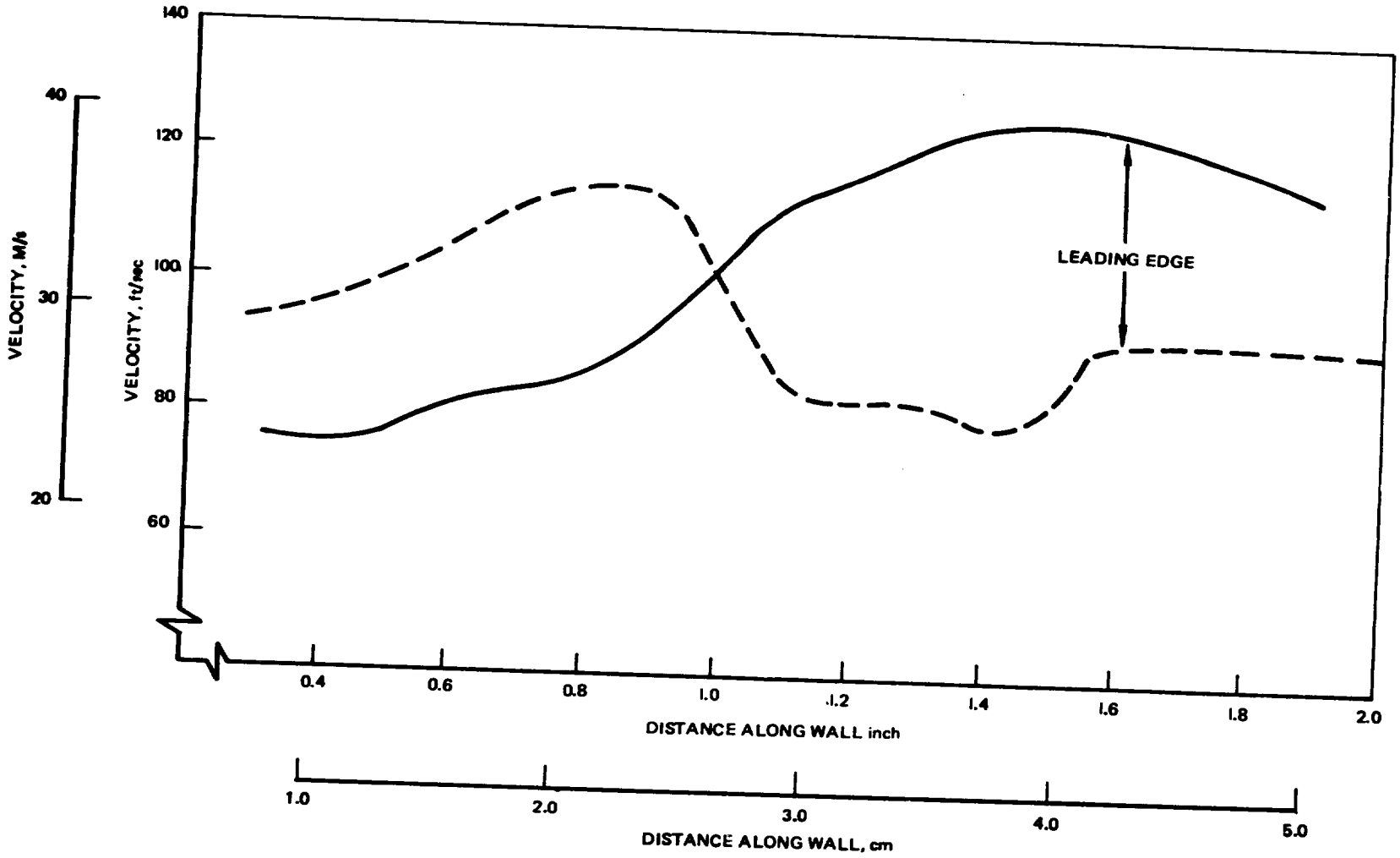

Figure 77. Inducer Passage Flow Velocities

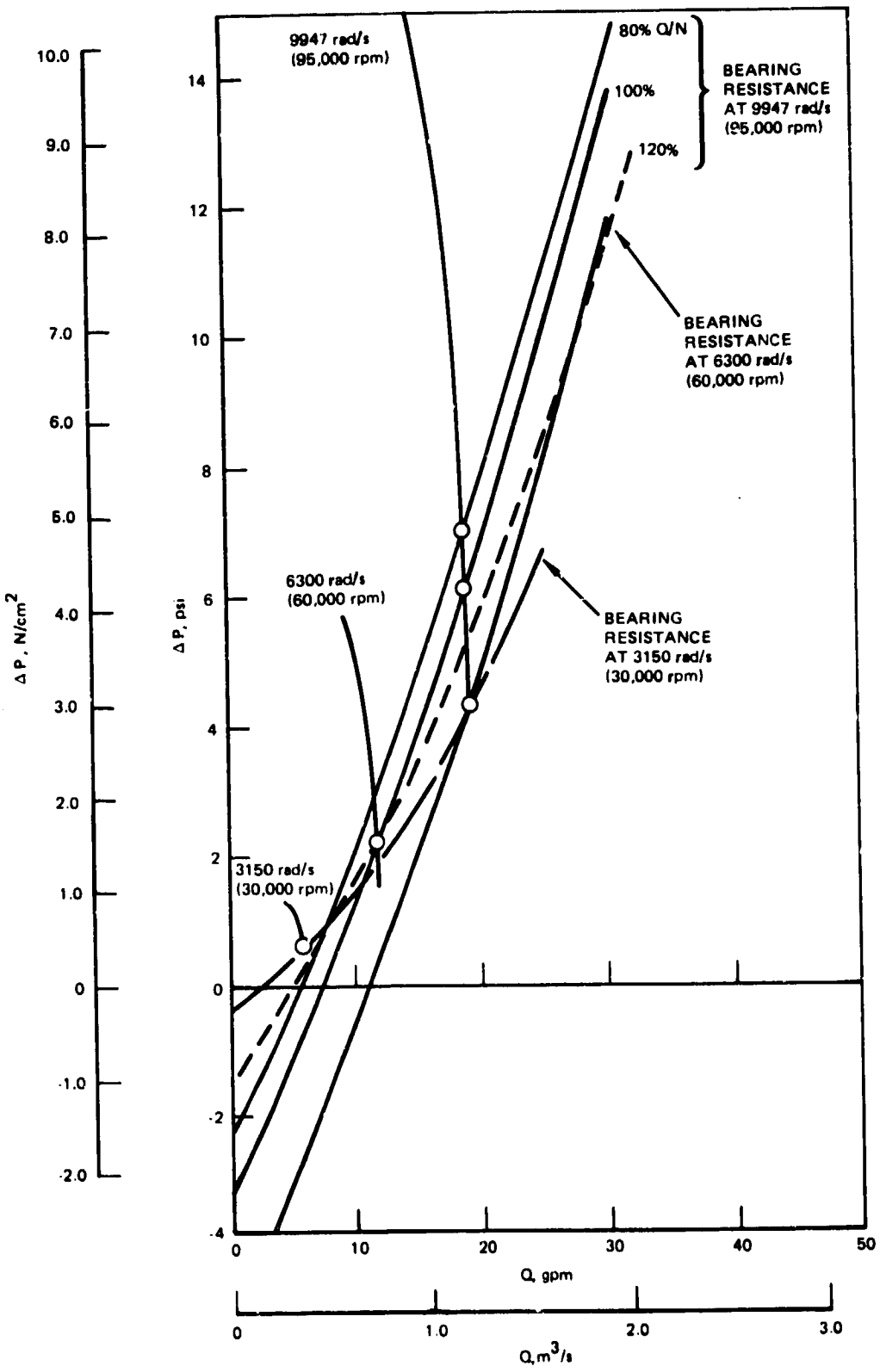

Figure 78. Mark 48-F Bearing Resistance

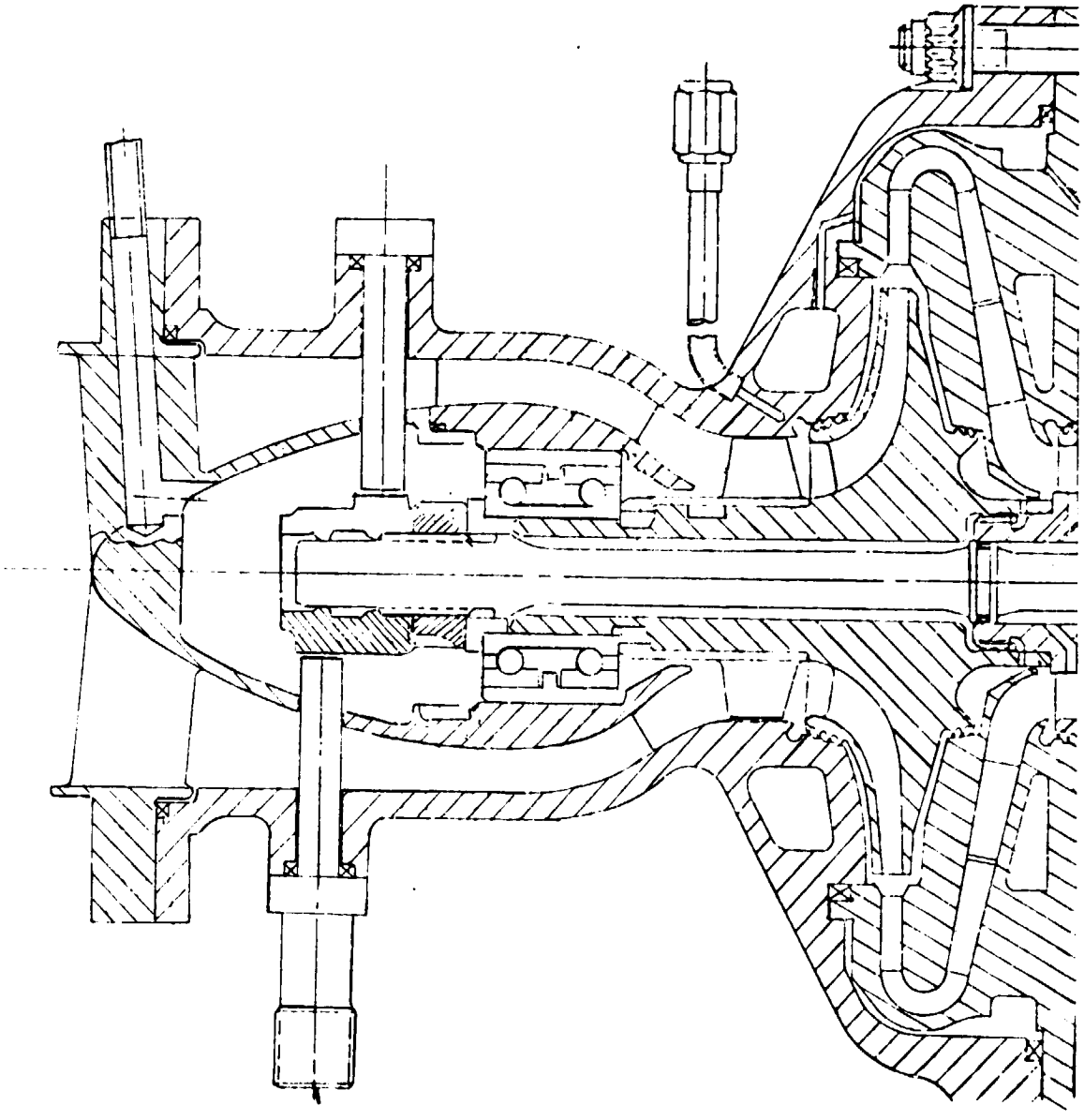

Figure 79. Optimized Inlet Design, Final Version

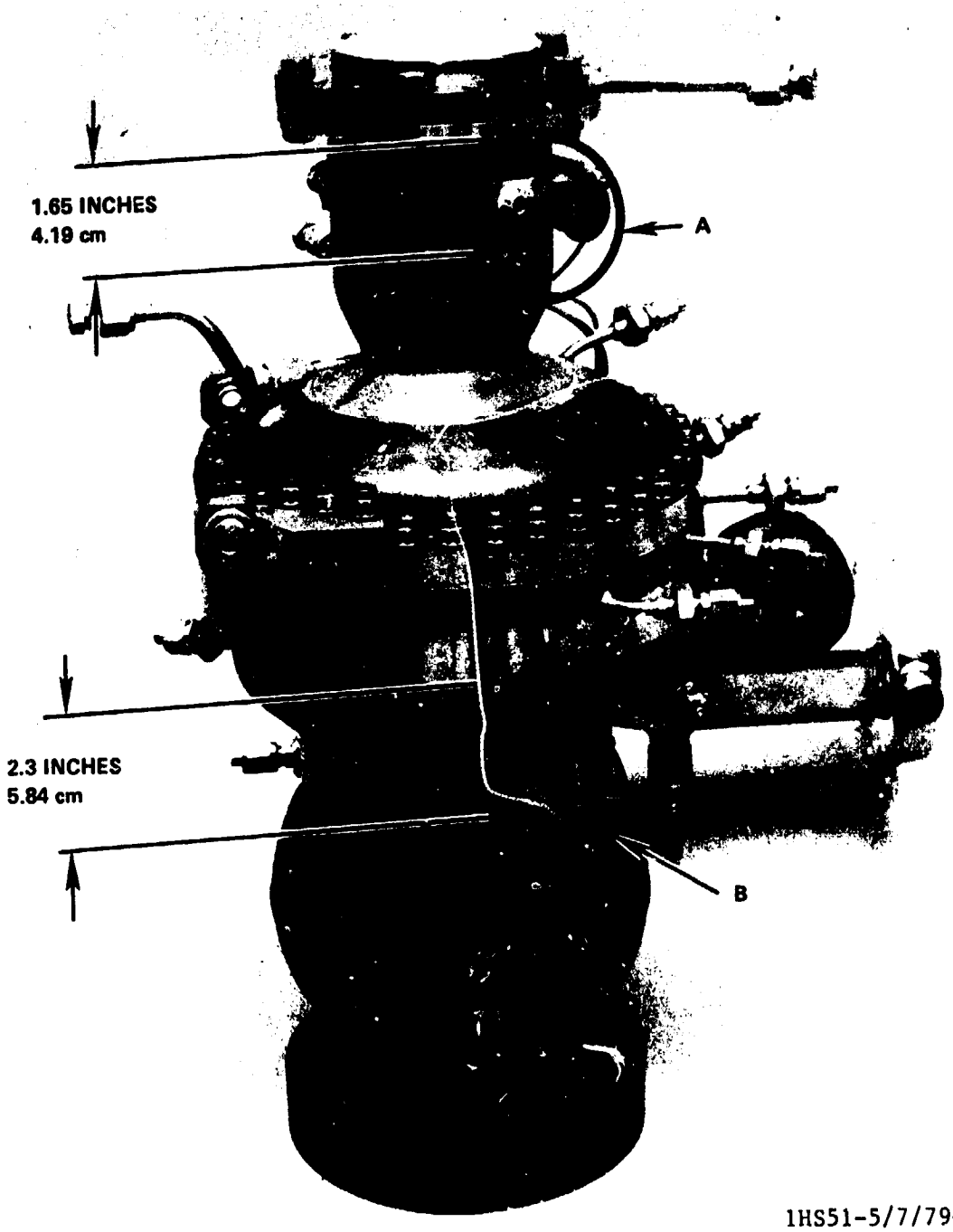

1HS51-5/7/79-C1C*

Figure 80. Mark 48-F Turbopump Showing Axial Position of Accelerometer Blade Weldments in Zones A and B

Fabrication of the hardware followed without difficulty, and the new parts were received on schedule and are shown in Fig. 81.

Assembly of Turbopump S/N 01-2

Critical balancing of the rotor assembly was undertaken first. Because of the high operating speed involved, it is essential that the rotor be balanced to the best precision available with present balancing equipment. As described, the balancing procedure was initiated with a preliminary rotor assembly consisting of the first- and second-stage impellers and a dummy sleeve replacing the second-stage impeller. The imbalance in the planes of the first- and second-stage impellers was established in this setup. Some delay in accomplishing this step was experienced when a lack of repeatability was noted on successive buildups. The problem was traced to local yielding of the dummy sleeve, which was eventually resolved by fabricating a new sleeve of a high-strength steel alloy.

The balancing operation was subsequently continued by including the second-stage impeller in the rotor and making temporary corrections in its plane. Finally, the turbine wheels and miscellaneous nuts and locks were added, and final corrections were effected by grinding material in the following planes: instrumentation nut; first-, second-, and third-stage impeller; and both turbine wheels. Figure 82 shows the balance assembly.

The final corrections were made based on imbalance readings obtained on a Schenck hard bearing balancing machine. This equipment has an improved precision capability compared with the soft bearing Gisholts used in the past.

The significant assembly clearances are presented in Fig. 83 through 87. All values are within the intended design range.

Testing

The assembled insulated turbopump was installed into the LIMA stand of the APTF (formerly termed PRA) in the Santa Susana Field Laboratory.

The new axial inlet turbopump facility propellant line was designed and the design was approved by the Stress Department. This line was fabricated and installed.

Nineteen tests were accomplished during this program, bringing the total test time on turbopump S/N 01-2 to 1353 seconds in 19 starts. A summary of all the tests conducted is presented in Table 13.

The first test (001) of the "Mark 48-F Turbopump Test Matrix", as shown in Table 13, was conducted for a programmed duration of 228 seconds. A steady-state operating point at 2615 rad/s (24,902 rpm) and $Q/N/(Q/N)_{DES} = 1.224$ was attained and an isentropic pump efficiency of 80% was achieved. The speed was increased to 4801 rad/s (45,728 rpm) and a $Q/N/(Q/N)_{DES} = 0.822$ was attained and an isentropic pump efficiency of 67.7% was achieved.

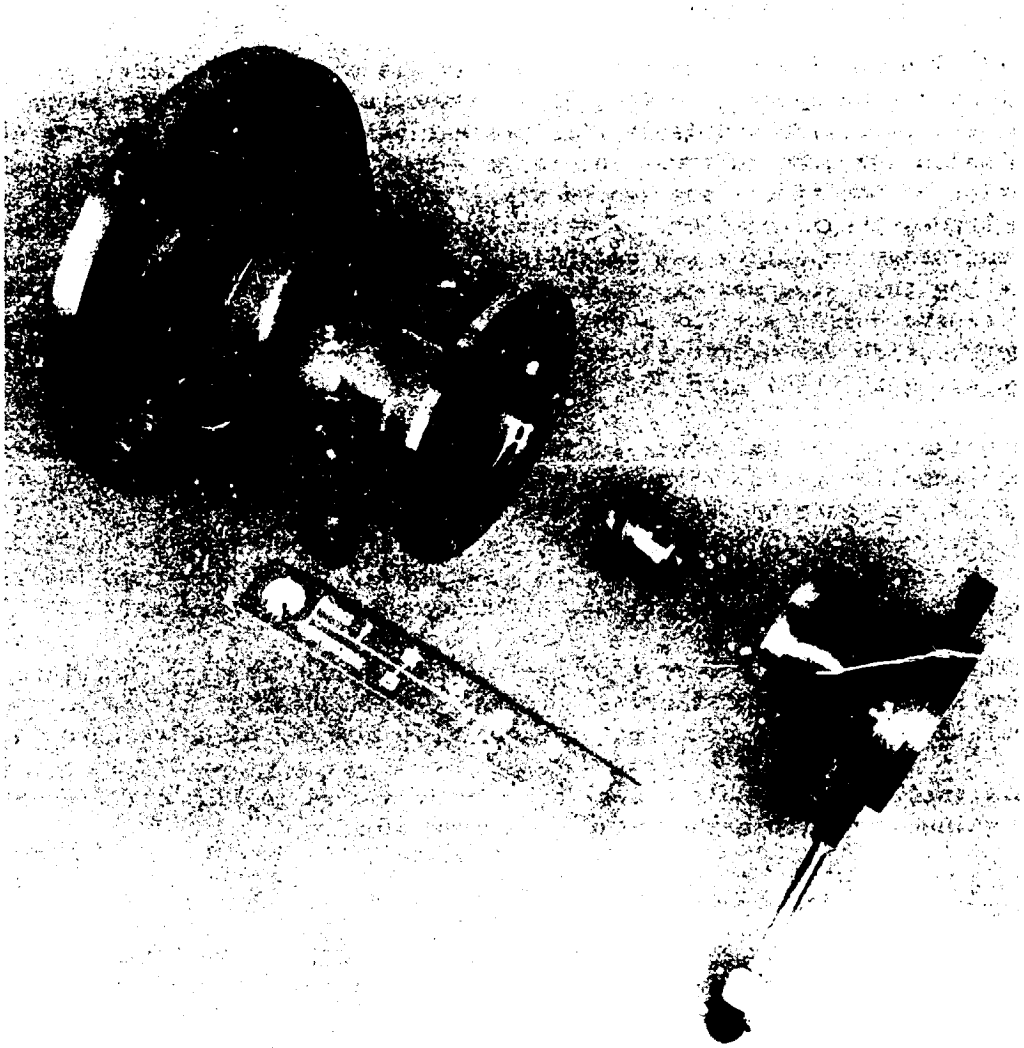

Figure 81. Mark 48-F LH_2 Turbopump Axial Inlet With Inducer

Figure 82. Mark 48-F Rotor Balance Assembly

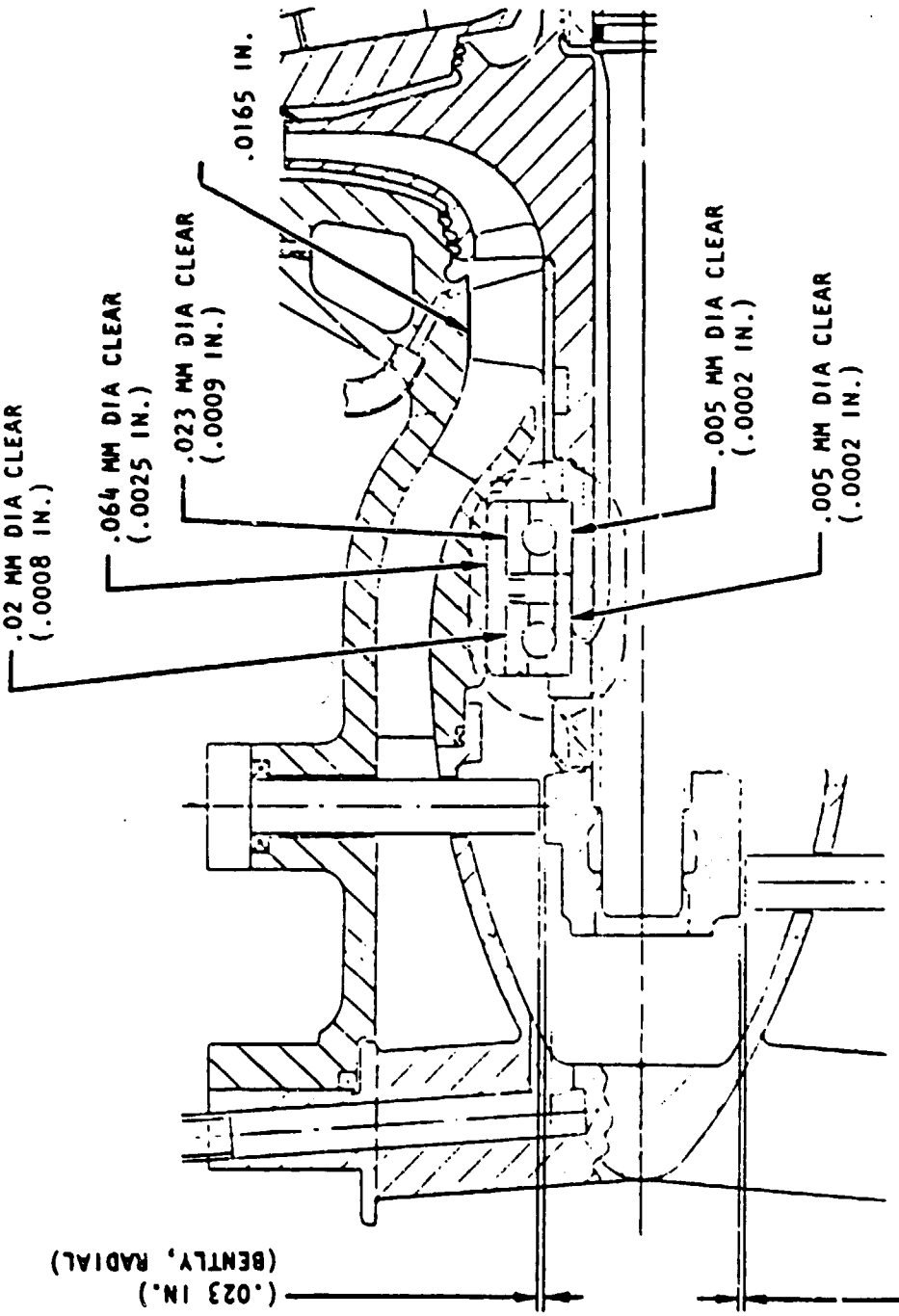

Figure 83. Pump Inlet End Clearances

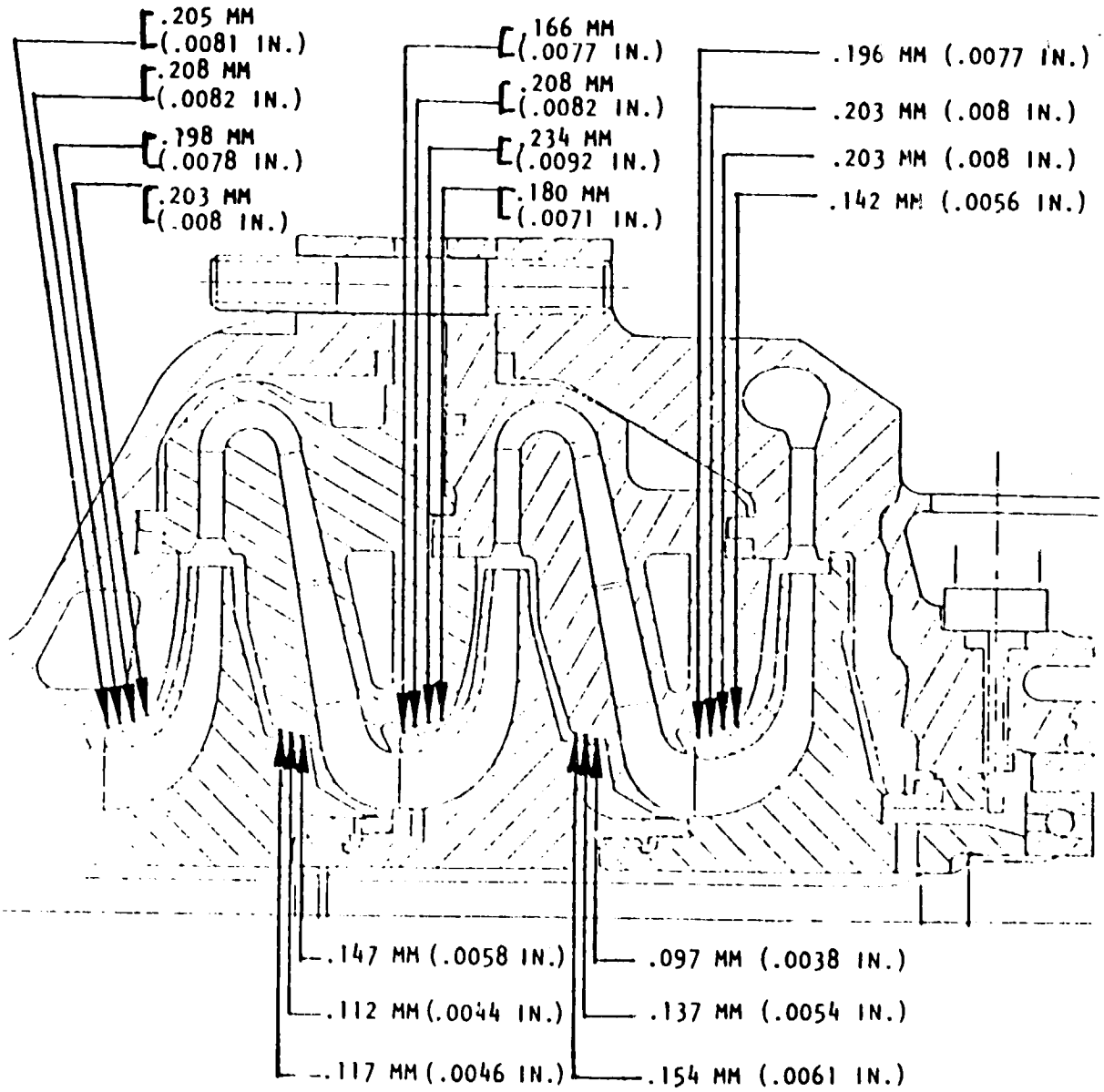

Figure 84. Impeller Wear Ring Diametral Clearances

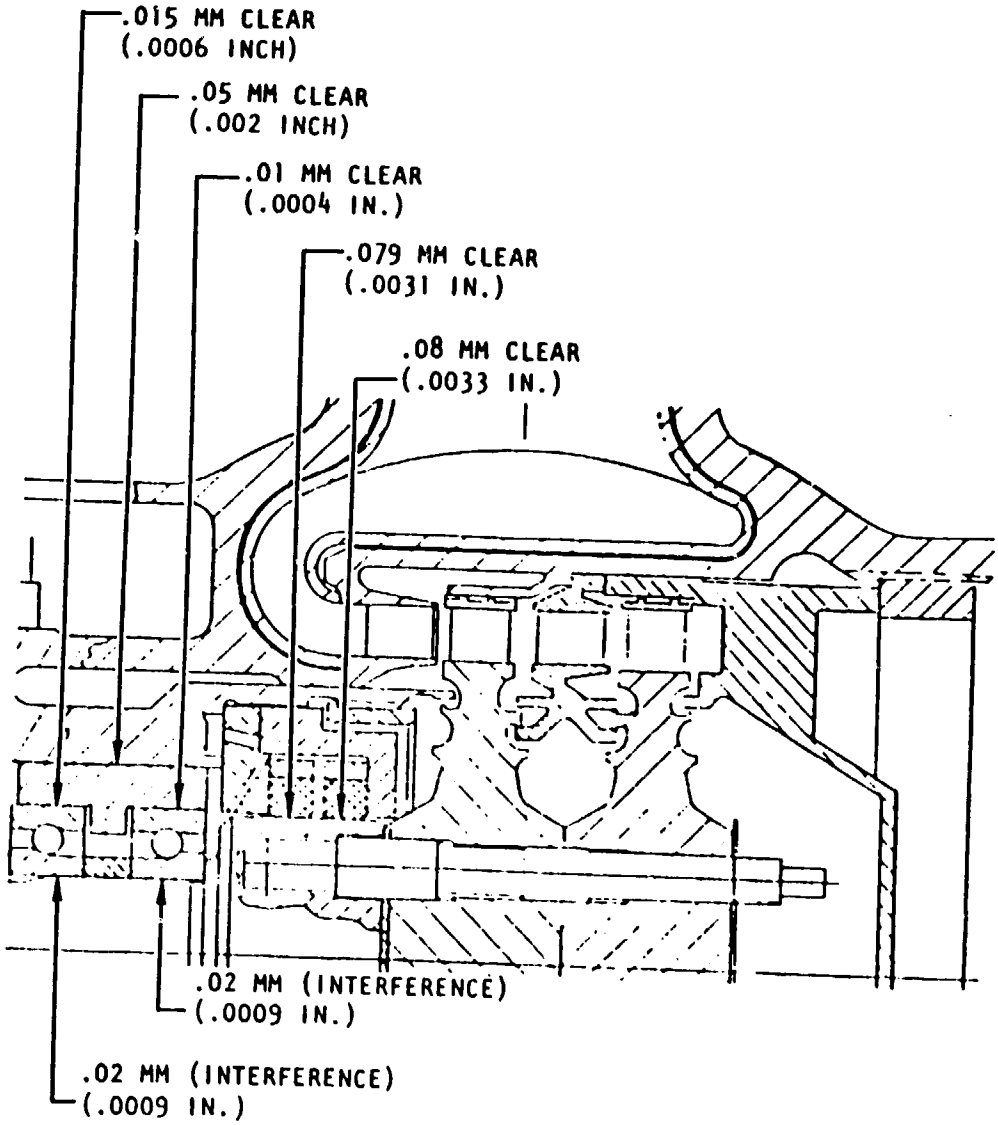

Figure 85. Turbine End Bearing and Seal Diametral Clearances

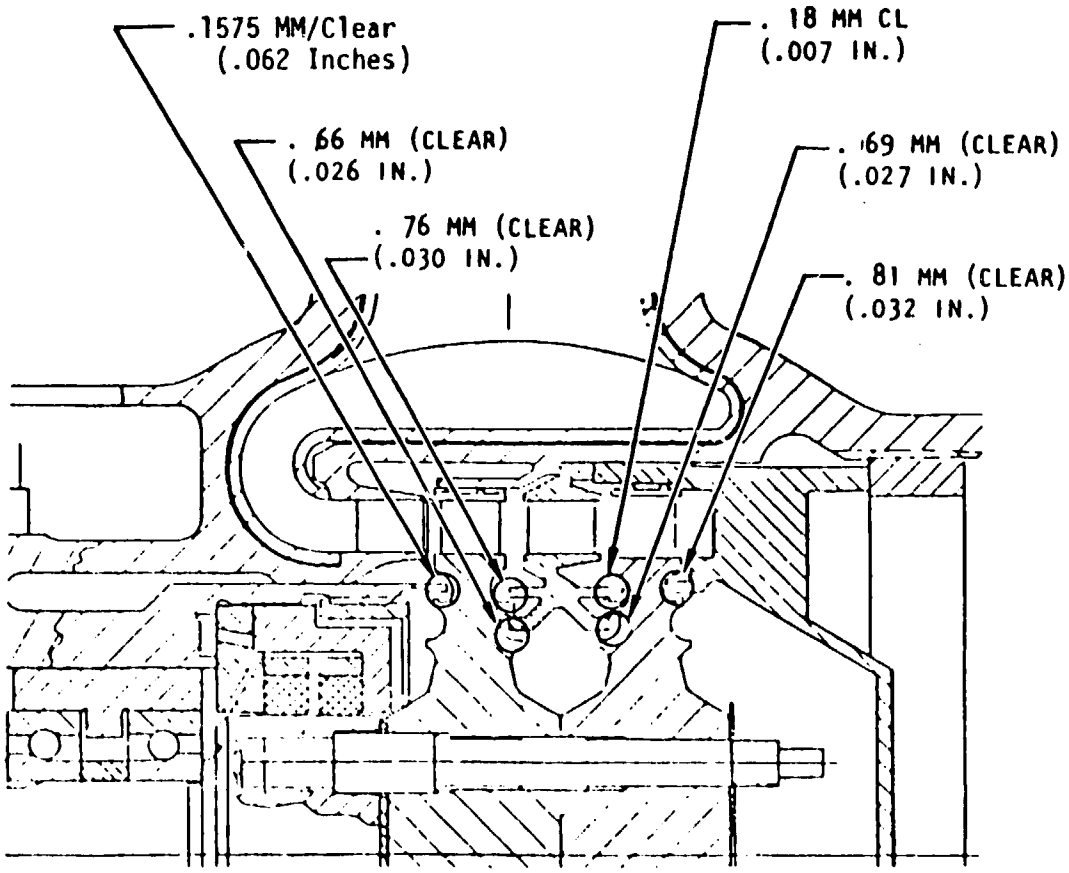

Figure 86. Turbine Diametral Clearances

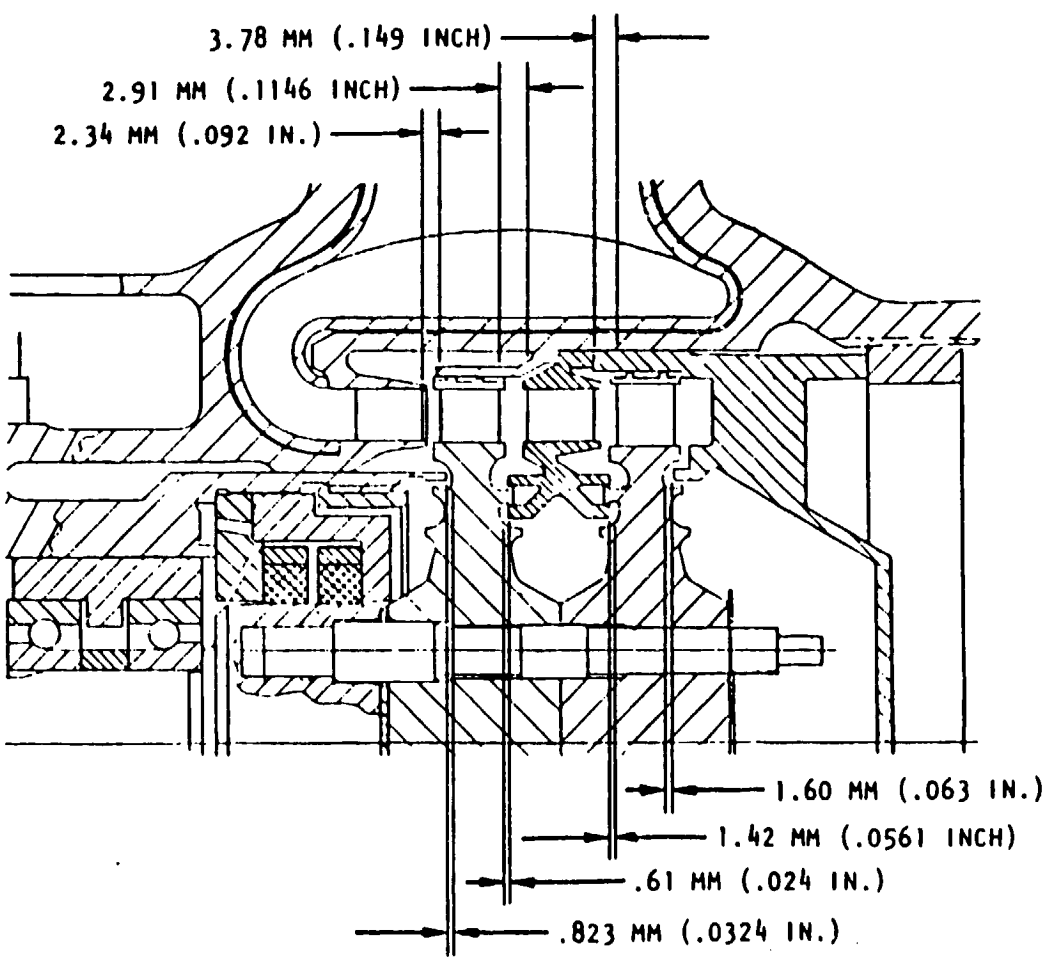

Figure 87. Turbine Axial Clearances

TABLE 13. MARK 48-F S/N 01-2 TEST SUMMARY

Date	Test No.	Duration, seconds	Objective, rad/s (rpm)	Speed rad/s (rpm)	Results
6-28-9	001	228	H-Q at 4725 (45K)	2625 and 4725 (25K, 45K)	Successful H-Q test Programmed cut
7-2-9	002	36	H-Q at 6825 (65K)	2625 and 3360 (25K, 32K)	Cut During transition by negative seal-turbine ΔP
7-2-9	003	28	H-Q at 6825 (65K)	2625 and 4725 (25K, 45K)	Cut during transition by low pump inlet pressure
7-6-9	004	34	H-Q at 6825 (65K)	2625 and 6510 (25K, 62K)	Cut due to facility leak
7-6-9	005	130	H-Q at 6825 (65K)	2625 and 6825 (25K, 65K)	Successful H-Q test Programmed cut
7-10-9	006	38	H-Q at 9947 (95K)	2625 and 9030 (25K, 86K)	Successful H-Q point speed limited by turbine gas
7-11-9	007	45	NPSH at $\frac{Q}{N}$ nominal	2625 and 8295 (25K, 79K)	Successful NPSH test cut by drop in P_D at P_S = 15.2 N/cm^2(7 psig)
7-12-9	008	52	NPSH at high $\frac{Q}{N}$	2625 and 8190 (25K, 78K)	But by turbine gas supply P_S = 29.7 N/cm^2 (28 psig)
7-13-9	009	28	NPSH at low $\frac{Q}{N}$	8610 (82K)	Cut due to discharge pressure drop
8-10-9	010	0	H-Q at 2415 and (23K) NPSH at nominal Q/N	525 (5K)	Cut during transition by Negative seal-turbine ΔP
8-11-9	011	278	H-Q at 2415 and (23K) NPSN at nominal Q/N	2415 (23K)	Successful Test. Cut by drop in P_D at P_S = 14.5 N/cm^2 (6 psig)
8-14-9	012	141	NPSH at 2415 and (23K) Low Q/N	2415 (23K)	Successful test. Cut by drop in P_D at P_S = 16.6 N/cm^2 (9 psig)
8-14-9	013	148	NPSH at 2415 and (23K) High Q/N	2415 (23K)	Successful test. Cut by drop in P_D at P_S = 13.0 N/cm^2 (3.8 psig)
8-15-9	014	71	NPSH at 8400 and (80K) Low Q/N	8190 (78K)	Successful test. Cut by drop in P_D at P_S = 13.1 N/cm^2 (4 psig)
8-16-9	015	41	NPSH at 8400 and (80K) High Q/N	8190 (78K)	Successful test. Cut by turbine drive gas limitation
8-17-9	016	5	9947 at Nominal Q/N (95K)	9450 (90K)	VSC Cutoff. Radial acceleration exceeded redline of 15 g rms
9-11-9	017	30	NPSH at 8400 and (80K) High Q/N	8400 (80K)	Successful test. Cut by turbine gas limitation
9-13-9	018	0	H-Q at 9555 (91K)	9524 (90.7K)	VSC Cutoff. Radial acceleration exceeded redline of 15 g rms. Shot bags added to detune housing
9-26-9	019	20	54 Q/N at 8505 (81K)	8610 (82K)	Turbine Overspeed Cutoff at 66% Q/N due to pump stall. Shot bags removed.

An H-Q excursion between Q/N $(Q/N)_{DES}$ = 0.822 and 1.403 was performed, and pump isentropic efficiencies of 67.7 to 70.6% were achieved. No indications of cavitation were noted. Rotor dynamic analysis indicated smooth pump operation at 2520 rad/s (24,000 rpm) and 4725 rad/s (45,000 rpm), and during transients.

Front or pump bearing coolant flowrates averaged 1.860×10^{-2} kg/s (0.0410 lb/sec) LH_2. Maximum coolant temperature rise across the pump bearing was 2 K (3 F).

Balance piston operation was smooth and as predicted.

The objective of tests 002, 003, and 004 was to obtain H-Q data at 6825 rad/s (65,000 rpm). All three tests were terminated prematurely after some period of operation at 2625 rad/s (25,000 rpm), when attempts were made to ramp to 6825 rad/s (65,000 rpm). Test 002 was cut during transition because of negative pressure differential between the shaft seal and the turbine wheel upstream cavity. This temporary condition was rectified by modifying the start rate to reduce the rate of pressure buildup in the turbine. Test 003 was cut when the pump inlet pressure dipped below redline as a result of accelerating the long column of fluid in the inlet pipe. On test 004, a speed of 6510 rad/s (62,000 rpm) was attained, but a liquid hydrogen leak in the facility system forced termination of the test.

Corrective measures were taken for the above anomalies, and on test 005 a successful H-Q sweep was accomplished between 6090 and 7035 rad/s (58,000 and 67,000 rpm). No evidence of cavitation was found over the entire operating range. On test 006, the goal was to operate at the design speed of 9947 rad/s (95,000 rpm). In actuality, a speed level of 9030 rad/s (86,000 rpm) was achieved. The lower speed level resulted from a substantially higher head produced by the axial inlet pump configuration, evidently because of the absence of cavitation and the fact that speed was limited by available turbine power.

Tests 007, 008, and 009 were conducted at nominally 8400 rad/s (80,000 rpm) with the objectives of obtaining cavitation data at nominal, high and low Q/N values. Very low NPSH values of 27.5 m, (~90 ft) were achieved at each of the three tests, but only at the nominal Q/N value (test 007) was actual cavitation realized. The results of the tests bracketed the NPSH requirement of the pump to low values over the entire operating range.

Test 010 with the objective of H-Q excursions at pump inlet pressures of 65.5 and 13.8 N/cm^2 (95 and 20 psig), followed by a NPSH evaluation from 13.8 N/cm^2 (20 psig) at nominal Q/N, was terminated in transition by the negative differential pressure between the shaft seal and turbine upstream pressure. An automatic ramp rate rather than manual speed increase was utilized for the first time. Corrective measures were undertaken and test 011, with the identical objectives as test 010, was then successfully conducted. No cavitation was experienced down to a pump inlet pressure of 4.14 N/cm^2 (6 psig) at cutoff.

Tests 012 and 013 were conducted successfully, which demonstrated NPSH characteristics at 2415 rad/s (23,000 rpm) for low and high Q/N. No cavitation was experienced at low Q/N down to a pump inlet pressure of 6.2 N/cm^2 (9 psig) nor was cavitation noted at high Q/N down to 2.61 N/cm^2 (3.8 psig) pump inlet pressure.

The objective of test 014 was NPSH at 8400 rad/s (80,000 rpm) and low Q/N. The test was successful and no cavitation was experienced down to a pump inlet pressure of 2.75 N/cm^2 (4 psig). Actual speed was 8190 rad/s (78,000 rpm).

Test 015 was cut off during NPSH testing at high Q/N at 8190 rad/s (78,000 rpm) due to turbine drive-gas limitations. The test was successful and no cavitation was experienced.

The objective of test 016 was to obtain data at 9947 rad/s (95,000 rpm) at nominal Q/N. The test was terminated at 9450 rad/s (90,000 rpm) by the two radial accelerometers exceeding the 15 g rms redline. High-frequency data are analyzed in another section of this report. No hardware damage resulted, and examination of the pump end bearings detected no problems or wear.

Test 017 was to determine NPSH characteristics at 8400 rad/s (80,000 rpm) and high Q/N. The test was terminated by the turbine drive-gas limitations.

Shot bags were added to the turbopump housing in an attempt to detune the resonance previously noted on test 016 at 9450 rad/s (90,000 rpm). Test 018 was conducted with the objective of an H-Q excursion at 9555 rad/s (91,000 rpm). The test was terminated by the VSC at 9524 rad/s (90,700 rpm) by the radial accelerometers exceeding the 15 g rms level. The shot bags increased the resonance level, but not as much as anticipated.

Test 019 was conducted to attempt a 54% operating point at 8505 rad/s (81,000 rpm). This data point corresponds to a 10K thrust expander cycle operating point. The test was terminated at 66% Q/N by the turbine overspeed cutoff device when the pump stalled and fluid boiled out of the turbopump. No apparent hardware damage was sustained as a result of the test. Preliminary data analysis revealed no anomalies. Turbopump speed after the overspeed cutoff reached approximately 11550 rad/s (110,000 rpm), which is the highest rotor speed attained by the Mask 48-F turbopump.

The mechanical operation of the turbopump was excellent on all tests. Accelerometer data indicated good rotor balance and smooth operation on all tests except for the high resonance at 9450 to 9660 rad/s (90,000 to 92,000 rpm) on tests 016 and 018.

Pump Hydrodynamic Performance

A discussion of the pump hydrodynamic performance observed in the turbopump test data is presented.

Head and Efficiency. The pump pressure rise is shown as a function of the discharge flow in Fig. 88. Representative data points are shown at speeds of 4712, 6282, 7853, and 9947 rad/s (45,000, 60,000, 75,000, and 95,000 rpm). For comparison, the predicted pressure rise for each of these speeds is also shown over a broad flow range. The predicted performance curve is based upon predictions before adding the axial inlet and inducer. The inducer stage adds additional pressure rise of a magnitude of approximately 55.2 N/cm^2 (80 psi) at design flow and 9947 rad/s (95,000 rpm). As can be seen from the figure, the head rise at all four speeds exceeds the prediction over the entire flow range. At 7853 and 9947 rad/s (75,000 and 95,000 rpm) pressure rise exceeds the predicted by 11% at the design flow coefficient. At the two lower speeds, the slope of the measured head-flow characteristic is nearly identical to the prediction; however, the data indicate a trend toward a somewhat steeper head-flow relationship at 6853 rad/s (75,000 rpm). The data points at 9947 rad/s (95,000 rpm) show a higher pressure rise than predicted. There were several data points measured during test -006 at this speed; however, the measurements were taken at a constant flow-rate, and all the points fell on top of one another. Therefore, only one point at the highest speed for test -006 is shown on the graph. The other points are from test -016 and -018 just before cutoff. The large improvement in performance observed at 9947 rad/s (95,000 rpm) is attributed to the axial inlet and inducer design and its effect on eliminating the former existing cavitation problem.

Using the pump inlet and discharge pressures and temperatures, the pump isentropic efficiency can be calculated. This isentropic efficiency is very sensitive to the temperature differential across the pump; therefore, at the higher speeds with corresponding higher temperature differentials, the accuracy of the temperature measurement is not as critical and a more accurate efficiency can be determined. For example, near 9423 rad/s (90,000 rpm), the temperature differential across the pump is 28 to 33 K (50 to 60 F) but, at 4712 rad/s (45,000 rpm), it is only approximately 8 K (12 F).

The efficiency is expected to vary with Q/N (where Q equals pump flow in gpm, and N is pump speed in rpm) and, due to the thermodynamic characteristics of the hydrogen, will vary with speed. These effects are seen in Fig. 89, which shows the isentropic efficiency versus pump flow at four different test speeds scaled to 9947 rad/s (95,000 rpm). The predicted efficiency-flow characteristic is also shown on the figure. Measured efficiencies are higher than predicted and considered to be very good for the size and complexity of this pump. The flow data cover a fairly wide range, and the shape of the test data curves agree very well with the predicted curve at both the high- and low-flow conditions. With these curves, the data indicate that the peak efficiency occurs at a somewhat higher flow than design point, but very near the peak of the predicted curve.

Numerous internal pressure measurements were made at different points through the pump. These internal pressures are, of course, most useful as diagnostic information to uncover the source of performance deficiencies, but no significant performance deficiencies were uncovered in the present test effort. With these internal pressures, a comparison with predicted internal pressures is possible to indicate the consistency of the prediction at intermediate steps.

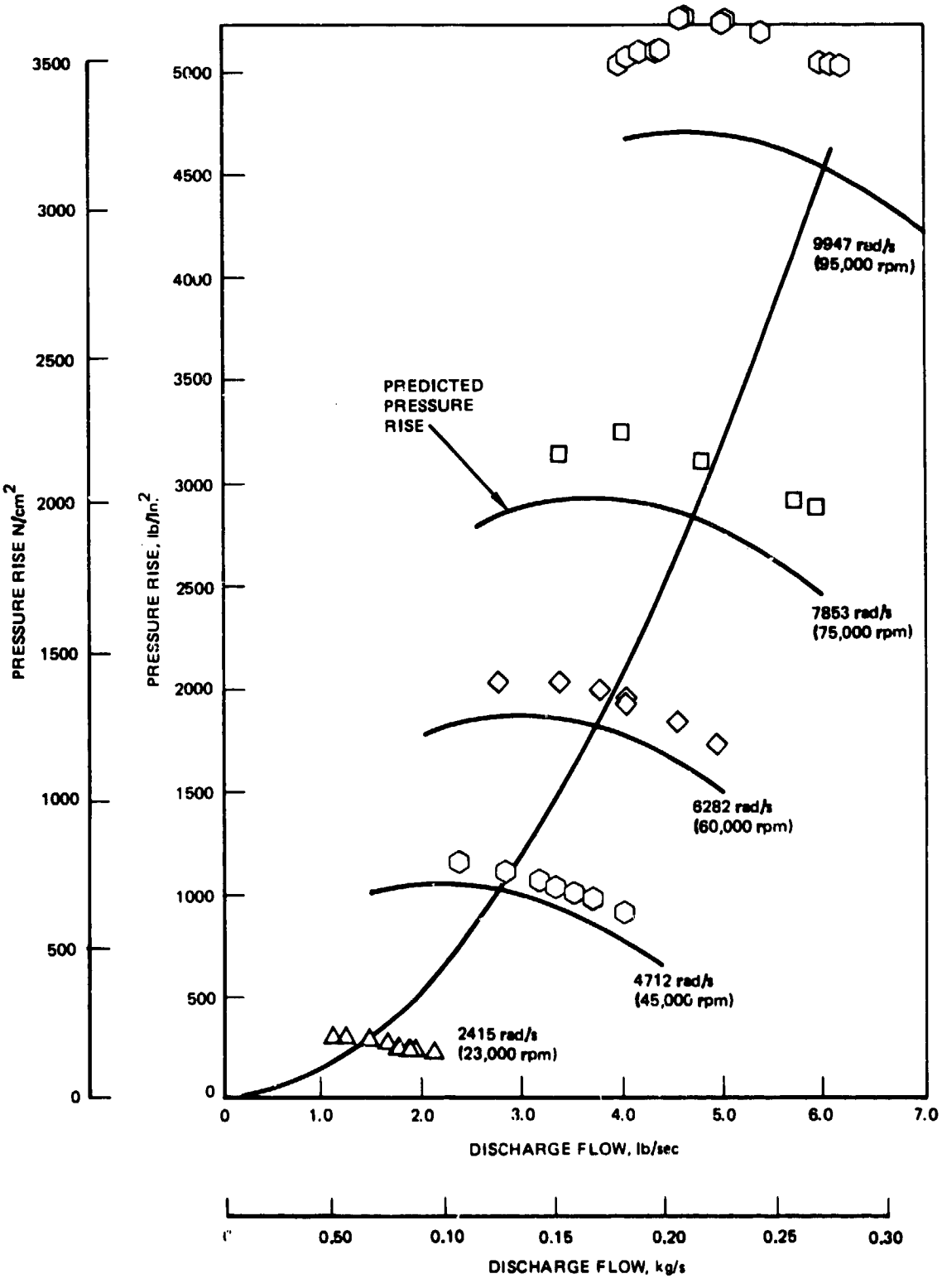

Figure 88. Pump Scaled Performance (Test 001 to 019, 1979)

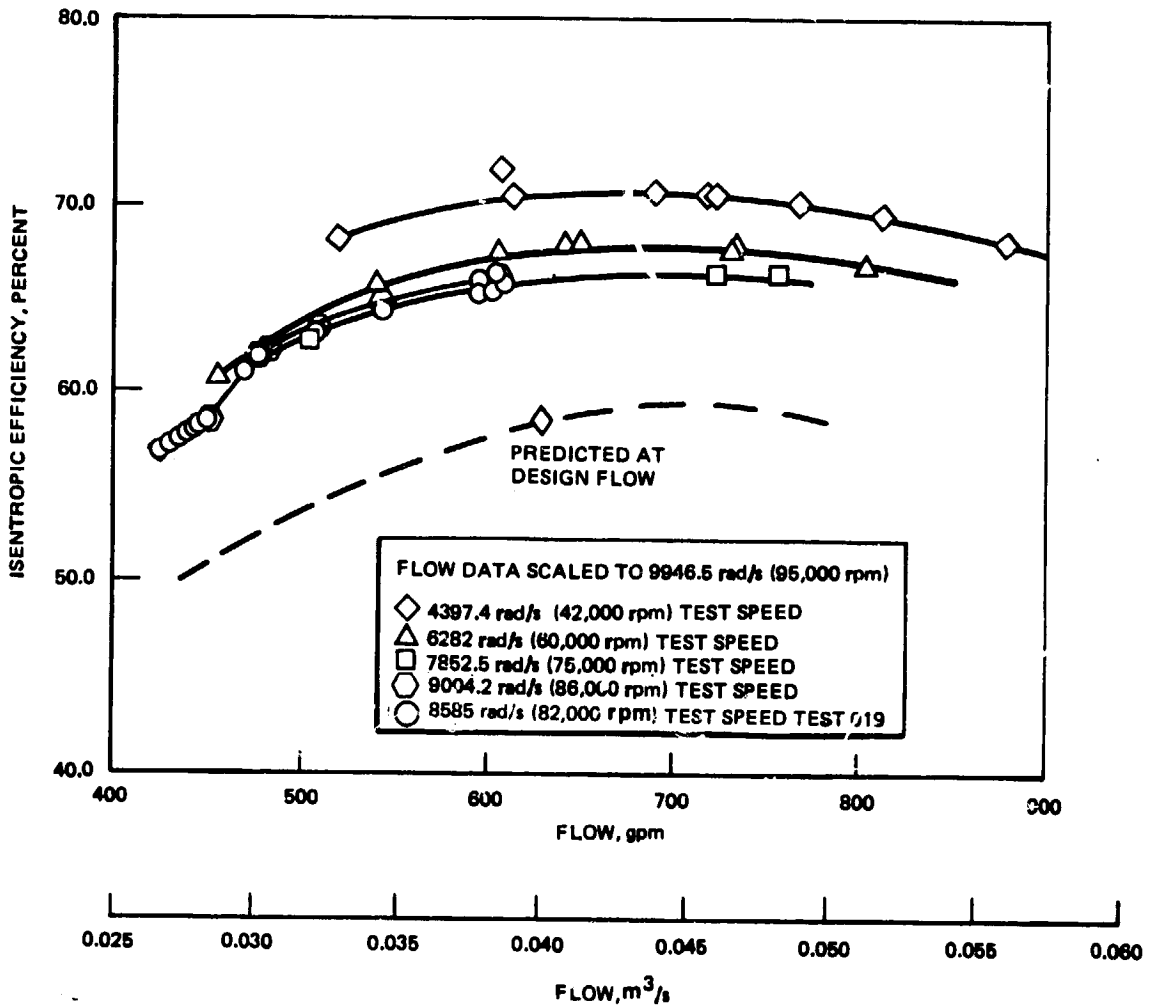

Figure 89. Mark 48-F Turbopump Efficiency

Having met the overall pump performance prediction, it was expected that the intermediate pressures would also be met. This is seen to be the case from Fig. 90 and 91 , which compare predicted and test pressures at several stations and at two different speeds. The actual test values are shown by symbols and are arbitrarily connected by straight lines. This does not necessarily imply that the pressure varies linearly with distance. For the predicted values, the actual measured inlet and bearing coolant temperatures were used as a starting point.

At the speed of 6125 rad/s (58,500 rpm) (Fig. 90), the measured values are somewhat higher than the predicted values through the first-stage impeller and diffuser, and the measured data exceed the predicted values by an even greater margin in the second diffuser. At 9423 rad/s (90,000 rpm) (Fig. 91), the measured and predicted values are fairly close at each point through the first-stage, with the measured data showing better pressure recovery through the second stage radial diffuser than was predicted. The good performance in the first stage, shown by the measured data at both speeds, is indicative of good suction performance. Any potential cavitation problems have been eliminated with the design of an axial inlet and inducer configuration. It should be kept in mind that these measured pressures are local static pressure and may not be truly representative of the average static pressure across the station, and that this local value could easily vary from a true average at changing speeds and flows. In general, the overall agreement between measured and predicted values is considered to be very good. Figure 92 shows the variation of the internal pressures versus flowrate for test -005 scaled to 9947 rad/s (95,000 rpm).

Suction Performance. Two tests were run at 8295 rad/s (79,000 rpm) in which the pump inlet static pressure was reduced to the vapor pressure with two-phase flow at the pump inlet. The ratio of flow to design flow was 0.70 and 0.95 on the two tests. Maximum recorded liquid-phase suction specific speed was 39.42 rad/s $(m^3/s)^{\frac{1}{2}}$ $(J/kg)^4$ (108,000 rpm $gpm^{\frac{1}{2}}/ft^{3/4}$), and minimum NPSH was 13.1 meters (43 feet) as shown in Fig. 93. Pump inlet static pressure is shown versus pump pressure rise in Fig. 94 , indicating significant head falloff did not occur until there was two-phase flow at the inlet. Figure 95 shows NPSH versus pump pressure rise with the two-phase inlet test points plotted at zero NPSH for indication. With two-phase flow at the inlet, the fluid quality must be known to determine density, inlet velocity head, and NPSH.

Idle-Mode Test Results. Three tests were run at the idle-mode speed of 2415 rad/s (23,000 rpm). Pressure rise versus flowrate is shown in Fig. 96. Flowrate range was from 0.359 to 0.972 kg/s (0.79 to 2.14 lb/sec) at an NPSH of 128 meters (420 feet) and above. The pressure rise slope is flat from 0.363 to 0.545 kg/s (0.8 to 1.2 lb/sec) flowrate. The pressure rise at lower NPSH is essentially the same as at higher NPSH. Pump isentropic efficiency could not be determined accurately at 2415 rad/s (23,000 rpm) due to the low pump temperature rise of about 1.7 K (3 F).

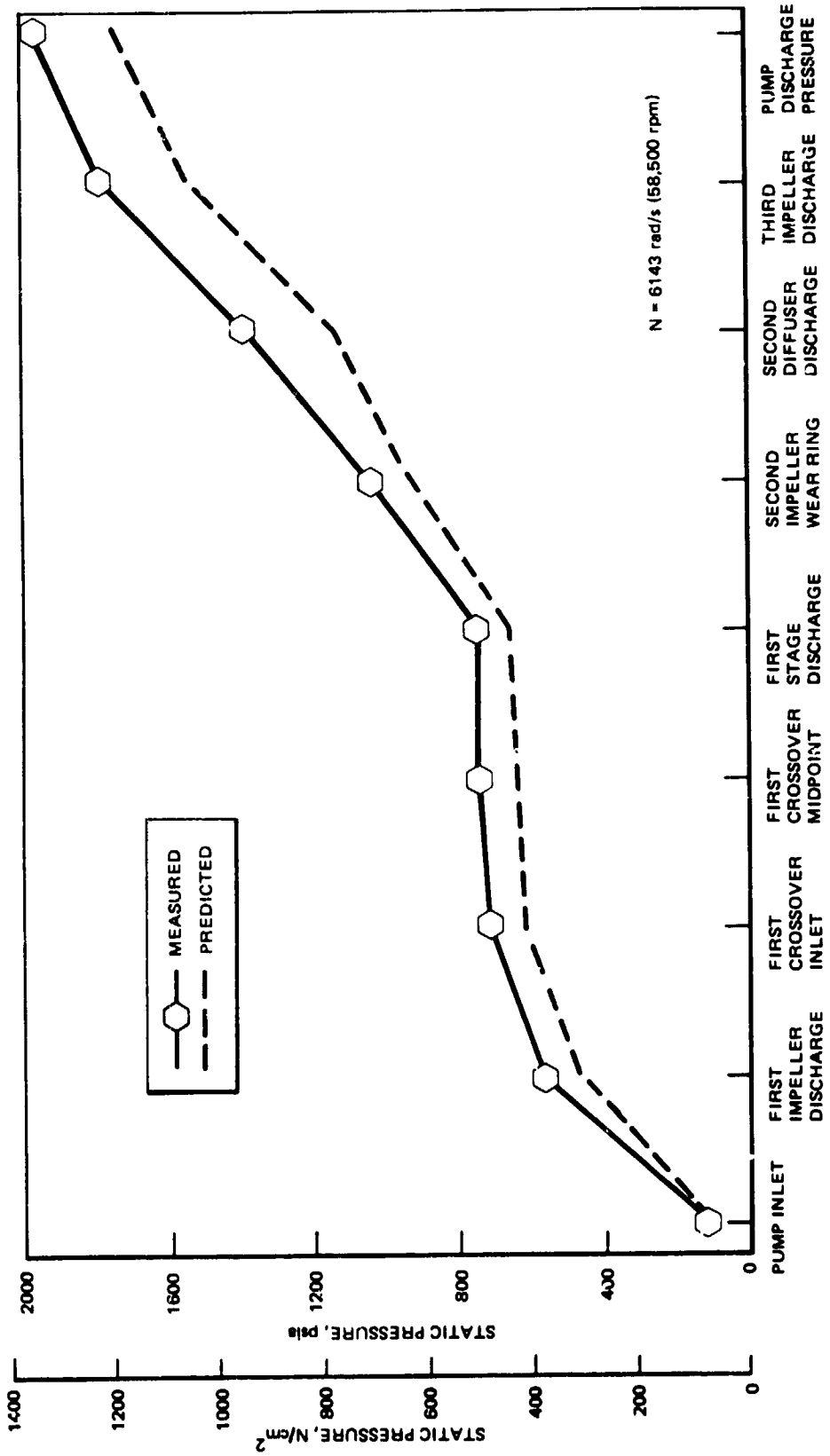

Figure 90. Static Pressure Rise Through Pump (Test 5)

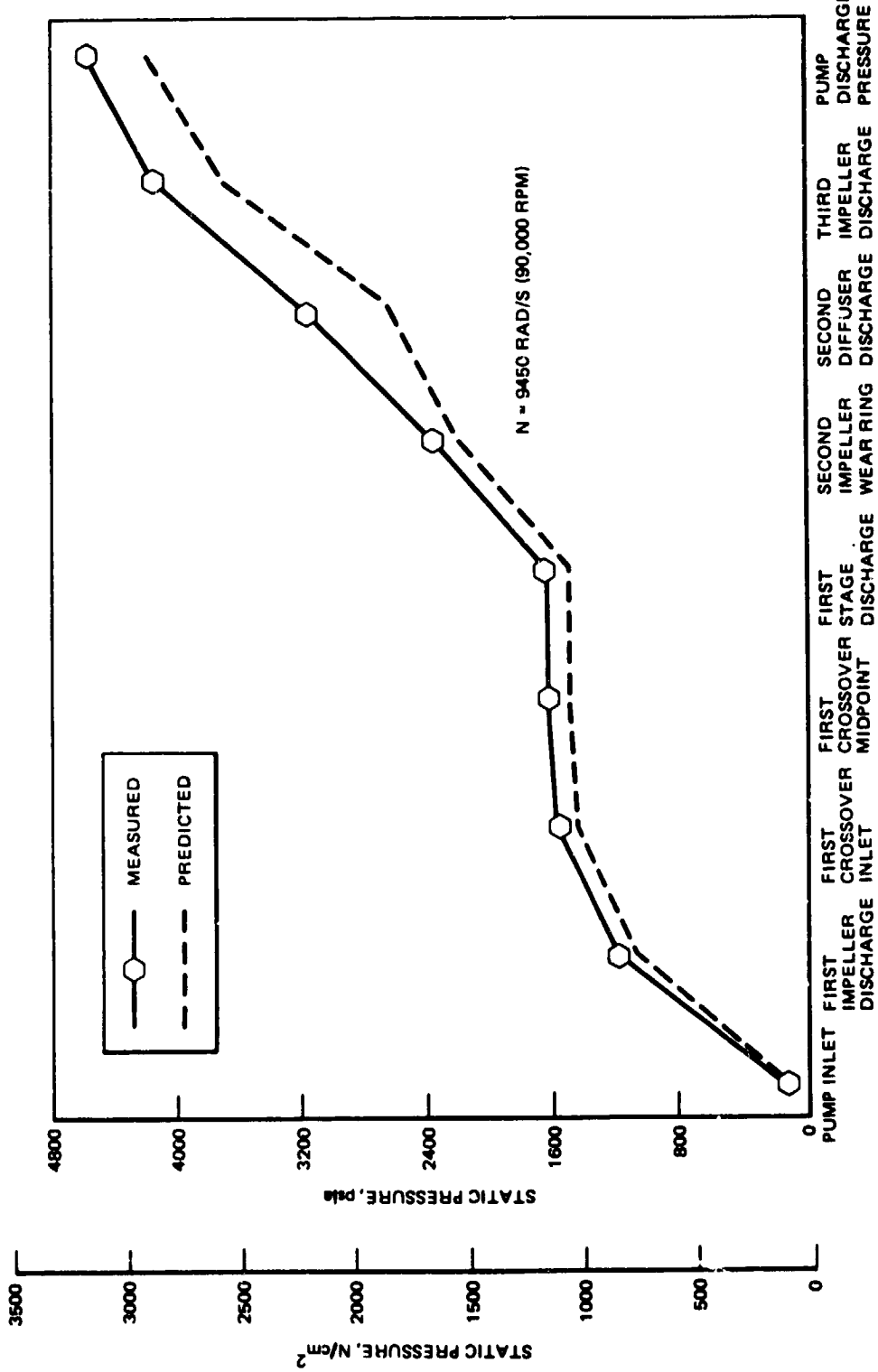

Figure 91. Static Pressure Rise Through Pump (Test 7)

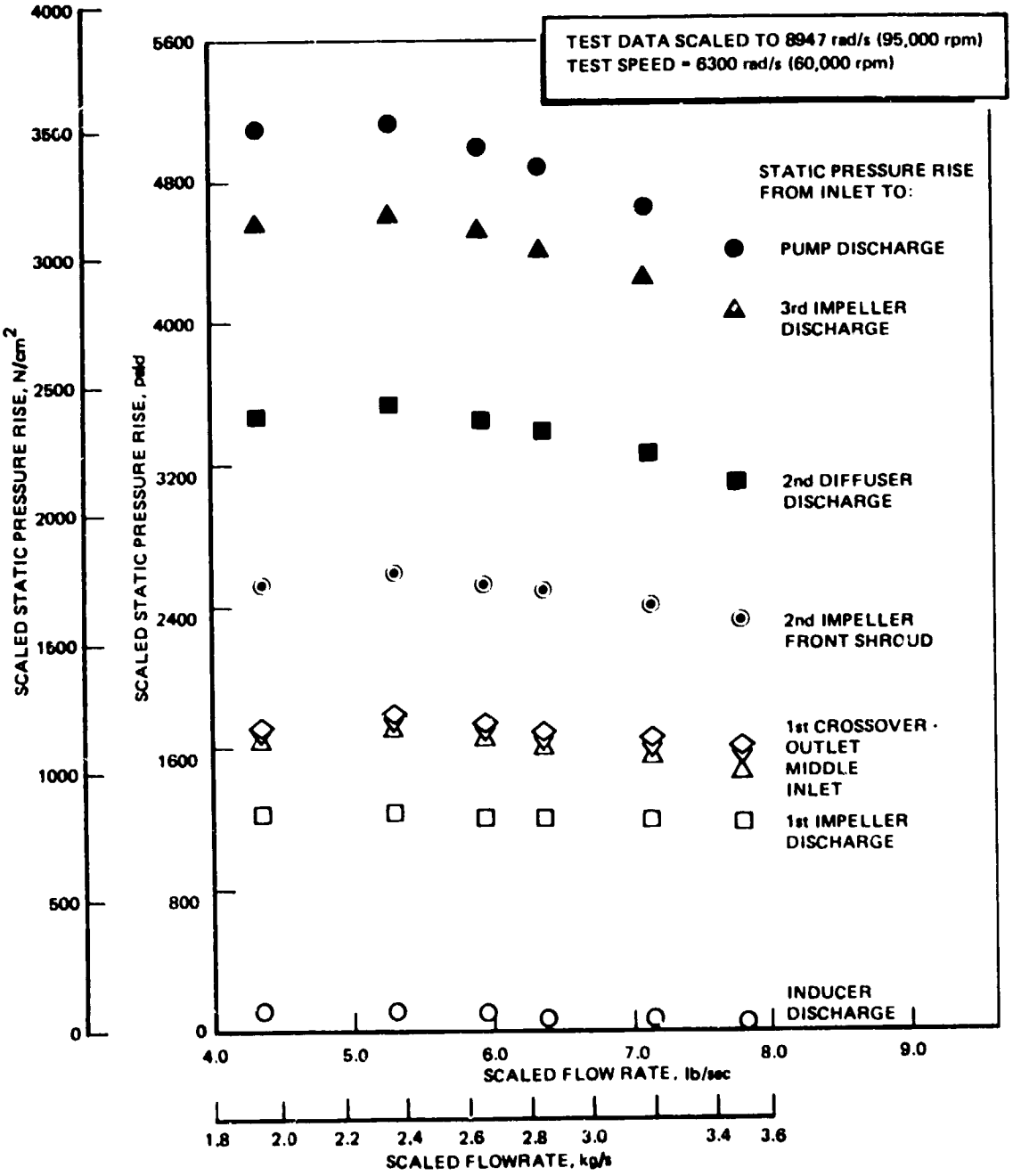

Figure 92. Scaled Static Pressure Rise in Pump Test 5 to 9947 rad/s (95000 rpm)

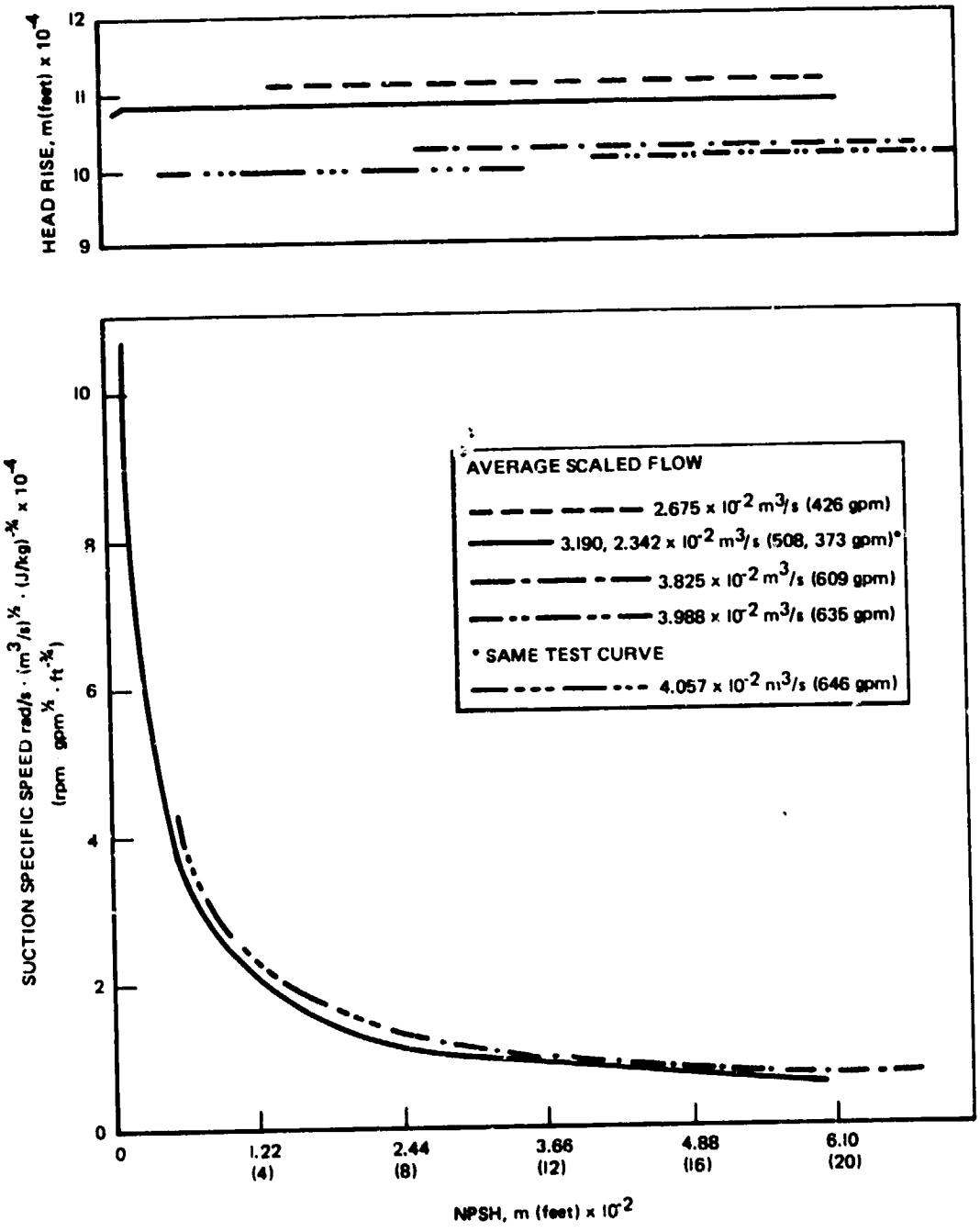

Figure 93. Pump Suction Specific Speed (Tests 7 through 17)

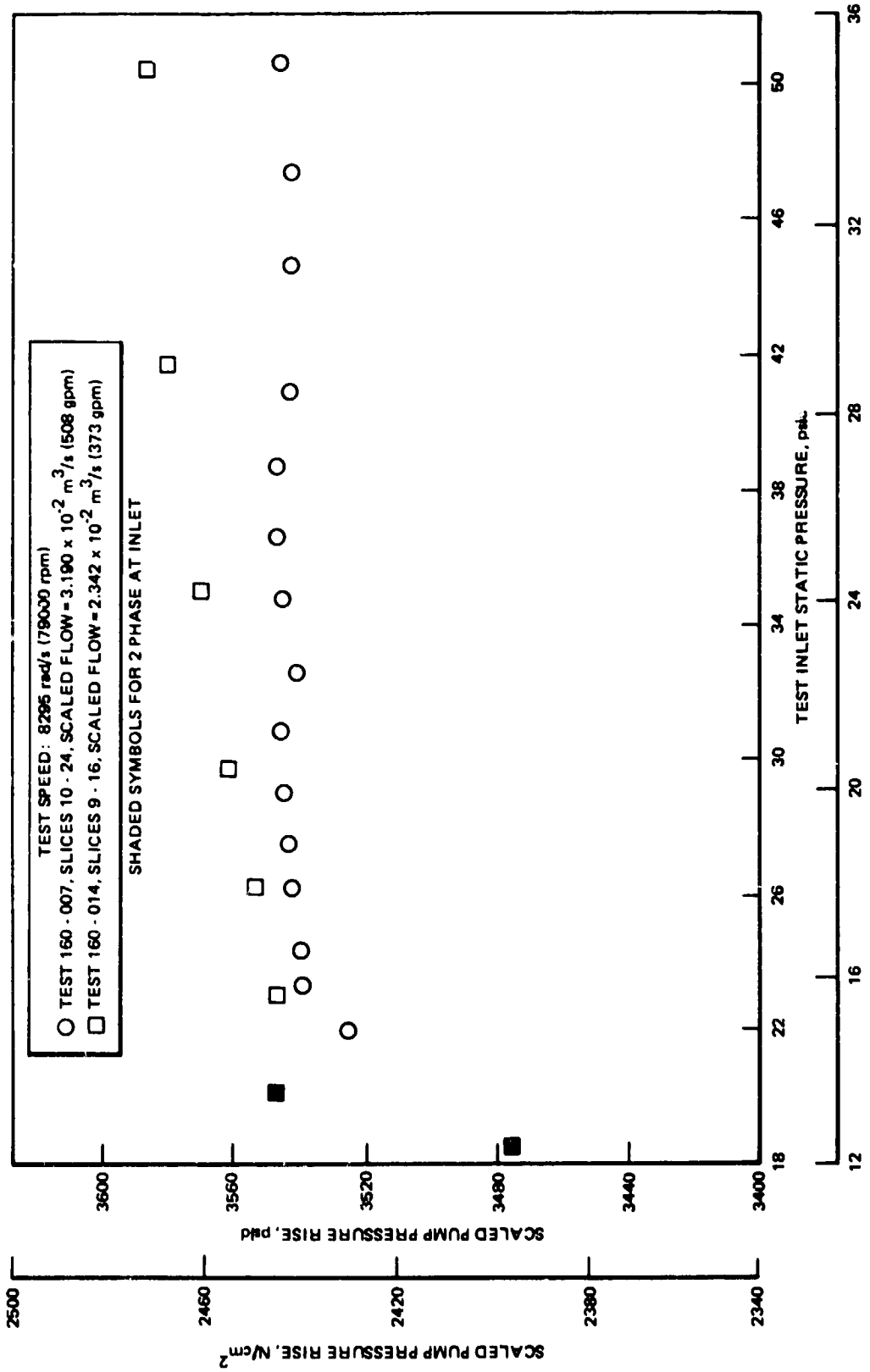

Figure 94. Pump Pressure Rise Versus Inlet Static Pressure

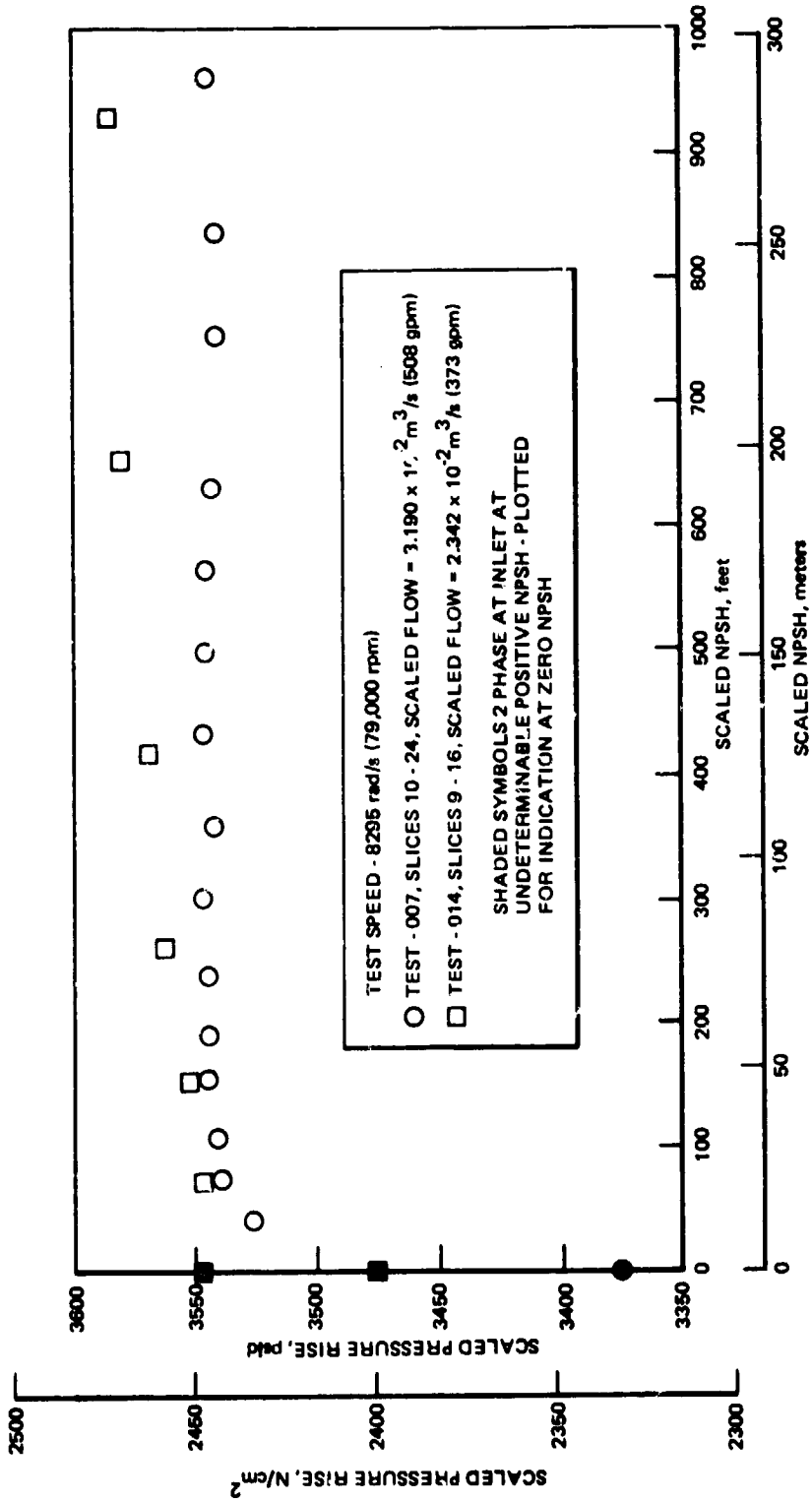

Figure 95. Pump Pressure Rise Versus NPSH

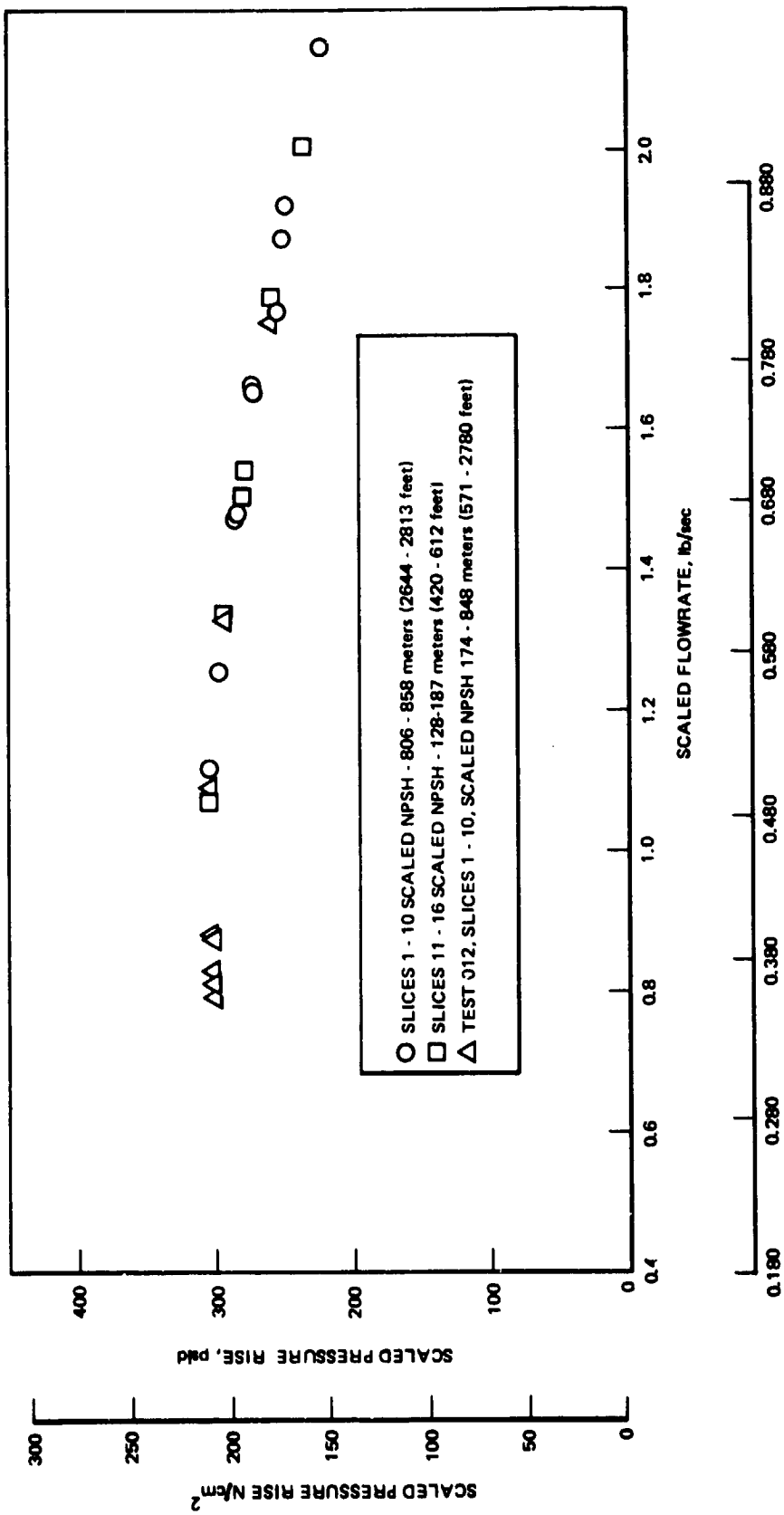

Figure 96. Pump Head-Flow Performance

Suction performance tests showed no pressure rise falloff down to where pump inlet static pressure equalled the vapor pressure. Figure 97 shows pressure rise versus NPSH. Shaded points have two-phase flow at the inlet. NPSH could not be determined for the shaded points because fluid quality and density are not known. Density is required to determine inlet velocity head for NPSH. Figure 98 shows pump pressure rise versus pump inlet static pressure. No pressure falloff is shown for some points at lower inlet pressures than when the vapor pressure first occurred. Figure 99 shows that discharge flow did not decrease until after pressure falloff occurred.

Balance Piston Performance. In all of the tests, the balance piston appeared to be functioning to achieve a good axial thrust balance. Internal pressures were available at the third impeller discharge, within the balance cavity and at the balance piston sump. The pressure within the balance cavity would be expected to have a magnitude between the other two pressures. Observation of the data indicated that the balance cavity pressure also seemed to maintain a relatively constant position between the other two, indicating a very stable operation through all of the tested points of operation. Selected data slices are presented in Fig. 100 to illustrate this. The balance piston position was between 23 and 26% of the balance piston travel from where the high-pressure orifice was closed for all slices analyzed. This is shown in Fig. 101 through 108 which present the balance piston parameters and indicated point of operation over a wide speed range.

Pump Stall Characteristics

The data obtained in test 019 is of particular value in that it defined the low specific speed limits of the Mark 48-F turbopump from the standpoint of stall and fluid boilout. Consequently, test 019 warrants a detailed examination, which is presented below.

Test 019 was planned to be a head-flow excursion at a constant speed of 8587 rad/s (82,000 rpm) from design flow coefficient to 54% of the design flow coefficient. At 73% of the design flow coefficient, the pump head rise dropped 3.2%, and the head-flow slope changed from negative to positive with test time and decreasing flow. At 67% of the design flow coefficient, pump discharge flow and pressure dropped sharply, unloading the pump at full turbine power, and causing an overspeed cutoff. Maximum pump speed at the cutoff was 11414 rad/s (109,000 rpm). Analysis of stage and diffuser pressure indicated the shift at 73% of design flow coefficient was the result of a performance change in the first-stage diffuser reducing pressure recovery across the diffuser. A review of earlier tests with flow coefficients near 70% of design showed the shifted, reduced head operating point was stable, repeatable, and independent of speed and pump inlet pressure.

Observations from the CRT plots at the overspeed cutoff indicated pressures upstream of the first-stage diffuser had increasing pressure spikes responding to the flowrate drop and speed increase with some liquid in the rotating elements. Pressures downstream of the first-stage diffuser showed a sharp dropoff which indicated low density, vaporized hydrogen in the second- and third-stage rotating elements.

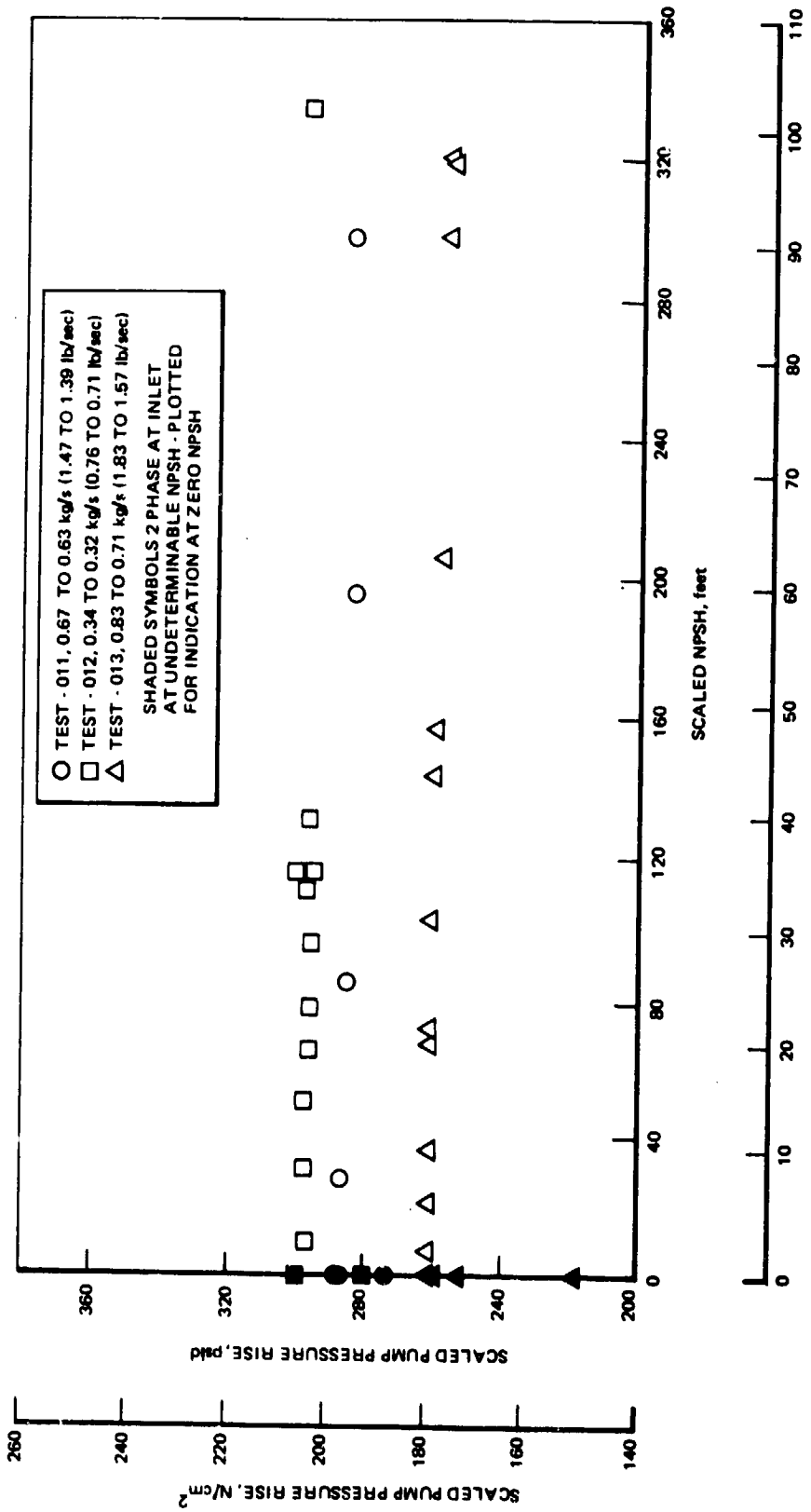

Figure 97. Pump Suction Performance (Test 11 through 13)

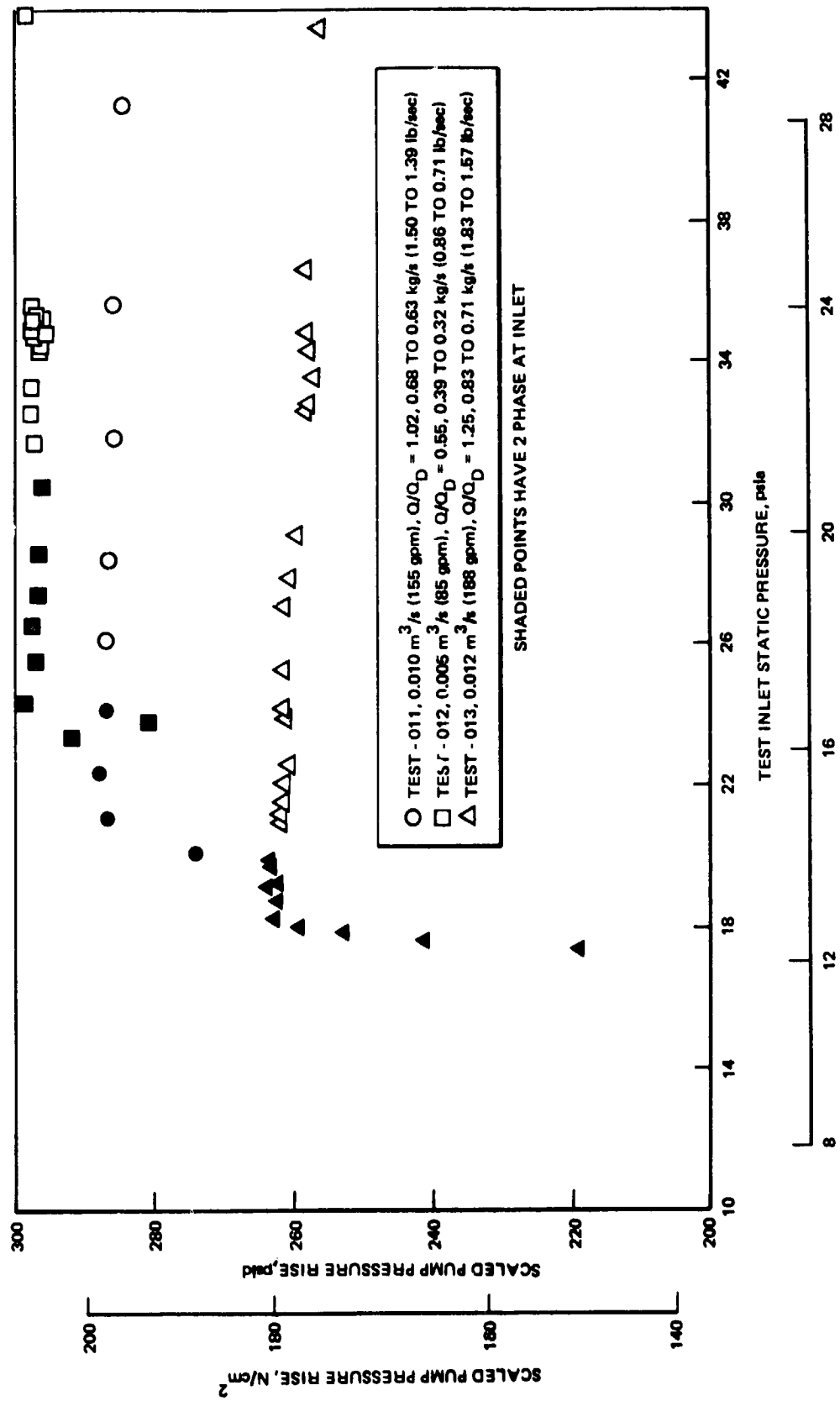

Figure 98. Pump Suction Performance (Test 11 through 13)

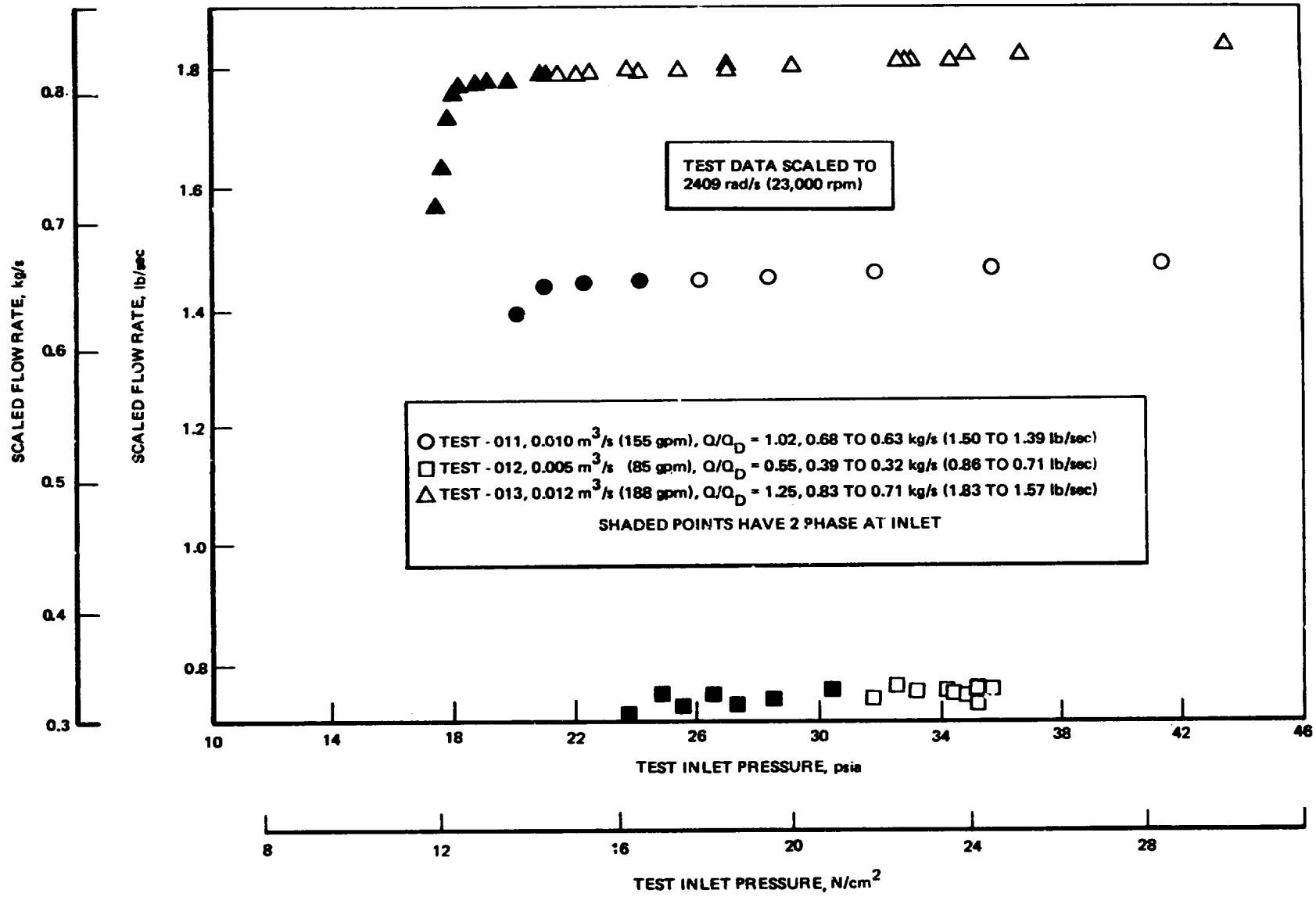

Figure 99. Pump Flow vs Inlet Pressure (Test 11 Through 13)

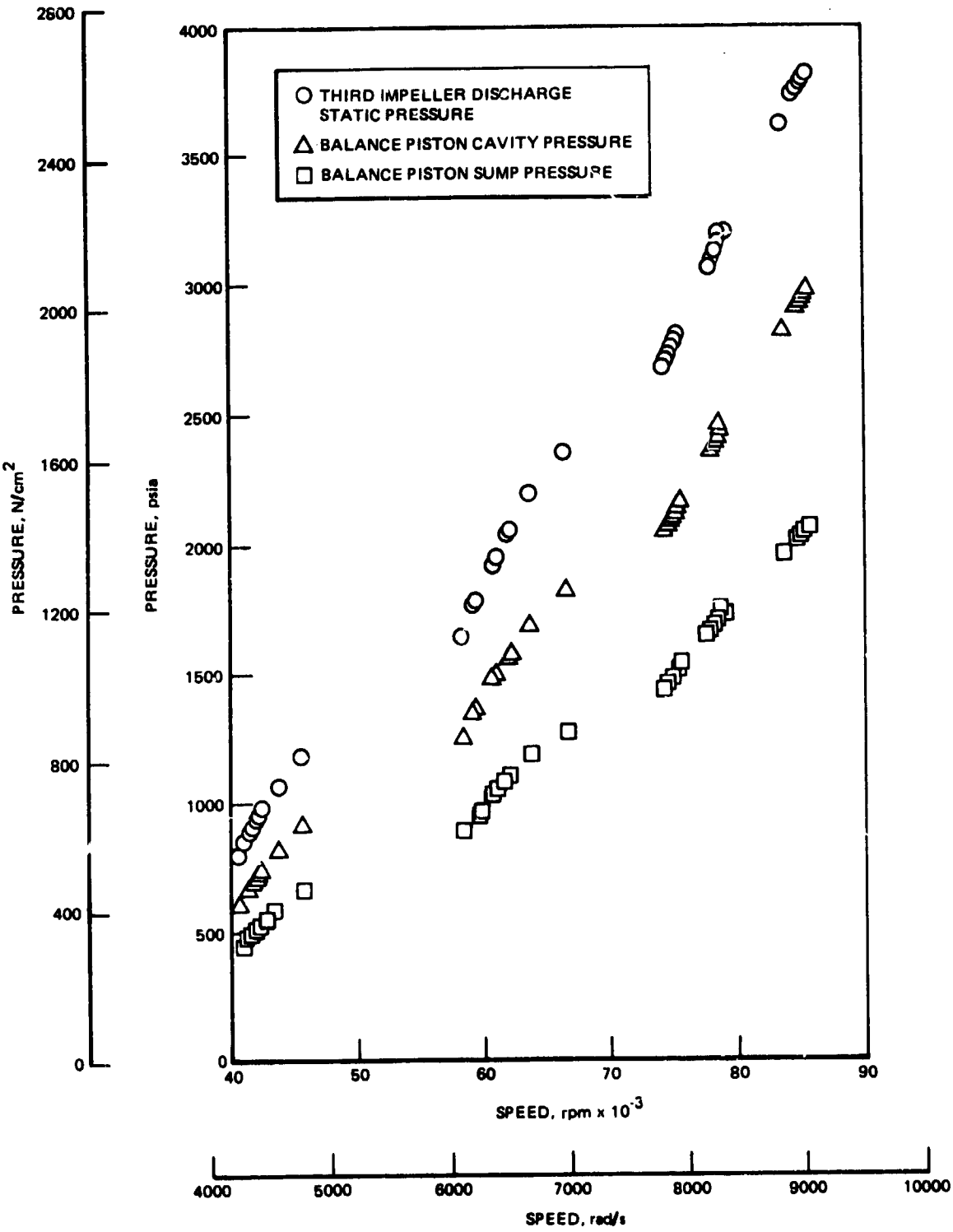

Figure 100. Balance Piston Pressures

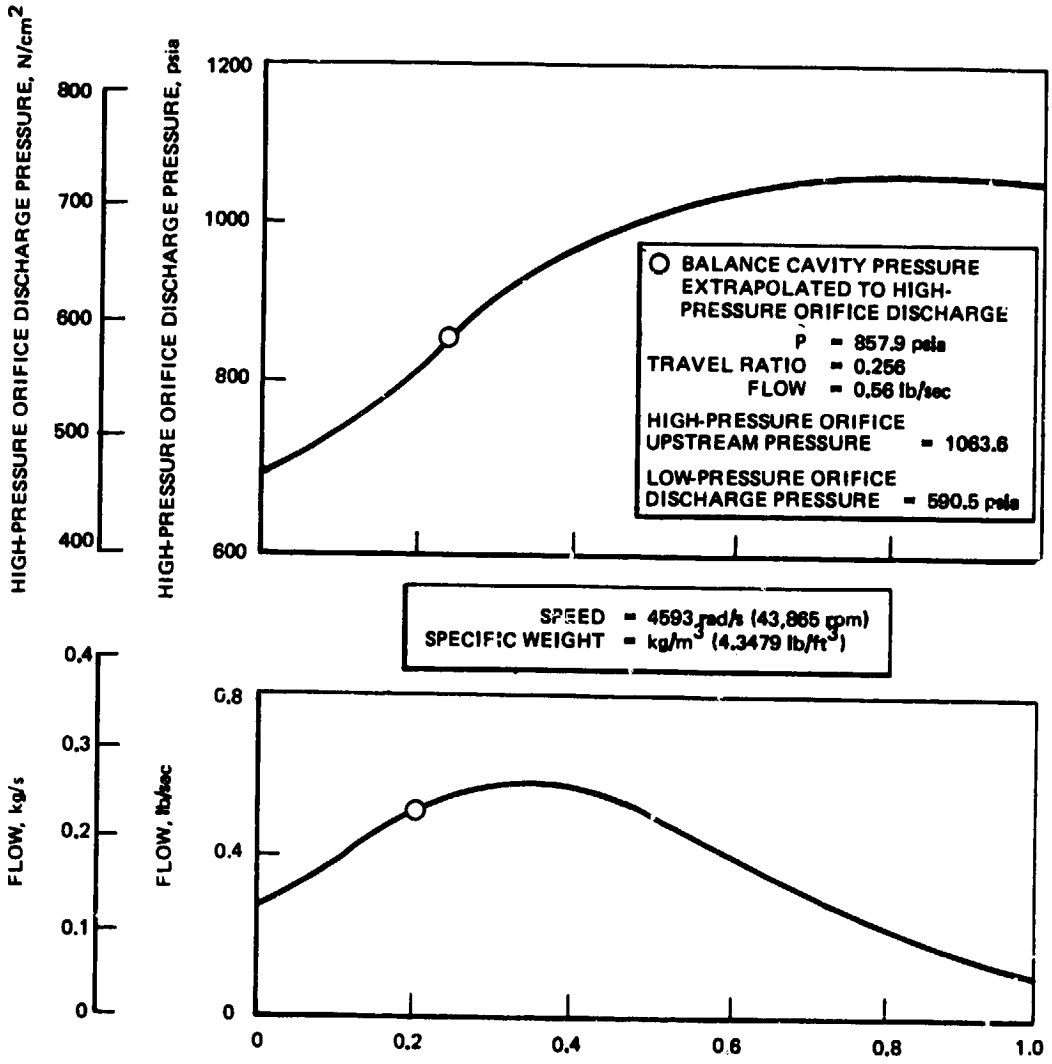

Figure 101. Balance Piston Performance (Test 1, Slice 7)

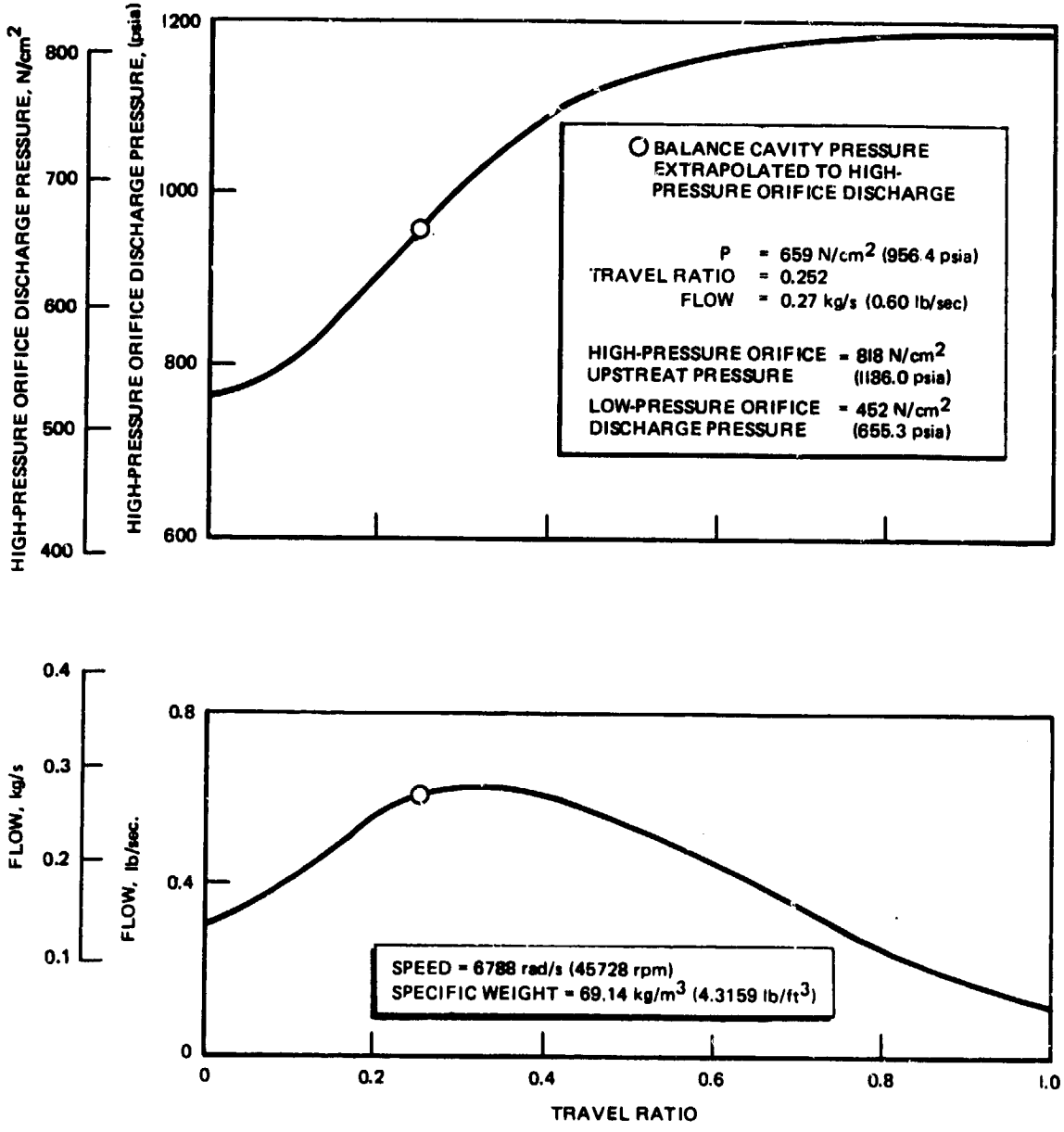

Figure 102. Balance Piston Performance (Test 1, Slice 6)

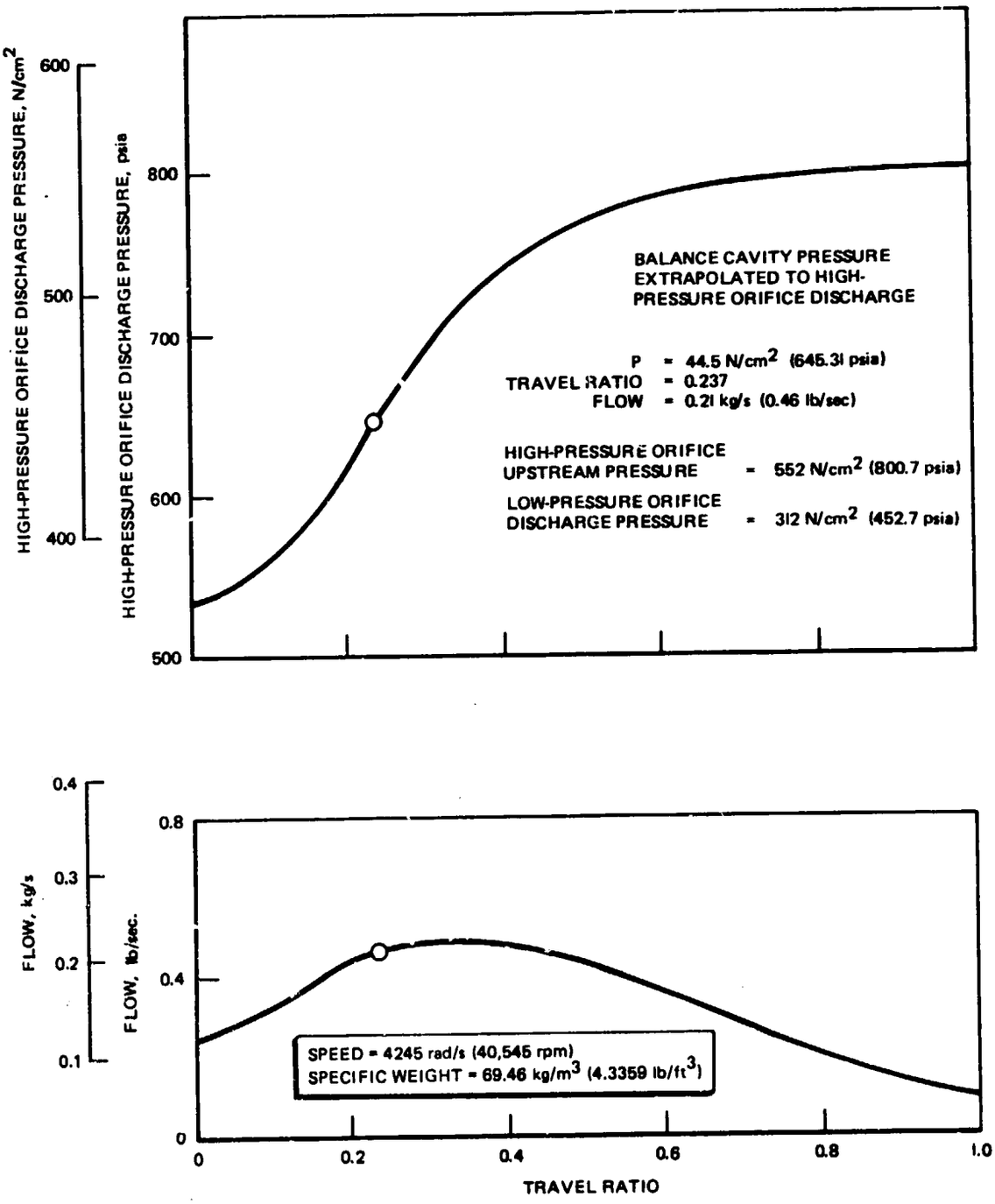

Figure 103. Balance Piston Performance (Test 1, Slice 10)

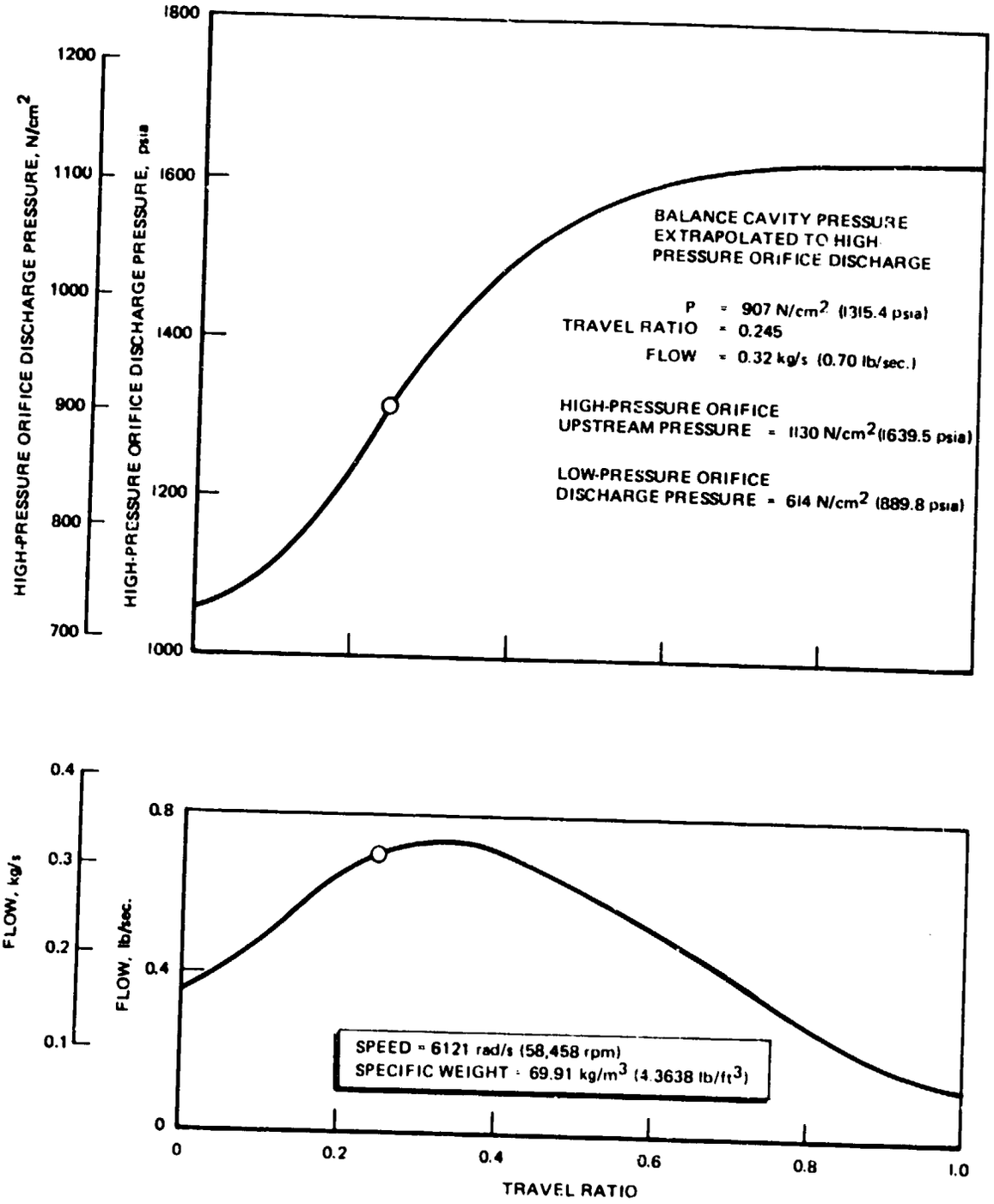

Figure 104. Balance Piston Performance (Test 5, Slice 10)

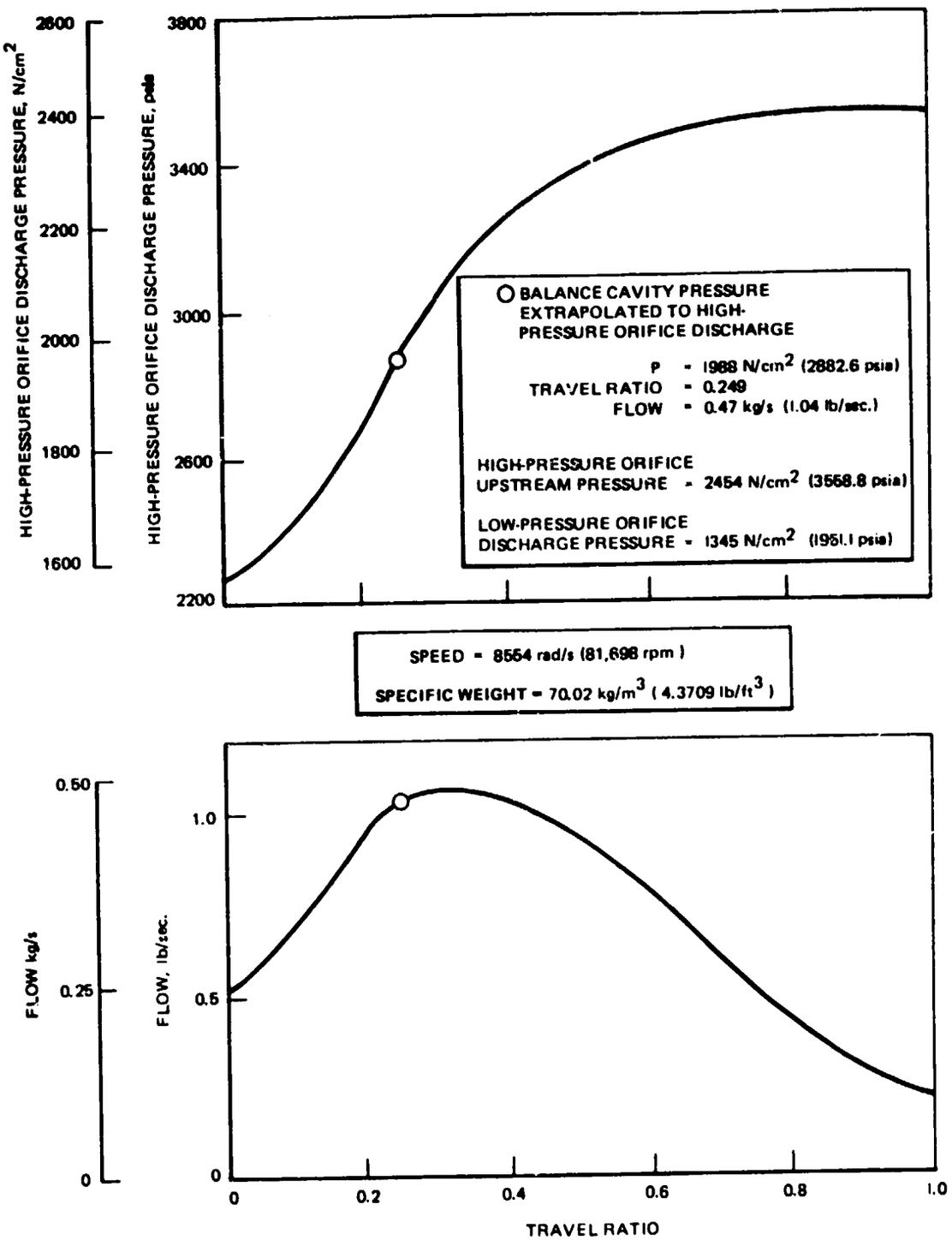

Figure 105. Balance Piston Performance (Test 9, Slice 2)

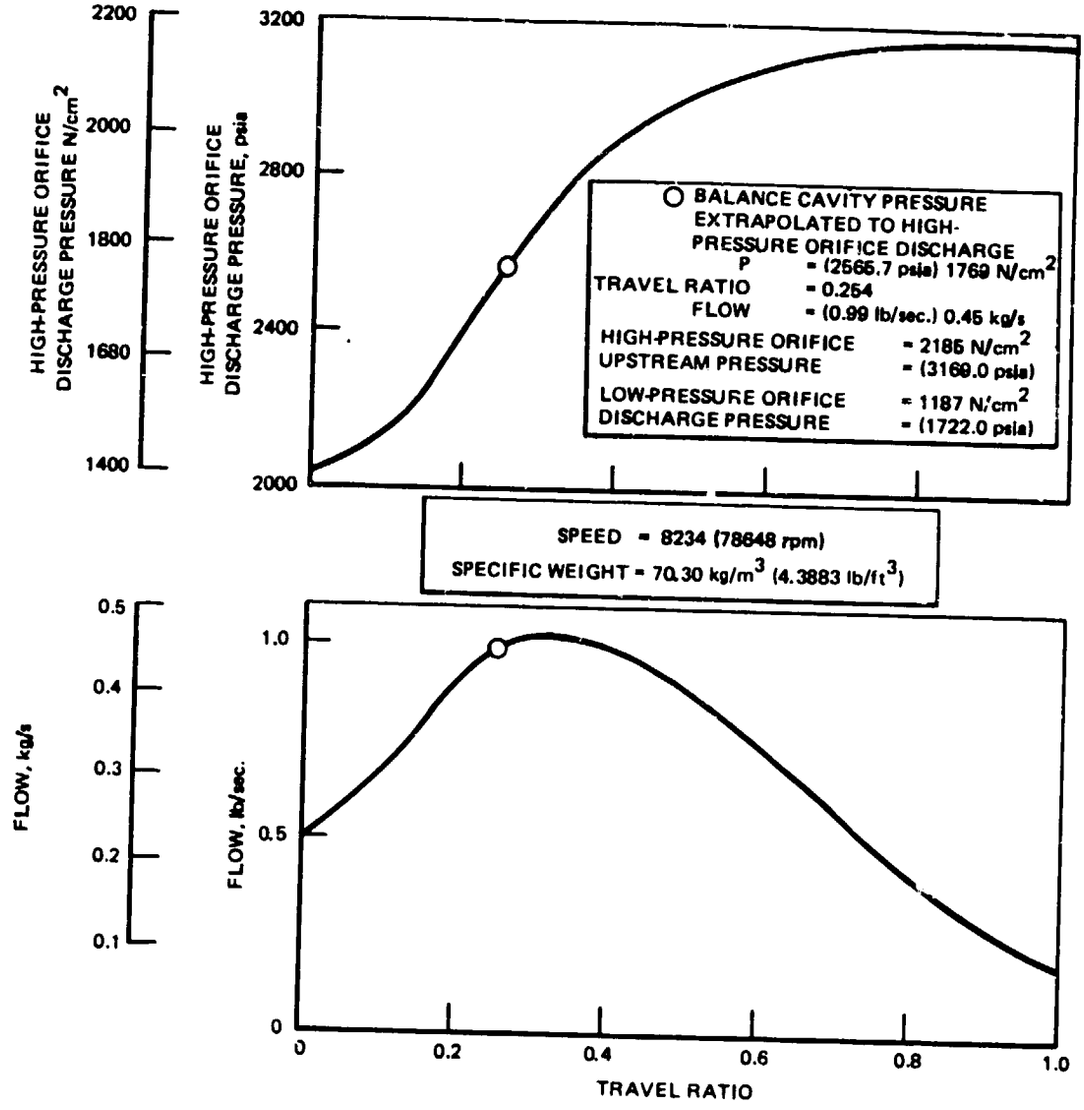

Figure 106. Balance Piston Performance (Test 9, Slice 11)

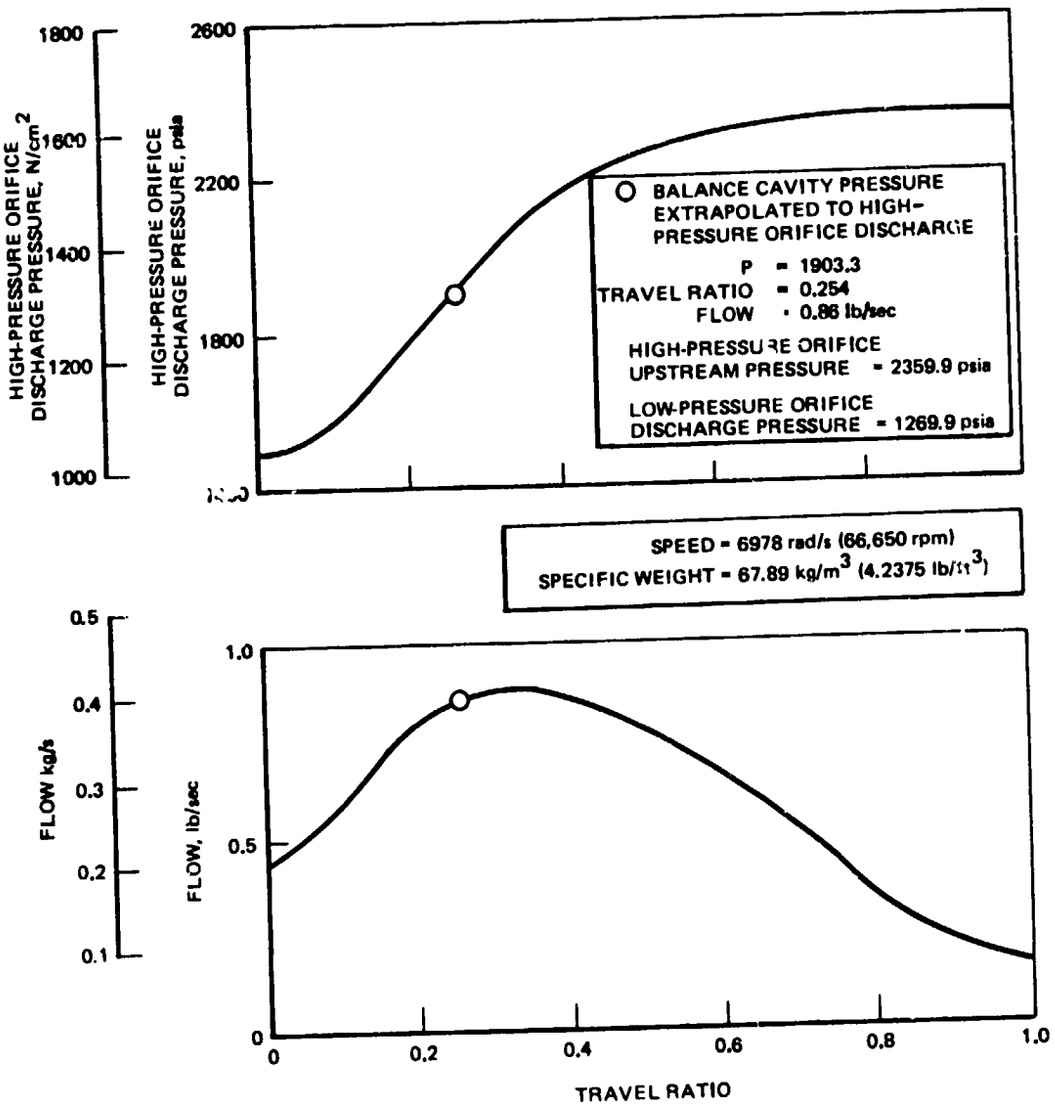

Figure 107. Balance Piston Performance (Test 5, Slice 6)

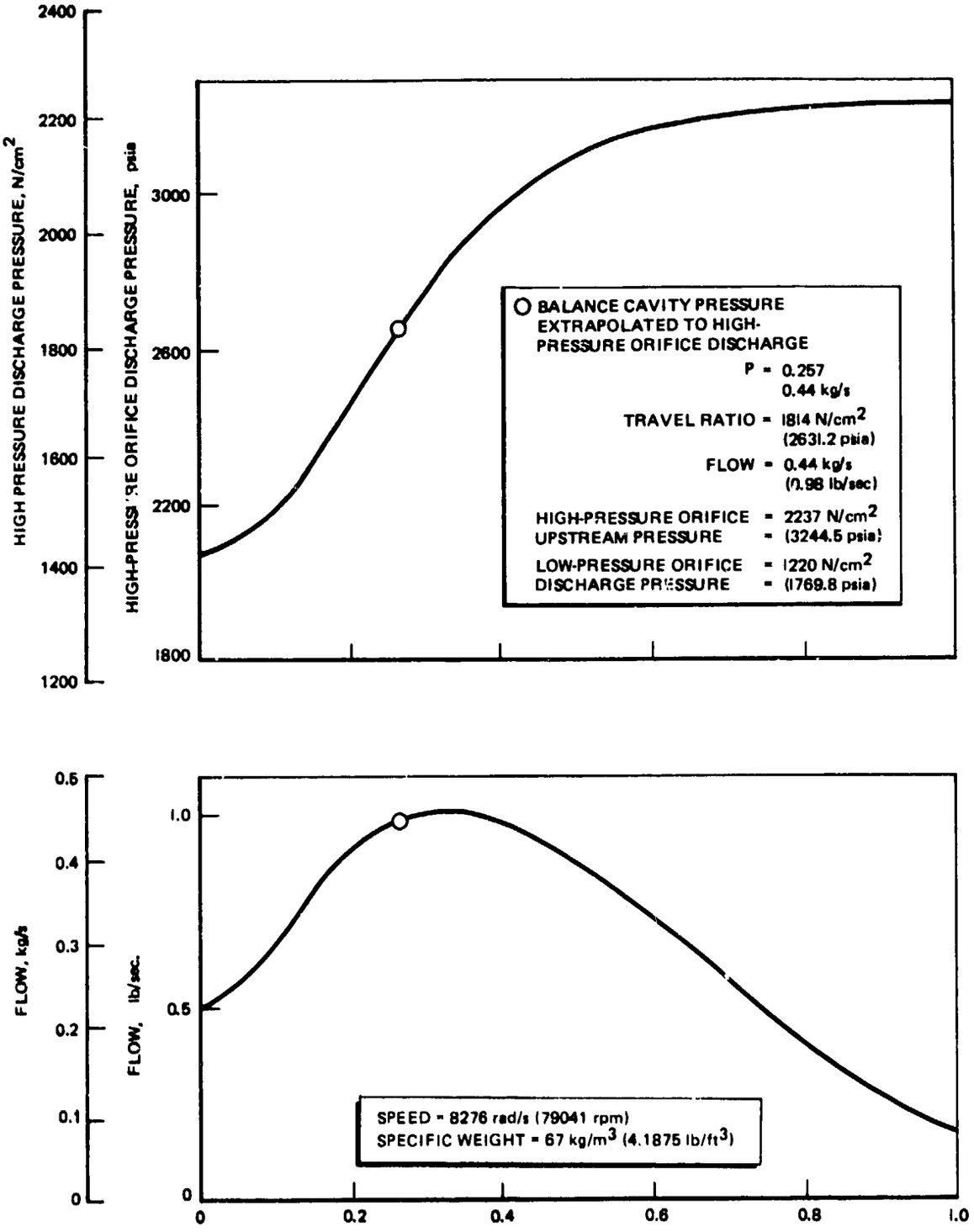

Figure 108. Balance Piston Performance (Test 14, Slice 5)

Both the performance shift at 73% of design flow coefficient and the overspeed cutoff at 67% of design flow coefficient were the result of performance changes in the first-stage diffuser.

The pressure shift and overspeed cutoff are documented in the CRT plots in Fig. 109 through 112 . In Fig. 109 , the shift in pump discharge pressure and the change in slope with time and reducing flow are shown along with the sharp drop at the overspeed cutoff. Pump speed is shown in Fig. 110 . The test was controlled for constant speed of 8587 rad/s (82,000 rpm) which is shown across the shift and up to the time when the pump overspeed occurred causing the cutoff. Figures 111 and 112 show the pump discharge flow-measuring venturi pressure drop and the flow-controlling throttle valve position. No significant deviation was observed at the time of the shift. The throttle valve continued to reduce the flow toward the target of 54% of design flow coefficient until interrupted by the overspeed cutoff.

Performance Shift. The overall pump head rise versus flow curve for the data scaled to 9948 rad/s (95,000 rpm) is shown in Fig. 113 . The test began near the design flow of 0.0396 m^3/s (627.5 gpm). The head-flow characteristic from design flow to the point of shift was comparable with previous tests at 8578 rad/s (82,000 rpm). The head rise dropped 3.2% across the shift. The head-flow slope changed from a negative stable slope to a positive, unstable slope, as the flow was reduced by the throttle valve.

The overall pump isentropic efficiency is shown versus scaled flow in Fig. 114 . Prior to the shift, the efficiency characteristic was comparable to previous tests. Efficiency dropped 4.9% or 3 points across the shift.

The turbopump was thoroughly instrumented with interstage static pressure taps as shown in Fig. 115 . The pressure change across each element and stage could be analyzed.

The scaled static pressure changes across each stage versus scaled flow are shown in Fig. 116 . The characteristics that did not indicate a shift were:

1. The long diamonds of pressure change across the third stage
2. The square diamonds for the second stage
3. The triangles indicating the pressure change across the first-stage inducer and impeller

The parameters that did indicate a shift were:

1. The circles for the first-stage diffuser and crossover and the second-stage impeller
2. The squares for the first-stage inducer, impeller, and diffuser.

Parameters including the first-stage diffuser showed the shift.

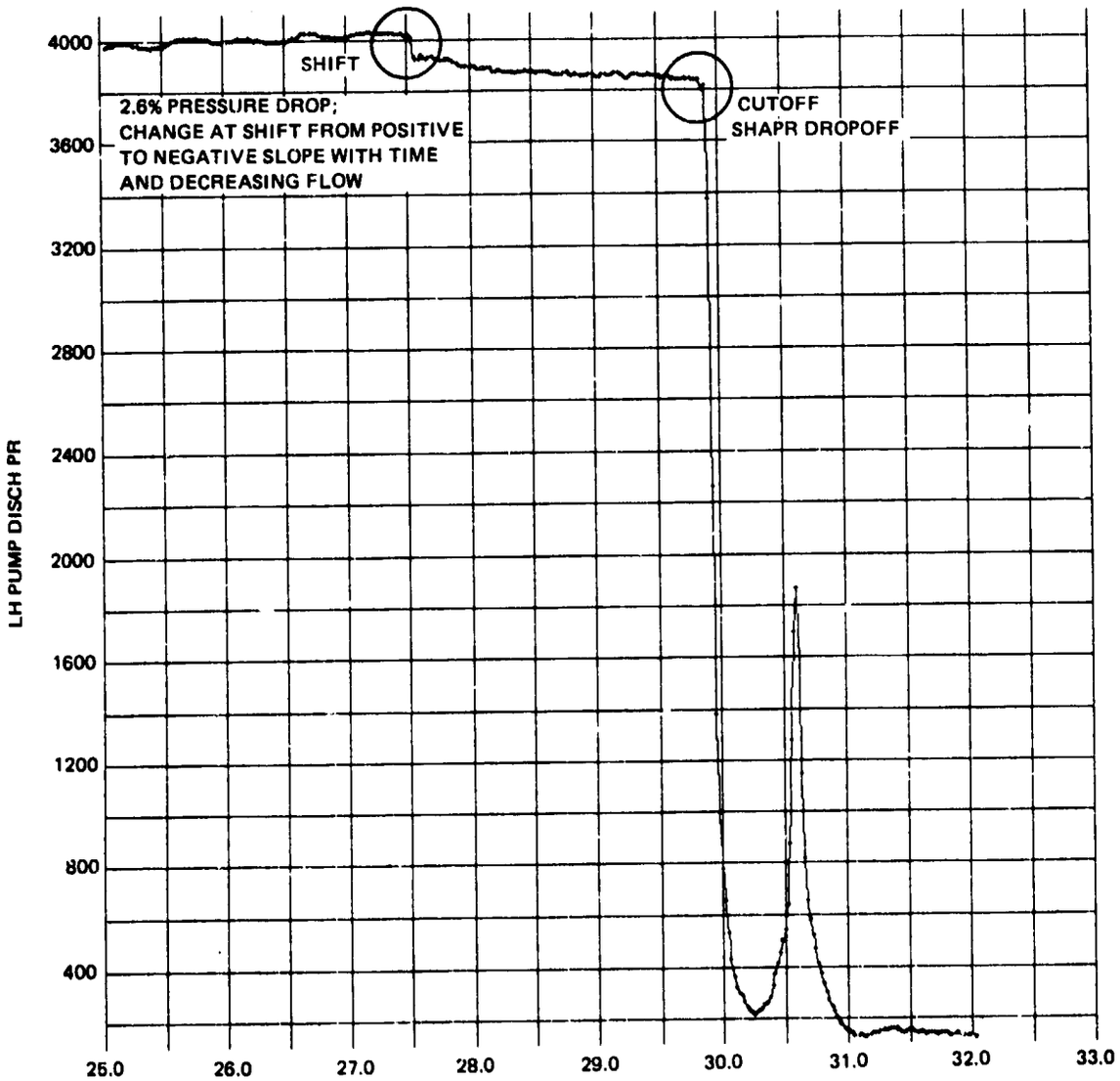

Figure 109. Pump Discharge Pressure vs Time
(Test 019, 1979)

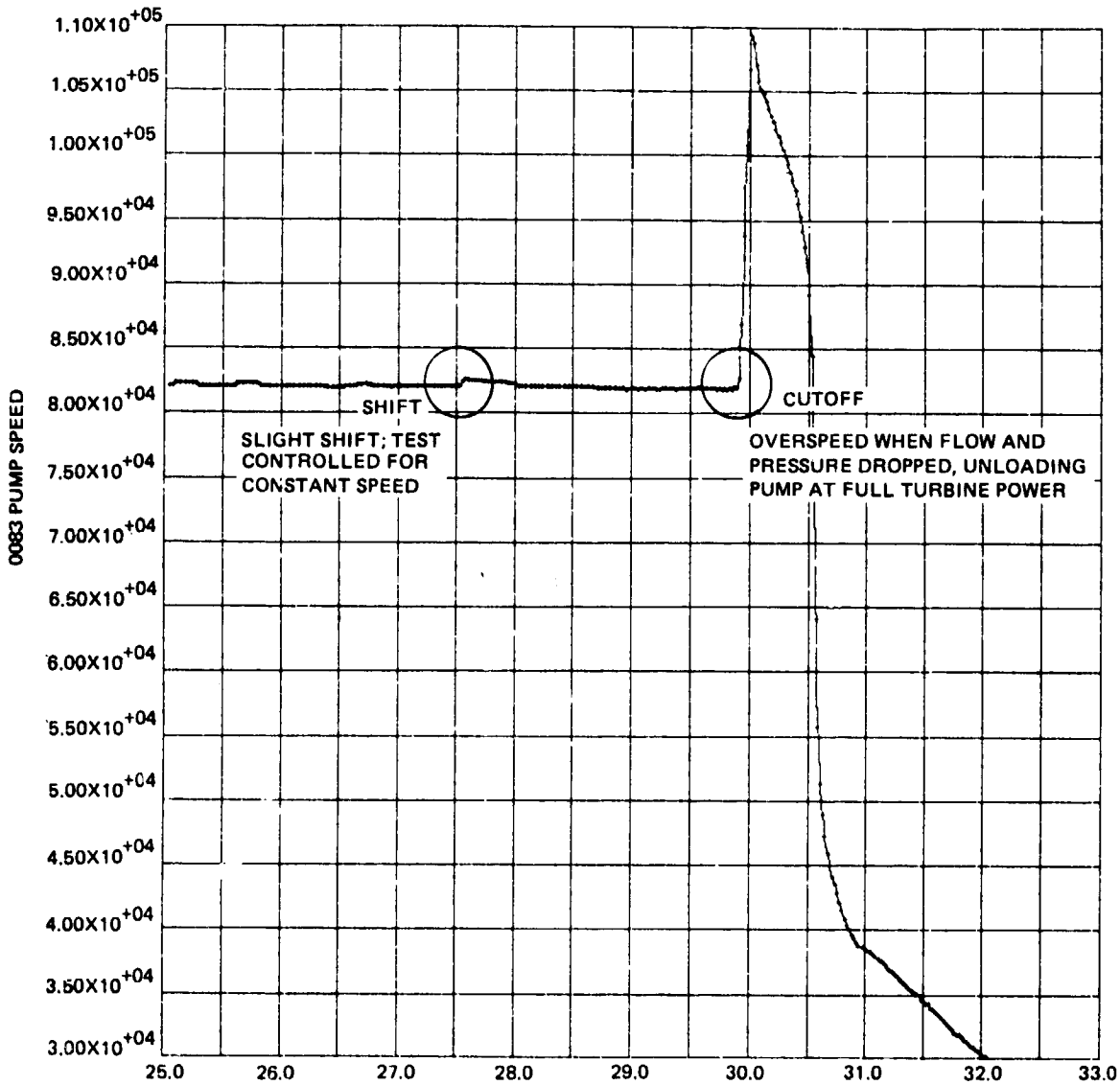

Figure 110. Pump Speed vs Time (Test 019, 1979)

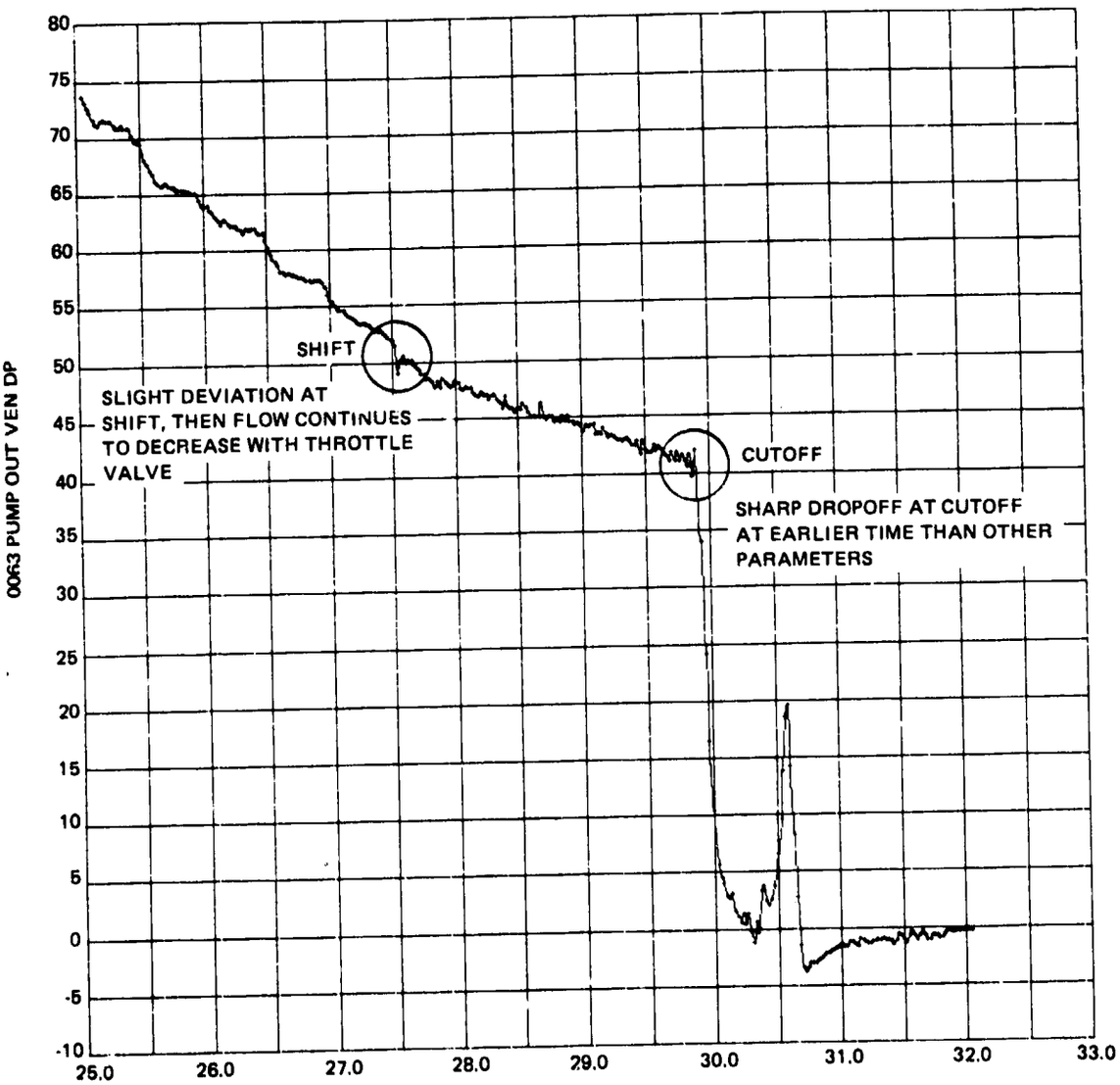

Figure 111. Pump Discharge Flow Venturi ΔP vs Time
(Test 019, 1979)

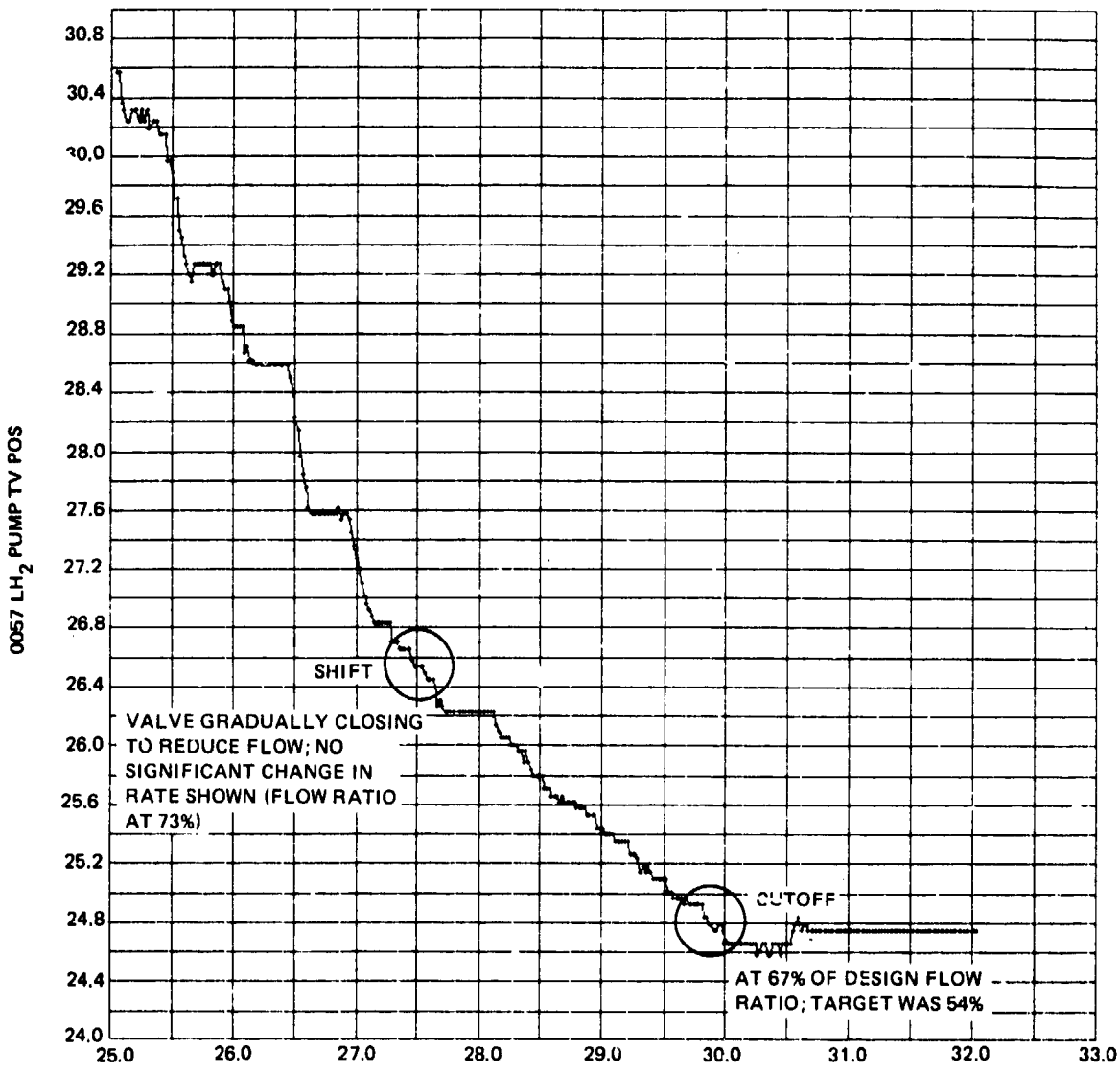

Figure 112. Pump Discharge Throttle Valve Position vs Time (Test 019, 1979)

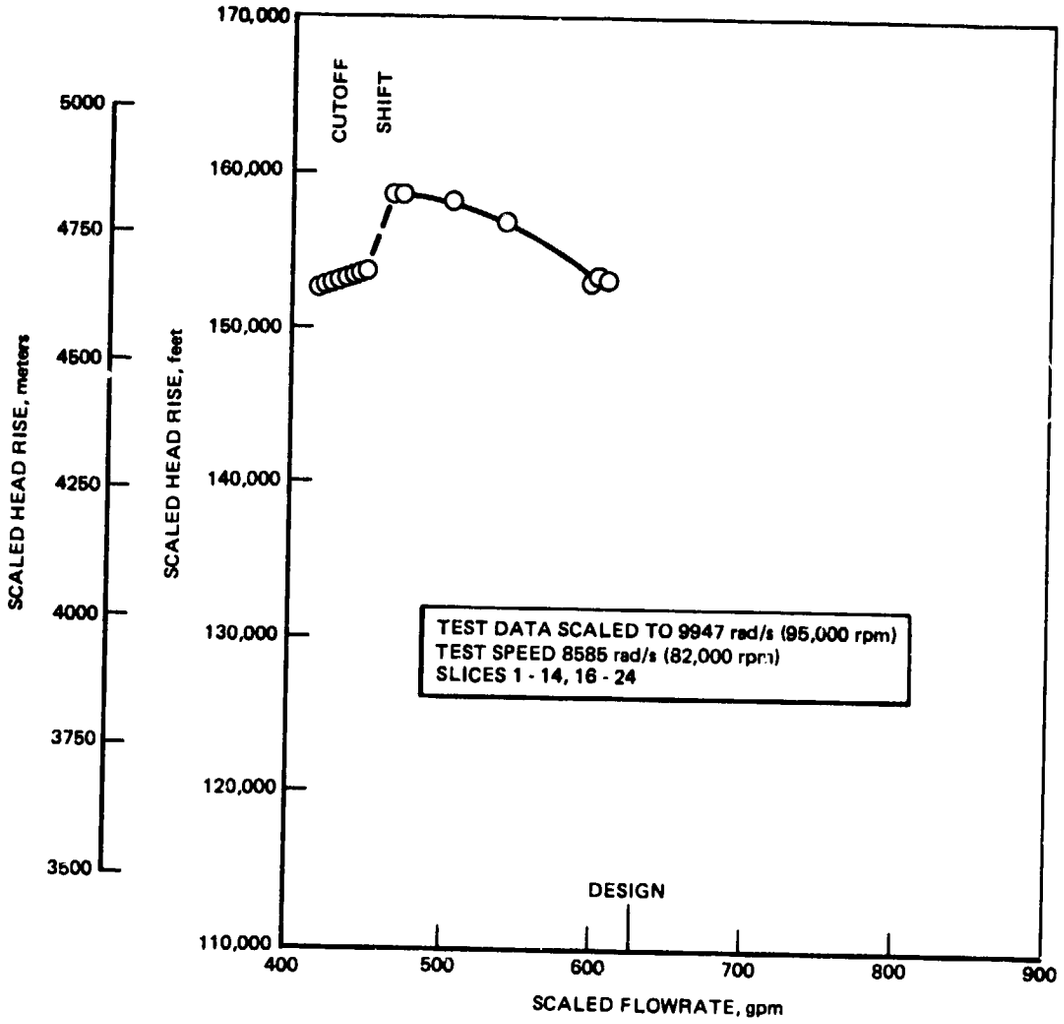

Figure 113. Pump Head-Flow Performance (Test 019)

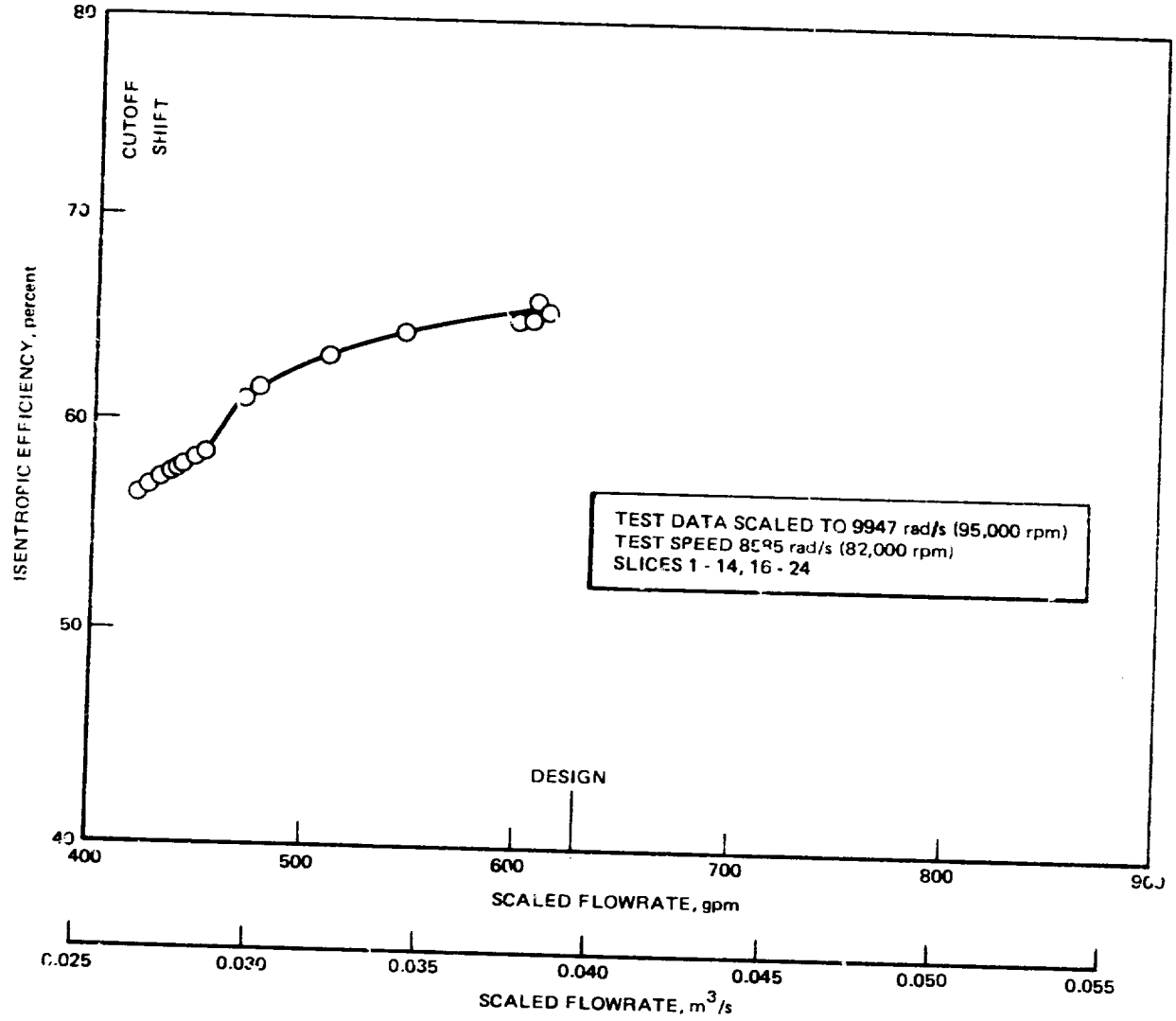

Figure 114. Pump Isentropic Efficiency (Test 019)

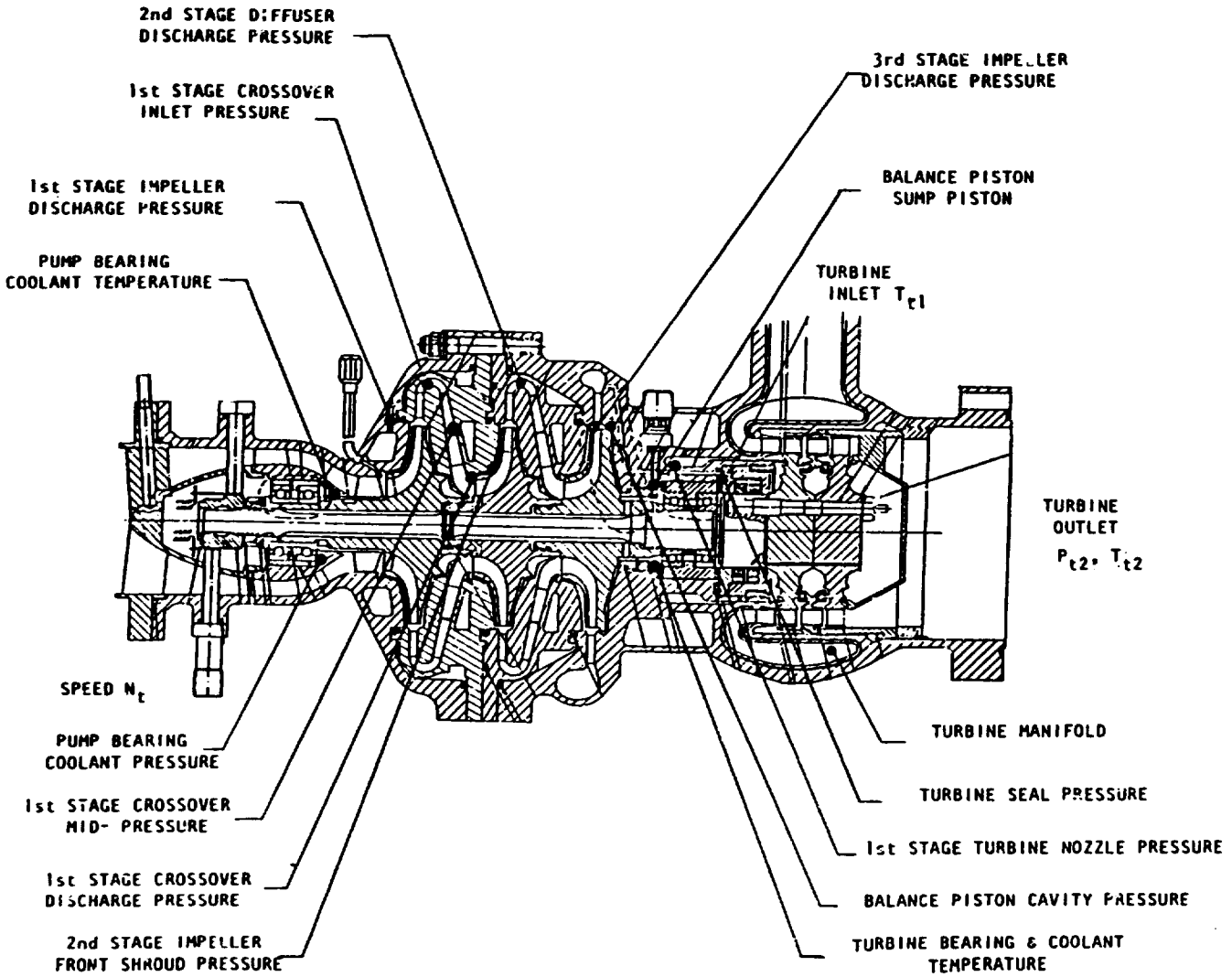

Figure 115. H_2 Turbopump

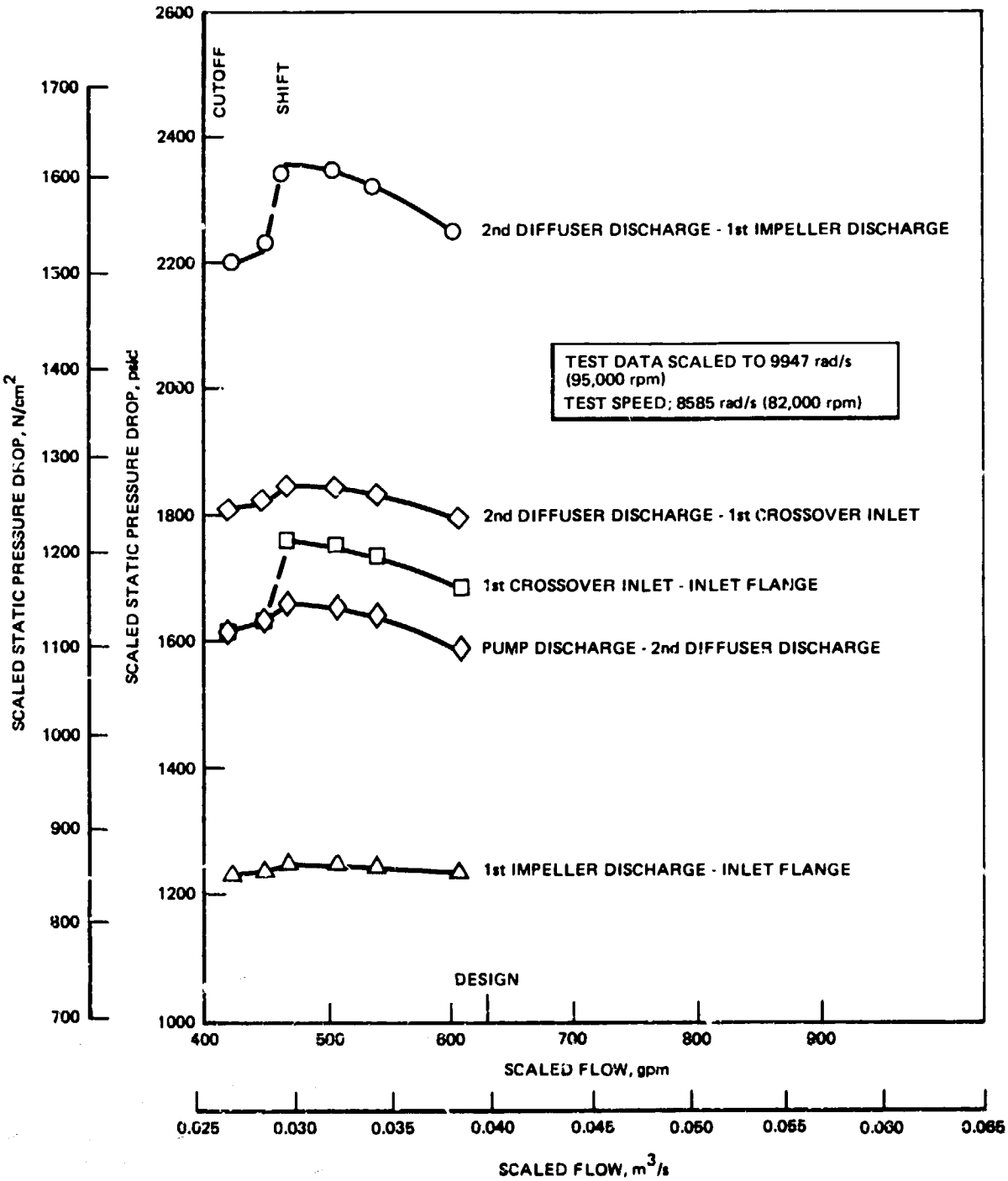

Figure 116. Static Pressure Changes With Flow (Test 019)

The scaled static pressure changes across each stage diffuser are plotted in Fig. 117 . No shift is seen across the second- or third-stage diffuser. A shift of 22% is shown in the pressure recovery across the first-stage diffuser.

The conclusion drawn from Fig. 116 and 117 was that the pump performance shift at 73% of design flow coefficient was the result of a performance change in the first-stage diffuser.

After observing the shift in test 160-019 at 73% of design flow coefficient, the other low flow coefficient tests, 160-005, 160-012, and 160-014 were reviewed.

Tests 160-005 was a head-flow test at 6283 rad/s (60,000 rpm). The lowest flow was 72% of the design flow coefficient. The head rise shifted downward as the throttle valve was closed to get the 72% flow. The head rise at 72% flow was below the characteristics curve generated from the higher flow data. As the throttle valve was opened to get higher flow points, the head rise shifted upward.

Test 160-012 was a 2409 rad/s (23,000 rpm) suction performance test with a minimum target of 50% of design flow coefficient. As the throttle valve was closed from 76% to 62% of design flow coefficient, the head rise shift occurred similar to higher speed tests.

Test 160-014 was a suction performance test at 71% of the design flow coefficient and 8273 rad/s (79,000 rpm). Head rise at high NPSH was plotted directly on Fig. 113 after the shift at a scaled flowrate of 0.0280 m^3/s (443 gpm) and scaled head rise of 46634 m (153,700 feet). No significant dropoff of head rise occurred for an inlet pressure reduction from 69.6 N/cm^2 (101 psia) (NPSH of 1067 m (3,500 feet) to 13.78 N/cm^2 (20 psia) (below liquid vapor pressure)(Fig. 9[illegible]).

No hardware changes were noted during the post test 160-019 disassembly that would affect the first-stage diffuser performance.

The performance shift appears to be a stall condition in the first-stage diffuser. The stall is relatively mild from an overall pump standpoint although it results in over a 20% drop of static pressure rise across the first diffuser. Prediction of this stall phenomenon would require analysis of the diffuser vanes with the Rocketdyne Three-Dimensional Analysis Program (R3DAP) and the boundary layer program. The occurrence of something very similar was encountered during model testing of the Grand Coulee pumps. This effect was greatly reduced by opening up the inlet area to the diffuser by such means as cutting back the diffuser leading edges or by using a fewer number of vanes. Similar techniques could be potentially used to eliminate the performance shift on this pump. This "step" caused no problems in pump operation on the Grand Coulee pump.

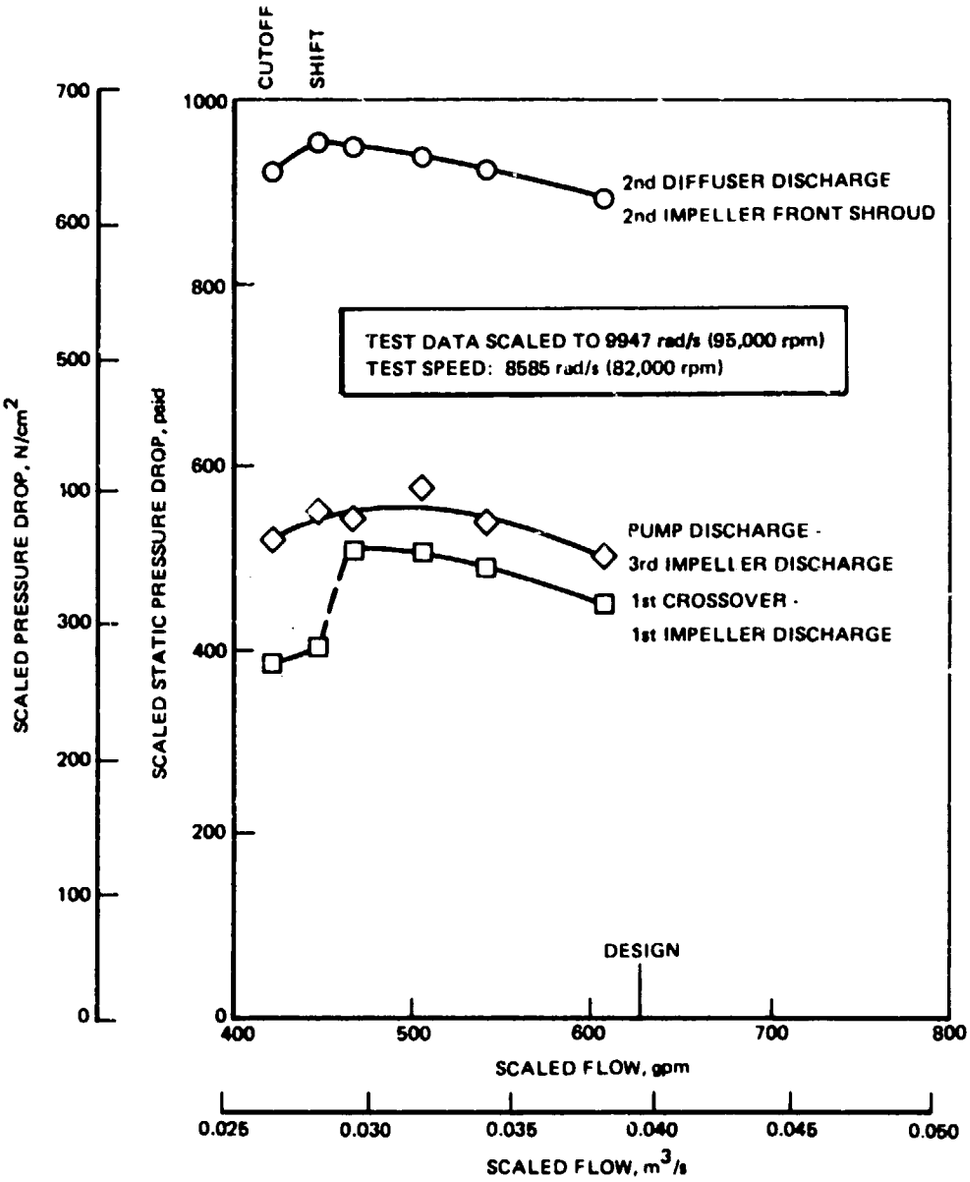

Figure 117. Pump Static Pressure Changes With Flow (Test 019)

Boil Out. Figures 118 through 120 are CRT plots of inducer discharge tip static pressure, first-stage impeller discharge static pressure, and first crossover inlet static pressure which also represents first-stage diffuser discharge static pressure. At the overspeed cutoff, the pump inlet and inducer and first-stage impeller discharge pressures spiked responding to the increase in speed and decrease in flow. The pressure increase with speed and flow drop indicates some liquid hydrogen in the first-stage rotating elements after flow and pressure had dropped at the pump discharge. Inducer static pressure rise head coefficients calculated before the cutoff and at the maximum spike conditions were within 36% of each other showing the inducer pressure approximately responding to the speed change during the overspeed. However, because the pump inlet pressure also showed a spiking condition, a waterhammer type of effect must also be present. That is, as the flow is abruptly shut off, the pressure in the first-stage rotating elements experience a waterhammer type of upsurge. This, too, indicates a liquid in the inlet regions of this first stage. The first-stage diffuser discharge pressure showed no pressure rise with the overspeed, only the sudden dropoff that was typical of all pressures downstream of the first diffuser.

There are four potential explanations of the sudden performance change:

1. Pump stall
2. Cavitation due to velocity mismatch at the diffuser
3. Cavitation due to thermodynamic heating effects in the pump
4. Increased thermodynamic heating due to a crack in the second-stage impeller.

Each of these are discussed below and related to the observations from the test data.

The pump has already demonstrated a stall phenomenon as experienced in the performance shift previously discussed. The diffusion factor at the time of the cutoff was 0.736 ignoring the effects of the initial stall; that is considered to be much too high for safe operation without stall. Another indication is that all pressures from the first-stage impeller discharge and on upstream rose as the speed increased before they also decreased. All pressures measured downstream of this impeller fell off without rising first.

This problem is magnified by the arrangement of the leakage path. The first diffuser sees the rear wear ring flow which has been heated by the rear shroud pumping action. It is returned to the diffuser at an angle which is different from the vane angle. The second diffuser sees more than the pump inlet flow by an amount equal to the balance piston flow. The third diffuser flow is essentially equal to the pump inlet flow.

The primary argument against a pure stall phenomenon is that test 160-012 had previously been run to an even lower flow coefficient without experiencing any similar effect. Test 160-012 was run at a lower speed 2409 rad/s (23,000 rpm), and this could effect other operating features, but a pure stall phenomenon should be flow coefficient related.

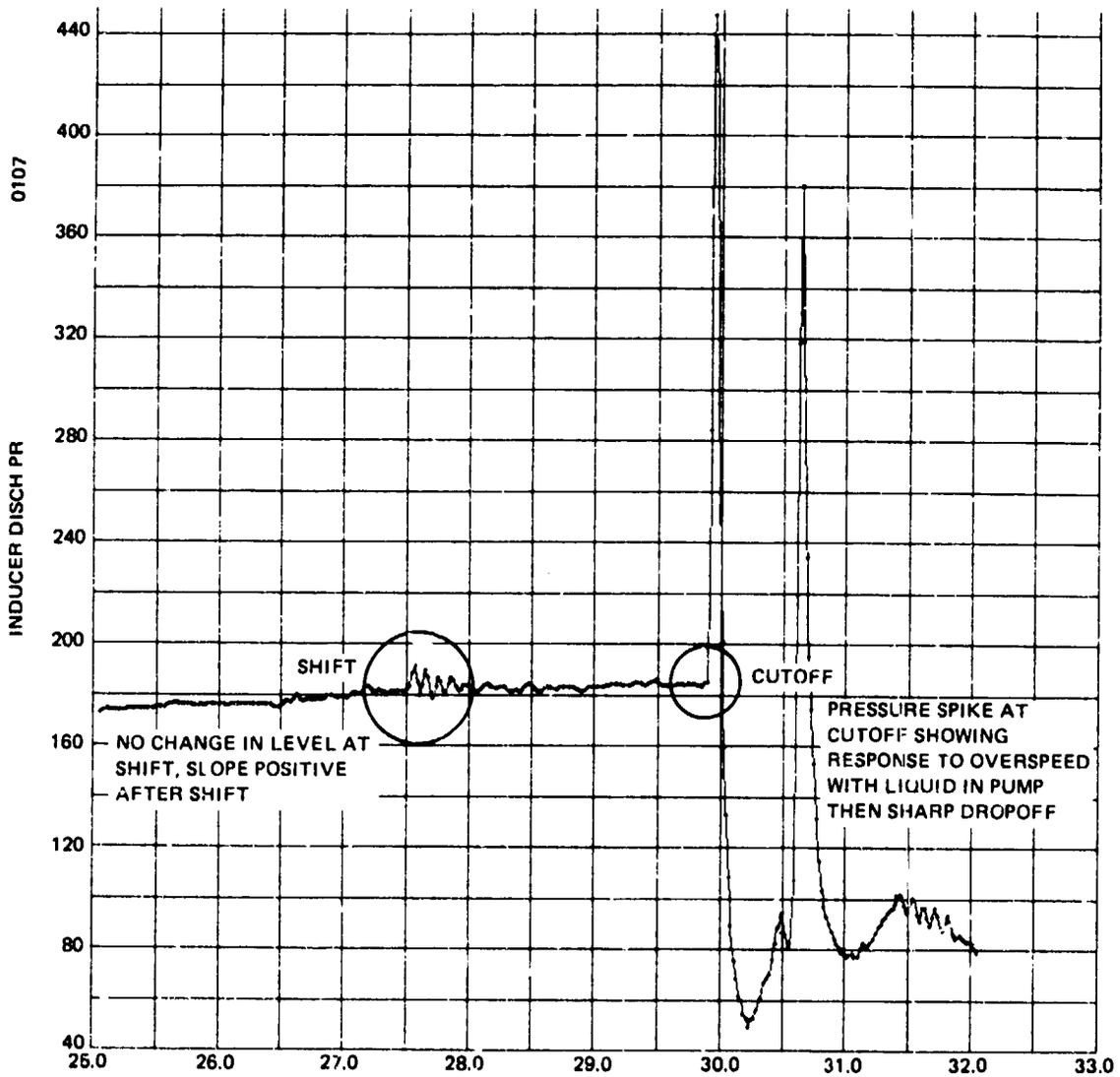

Figure 118. Inducer Discharge Tip Static Pressure vs Time (Test 019, 1979)

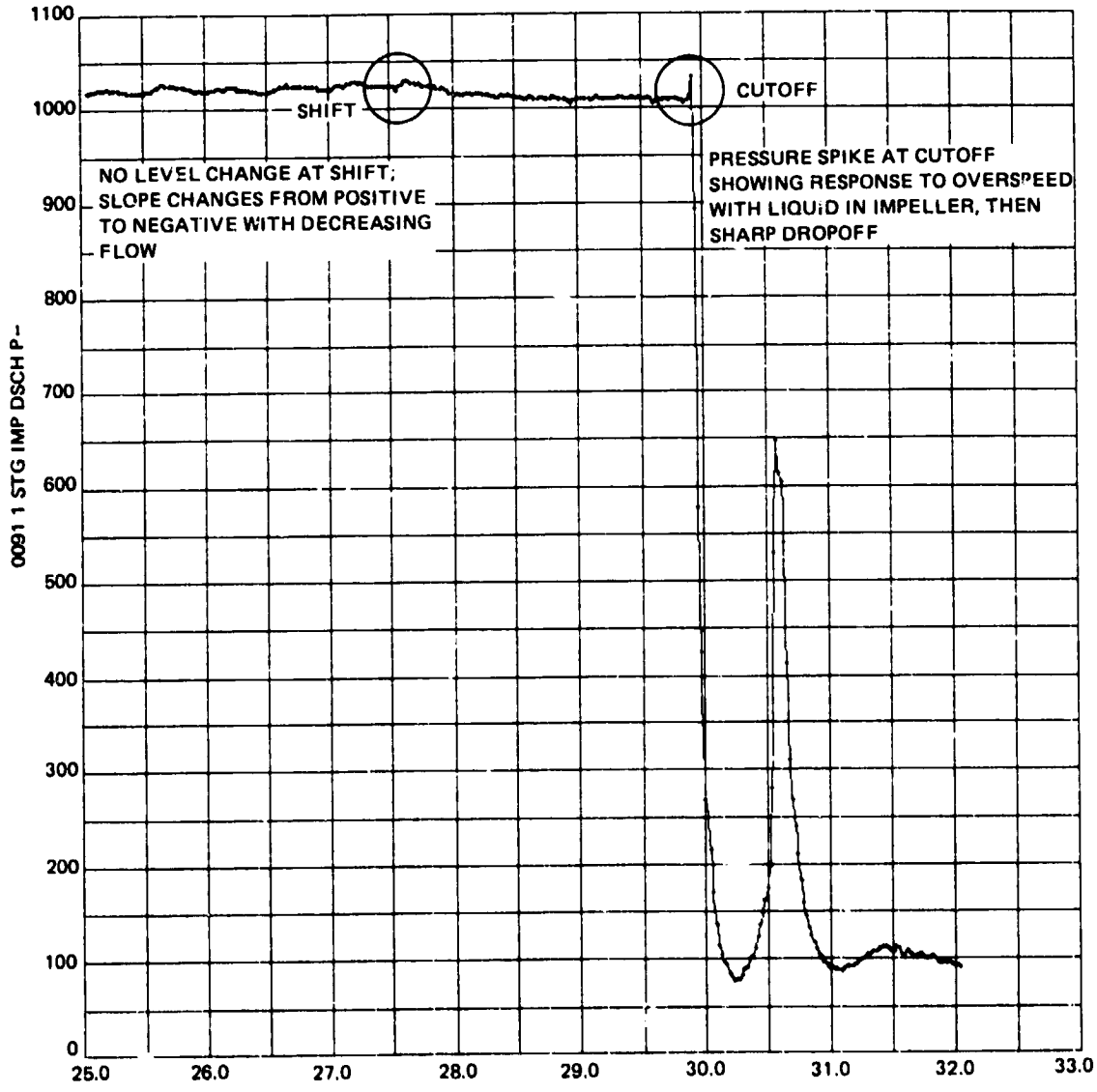

Figure 119. First-Stage Impeller Discharge Static Pressure vs Time (Test 019, 1979)

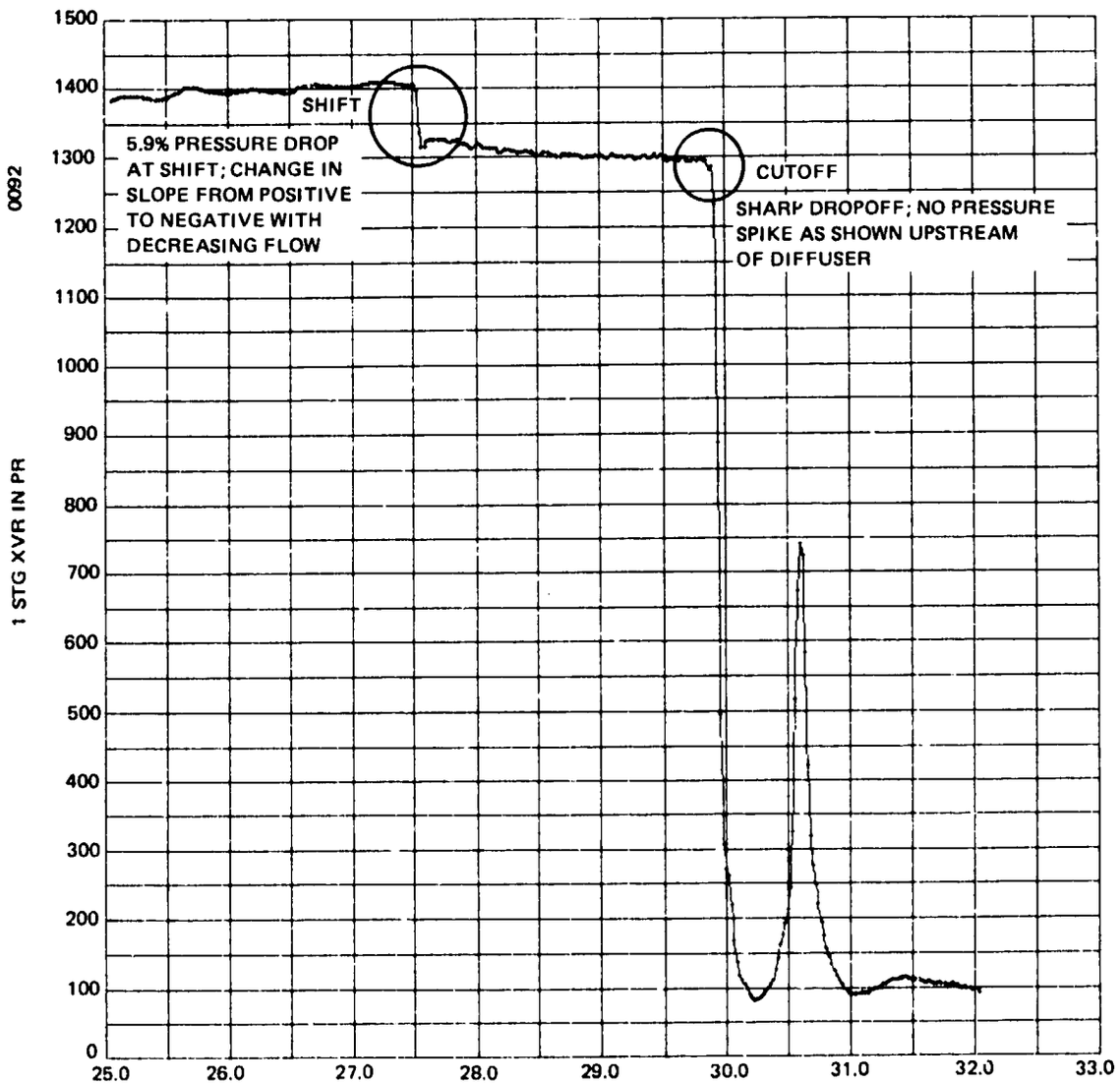

Figure 120. First Crossover Inlet (Diffuser Discharge) Pressure vs Time (Test 019, 1979)

Also, pump stall usually results in a loss in head and efficiency, but without causing a sudden dropout of head so that a large change occurs in the absorbed horsepower.

Cavitation is another possible cause. The pressure in this area at the time of the performance breakdown was of the order of 689 N/cm^2 (1,000 psi). If cavitation did occur, it would be due to high local over-velocities resulting from the average calculated incidence angle of 0.0419 radians (2.4 degrees) and the diffuser leading edge shape. The diffuser vane inlet angle is 0.140 radians (8 degrees). An inlet local velocity 1.53 times the average diffuser upstream velocity can lead to cavitation.

The primary argument against a pure cavitation explanation is that test 160-014 was a suction performance test run at almost the same speed 8273 versus 8587 rad/s (79,000 versus 82,000 rpm) and almost the same flow coefficient (0.71 versus 0.67 times design flow coefficient). Test 160-014 demonstrated two-phase flow pumping capability at much lower operating inlet pressures than test 160-019. It is very unlikely that a major change in suction performance capability would occur with such a small change in flow coefficient.

From the purely thermodynamic heating standpoint, the first sign of a problem would appear at the eye of the second impeller. This is the result of adding hot hydrogen from the front wear ring and the balance piston. However, the analysis shows that this heating is not a problem until the inlet flow coefficient is much lower. Thus, it appears that the problem is not basically a thermodynamic one. This is further supported by the results of test 160-014 which experienced much lower inlet static pressures which would lead to a more likely thermodynamic heating problem, yet none occurred.

The pump teardown did show that the second impeller had experienced a crack completely around the front shroud that would permit extra leakage flow from the second impeller discharge into the second impeller near the eye. It is generally assumed that the crack actually occurred due to the overspeed, thus making it an effect of the problem rather than a cause. This assumption is based on the fact that the pump had been previously run at over 9425 rad/s (90,000 rpm) without any indication of a crack developing such that a crack would not be expected to initiate at 8587 rad/s (82,000 rpm). However, if the crack did occur at operating speed due, e.g., to dynamic loading associated with off-design operation, the resulting effect on pump performance would be significant. The Stress Department has indicated that the crack width would be of the magnitude of 0.076 mm (0.003 inch) at 8587 rad/s (82,000 rpm). This is comparable in magnitude to the front wear ring clearance so that a comparable flowrate would be bypassed to the impeller eye. This flow would have two negative effects. First it adds extra heating to the impeller inlet flow, and secondly, it enters into the impeller flow path as a sheet that would have a major disruptive effect on the second impeller flow field. This can be seen in Fig. 121 which shows the jet of flow discharging in a direction almost opposing the through flow.

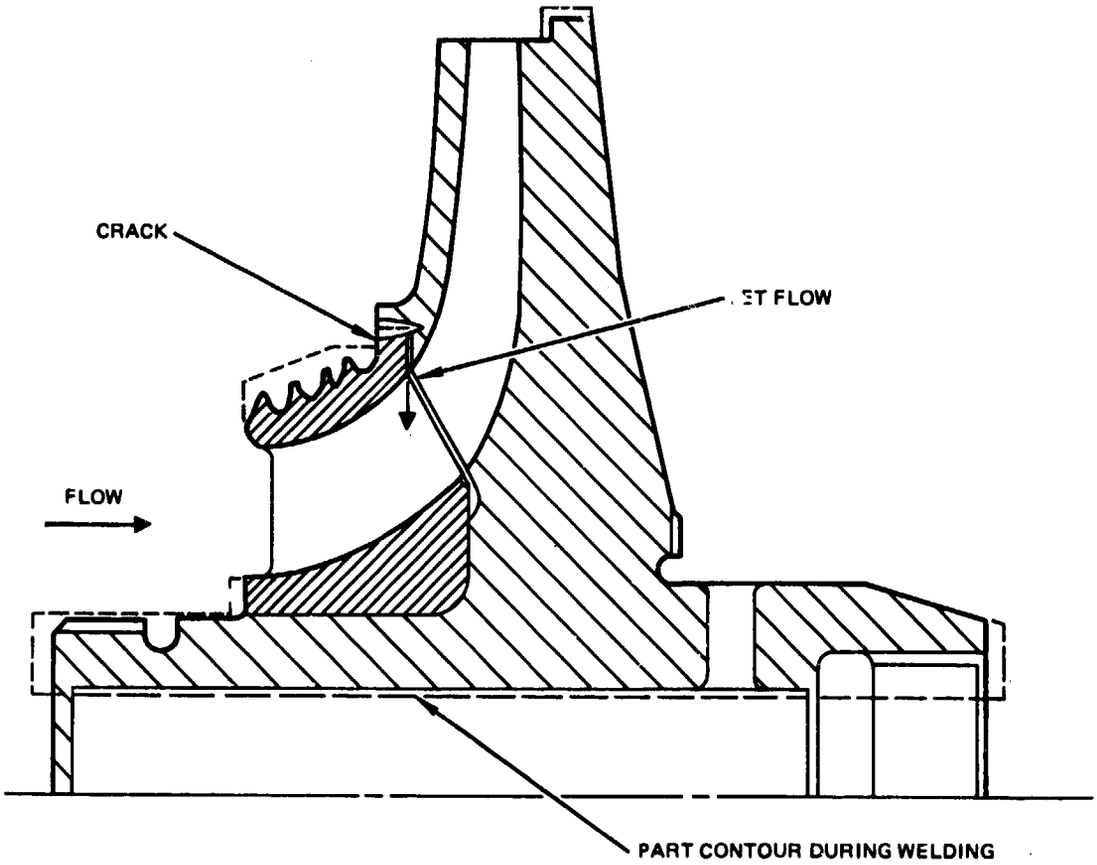

Figure 121. Mark 48-F Welded Impeller Configuration Flow Pattern

Based on previous wear ring flow studies, the front wear ring flow at design flow conditions would be approximately 0.09 kg/s (0.2 lb/sec). This compares with an estimated impeller design flow of 3.33 kg/s (7.35 lb/sec). However, at the low flow coefficient of test 160-019, the impeller flow would be reduced by approximately 30% with an increase in leakage flow. Assuming only a 10% increase, the percent of flow entering the impeller through the crack would be approximately

$$100* \frac{1.1\ (0.2)}{0.7\ (7.35)} = 4.3\%$$

However, the crack through which this flow enters the impeller is only about 0.178 mm (0.007 inch) wide which would lead to jet velocity of approximately 50 m/s (164 fps) where

$$V = \frac{1.1\ (0.2)\ (144)}{4\ (\pi)\quad (2.2)\quad (0.007)} = 50 \text{ m/s } (164 \text{ fps})$$

The impeller flow meridional velocity is of the magnitude of 30.5 m/s (100 fps) at this condition so that the jet could easily block a significant amount of flow area and lead to a severe separation problem in the impeller and possibly to a cavitation problem due to the resulting overspeeds near the blocked inlet.

Thus, it can't be proven that the crack initiated at the 8587 rad/s (82,000 rpm) operating condition; if it did, this could have caused the resultant effects noted in the hydrodynamic parameters. If the crack were not the cause, then some combination of separation and thermodynamic effects would have to be postulated. For example, the initial separation, experienced at even lower pump speeds resulted in cavitation. These two effects would then interact to cause a significant blockage of flow at the diffuser inlet which resulted in thermodynamic boilout or total stall such that the pump horsepower absorbtion dropped off and caused the pump to overspeed.

Turbine Performance

The first-phase performance evaluation tests of the Mark 48-F turbopump assembly were conducted with GH_2 turbine working fluid, and with LH_2 flow through the pump. The results of these tests provide a comparison of the power developed by the turbine with the power required by the pump to deliver the measured pump heads and flows. These data additionally will establish the overall turbopump performance.

The following power calculations were made:

1. Turbine-developed horsepower calculated with turbine isentropic enthalpy [$\Delta H_{(T-T)}$] available at the test pressure ratio, GH_2 working fluid mass flowrate [$\dot{W}_t$], turbopump speed [N_t], and turbine component efficiency at the respective test conditions

2. Turbine Horsepower calculated with working fluid total temperature drop [$\Delta T_{(T-T)}$] measured across the turbine, and GH_2 working fluid mass flow [$\dot{W}_t$]

3. Pump horsepower calculated with pump head and flow data at the respective speeds selected for the analysis

Turbine test instrumentation was located as shown on the turbopump assembly drawing 9K0011560 in Appendix A and in Fig. 115 to obtain the following turbine test parameters for the performance analysis:

1. Turbine total inlet temperature, T_{t1}, measured at the turbine inlet, downstream of the preburner
2. Turbine inlet static pressure, P_{s1}, measured at the entrance to the first-stage nozzle
3. Turbine exhaust total pressure, P_{t2}, measured downstream of the turbine exhaust flange
4. Turbine exhaust total temperature, T_{t2}, measured downstream of the turbine exhaust flange
5. Turbine speed, N_t

Turbine mass flowrate was calcualted with data obtained with a venturi and orifice which were located, respectively, upstream and downstream of the turbine.

The analysis was performed for a range of turbine velocity ratios (U/C_o T-T) from 0.220 to 0.389 and turbine speeds from 4398 to 9027 rad/s (42,000 to 86,200 rpm). A tabulation of pertinent test data appears in Table 14. The performance calculations, which utilized process hydrogen gas properties at the test state conditions, are identical to those used previously to establish turbine aerothermodynamic performance with GN_2 at the Wyle Laboratories, El Segundo, California.

Turbine inlet total pressure was calculated as the sum of the first-stage nozzle inlet static pressure, and dynamic pressure calculated at the entrance plane of the first-stage nozzle. The total-to-total pressure ratio was established with calculated inlet total pressure and turbine test exhaust total pressure. The turbine-developed horsepower calculation utilized turbine isentropic available energy (T-T) for the respective test pressure ratio, calculated GH_2 mass flowrate corrected for GH_2 compressibility (Z) effects, and turbine efficiency (T-T) corresponding to the test velocity ratio.

Turbine-developed horsepower was calculated from the equation

$$h_{ptd} = 1.415 \times \Delta T_{(T-T)} \times C_p \times W_t$$

where C_p = process specific heat

TABLE 14 . MARK 48-F HYDROGEN TURBOPUMP
TURBINE PERFORMANCE EVALUATION TABULATION

1.	Test	001	005	006	007	008	009
2.	Slice	12	8	15	2	3	2
3.	Speed rad/s (rpm)	4406 (42,079)	6410 (61,223)	9021 (86,166)	8275 (79,033)	7962 (76,044)	8554 (81,698)
4.	Turbine Flow, kg/s (lb/sec)	0.765 (1.6868)	1.6877 (3.6978)	3.295 (7.2636)	2.854 (6.2911)	2.864 (6.3135)	3.039 (6.6993)
5.	Turbine Inlet Temperature Total, K (R)	295 (531.54)	304 (547.08)	318 (572.56)	311 (559.35)	307 (552.59)	304 (546.42)
6.	Turbine Outlet Temperature Total, K (R)	262 (472.01)	273 (491.15)	288 (517.93)	280 (503.35)	278 (499.53)	273 (491.30)
7.	Turbine Pressure Ratio Total-Total	--- (1.3967)	--- (1.4735)	--- (1.5066)	--- (1.4946)	--- (1.4945)	--- (1.5006)
8.	Turbine Available Energy (ΔHa) Total-Total kJ/kg (Btu/lb	394 (169.57)	473 (203.73)	531 (228.46)	508 (218.46)	502 (216.09)	502 (216.10)
9.	Turbine Velocity Ratio	--- (0.2205)	--- (0.2927)	--- (0.3890)	--- (0.3649)	--- (0.3530)	--- (0.3792)
10.	Turbine Power (W, h, $\eta_{comp.}$) kw (hp)	209 (279.7)	618 (828.9)	1413 (1895.4)	1171 (1570.3)	1161 (1555.7)	1235 (1655.0)
11.	Turbine Power (W, η_{T-T}), kw (hp)	379 (508.6)	784 (1051.1)	1513 (2028.5)	1343 (1800.5)	1279 (1715.0)	1413 (1894.3)
12.	Pump Power (hp_{fluid}/η_P ISENTROPIC), kw/(hp)	176 (236.06)	224 (299.78)	1419 (1902.36)	1096 (1469.09)	1092 (1464.44)	1079 (1446.45)
13.							
14.	η_{turb} Component	(0.6911)	(0.776)	(0.8072)	(0.8075)	(0.8059)	(0.8079)
15.	η_{pump} Isentropic	(0.7049)	(0.6805)	(0.6534)	(0.6568)	(0.6636)	(0.6321)
16.	$\eta_T \times \eta_P$	(0.4872)	(0.5292)	(0.5274)	(0.5304)	(0.5348)	(0.5107)
17.							
18.	$\eta_{unit} = \frac{hp\ fluid}{hp_{avail}\ (W,\Delta Ha)}$	(0.4112)	(0.4468)	(0.5294)	(0.4962)	(0.5034)	(0.4464)
19.							
20.							
21.	Pump Fluid Power, kw (hp)	124 (166.4)	355 (476.2)	927 (1243.0)	720 (964.9)	725 (971.8)	682 (914.3)
22.							
23.	$HP_{avail.}$, kw (hp)	302 (404.70)	795 (1065.92)	1752 (2347.94)	451 (1944.57)	1440 (1930.32)	1528 (2048.38)

Pump horsepower (h_{pp}) required to drive the liquid-hydrogen pump stages was established with pump fluid horsepower (h_{ppf}) and the pump isentropic efficiency parameter η_{pi} as follows:

$$\text{Pump horsepower, } h_{pp} = \frac{h_{Ppf}}{\eta_{pi}}$$

A plot of test h_{Ptd}, h_{Pt}, and h_{pp} versus turbine velocity ratio (U/C_o (T-T)) data appears in Fig. 122 for the test points appearing in Table 14. The overall agreement is not as good as would be expected. The turbine horsepower calculations would be expected to be somewhat larger than the pump horsepower because of parasitic losses.

A review of the test results indicates the best agreement between h_{Ptd} and h_{pp} is at a speed of 9027 rad/s (86,200 rpm) and $/C_o$ of 0.389. At this operating point, a difference of 333 kw (446 hp) exists between the 1752 kW (2348 hp) turbine developed horsepower and the 1419 kW (1902 hp) absorbed by the pump; this represents a 19% difference when referred to turbine-developed horsepower. This variance is attributed to the following conditions, which influenced the test results:

1. The mixing loss resulting from hydrogen seal leakage entering the turbine gas path -- This colder hydrogen flow originates at the pump and reduces the available energy of the gas path turbine working fluid by disrupting channel state conditions and velocities.

2. Turbine mass flow data were calculated with venturi and orifice test parameters which experienced some calibration shifts and instabilities in the higher turbine power test points -- A review of test conditions and data indicates that calculated turbine mass flows were higher than experienced during the test. An additional mass flow disruption was caused by seal leakage entering the turbine gas path.

The net effect of these variances upon the calculated values of turbine-developed horsepower, h_{Ptd}, could possibly account for it being 19% greater than pump required horsepower. A comparison of turbine (h_{Pt}) horsepower, calculated with total temperature drop across the turbine indicates much better agreement; there is only a 6.2% power difference with pump required horsepower.

In conclusion, a review of the turbine test results indicates the demonstrated overall turbopump efficiency has met the performance objectives of this program.

Bearings and Seals

Turbine Shaft Seal. Figure 123 shows the pressure drop across the turbine shaft seal as a function of pump speed. The results indicate that the pressure drop across the seal increases as the speed increases which would be expected. This results in a positive purge flow across the turbine seal, thus preventing contamination of the turbine coolant from the turbine gas.

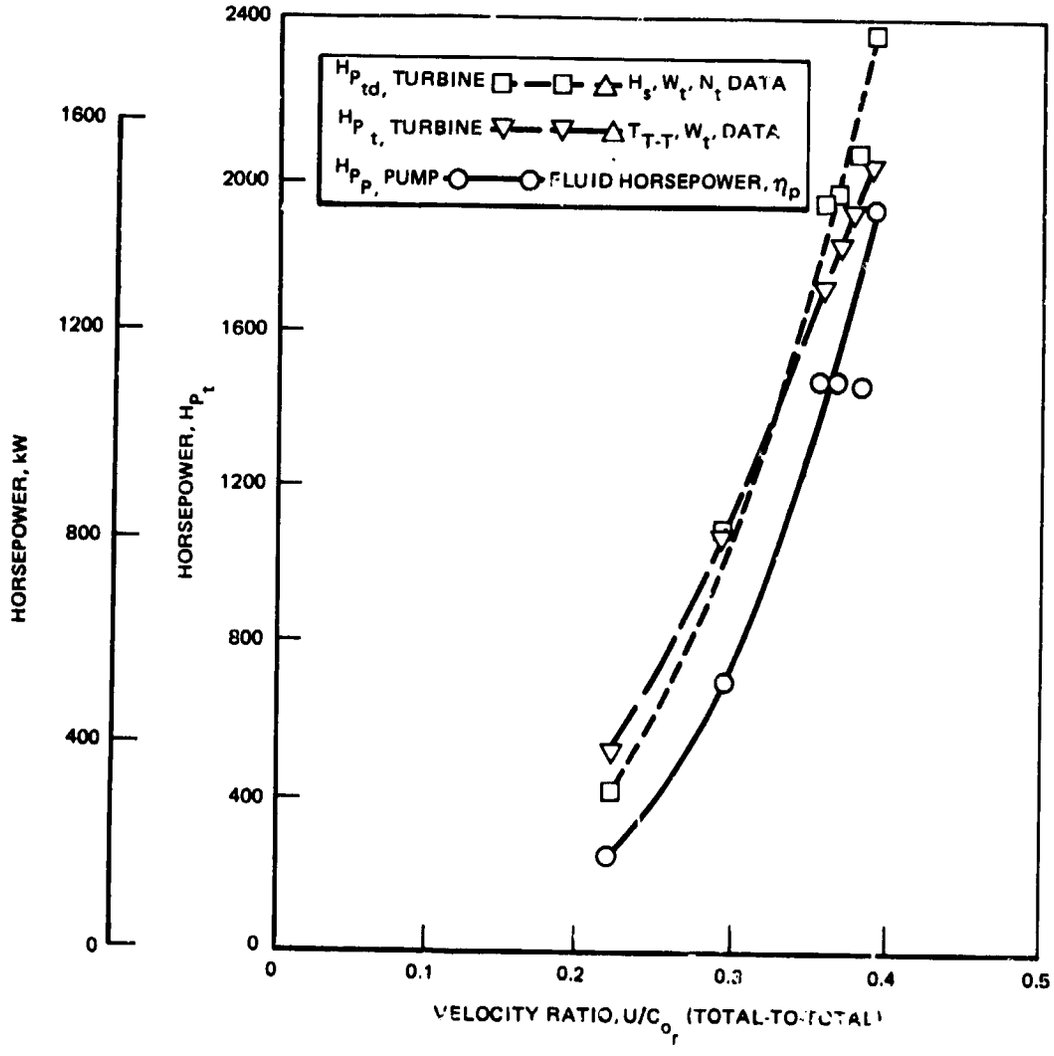

Figure 122. Turbine Horsepower Correlation

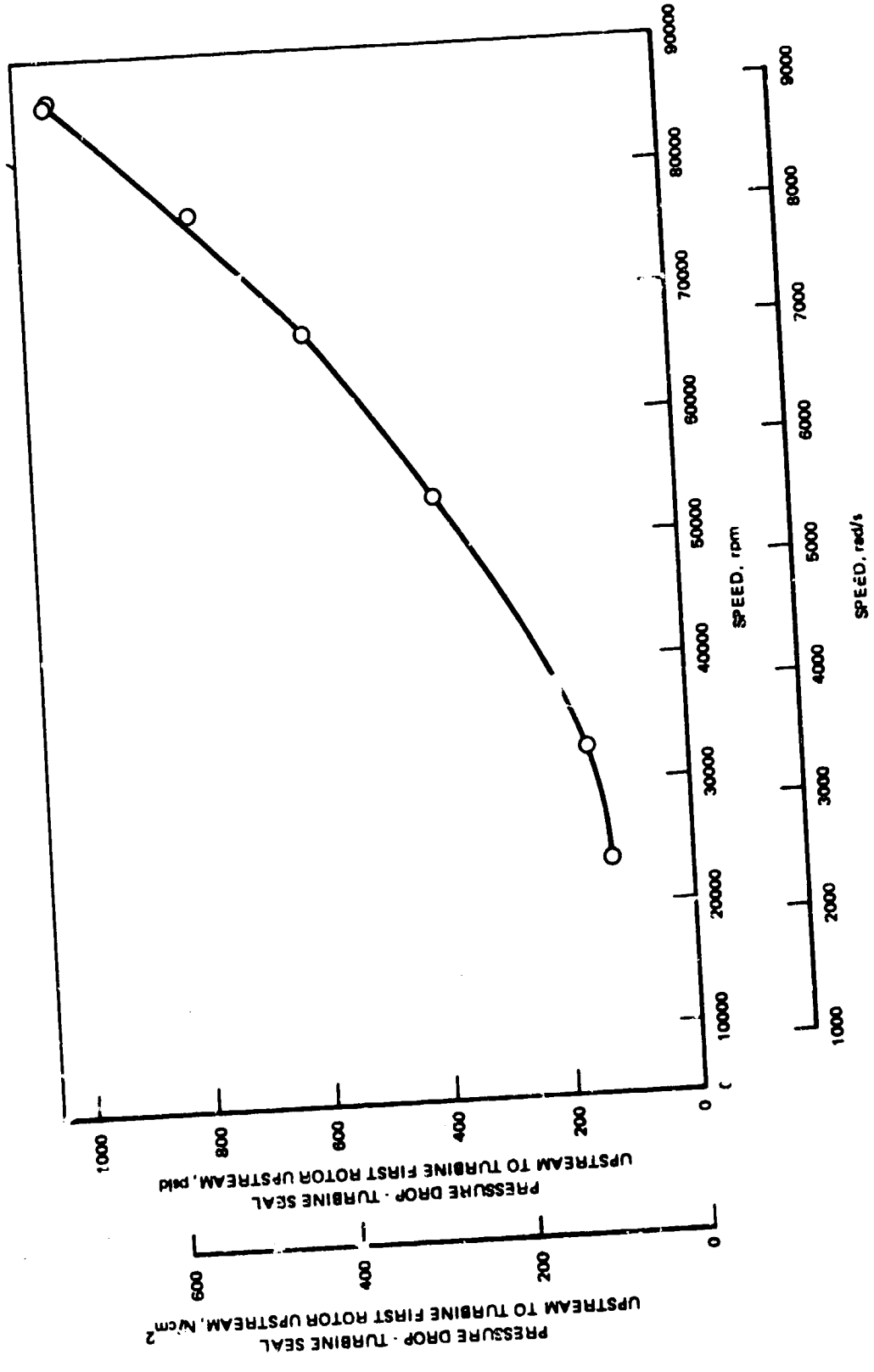

Figure 123. Turbine Shaft Seal Pressure Drop (Test 006)

Pump Bearing. The pump bearing temperatures as a function of pump speed are presented in Fig. 124. The pump inlet temperature, orifice upstream temperature, and the pump bearing temperature rise (i.e., the difference between the inlet and orifice upstream temperatures) are shown in the Figure. It is shown that the pump inlet temperature remains fairly constant over the entire speed range, and the orifice temperature increases as the speed increases. The pump bearing temperature increases as the speed increases. The pump bearing temperature rise is approximately 4 K (8 R) at 9004 rad/sec (86,000 rpm) and 0.5 K (1 R) at 2408 rad/sec (23,000 rpm), which indicates that the temperature rise across the bearing is higher at high rpm since the load on the bearing is greater. These data reveal that the pump bearing is performing as expected.

Pump bearing flowrate could not be accurately calculated because the temperature upstream of the measuring orifice indicated the flow was two-phase due to the bearing pressure drop and heat addition. With two-phase flow, the quality of the fluid must be known to determine density and enthalpy. The data reduction program used the vapor side density to calculate coolant flowrate.

Pump bearing parameters during two suction performance tests are shown in Fig. 125 and 126. A bearing temperature rise of about 4 K (8 R) is shown for both tests at high inlet pressures which compares with Fig 124. Test 007 in Fig. 125 was near the design flow coefficient. The bearing temperature rise is shown to decrease with reducing inlet pressure. It would be expected that the bearing temperature rise would increase with reducing inlet pressure because the bearing coolant flow decreases as shown by the decreasing bearing orifice pressure drop. However, the fluid at the bearing orifice is two-phase for all slices in test 007. Since bearing heat addition should be nearly constant at constant speed during the cavitation test, Fig. 125 indicates the pump bearing coolant was adequate even at very low flow because the coolant did not fully vaporize. The bearing fluid enthalpy may be increasing, but it did not because sufficiently to get to the vapor side of the dome.

Test 014 in Fig. 126 was run at a design flow ratio of 0.71. The bearing pressures and temperatures are similar down to an inlet pressure of 20.6 N/cm^2 (30 psia). Below 20.6 N/cm^2 (30 psia), the pressure drops are similar, but the orifice downstream temperature increases indicating that the bearing coolant has fully vaporized. Even then, the temperature rise was less than 14 K (25 R).

It is recommended that the turbopump not be operated at very low inlet pressures for long periods because of the low coolant flow and potential coolant vaporization and loss of effectiveness.

Turbine Bearing. The performance of the turbine bearing is presented in Fig. 127. The pump discharge temperature, turbine bearing coolant temperature, and turbine bearing temperature rise is shown at various pump speeds. The pump discharge temperature is seen to increase as the pump rpm increases; however, the turbine bearing coolant temperature remains nearly constant at about 46 K (83 R) up to 7014 rad/sec (67,000 rpm) before increasing to 61 K (110 R) at 9004 rad/sec (86,000 rpm). This results in a higher turbine bearing temperature rise at 2408 rad/sec (23,000 rpm) than at 9004 rad/sec (86,000 rpm).

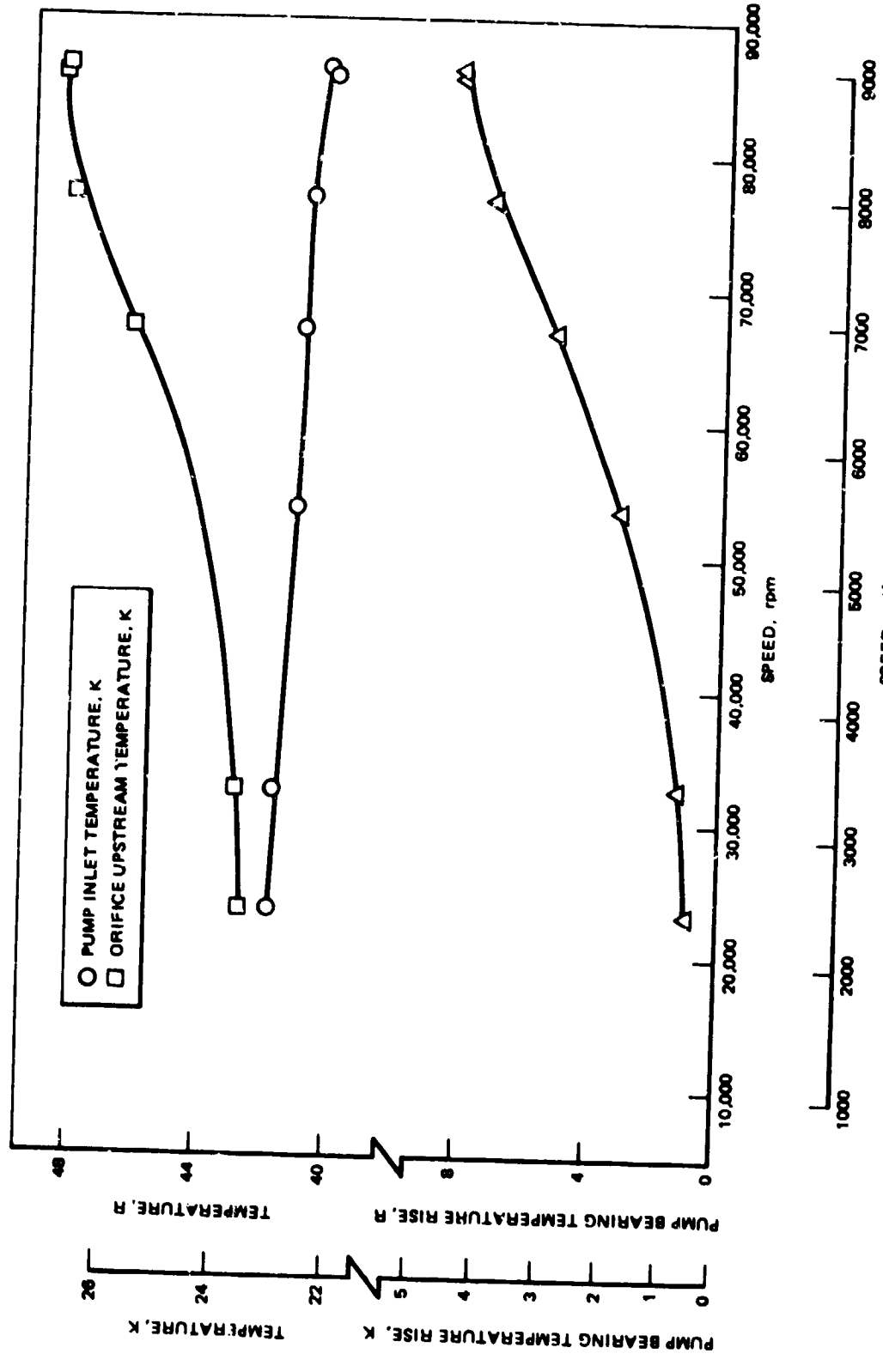

Figure 124. Pump Bearing Temperature Rise

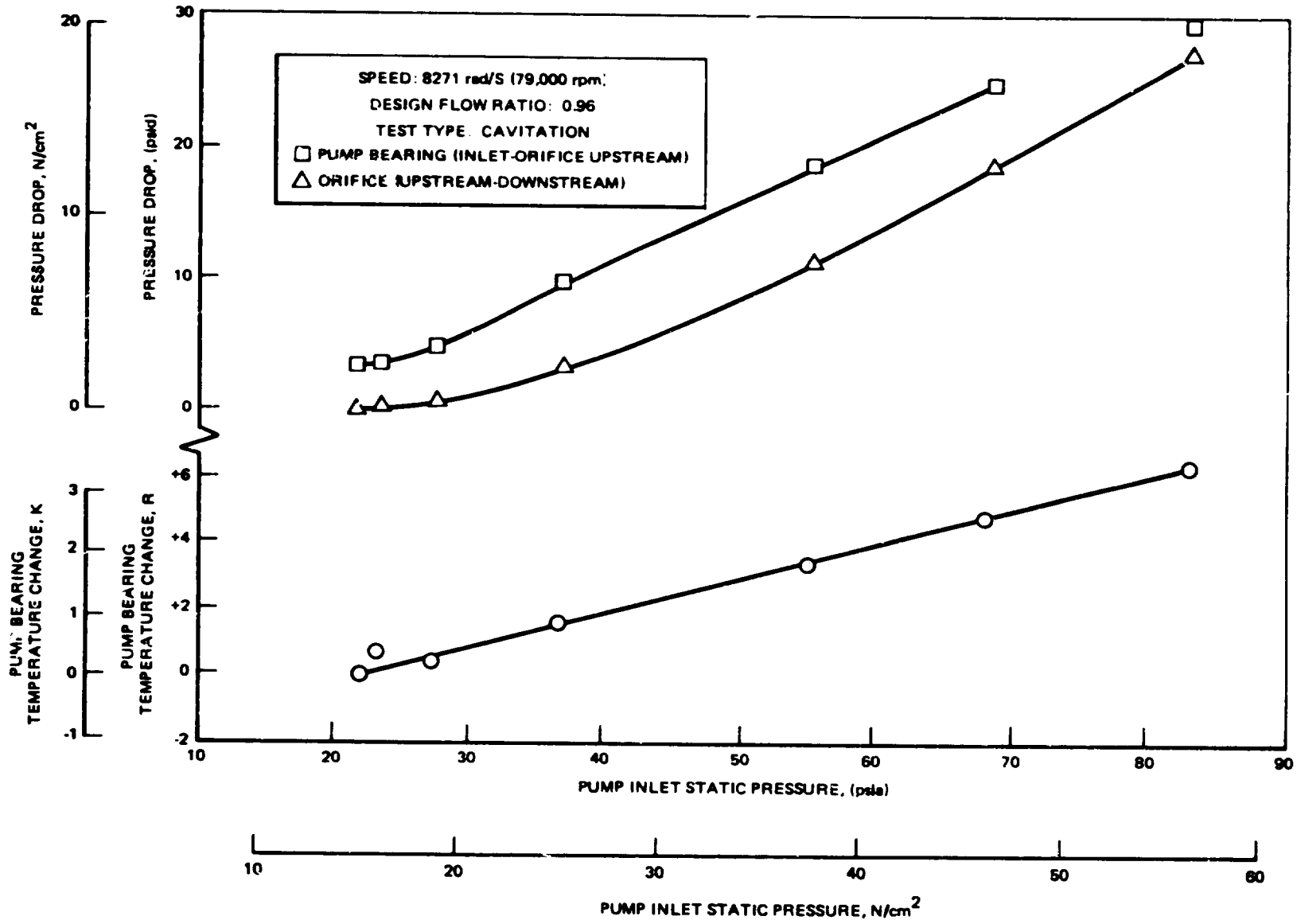

Figure 125. Pump Bearing Parameters (Test 7, 1979)

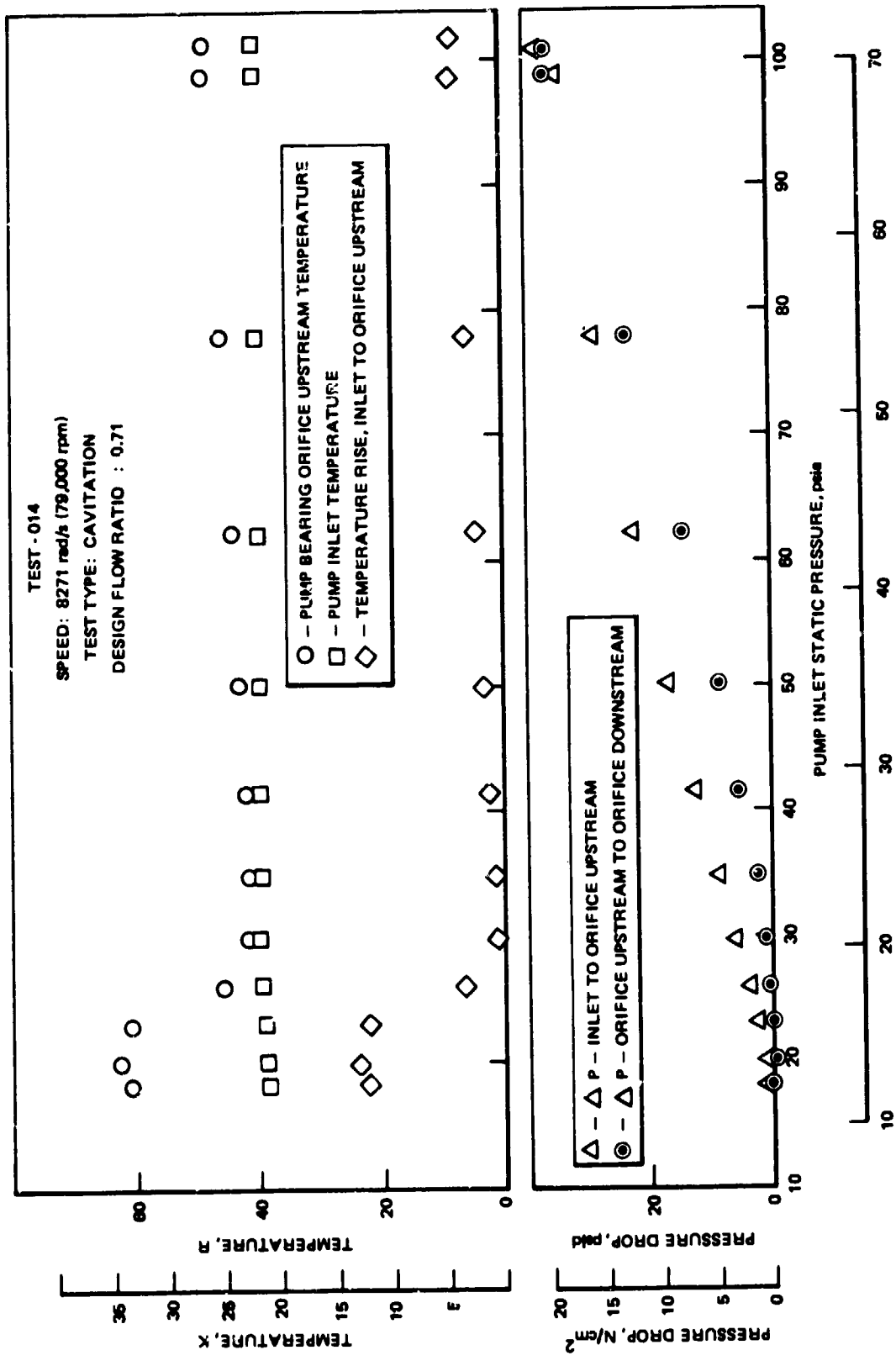

Figure 126. Pump Bearing Parameters (Test 14, 1979)

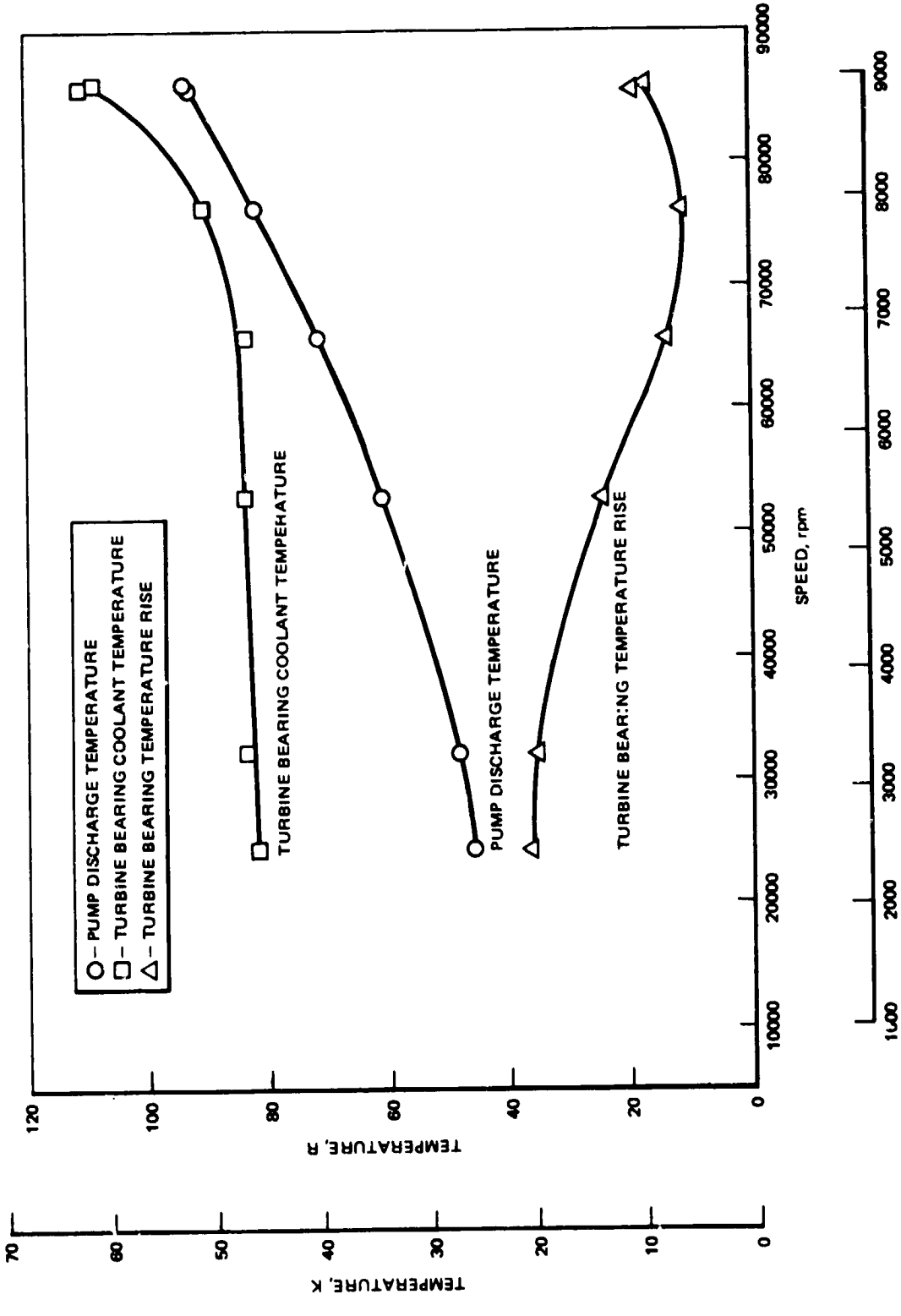

Figure 127. Turbine Bearing Temperatures

The temperature rise is 20 K (36 R) at 2408 rad/sec (23,000 rpm) as compared to 9 K (17 R) at 9004 rad/sec (86,000 rpm). This probably indicates that more flow is going through the bearing at the higher pressures associated with the higher speeds. It probably also suggests that the bearing load is small even at high speeds so that little heat addition is occurring.

Dynamic Analysis

The objectives of the Mark 48-F dynamics investigation have been to identify critical speeds, subsynchronous whirl or other dynamic anomalies which may be present within the operating range. Analytical and experimental methods were used. A finite element computer model of the rotor was developed and run to obtain the calculated critical speeds and mode shapes.

During turbopump operational tests at the LIMA test facility, dynamic data were collected from casing accelerometer and Bently proximeter instrumentation. Rap testing of the test apparatus was also done. The dynamic data were processed in oscillograph, amplitude mean squared (AMS), isoplot, and amplitude spectrum forms. Analytical and experimental results were compared for correlation.

It was concluded that critical speeds exist at 3351 rad/s (32,000 rpm) and 6750 rad/s (64,460 rpm). No subsynchronous characteristics were observed. An indication of a 12 per revolution blade wake amplitude was noted on tests 106 and 019. Amplitude increased significantly at approximately 2.2 seconds prior to cutoff.

It is recommended that prior to any future testing, the rotor and casing be independently rap tested to determine natural frequencies as an aid for future analysis of system dynamics and bearing loads.

Objectives. The overall objectives of dynamics analysis of the Mark 48-F turbopump were to note any possible dynamic problems and to make recommendations concerning their resolution. Several areas of interest are of obvious importance. These are identification of critical speeds, subsynchronous whirl, or dynamic anomalies which could be present within the operating range. To identify these phenomena, a combination of analytical and experimental techniques were used. With this in mind, the specific objectives of the dynamic investigation may be stated as follows:

1. To develop and use an analytical model to determine the calculated critical speeds and mode shapes for the Mark 48-F rotor over a range of bearing spring rates

2. To experimentally identify the critical speeds of the Mark 48-F turbopump and compare the model to these

3. To check for the presence of subsynchronous whirl characteristics in experimental data for the Mark 48-F turbopump

4. To check for the presence of dynamic anomalies in experimental data for the Mark 48-F turbopump

5. To make appropriate recommendations concerning the future design, development and testing for the Mark 48-F turbopump

Analytical. For analytical determination of critical speeds for the turbopump, the in-house structural response analysis program, V9567, was used. A finite beam element model of the Mark 48-F rotor was developed for input to the program. The important input quantities are stiffness and mass properties for the rotor. Stiffness properties are estimated from the development of a "load-line diagram" which depicts the amount of rotor material available for stiffness contribution. It is from this diagram that model element size is determined Mass and inertia properties are calculated from a drawing of the rotor, knowledge of material density, and use of the in-house PROP computer program. The resulting model for the Mark 48-F turbopump contained 59 nodes and 67 beam elements.

Two cases were considered. Case 1 is a case where the tie-bolt for the rotor assembly is not supported at its midspan and is thus free to assume its own mode of vibration, independent from the rotor as a whole. Case 2 represents the case where the tie-bolt is stiffly fixed to the rotor assembly at its midspan and thus not independent of the rotor assembly. Physically, these two cases represent the times when the midspan tie-bolt bushing does not snub and does snub against the inner diameter of the rotor assembly, respectively. Since any deflection of the tie-bolt relative to the rest of the rotor assembly will cause it to snub, Case 2 is considered to be most realistic. Each of these cases was run for a range of bearing spring rates.

Experimental. The Lima facility testing of the Mark 48-F turbopump were fully assembled operational tests. The Mark 48-F turbopump was driven by pressurized hydrogen gas and pumped liquid hydrogen during these tests. Dynamic instrumentation consisted of casing accelerometers, Bently proximeters, and a shaft speed probe.

The casing accelerometers were capable of detecting primarily rotor/casing accelerations, but would also detect the accelerations of the test structure as a whole. Five accelerometers were used and their zonal locations are shown in Fig. 128.

Bently proximeters are magnetic probes which sense the gap between the casing and the rotor shaft. Two Bently proximeters were installed on the Mark 48-F turbopump; one at the pump end and one at the turbine end.

The speed probe is a magnetic sensor which detects spotfaces on the rotor shaft. Four spotfaces are on the Mark 48-F turbopump speed nut, and therefore the oscillograph of the speed probe shows four pulses per shaft revolution. Shaft speed is then found by determining pulses per unit time.

All data from these devices were recorded simultaneously with an IRIG B time channel on magnetic tape for data processing. Three types of data processing were used. These are oscillograph records, AMS records, and isoplots. Oscillograph records are time histories of instrumentation responses. They give

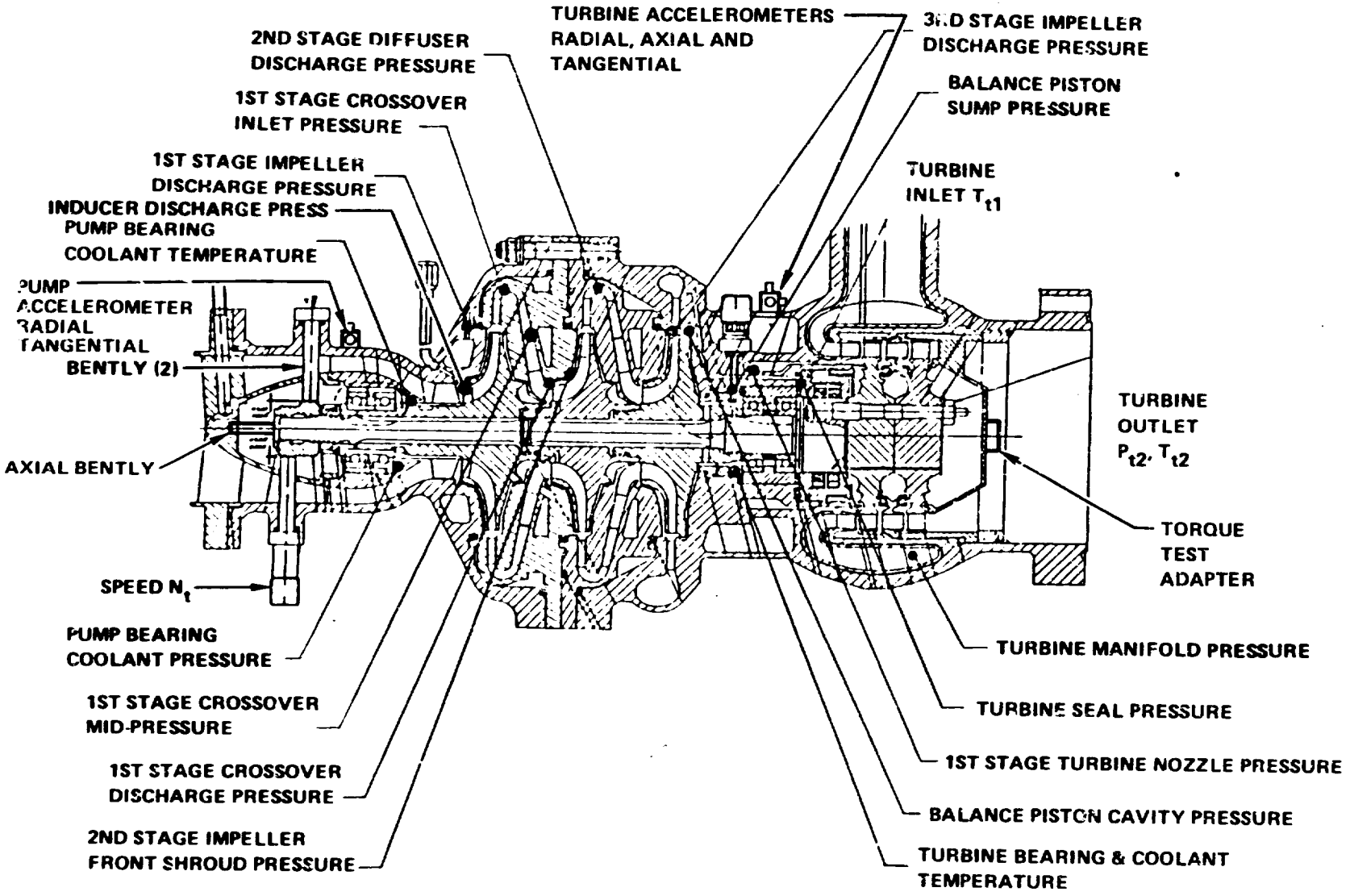

Figure 128. Mark 48-F Pump Instrumentation

discrete data for each test at some point in time. Amplitude mean squared (AMS) records display the squared value of a time averaged instrumentation response, usually versus pump speed (normal averaging time is 200 ms). Isoplots give relative frequency response (much like a power spectral density) as a function of test time for accelerometer responses. Each of these data processing techniques has a different value in analyzing test results.

Detection of Critical Speeds From Experimental Data. During testing, the Mark 48-F turbopump was instrumented with accelerometers, Bently proximeters, and a speed probe for measurement of dynamic characteristics. Using this instrumentation and the subsequent data processing (oscillograph and AMS records), three methods were devised for the detection of critical speeds.

ID Method No. 1 utilizes accelerometer measurements and the oscillograph record. Accelerometers are mounted on the case of the turbopump (Fig. 128). Accelerations detected at the case may be expected to be large while the rotor is precessing at its critical speed. Thus, as pump speed approaches the critical speed, acceleration levels tend to increase and, as pump speed moves away from the critical speed, accelerations tend to decrease. During speed ramps in the test, this phenomenon manifests itself as a "blossom" in the oscillograph record. Since the oscillograph relates all parameters of interest simultaneously, pump speed may be read from one track, directly below the blossom.

Depending on how the data for each test have been processed, speed may be read by counting speed probe pulses per unit time, from a d-c conversion or by counting the one pulse per revolution disturbance noted by the accelerometers themselves.

This method of critical speed identification is considered by the author to be the most reliable.

ID Method No. 2 utilizes the speed probe itself and the oscillograph record for detection of a critical speed, the speed probe senses the slots cut in the speed nut on the rotor shaft. On the Mark 48-F, the speed nut has four slots. Thus, for each revolution of the shaft, the speed probe senses four pulses. While operating at a speed other than the critical speed, these pulses appear nearly equal in magnitude on the oscillograph record. While operating at a critical speed, however, the precession of the rotor may cause the speed nut to assume varying positions with respect to the speed probe during a shaft revolution. Due to the varying distance of the slots from the speed probe, the amplitude of the pulses begins to modulate. The frequency of the modulation should be close to one fourth that of the speed probe pulses. An inspection of the oscillograph record may reveal this modulation, and the critical speed can be taken at that point from the oscillograph.

ID Method No. 3 utilizes the AMS record of casing accelerometers. A critical speed appears as an abrupt resonance on the AMS (since the AMS is a square function). From experience, a critical speed is considered to be positively identified when at least 60% of the accelerometers respond simultaneously.

Discussion of Results. Figures 129 through 133 show calculated critical speeds and mode shapes for the cases with and without the tie-bolt spring included in the analytical model. Case 1 represents that where the tie-bolt does not snub against the ID of the rotor assembly. Thus, the tie-bolt is free to assume its own critical speed independent of the rotor assembly as a whole. Case 2 represents the case where the tie-bolt is stiffly tied to the rotor assembly at its midpoint and is therefore not independent of the rotor assembly. Case 1 shows a much lower third critical speed and greatly different mode shape than those of Case 2. This third critical speed of Case 1 may be interpreted as the "tie-bolt mode." It may be seen that the fourth critical speed of Case 1 is nearly equivalent to the third critical speed of Case 2. Thus, when the tie-bolt is stiffly fastened to the rotor assembly, the third mode of Case 1 vanishes. This accounts for the differences in the mode shape. Since any deflection of the tie-bolt will cause it to snub against the rotor assembly ID, Case 2 is the analytical model which most closely represents the real conditions.

A summary of the dynamic analysis data developed during the study of the turbopump is presented. Table 15 through 17, presents the identification of the first through third critical speeds found from the three methods of critical speed determination. Table 18 presents a comparison of the calculated and observed critical speeds from the test program. Table 19 summarizes the turbopump acceleration levels at 8545 rad/s (81600 rpm) for the Lima test stand tests 17 through 19. The results show a reasonable correlation between the calculated critical speeds and those observed for the first two modes from oscillograph data. Case 2 shows poor correlation with the observed critical speed for the third mode. Case 1 shows good correlation with the third mode, but this seems unreasonable since its correlation is even better than that of mode 1. Decreasing correlation would be expected with higher modes of vibration. Recalling that the predicted third mode is the tie-bolt mode and is not a realistic representation of the Mark 48-F turbopump, explains why this improvement in correlation occurs. Therefore, according to the model, the third critical speed should be near 13509 rad/s (129000 rpm) and according to experimental results, a critical speed occurs at 9676 rad/s (92400 rpm).

The mode shape for the third critical speed is a whipping of the pump end of the rotor. If the observed 9676 rad/s (92400 rpm) critical speed is real, then the speed probe and Bently proximeter data should detect this motion. Examination of the oscillograph data for -018 and -019, however, does not indicate its presence. The possibility exists that the observed critical speed is really a pump excited structural resonance. Posttest inspection of the components shows them to be in good condition. Although vibration "cuts" were experienced in testing, no signs of rubbing appear on the rotor.

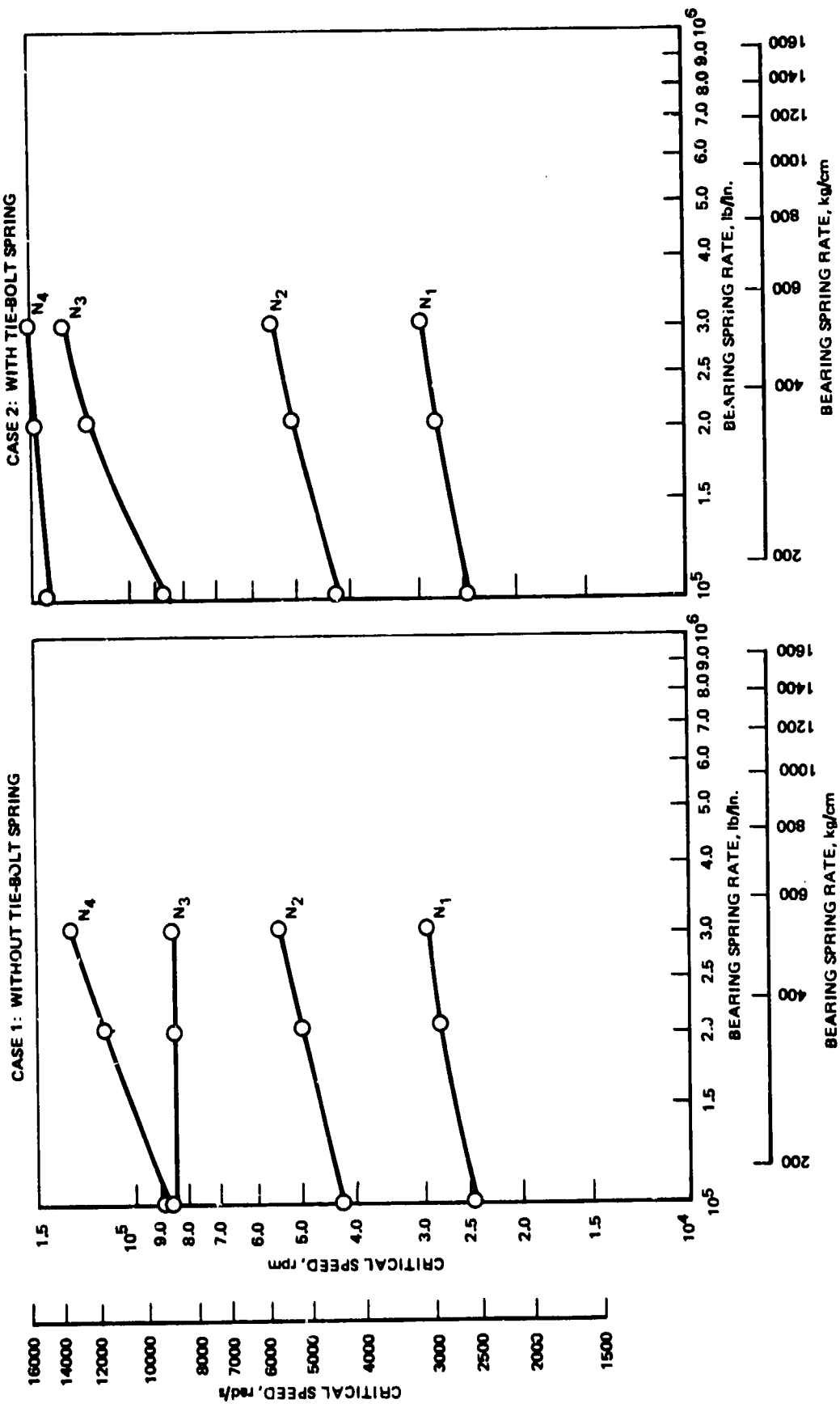

Figure 129. Critical Speeds as Function of Bearing Spring Rate

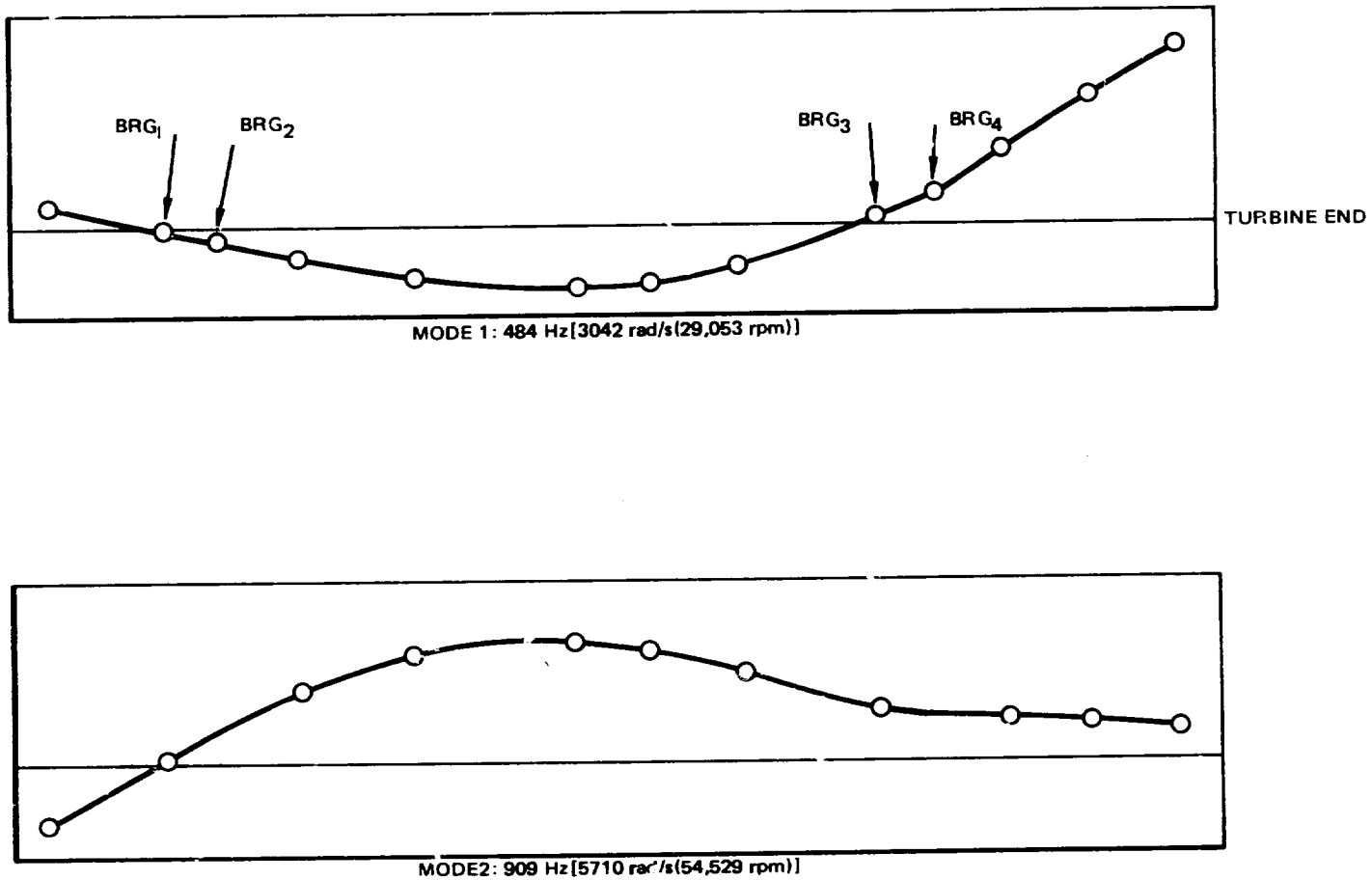

Figure 130. Calculated Mode Shapes for Turbopump Without Tie Bolt Spring (Mode 1 and 2)

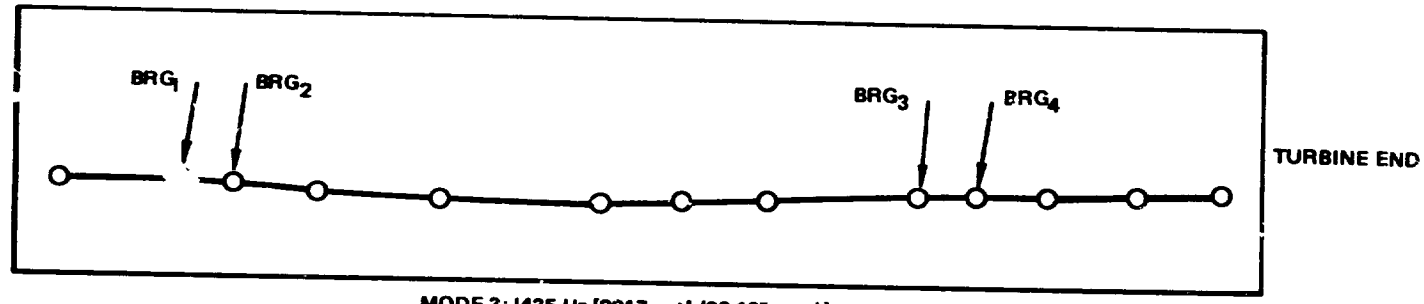

MODE 3: 1435 Hz [9017 rad/s(86,107 rpm)]

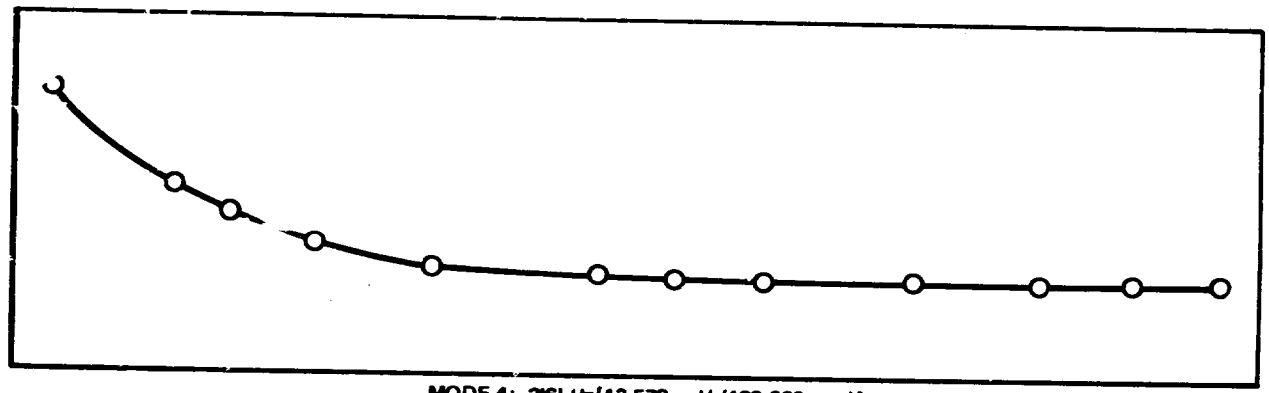

MODE 4: 2161 Hz[13 578 rad/s(129,663 rpm)]

Figure 131. Calculated Mode Shapes for Turbopump Without Tie Bolt Spring (Mode 3 and 4)

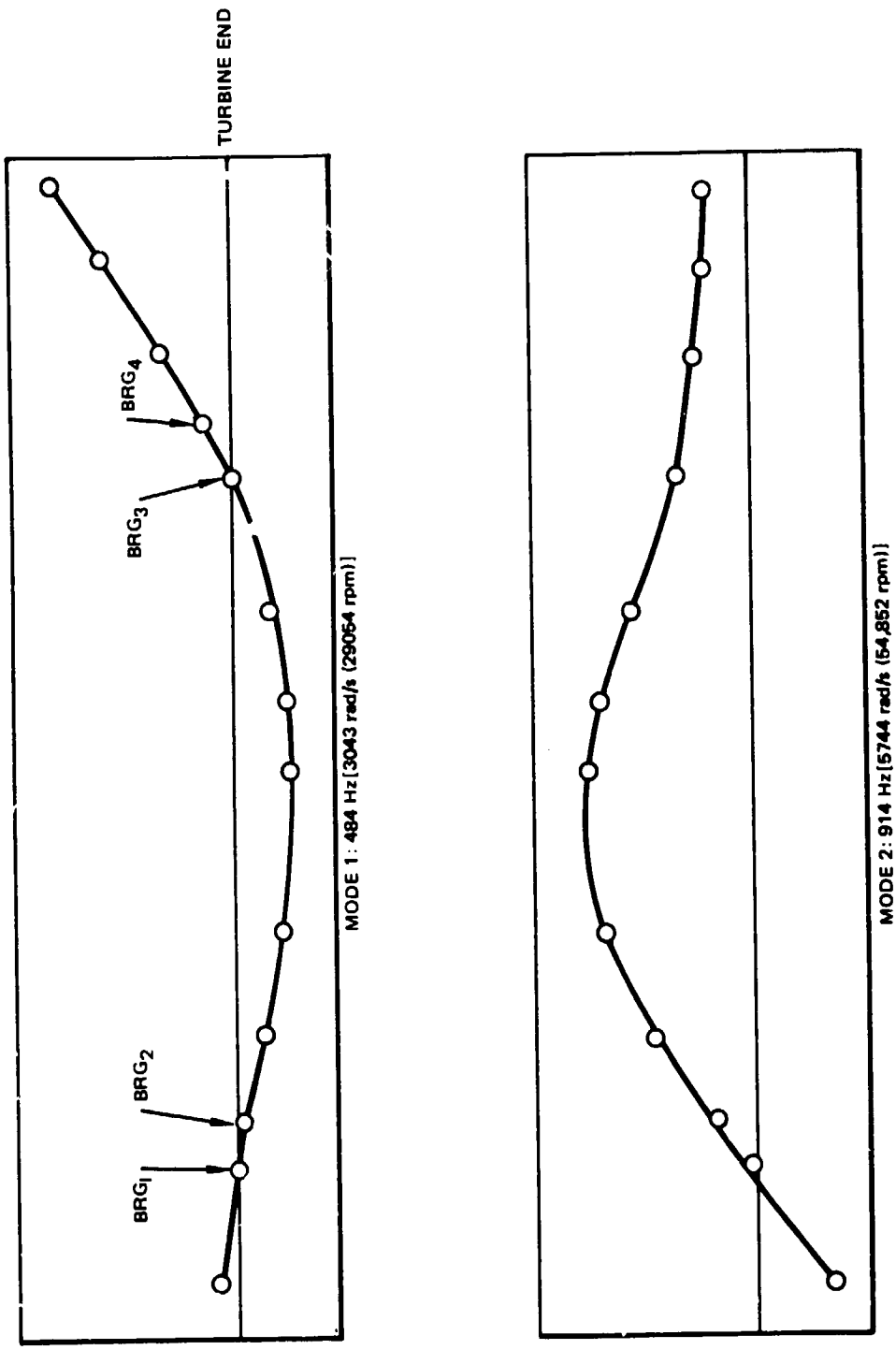

Figure 132. Calculated Mode Shapes for Turbopump With Tie Bolt Spring (Mode 1 and 2)

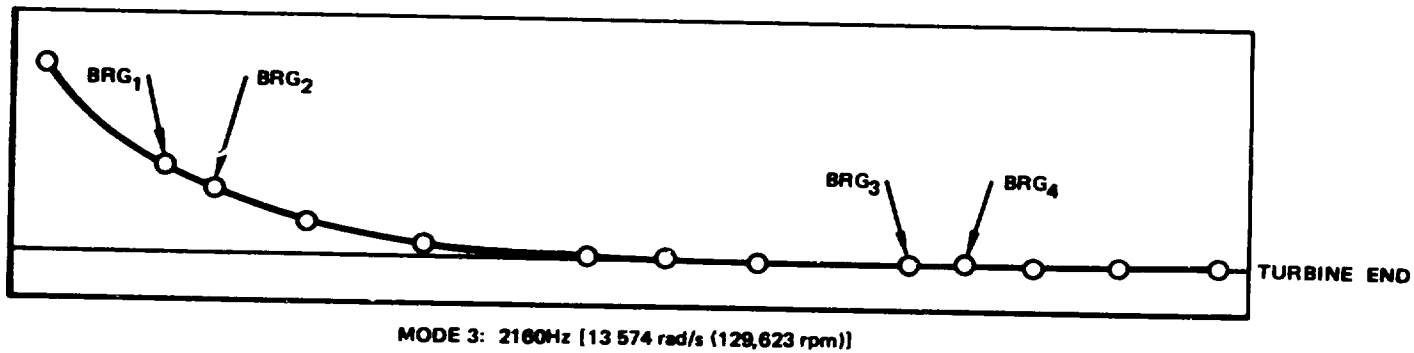

Figure 133. Calculated Mode Shapes for Turbopump With Tie Bolt Spring (Mode 3)

TABLE 15. IDENTIFICATION OF FIRST CRITICAL SPEED FOR MARK 48-F TURBOPUMP

Lima Test No.	Critical Speed, rad/s (rpm)		
	Identification Method No. 1	Identification Method No. 2	Identification Method No. 3
-015	ND*	ND	ND
-016	3,299 3,848 (31,500)/(36,750)	NA**	NA
-017	3299 (31,500)	NA	3519 (33,600)
-018	3299 (31,500)	ND	NA
-019	3519 (33,600)	ND	3560 (34,000)

*ND - Data "Not Distinguishable"
**NA - Data "Not Available"

TABLE 16. IDENTIFICATION OF SECOND CRITICAL SPEED FOR MARK 48-F TURBOPUMP

Lima Test No.	Critical Speed, rad/s (rpm)		
	Identification Method No. 1	Identification Method No. 2	Identification Method No. 3
-015	6676 (63,750)	ND*	6723 (64,200)
-016	6597 (63,000)	NA**	NA
-017	6880 (65,700)	NA	6912 (66,000)
-018	ND	ND	NA
-019	6849 (65,400)	ND	7137 (68,150)

*ND - Data "Not Distinguishable"
**NA - Data "Not Available"

TABLE 17. IDENTIFICATION OF THIRD CRITICAL SPEED FOR MARK 48-F TURBOPUMP

Lima Test No.	Critical Speed, rad/s (rpm)		
	Identification Method No. 1	Identification Method No. 2	Identification Method No. 3
-015	--	--	--
-016	9425 (90,000)	NA*	NA
-017	ND	NA	8419 (80,400)
-018	ND	ND**	NA
-019	9922 (94,800)	ND	8667 (82,760)

*NA - Data "Not Available"
**ND - Data "Not Distinguishable"
--Test -015 Not Run To Third Critical

TABLE 18. COMPARISON OF CALCULATED AND OBSERVED CRITICAL SPEEDS

Critical Speed	Average Observed Critical Speed, ID 1; rad/s (rpm)	Calculated Critical Speed, rad/s (rpm)			
		Case 1	% Difference	Case 2	% Difference
First	3,351 (32,000)	3,042 (29,053)	9.2	3,043 (29,054)	9.2
Second	6,750 (64,460)	5,710 (54,529)	15.4	5,744 (54,852)	14.9
Third	9,676 (92,400)	9.017 (86,107)	6.8	13,574 (129,623)	39.6

Note:
1. Observed critical speeds taken as true values for percent difference calculations.
2. Bearing spring rate taken as 300,000 lb./in.
3. Case 1: Model without tie-bolt spring
   Case 2: Model with tie-bolt spring

TABLE 19. MARK 48-F TURBOPUMP ACCELERATION LEVELS AT 8545 rad/s (81,600 rpm) FOR LIMA TESTS -017, -018, AND -019

Lima Test No.	Acceleration, g p-p				
	PRA	PTA	TRA	TTA	TAA
-017	8.7	5.5	10.1	11.5	20.5
-018	13.9	7.6	10.1	17.0	17.1
-019	13.4	8.5	10.5	19.1	30.0

Structural rap testing was performed at the Lima facility for the purpose of identifying test stand structural resonances. The raps were made in likely locations at the turbine end of the apparatus. Accelerometer data obtained from the rap test were processed into amplitude spectrum graphs (rms acceleration versus frequency) from which predominant frequencies were recorded. The rap locations and test results are summarized in Table 20.

Table 20 shows that the three structural resonances exist very near the observed critical speed. All three of these resonances were detected by rap testing near the turbine end exhaust support frame. Lima-018 and -019 tests show that the turbine end accelerometer responses are higher than those of pump end accelerometers at cutoff. The resonance of 1581 Hz shows identical correlation with test -019 observed critical speed of 9927 rad/s (94800 rpm). Therefore, it is concluded that the observed critical speed of 9676 rad/s (92400 rpm) is most probably a test stand structural resonance.

Test data from tests -018 and -019 are presented in the form of isoplots in Fig. 134 and 135. The Bently proximeter test data for test -019 is given in Fig. 136. From the data shown in Fig. 134 and 135 it may be observed that no subsynchronous characteristics are exhibited.

From analysis of the data in Fig. 135, it is concluded that a significant increase in the 12 per revolution blade wake amplitude occurs at approximately 2.2 seconds prior to cutoff. At approximately 2.6 seconds prior to cutoff, the Bently proximeter data of Fig. 136 show initiation of significant 40 Hz oscillations. Because of their close correlation in time, these occurrences are considered to be related.

Conclusions. From the results presented in Table 18, it is concluded that the Mark 48-F turbopump critical speeds for the first and second modes are 3351 rad/s (32000 rpm) and 6750 rad/s (64460 rpm), respectively. These critical speeds show reasonable correlation with the analytical model. It is further concluded that the observed critical speed of 9676 rad/s (92400 rpm) is most probably a test stand structural resonance.

TABLE 20. MARK-48F LIMA RAP TEST RTDA AMPLITUDE SPECTRUM DATA

TABLE REPORTS PREDOMINENT FREQ. BETWEEN 1400 & 2000 HZ

ACCEL LOCATION \ IMPACT LOCATION	① HZ	② HZ	③ HZ	④ HZ	⑤ HZ	⑥ HZ	⑦ HZ
PUMP RAD NO. 1 (VSC)	1680	1680 1920	–	–	1700	1710	–
PUMP TANG NO. 2	1775* 1854	1745 1920	–	–	1700 1775	1727 1830	–
TURBINE RAD NO. 3 (VSC)	1920	1854 1900 1980	–	–	1916	1980	–
TURBINE TANG NO. 4	1568* 1768 1920	1900	1968	–	1700 1775 1854	1742 1916	1581 1720 1960
TURBINE AXIAL	1980	1900	–	1968	1700 1775 1854	1716 1885 1935	1644 1710 1900

*NOISEY

IMPACT LOCATION
① TURBINE EXIT FLANGE RADIAL AXIS (3 HITS)
② TURBINE EXIT FLANGE TANGENT AXIS (3 HITS)
③ TURBINE INLET FLANGE AXIAL (3 HITS) POOR CONTACT
④ COMBUSTER BODY (3 HITS)
⑤ 4' DOWN TURBINE EXHAUST DUCT (3 HITS)
⑥ FLEX JOINT FLANGE (3 HITS)
⑦ PUMP SUPPORT FLANGE (3 HITS)

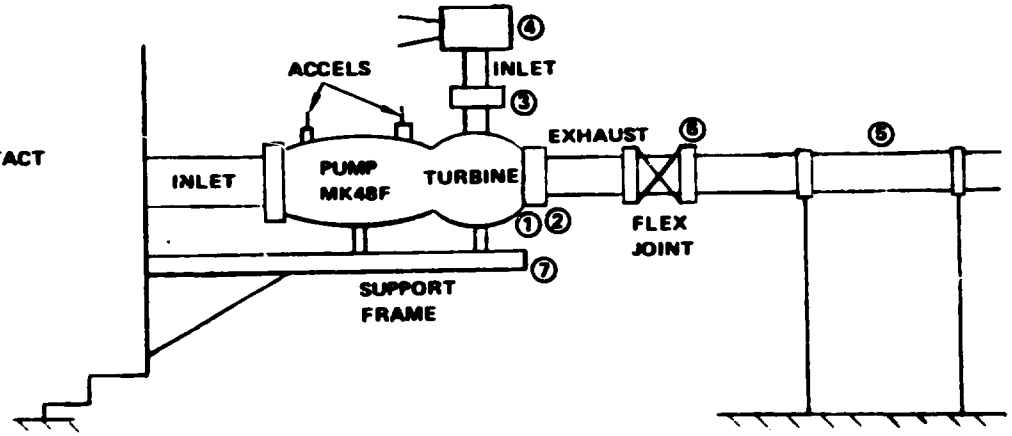

236-69

Rockwell International
Rocketdyne Division

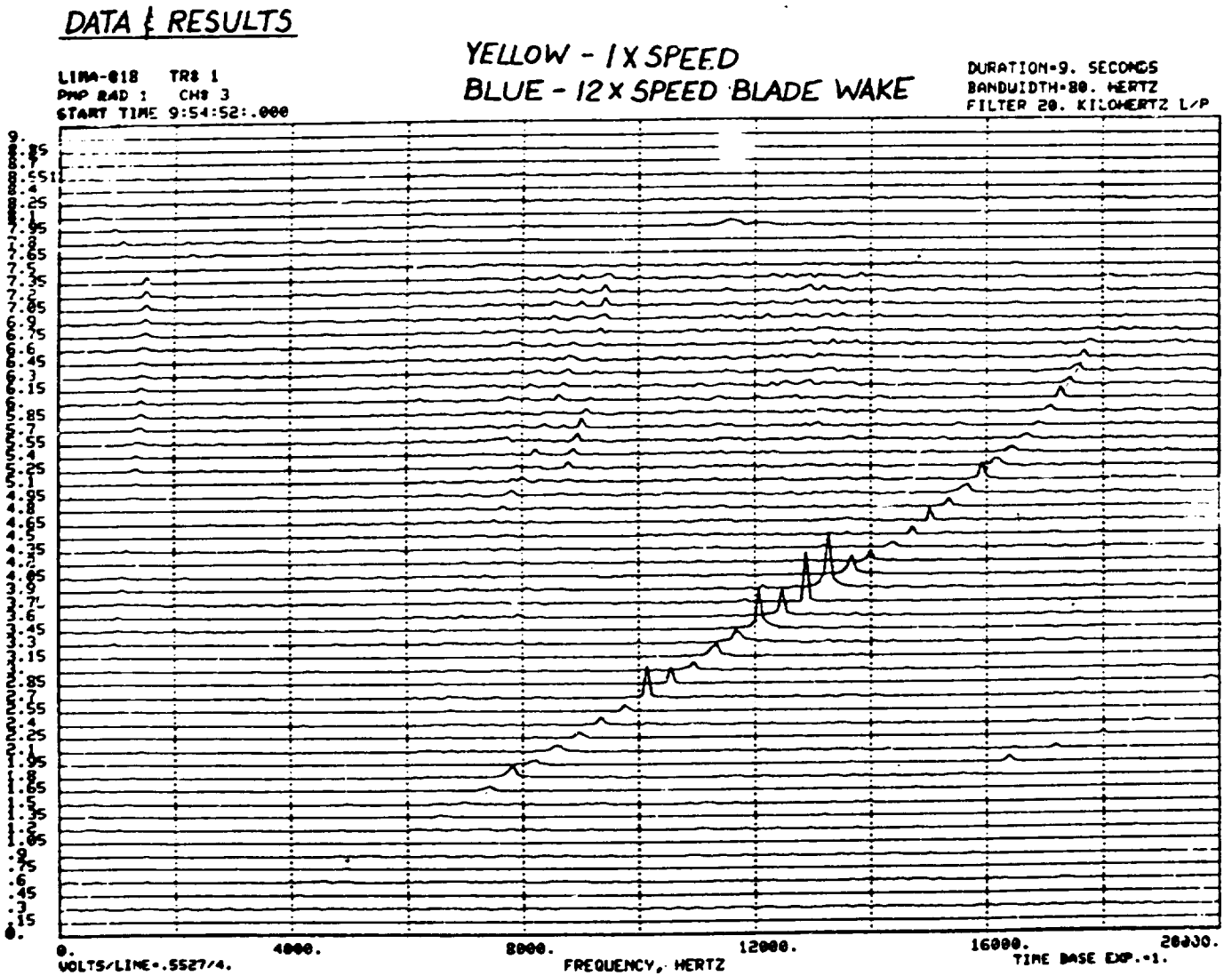

Figure 134. Test 018 Isoplot

DATA & RESULTS

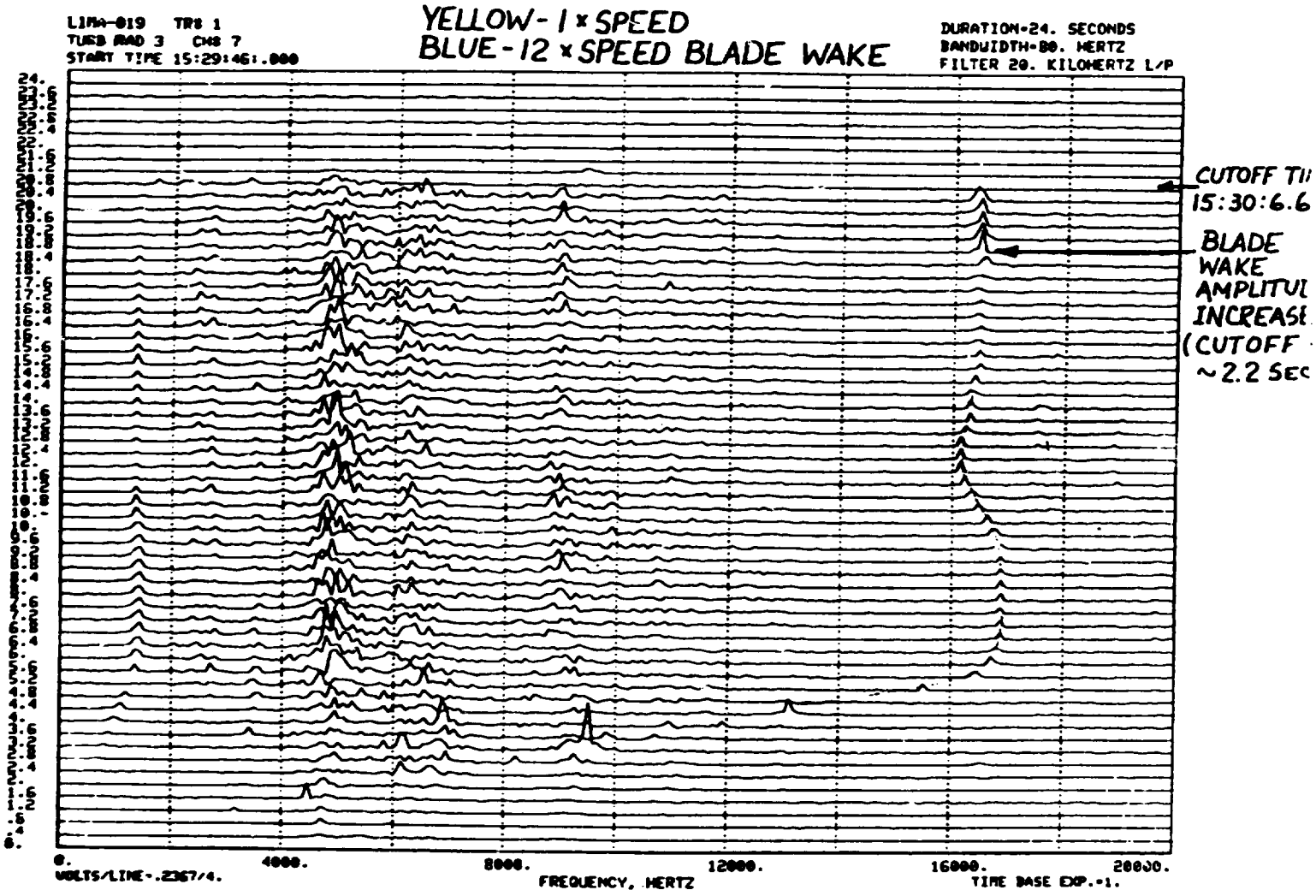

Figure 135. Test 019 Isoplot

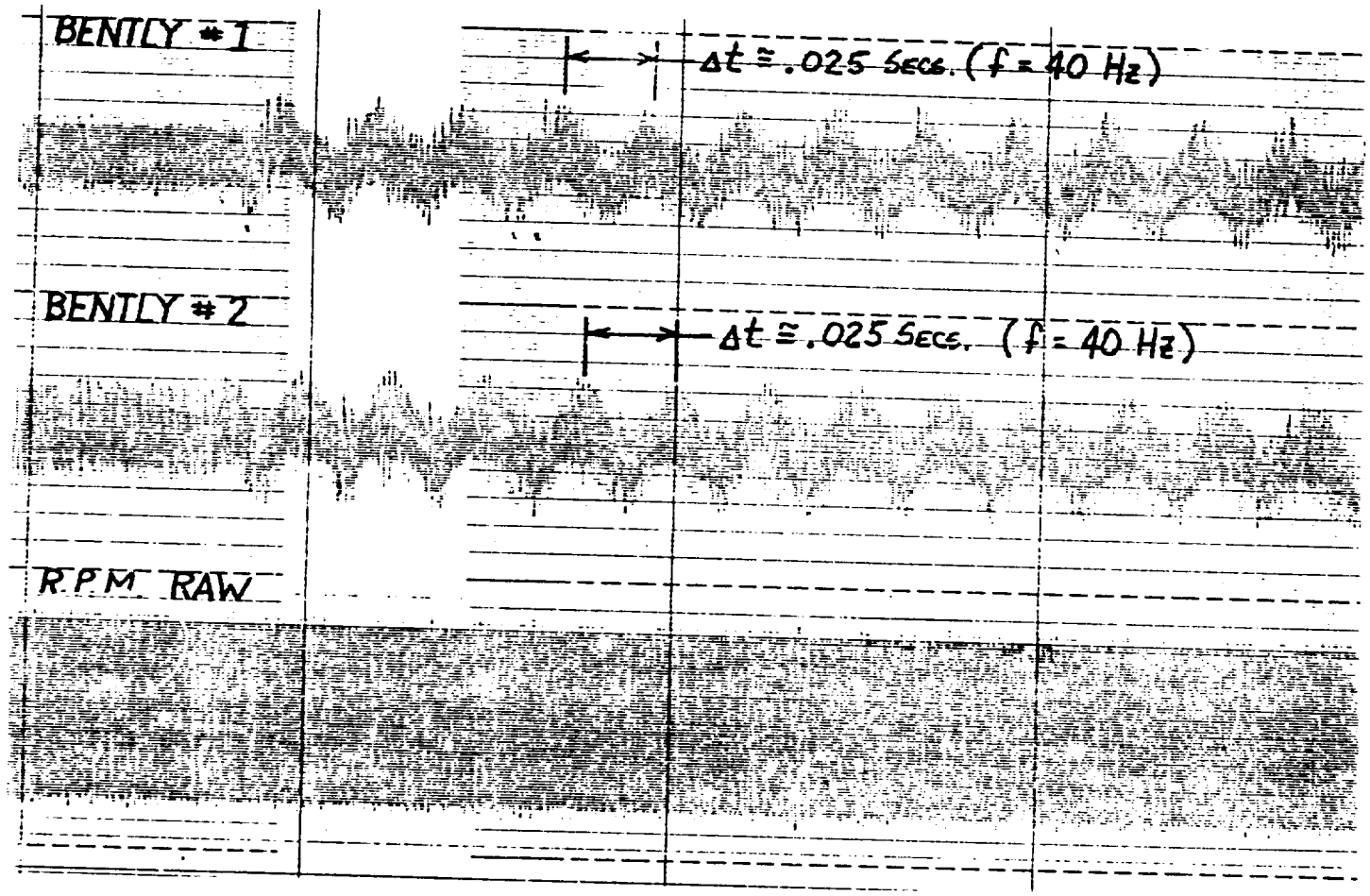

Figure 136. Bently Proximeter Data (Test 019)

From the data shown in Fig. 134 and 135, no characteristics of subsynchronous whirl are observed for the Mark 48-F turbopump.

From the analysis of the data in Fig. 133, it is concluded that a significant increase in the 12 per revolution blade wake amplitude occurs at approximately 2.6 seconds prior to cutoff. The Bently proximeter data of Fig. 135 shows initiation of significant 40 Hz oscillations. Because of their close correlation in time, these occurences are considered to be related.

Recommendations. It is recommended that prior to any future testing of the Mark 48-F turbopump, the rotor and casing be independently rap tested to determine natural frequencies as an aid in future analyses of system dynamics and bearing loads. The casing accelerometer data identifies resonances, but it is often difficult to determine whether the observed resonance is a rotor mode or a casing mode. Rap testing is a fast, accurate, cost-effective method of identifying rotor and casing frequencies.

Turbopump Disassembly and Hardware Evaluation

Turbopump S/N 01-2 was completely disassembled after the 1979 test series and the detail components were examined for signs of excessive wear or incipient failure. The hardware evaluation consisted of detailed visual inspection of all components, followed by penetrant and X-ray tests of the most critical parts. Figures 137 through 146 illustrate the posttest condition of the parts. All components were in excellent condition with the exception of the second-stage impeller which had a crack in the electron beam weld joining the pre-impeller to the main impeller front shroud. Figure 137 includes the three impellers, both turbine wheels, turbine second-stage nozzle, and bearing package components. The two crossovers and axial inlet ports are illustrated in Fig. 138. The first-stage turbine wheel and second-stage nozzle are included in Fig. 139. The second-stage wheel is shown in Fig. 140 with the cover which includes the copper plated tip seal. A satisfactory rub pattern in the copper plate is evident in Fig. 140. Some of the instrumentation is shown in Fig. 141 with the shaft seal and tie bolt. A close-up view of the latter two pieces is presented in Fig. 142, showing the rub pattern on the dynamic seal portion of the tie bolt. A typical bearing condition is exemplified in Fig. 143. The close-up views shown in Fig. 144 through 146 illustrate the condition of the silver plated first-, second- and third-stage inlet step labyrinths. Some rubbing has taken place at each step labyrinth, but without detrimental long term effects.

The crack incurred in the second-stage impeller is shown in Fig. 147. A cross section of the impeller, illustrating the location of the electron beam weld joint is included in Fig. 148. Analysis with the aid of X-rays revealed that the electron-beam weld center was not located precisely on the interface between the two parts. As a result, the interface was fused only over part of the depth. The weld is not a structural joint from the standpoint of either detail needing it to sustain centrifugal loads. Its function is to prevent fluid recirculation and to provide a path to transmit torque from the main impeller hub to the preimpeller. Since there is sufficient radial interference at the hub between the two components to accomplish the latter function, the impeller could have continued to operate with possibly some increase in internal leakage. The impeller was not destroyed for the analysis; plans are to reweld the joint with a properly located electron beam weld pass, and continue to use it in future testing.

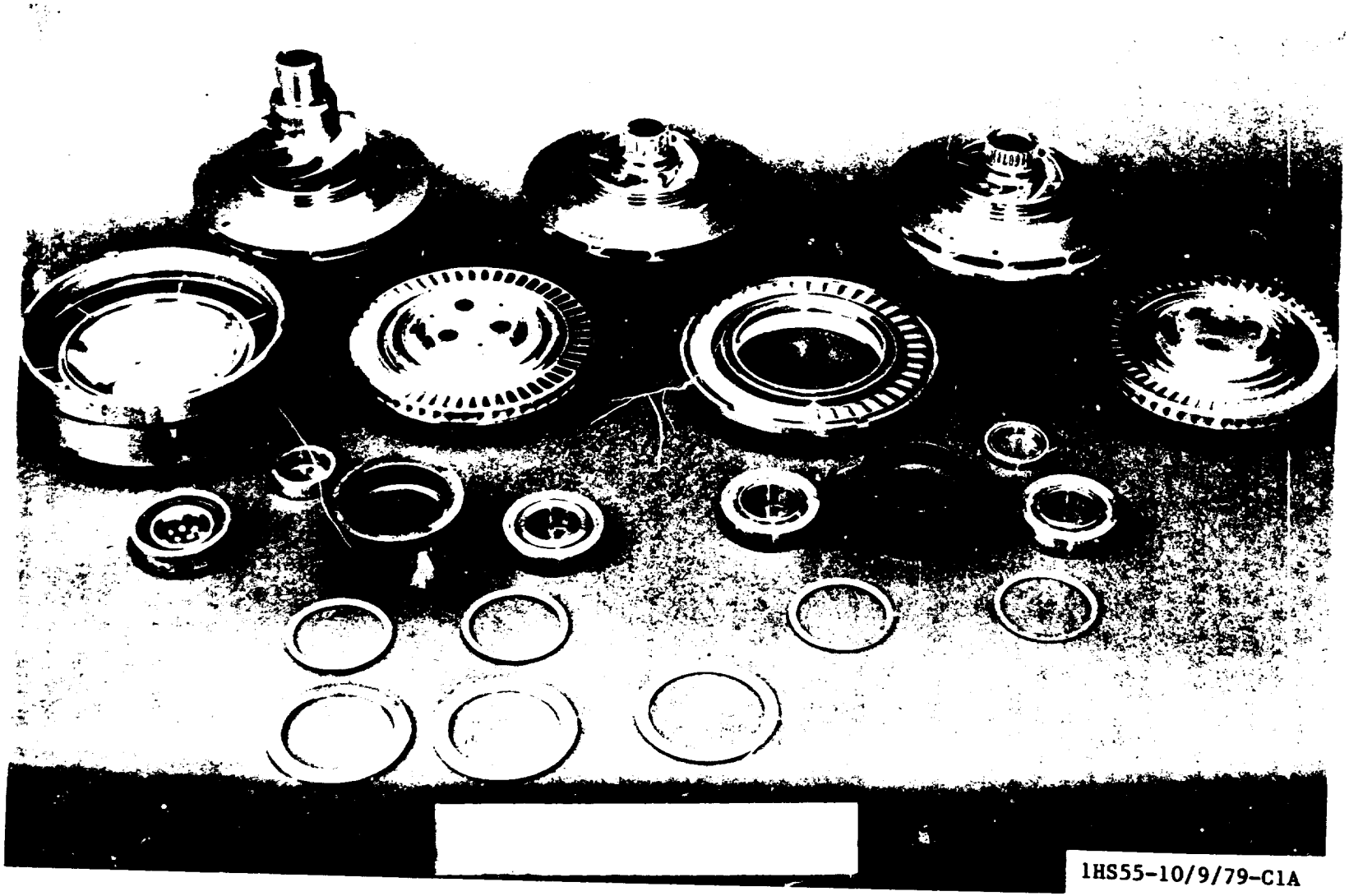

Figure 137. Rotating Elements and Bearings

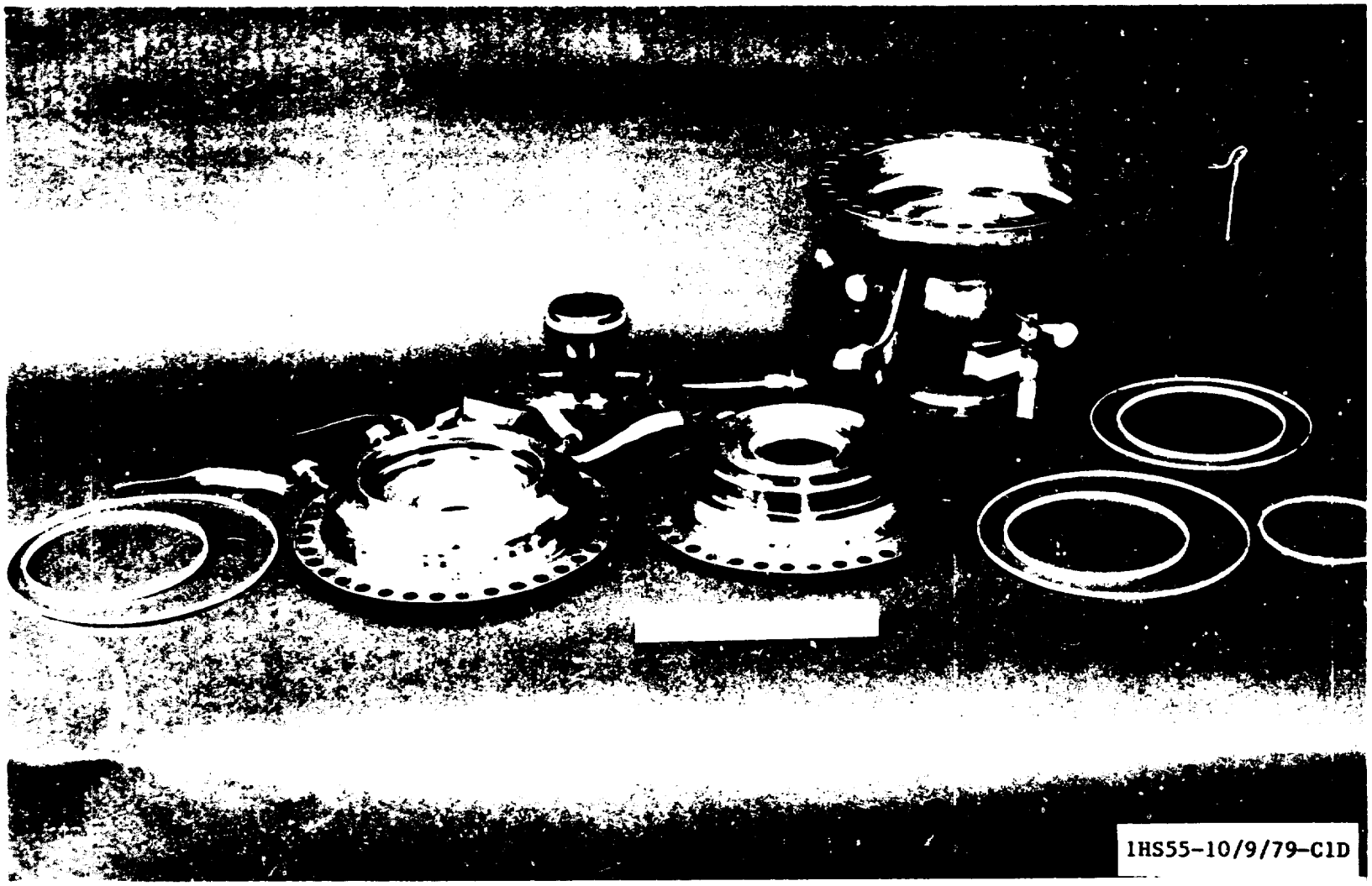

Figure 138. Axial Inlet and Crossover Components

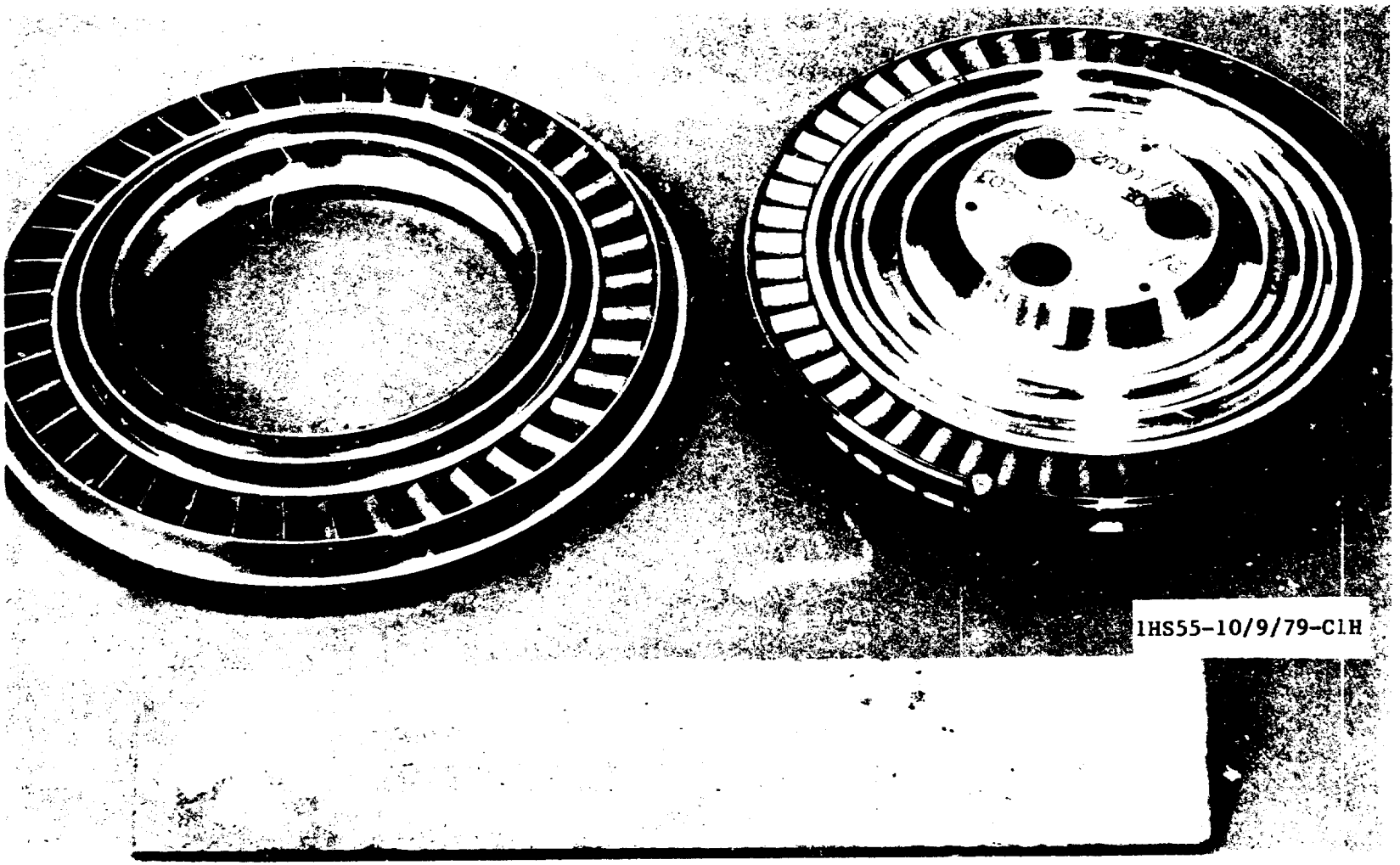

Figure 139. First Stage Turbine Wheel - Second Stage Nozzle

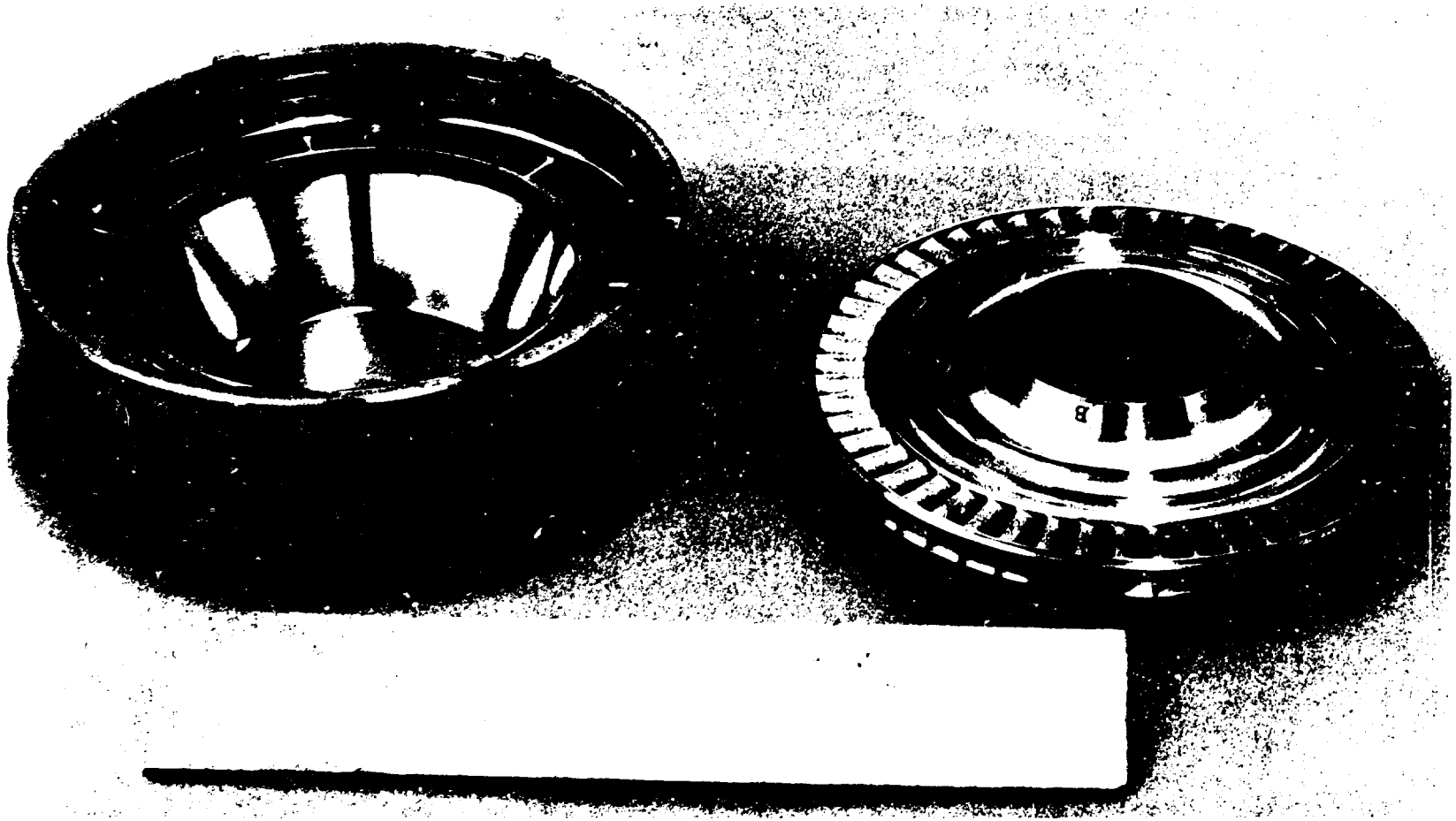

1HS55-10/9/79-C1G

Figure 140. Second Stage Turbine Wheel - Exhaust Cover

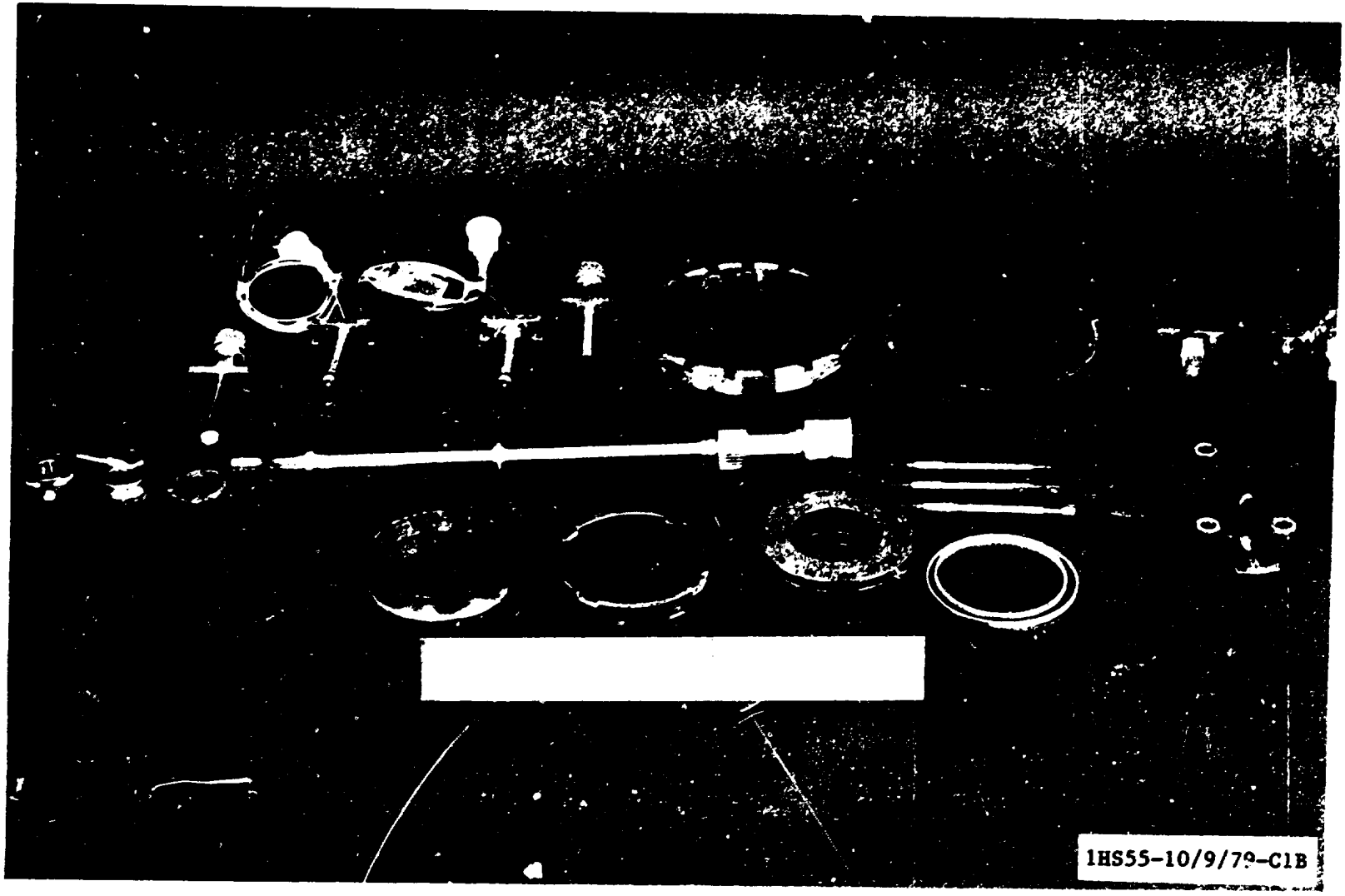

Figure 141. Pump Instrumentation, Shaft Seal and Tie Bolt

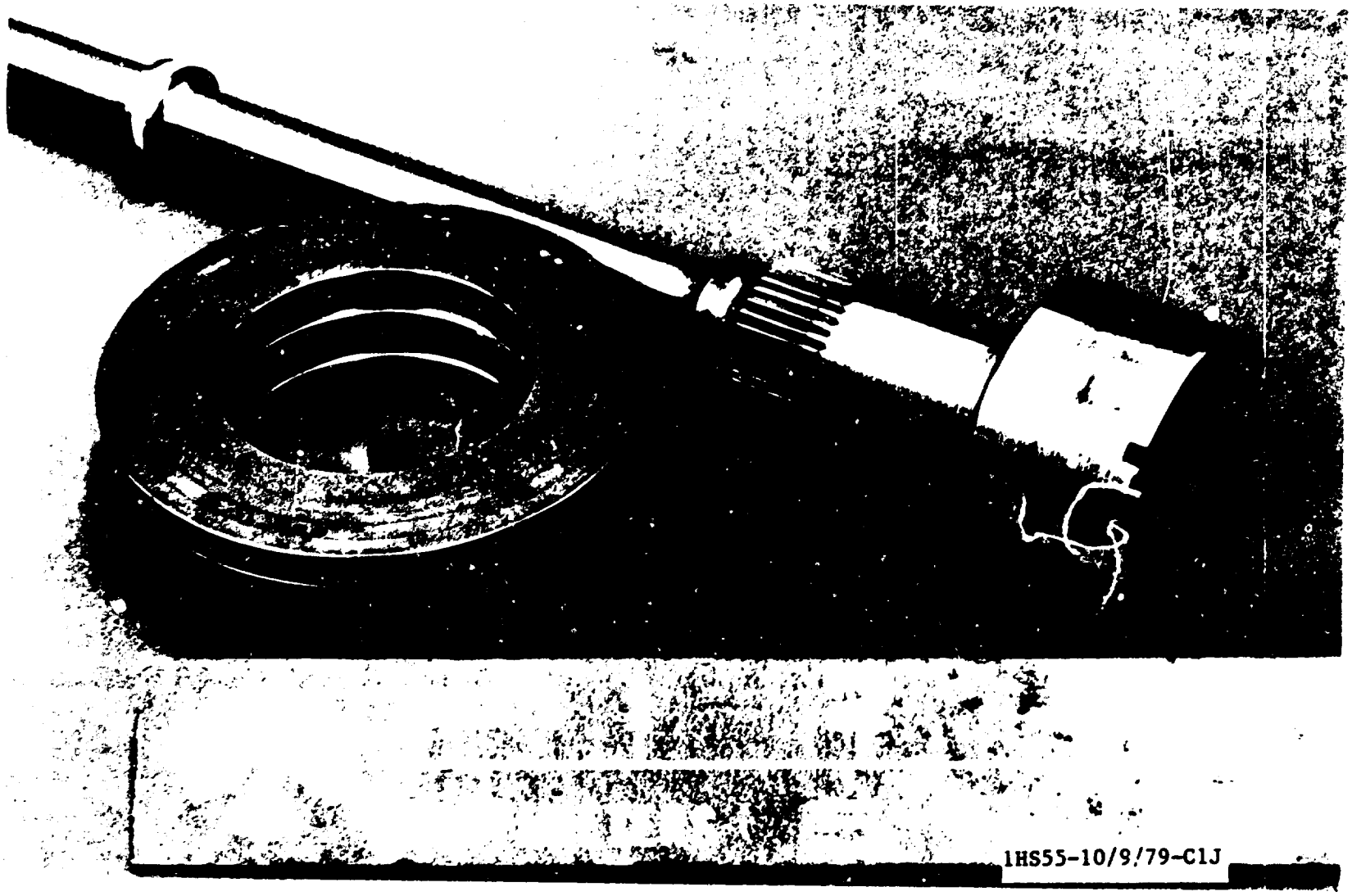

Figure 142. Shaft Seal and Tie Bolt

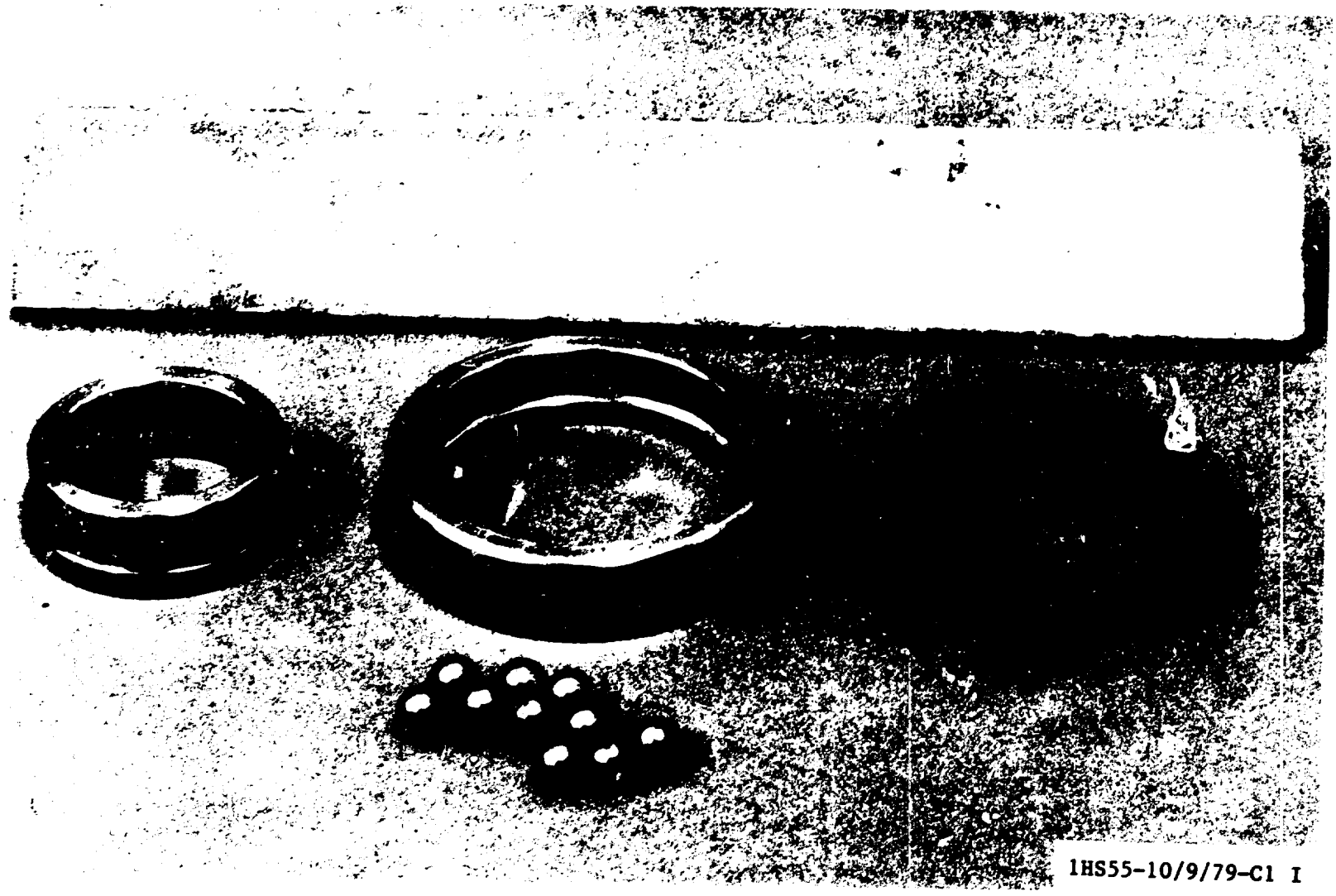

Figure 143. Closeup of Bearing Components

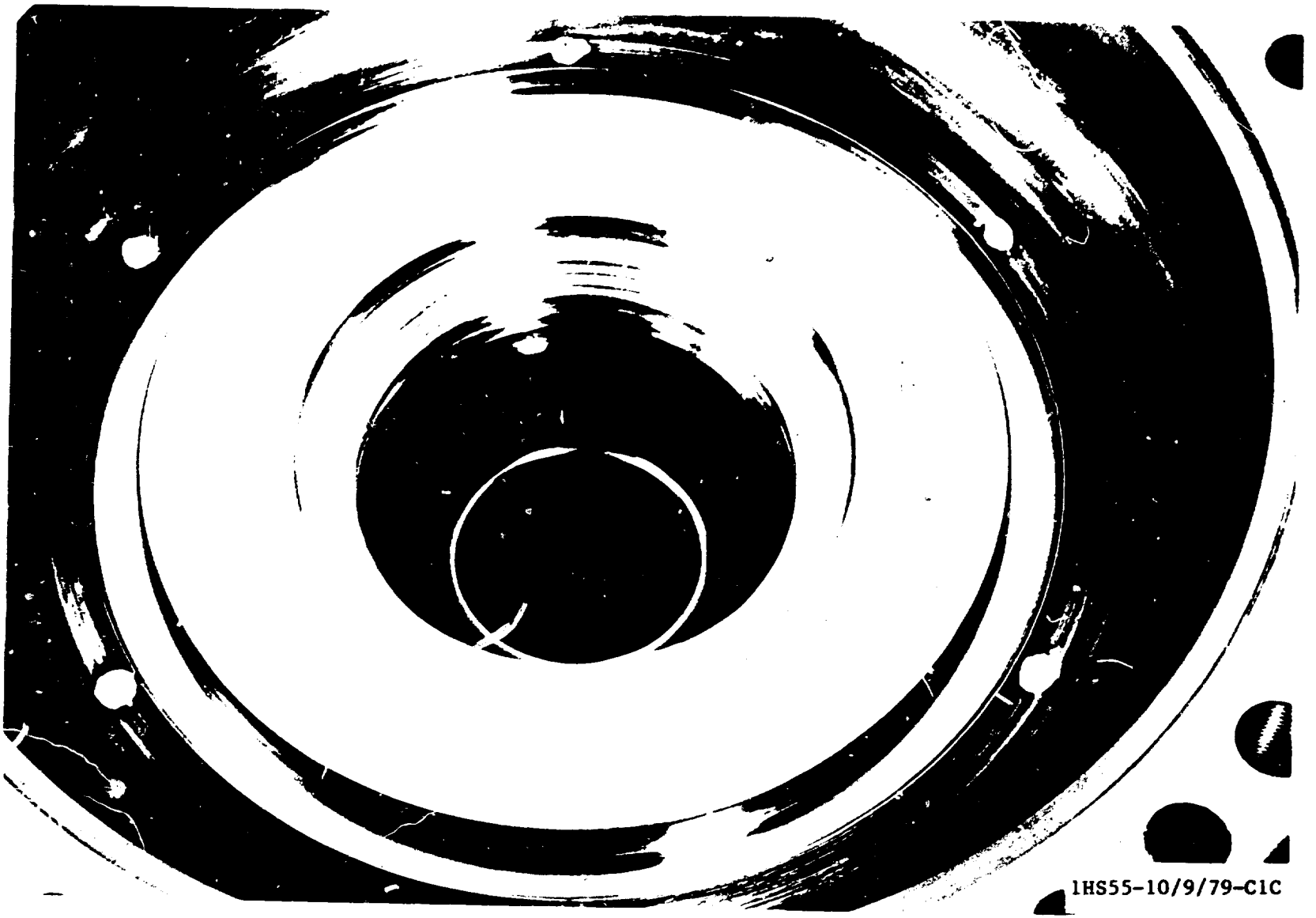

Figure 144. Axial Inlet and First Stage Wear Ring

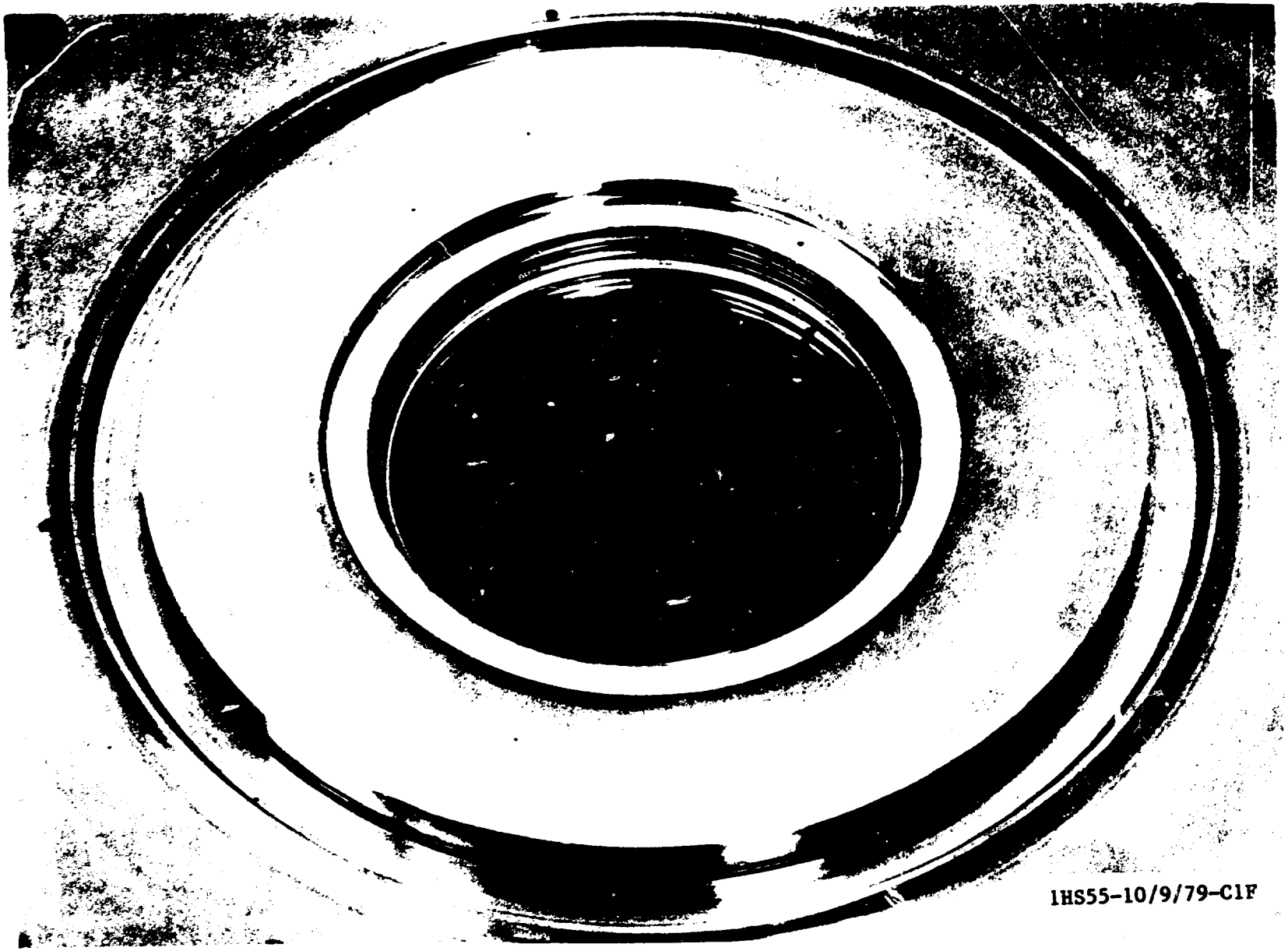

Figure 145. First Stage Crossover and Second Stage Wear Ring

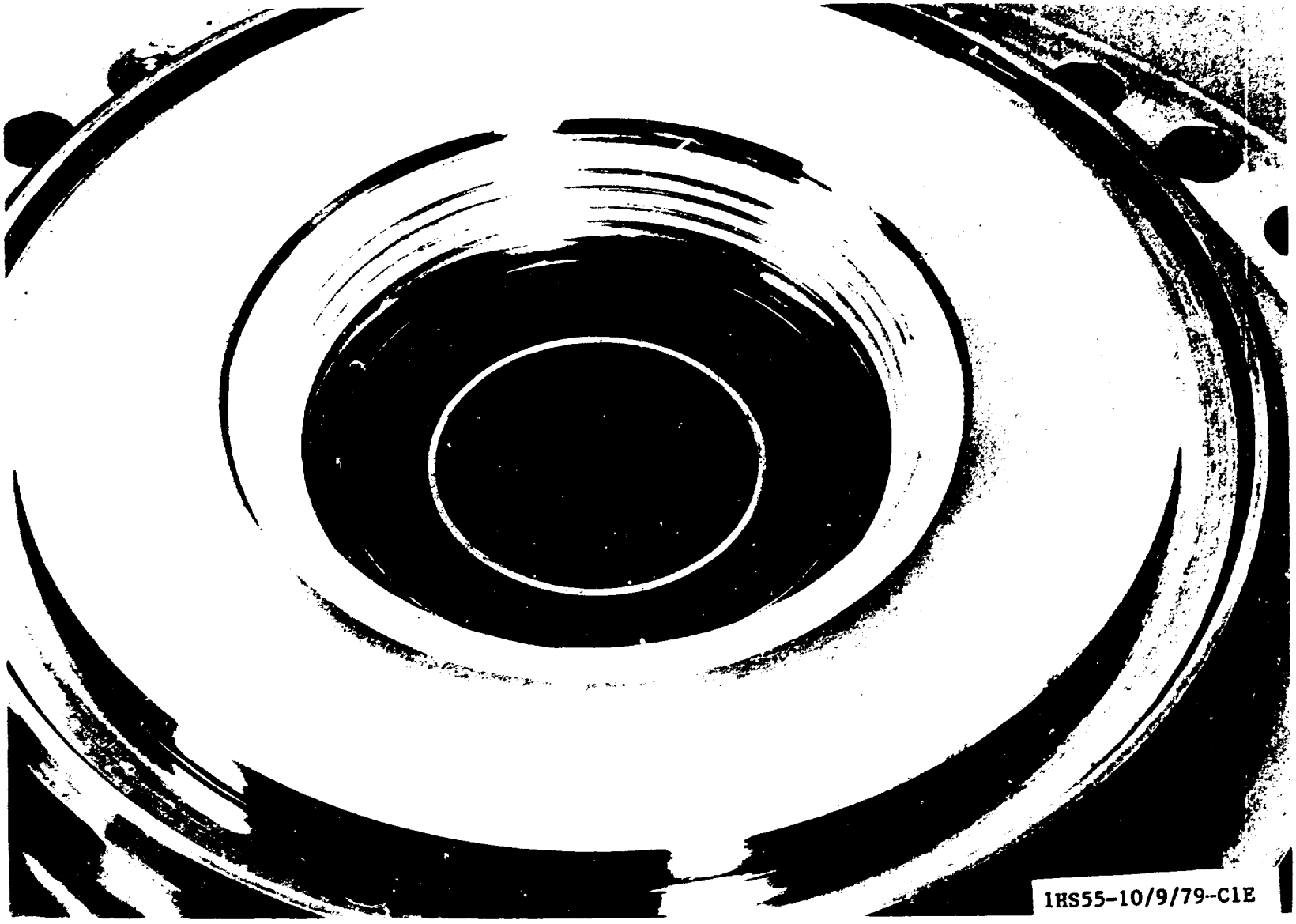

Figure 146. Second Stage Crossover and Third Stage Wear Ring

MK 48-F SECOND STAGE IMPELLER

Figure 147. Crack In Second Stage Impeller Shroud

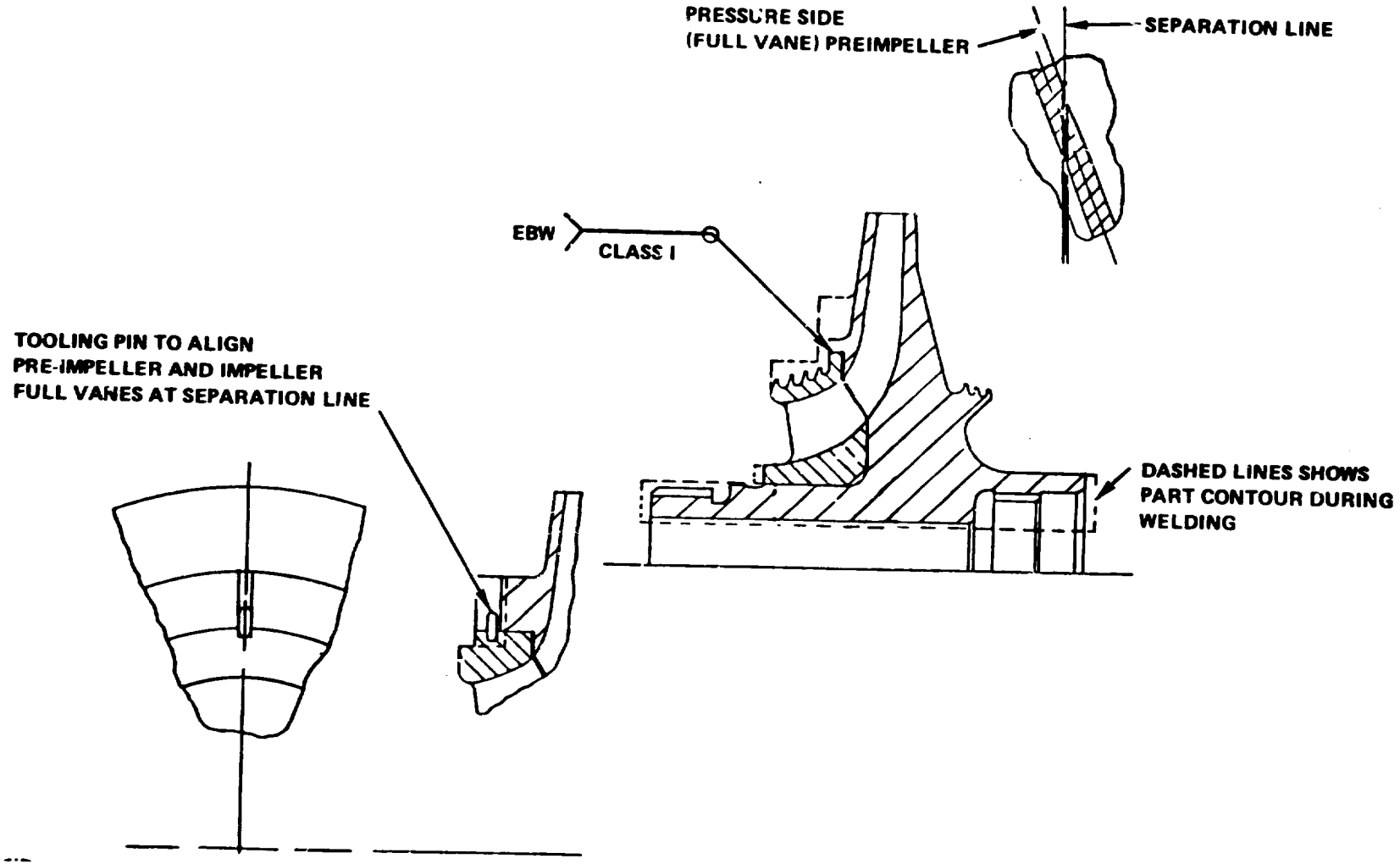

Figure 148. Electron Beam Weld of Split Impeller

CONCLUSIONS

From the results of the testing and analysis of the axial inlet configuration it can be concluded that the modified turbopump exhibits the following characteristics:

1. Adequate forward and aft bearing cooling during operation
2. Satisfactory balance piston operation at all speeds
3. Excellent suction performance at all operating speeds
4. Excellent head-flow efficiency pump characteristics

The high temperature level of the front bearing coolant noted in prior testing evidently was caused by heat soakback from the massive instrumentation cap. With the axial inlet, the temperature rise was small. Minor changes in the turbine end bearing coolant system to increase coolant flow corrected the high temperature levels of the coolant emanating from the bearing on previous testing programs.

The test results and analysis indicate the balance piston is operating satisfactorily at all operating speeds. Analysis indicates the balance piston position is nearly centered in its balance range, and adequate margin exists over the operating range of the turbopump.

From the test data, it can be concluded that the modifications implemented, including the axial inlet and inducer addition, has resulted in excellent pump suction performance. Values in excess of 36.7 (rad/s) $(m^3/s)^{1/2}/(J/kg)^{3/4}$ = (100,000 rpm•gpm $1/2/ft^{3/4}$) were obtained at high pump speeds. In the idle-mode conditions (2400 rad/s, 23,000 rpm), a capability of operating at zero NPSH without head loss was demonstrated. The increase in area at the inlet eye of the impeller to accept the wear ring leakage flow and the incorporation of an axial inlet with an inducer are credited to the large improvement in suction performance.

The head generated by the pump exceeded design requirements, and the isentropic efficiency was higher than predicted. It is concluded that this improvement over the previous test configuration is caused by the elimination of the cavitation effects by the aforementioned methods. A pump stall condition at flows below 70% of design flow was observed and documented.

During the testing, a resonance condition was identified around 9634 rad/s, (92,000 rpm) manifested by an increase in vibration levels. Rap tests of the turbopump and test stand and analysis of the test data indicate that it is a housing or test stand resonance condition. Additional effort is recommended to isolate and identify this phenomenon.

From the evaluation of mechanical integrity, the turbopump operated well. The disassembly of the unit disclosed a crack in a nonstructural weld in the second-stage impeller front shroud. This was traced to a weld quality deficiency and is easily correctable. All other turbopump components were in excellent condition.

In general, it can be concluded that the test program was extremely successful and the modifications made to the turbopump achieved their purpose, with the turbopump exhibiting excellent performance characteristics.

APPENDIX A

MARK 48-F TURBOPUMP
ASSEMBLY DRAWINGS
9R0011560
AND
RS009601E

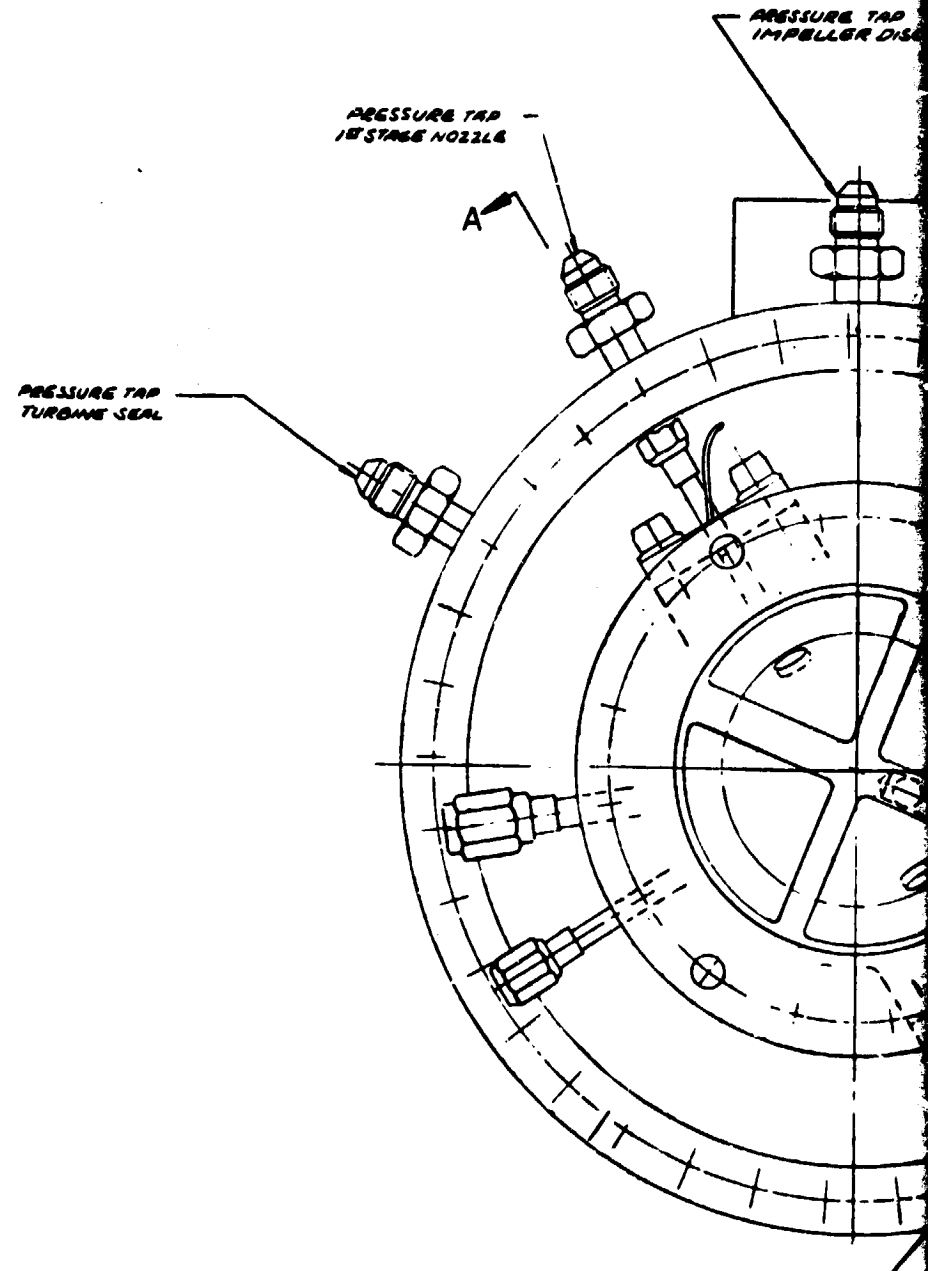

FOLDOUT FRAME

XEQP940368 SPEED TRANSDUCER 1 REQD
RD111-4010-0400 BOLT 2 REQD
RD173-5002-0004 WASHER 2 REQD
TORQUE 160 ± 8 IN LB

PRECEDING PAGE BLANK NOT FILMED

FOLDOUT FRAME 2

9R0011560

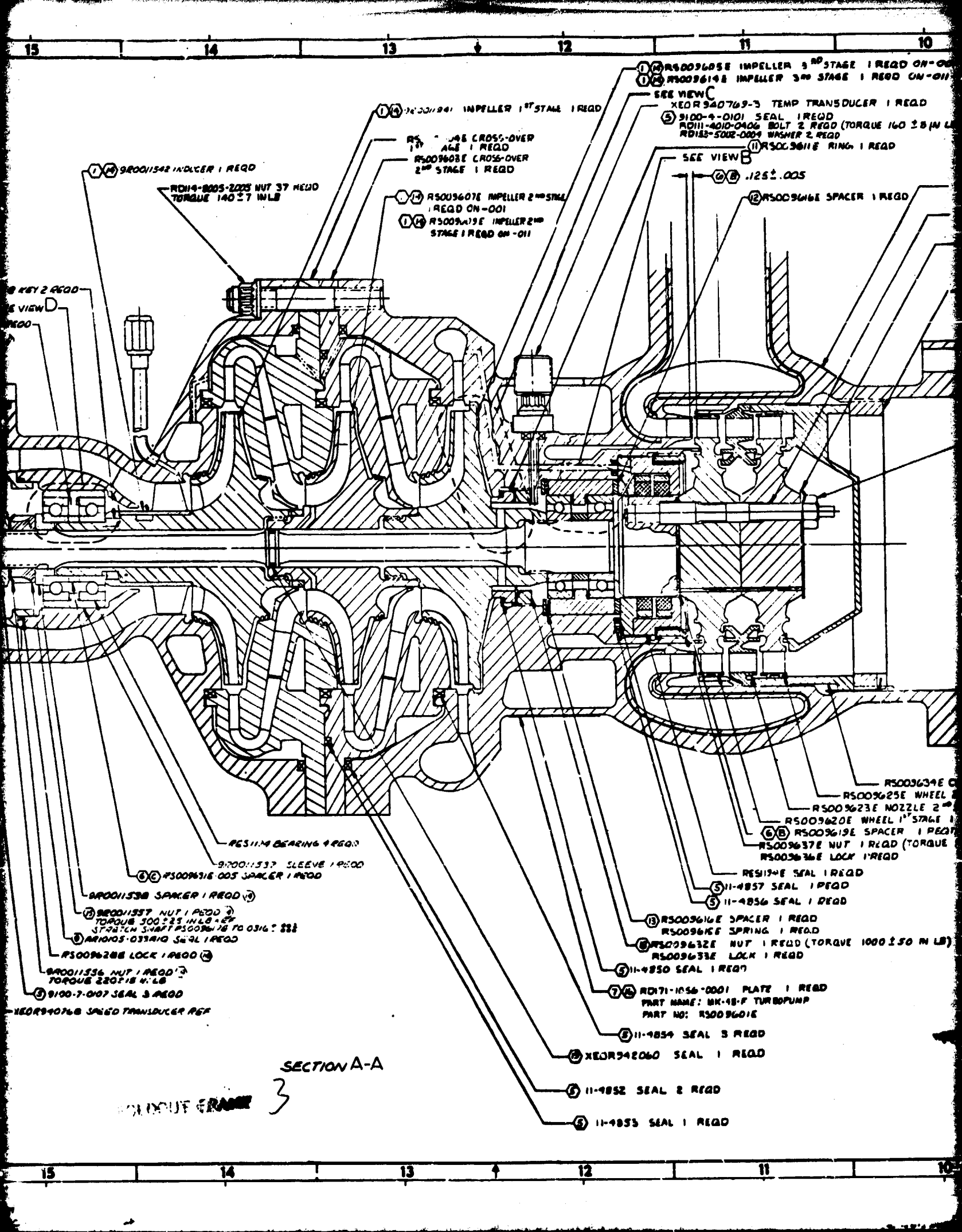
SEE VIEW C
SEE VIEW B
SEE VIEW D
.125 ± .005
RD114-8005-2005 NUT 37 REQD TORQUE 140 ± 7 IN LB
RD111-4010-0406 BOLT 2 REQD (TORQUE 160 ± 8 IN LB
RD183-5002-0004 WASHER 2 REQD
9100-4-0101 SEAL 1 REQD
XEOR940769-3 TEMP TRANSDUCER 1 REQD
RS0096118 RING 1 REQD
RS0096166 SPACER 1 REQD
RS0096085 IMPELLER 3RD STAGE 1 REQD ON-001
RS0096148 IMPELLER 3RD STAGE 1 REQD ON-011
RS0096038 CROSS-OVER 2ND STAGE 1 REQD
RS0096078 IMPELLER 2ND STAGE 1 REQD ON-001
RS0096198 IMPELLER 2ND STAGE 1 REQD ON-011
RS0096348
RS0096258 WHEEL
RS0096238 NOZZLE 2ND
RS0096208 WHEEL 1ST STAGE
RS0096198 SPACER 1 REQD
RS0096378 NUT 1 REQD (TORQUE
RS0096368 LOCK 1 REQD
RES1134 SEAL 1 REQD
11-4857 SEAL 1 REQD
11-4856 SEAL 1 REQD
RS0096168 SPACER 1 REQD
RS0096188 SPRING 1 REQD
RS0096328 NUT 1 REQD (TORQUE 1000 ± 50 IN LB)
RS0096338 LOCK 1 REQD
11-4850 SEAL 1 REQD
RD171-1056-0001 PLATE 1 REQD
PART NAME: MK-48-F TURBOPUMP
PART NO: RS0096018
11-4854 SEAL 3 REQD
XEOR942060 SEAL 1 REQD
11-4852 SEAL 2 REQD
11-4853 SEAL 1 REQD
RES1114 BEARING 4 REQD
9100-1-337 SLEEVE 1 REQD
RS0096318-005 SPACER 1 REQD
9R00-1538 SPACER 1 REQD
9R00-1557 NUT 1 REQD
TORQUE 500 ± 25 IN-LB + 6°
STRETCH SHAFT RS0096178 TO 0.316 ± .002
AR1005-033A10 SEAL 1 REQD
RS0096288 LOCK 1 REQD
9R00-1556 NUT 1 REQD
TORQUE 220 ± 8 IN-LB
9100-7-007 SEAL 3 REQD
XEOR940768 SPARE TRANSDUCER REF
KEY 2 REQD
VIEW D
REQD
SECTION A-A
3

STAGE 1 REQD ON-001
TAGE 1 REQD ON-011

NSDUCER 1 REQD
D
QD (TORQUE 160 ±8 IN LB)
QD
RING 1 REQD

SPACER 1 REQD

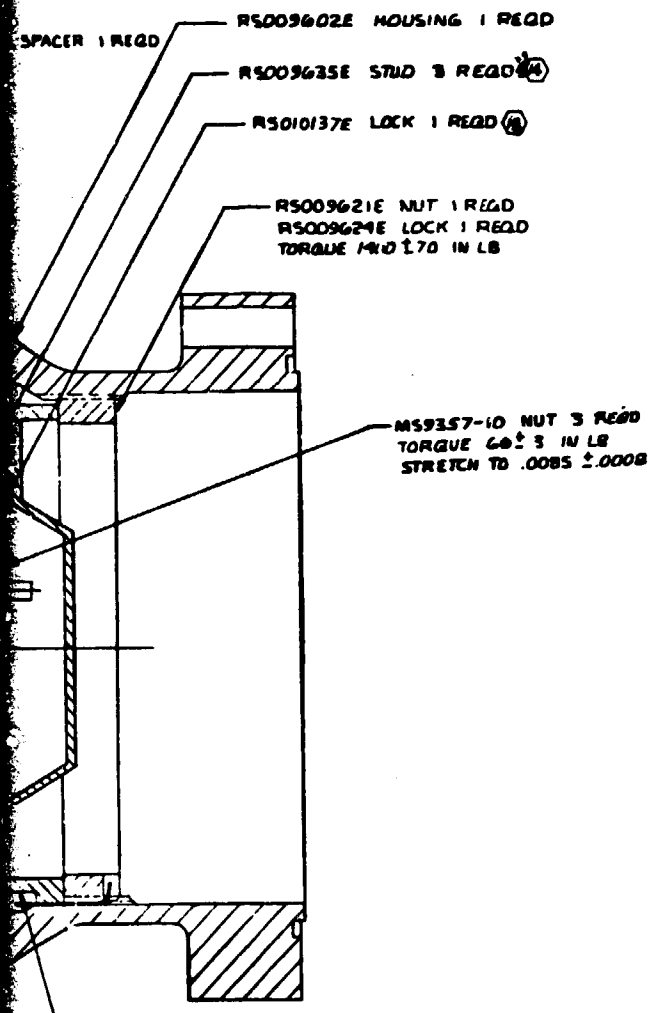

RS009625E WHEEL 2ND STAGE 1 REQD (14)
009623E NOZZLE 2ND STAGE 1 REQD
620E WHEEL 1ST STAGE 1 REQD (14)
9619E SPACER 1 REQD (14)
NUT 1 REQD (TORQUE 9200 ±460 IN LB)
LOCK 1 REQD
REQD
QD
QD

RQUE 1000 ±50 IN LB)

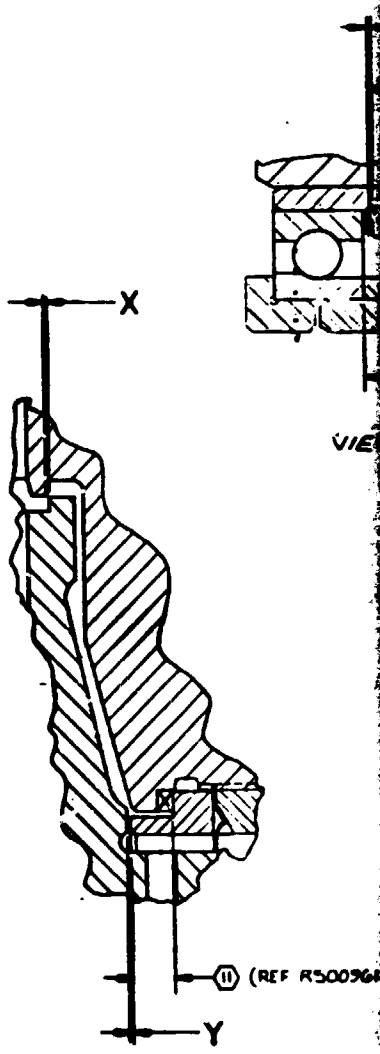

ORIGINAL PAGE IS
OF POOR QUALITY

4

Rockwell International Corporation
Rocketdyne Division
Canoga Park, California

SIZE	CODE IDENT NO.	DWG NO.	REV
		9R0011560	

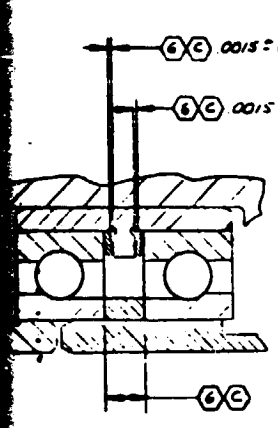

VIEW D

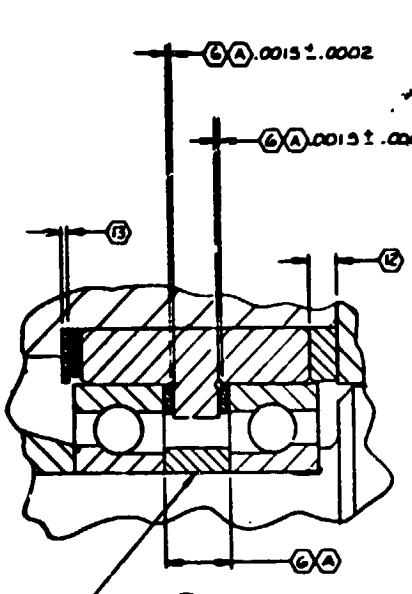

VIEW B

6A RS009631E -003 SPACER .1480

(F RS009611E RING)

38	INSTALL WITH OPEN END TOWARD TURBINE.
39	LUBRICATE WITH MOLYKOTE TYPE Z POWDER PER BAC112-002 METHOD V ON MATING SURFACE OF RS009632E & RS009633E.
37	PRIOR TO ASSEMBLY, CLEAN PER BAC110-000. USE MIL-C-81302 ONLY FOR PARTS CODED (1).
36	APPLY PER BAC106 OIL.
35	SPRAY GS-3 TEFLON LUBE, RAM CHEMICAL INC. GARDENA, CAL. TO RS009627E NUT & MATING SURFACES.
34	BALANCE ROTOR ASSEMBLY TO WITHIN .02 GRAM INCHES. MATCH MARK ALL ROTOR ASSEMBLY COMPONENTS PER BAC106-000 BY ELECTRO CHEM ETCH. CODED PARTS ARE COMPONENTS OF THE ROTOR ASSEMBLY. ALIGN MATCHMARKS.
33	MACHINE SPACER THICKNESS PER DETAIL DRAWING TO OBTAIN AT LIQUID NITROGEN TEMPERATURE A FORCE OF 400 ± 50 LB ON THE ROTOR WHEN CLEARANCE Y IS .000" INCH.
32	MACHINE SPACER THICKNESS PER DETAIL DRAWING TO OBTAIN AT LIQUID NITROGEN TEMPERATURE A FORCE OF 400 ± 50 LB ON THE ROTOR WHEN CLEARANCE Y IS ZERO.
31	MACHINE DIMENSION PER DETAIL DRAWING TO OBTAIN X = 0, WHEN Y = .0042 ± .0002 AT AMBIENT TEMPERATURE.
30	SEALOL-NEVADA CORP, MINDEN, NEVADA.
29	AEROHYDRONICS, JACK[illegible], MICH.
8	INSTALL FITTING AND TUBE ASSEMBLIES PER BAC102-003.
7	IDENTIFY PER BAC106-000.
6	MACHINE SPACER PER DETAIL DRAWING TO OBTAIN MATCH CODED DIMENSIONS.
5	HYDRODYNE DIVISION, F. P. I. INC, NORTH HOLLYWOOD, CA.
4	INSTALL PROTECTIVE COVERS OVER ALL EXPOSED FLANGES, TUBE FITTING & PORTS.
3	LEAK CHECK PUMP ASSEMBLY. ALLOWABLE LEAKAGE RATES: ALL EXTERNAL FLANGES ZERO; ALL FITTINGS ZERO; SHAFT SEAL 150 SCIM MAX He GAS
	TEST CONDITIONS FOR LEAK TEST: UP STREAM 30 ± 1 PSIG; DOWN STREAM ATMOS; TEMP AMBIENT
2	INSTALL THREADED FASTENERS PER BAC101-002.
(1)	TITANIUM PART. CLEAN WITH MIL-C-81302 ONLY.

ASSY NO
-001
-011

211

TURBOPUMP ASSY, FUEL

J 02602 9RC011560

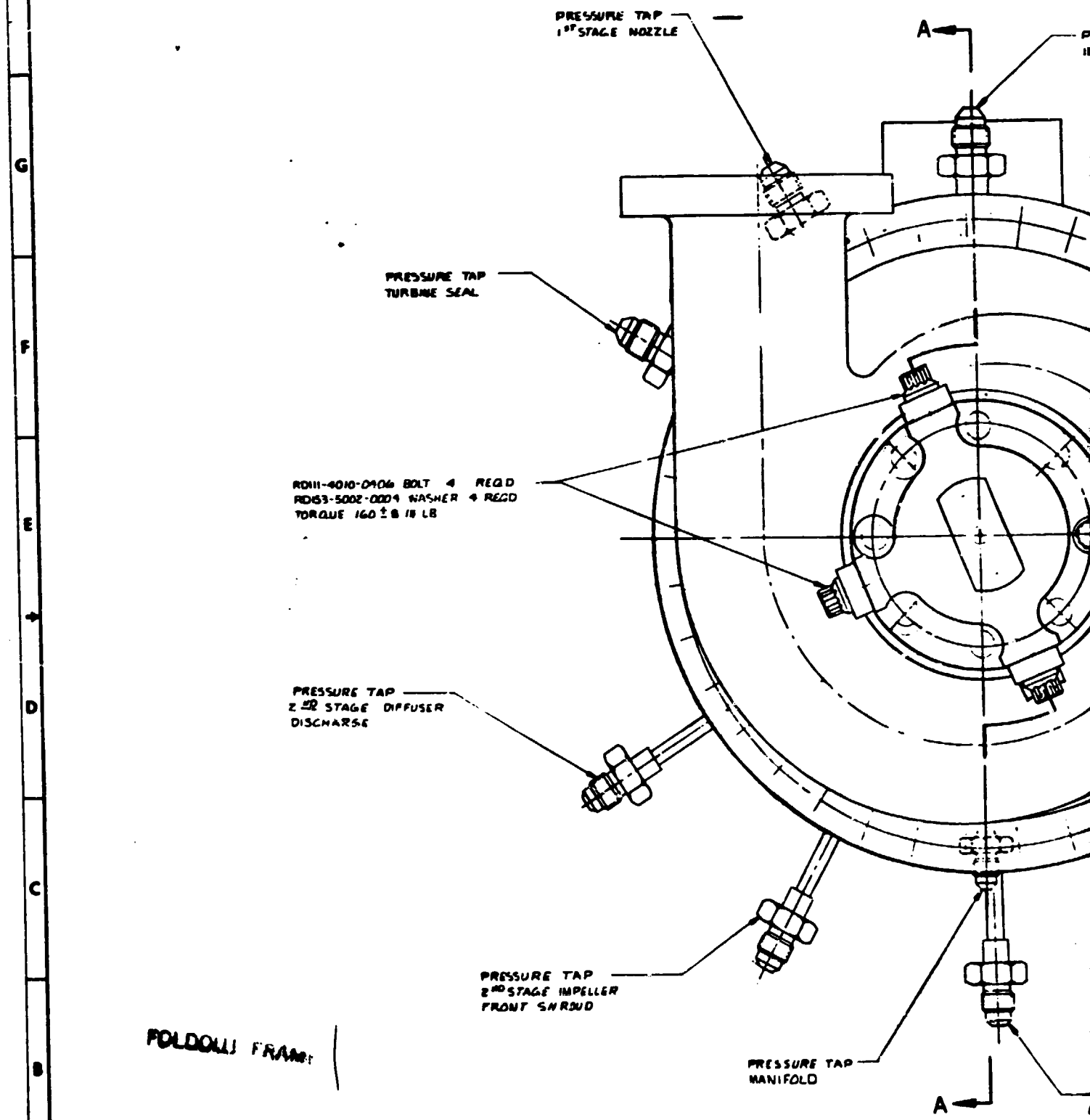

FOLDOUT FRAME

PRECEDING PAGE BLANK NOT FILMED

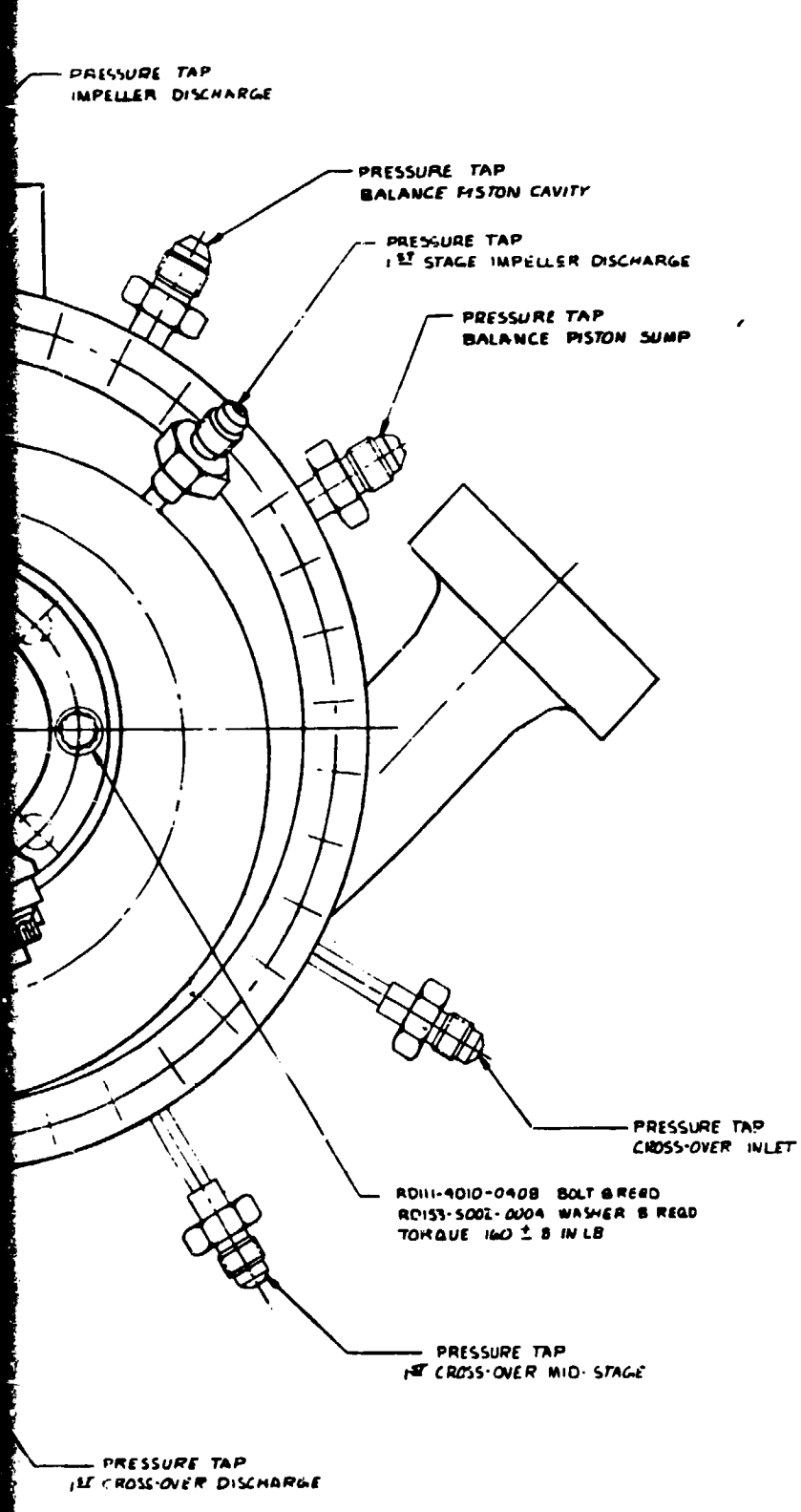

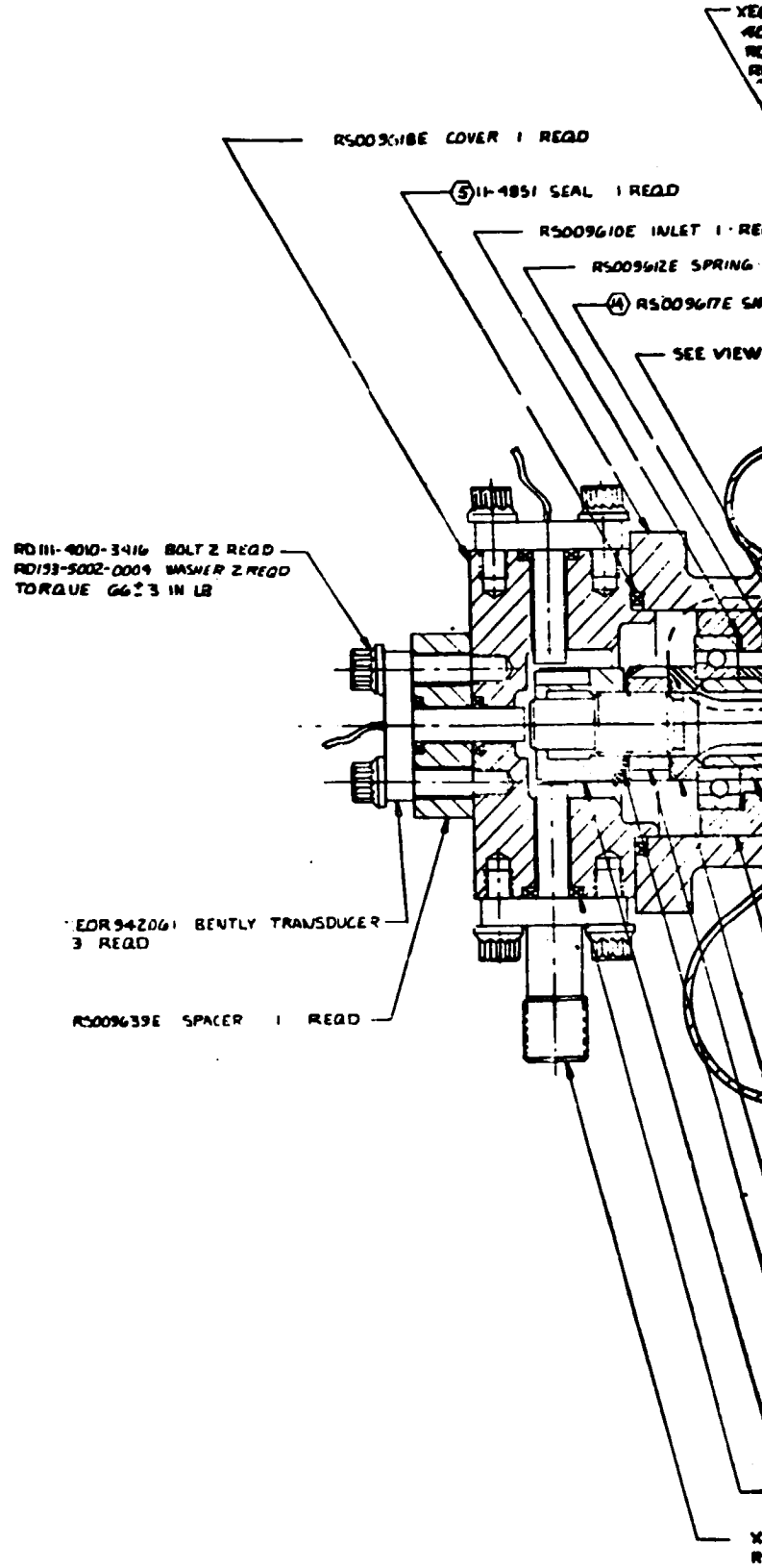

FOLDOUT FRAME 2

RS0096D1E

SEE VIEW C
SEE VIEW B
.125 ± .005
RS009634E COVER 1 REQD
RS009625E WHEEL 2ND STAGE 1 REQD
RS009623E NOZZLE 2ND STAGE 1 REQD
RS009620E WHEEL 1ST STAGE 1 REQD
RS009637E NUT 1 REQD (TORQUE 9200 ± 460 IN LB)
RS009636E LOCK 1 REQD
RES1194 SEAL 1 REQD
11-4857 SEAL 1 REQD
11-4856 SEAL 1 REQD
RS009616E SPACER 1 REQD
RS009615E SPRING 1 REQD
RS009632E NUT 1 REQD (TORQUE 1000 ± 50 IN LB)
RS009633E LOCK 1 REQD
11-4850 SEAL 1 REQD
RD171-1056-0001 PLATE 1 REQD
PART NAME: MK-48-F TURBOPUMP
PART NO: RS009601E
11-4854 SEAL 3 REQD
XEOR942060 SEAL 1 REQD
11-4852 SEAL 2 REQD
11-4853 SEAL 1 REQD
RES1174 BEARING 4 REQD
RS009631E SPACER 2 REQD
RS009630E SLEEVE 2 REQD
RS009629E SPACER 1 REQD
RS009627E NUT 1 REQD
TORQUE 500 ± 25 IN LB (REF)
STRETCH SHAFT RS009617E TO .0316 +.002 -.000
RS009628E LOCK 1 REQD
RS009626E NUT 1 REQD
TORQUE 220 ± 15 IN LB
9100-7-0107 SEAL 5 REQD
SECTION A-A
RS009605E WHEEL 3RD STAGE REQD
XEOR940769-3 TEMP TRANSDUCER 1 REQD
9100-4-0101 SEAL 1 REQD
RD111-4010-0406 BOLT 2 REQD (TORQUE 160 ± 8 IN LB)
RD153-5002-0004 WASHER 2 REQD
RS009611E RING 1 REQD
RS009608E IMPELLER 1ST STAGE 1 REQD
RS009604E CROSS-OVER 1ST STAGE 1 REQD
RS009603E CROSS-OVER 2ND STAGE 1 REQD
RS009607E IMPELLER 2ND STAGE 1 REQD
RS009616E SPACER 1 REQD
RS009602E HOU
RS009635E STUD
RS009638E LOCK
RS009621E
RS009624E
TORQUE 1400
940769-5 TEMP TRANSDUCER 1 REQD
664 SEAL 1 REQD
4010-0408 BOLT 2 REQD
53-5002-0004 WASHER 2 REQD
RQUE 160 ± 8 IN LB
RD114-8005-2005 NUT 37 REQD
TORQUE 140 ± 7 IN LB
REQD
T 1 REQD
OR940768 SPEED TRANSDUCER 1 REQD
4010-0406 BOLT 2 REQD
53-5002-0004 WASHER 2 REQD
QUE 160 ± 8 IN LB
FOLDOUT FRAME 3
FOLDOUT FRAME 2
14
13
12
11
10

REQD (14)

R 1 REQD

UE 160 ± 8 IN LB)

REQD

1 REQD — RS009602E HOUSING 1 REQD

RS009635E STUD 3 REQD (14)

RS009638E LOCK 1 REQD (14)

RS009621E NUT 1 REQD
RS009624E LOCK 1 REQD
TORQUE 1400 ± 70 IN LB

MS9357-10 NUT 3 REQD
TORQUE 60 ± 3 IN LB
STRETCH TO .0085 ± .0008

— RS009634E COVER 1 REQD
09625E WHEEL 2ND STAGE 1 REQD (14)
3E NOZZLE 2ND STAGE 1 REQD
WHEEL 1ST STAGE 1 REQD (14)
SPACER 1 REQD (14)
1 REQD (TORQUE 9200 ± 460 IN LB)
) REQD

000 ± 50 IN LB)

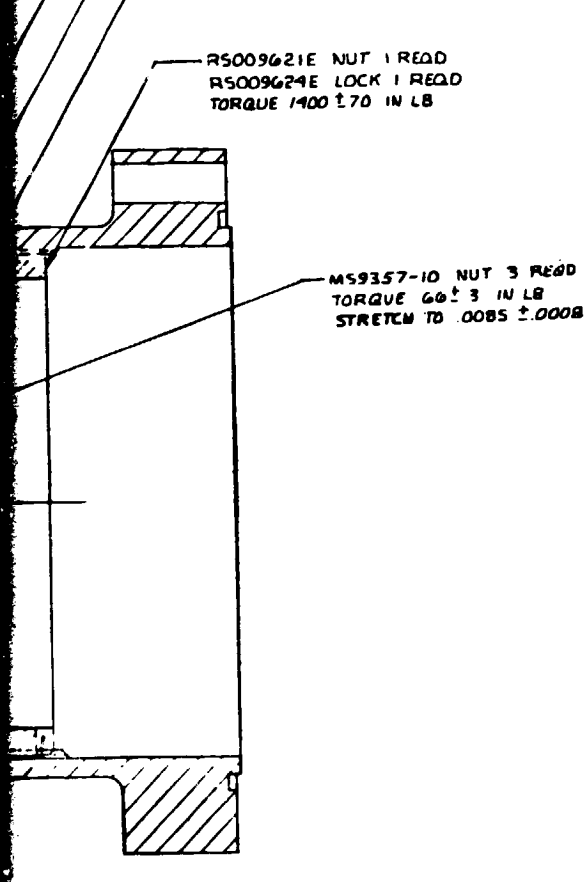

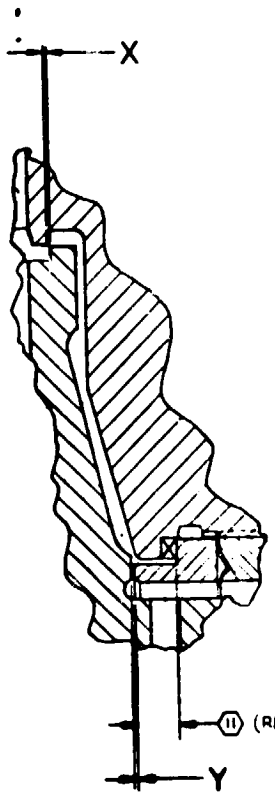

VIEW C

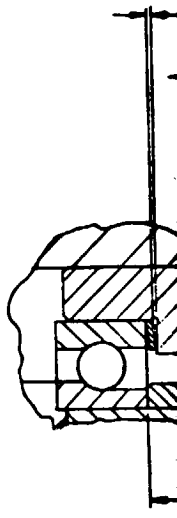

VIEW

FOLDOUT FRAME 4

Rocketdyne Division
RS009601E

REVISIONS					
SHEET	LTR	DESCRIPTION		DATE	APPROVED
1		1. NAV OR REVISED 2. RELEASE CHANGE 3. SHEET OR REVISED 4. NON SHOP PRACTICE 5. PARTS MADE OR			

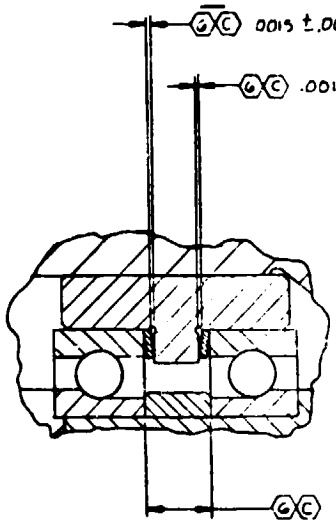

VIEW D

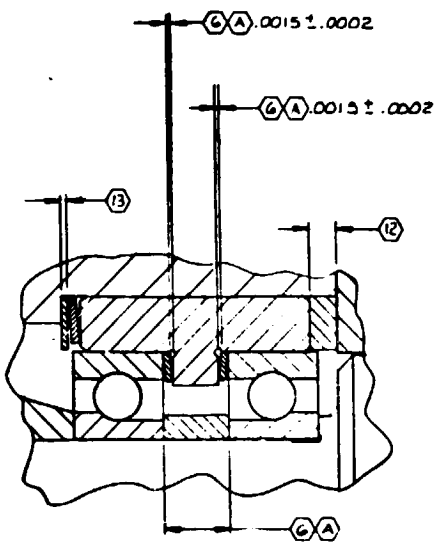

VIEW B

(REF RS0096IIE RING)

(18) INSTALL WITH OPEN END TOWARD TURBINE.
(17) LUBRICATE WITH MOLYKOTE TYPE Z POWDER PER RA0112-002 METHOD V ON MATING SURFACE OF RS0096332E & RS0096333E
(16) PRIOR TO ASSEMBLY, CLEAN PER RA0110-004. USE MIL-C-81302 ONLY FOR PARTS CODED (1).
(15) APPLY PER RA0106 010.
(14) SPRAY GS-3 TEFLON LUBT, RAM CHEMICAL INC. GARDENA, CAL, TO RS0096771E NUT & MATING SURFACES.
(13) BALANCE ROTOR ASSEMBLY TO WITHIN .02 GRAM INCHES MATCH MARK ALL ROTOR ASSEMBLY COMPONENTS PER RA0104-008 BY ELECTRO CHEM ETCH. CODED PARTS ARE COMPONENTS OF THE ROTOR ASSEMBLY. ALIGN MATCHMARKS.
(12) MACHINE SPACER THICKNESS PER DETAIL DRAWING TO OBTAIN AT LIQUID NITROGEN TEMPERATURE A FORCE OF 600 ± 50 LB ON THE ROTOR WHEN CLEARANCE Y IS .0097 INCH.
(11) MACHINE SPACER THICKNESS PER DETAIL DRAWING TO OBTAIN AT LIQUID NITROGEN TEMPERATURE A FORCE OF 600 ± 50 LB ON THE ROTOR WHEN CLEARANCE Y IS ZERO.
(10) MACHINE DIMENSION PER DETAIL DRAWING TO OBTAIN X = 0, WHEN Y = .0042 ± .0002 AT AMBIENT TEMPERATURE.
(9) BENTLY-NEVADA COMP. MINDEN, NEVADA.
(8) ACCROTRONICS, JACKSON, MICH.
(7) INSTALL FITTING AND TUBE ASSEMBLIES PER RA0102-005.
(6) IDENTIFY PER RA0104-008.
(5) MACHINE SPACER PER DETAIL DRAWING TO OBTAIN MATCH CODED DIMENSIONS.
(4) HYDRODYNE DIVISION, F. P. I. INC. NORTH HOLLYWOOD, CA.
(3) INSTALL PROTECTIVE COVERS OVER ALL EXPOSED FLANGES, TUBE FITTING & PORTS.
(2) LEAK CHECK PUMP ASSEMBLY. ALLOWABLE LEAKAGE RATES:

ALL EXTERNAL FLANGES	ZERO
ALL FITTINGS	ZERO
SHAFT SEAL	150 SCIM MAX No GAS

TEST CONDITIONS FOR LEAK TEST:

UP STREAM	30 ± 1 PSIG
DOWN STREAM	ATMOS
TEMP	AMBIENT

(1) INSTALL THREADED FASTENERS PER RA0101-002.
(1) TITANIUM PART. CLEAN WITH MIL-C-81302 ONLY.

FOLDOUT FRAME 5

213

NONE		Rocketdyne International Corporation Rocketdyne Division Canoga Park, California	
NONE		TURBOPUMP ASSY, F.I.E.	
		1	02602 RS0096IIE

MK48-F

APPENDIX B

DISTRIBUTION LIST